University of Warsaw

Faculty of Chemistry

Optical spectroscopy of selected divalent silver compounds

Jakub Gawraczyński

Doctoral thesis, 2013 – 2019

realized at the Laboratory of Technology of Novel Functional Materials, Center of New Technologies, University of Warsaw

under the guidance of Prof. Wojciech Grochala

Warsaw, April 2019

To my beloved wife, Weronika

Acknowledgments

I would like to thank my advisor, Professor Wojciech Grochala for guidance, valuable discussions, sharing his knowledge and giving me many opportunities to acquire new skills. I am grateful to my colleagues from the Geophysical Laboratory at Carnegie Institution of Washington: Dr. Maddury Somayazulu, Dr. Todd Zapata and others, for showing me the beauty of high-pressure experiments. In particular, I would like to thank Dr. Viktor Struzhkin, who gladly shared his vast knowledge with me, and helped me selflessly in all matters.

I would like to express my gratitude to dr. Mariana Derzsi D.Sc. and dr. Jose Lorenzana, for excellent cooperation and carrying out the theoretical calculations, which proved essential for my research.

I would like to thank all people with whom I have had the opportunity to cooperate, or whose work has helped me in my research, especially to Prof. Wojciech Gadomski, Dr. Maciej Ptak, and Mr. Maciej Zosicz, for technical assistance and keeping company during long measurements.

In particular, I would like to thank the current and former members of the LTNMF, especially:

- Dr. Dominik Kurzydłowski and dr. Tomasz Jaroń, for all mental and technical support with high-pressure experiments
- Dr. Piotr Leszczyński for fruitful discussions and performing literature searches
- Fellow PhD students: Agnieszka Starobrat, Rafał Owarzany, Wojciech Wegner, Piotr Orłowski, Kacper Koteras for sharing the amazing experience of slowly transforming into scientists
- My friend and collaborator, Dr. Adam Grzelak, for keeping spirits high, exchanging ideas with me, and the immeasurable help he provided.

I would like to thank my wife, Weronika, for her love and support during these years. I am very grateful to my whole family and all friends for motivating me and being there for me from start to finish. And finally, I am grateful for things that made it a little bit easier to focus and try again: escitalopram and caffeine.

Financial contributions

Studies presented in this work were made possible by contributions from following funding sources:

- "HP" project from Polish National Science Center (NCN), grant no. 2012/06/M/ST5/00344, led by Prof. Wojciech Grochala

NARODOWE CENTRUM NAUKI

- Calculations performed by Dr Mariana Derzsi were carried out using ADVANCE-PLUS supercomputer under grant no. GA67-13 at Interdisciplinary Center for Mathematical and Computational Modelling (ICM), led by Prof. Wojciech Grochala

- Raman scattering studies of AgF_2 sample under high-pressure, conducted in non-hydrostatic conditions were carried out as a DSM project funded by the Polish Ministry of Science, grant no. 501-D112-86-DSM-115100, led by myself.
- Inelastic neutron scattering studies of AgF_2 were carried out with Xpress access to the ISIS Facility at Rutherford Appleton Laboratory.

I would like to thank all funding bodies that enabled me conducting this research.

(EN) Abstract

This doctoral dissertation describes research on silver compounds carried out with a range of spectroscopic methods, based on absorption or on inelastic scattering. The main focus of the thesis was on divalent silver compounds: silver(II) fluoride AgF_2, silver(II) sulfate(VI), $AgSO_4$, and its monohydrate, fluorosilver(II) fluoroborate $(AgF)BF_4$, cesium fluoroargentate(II) $CsAgF_3$, rubidium fluoroargentate(II) $RbAgF_3$, and high-temperature form of $KAgF_3$. In addition, other silver compounds were investigated, particularly silver(I) fluoride (as a key reference sample) and silver(I, III) oxide AgO. All compounds were studied by Fourier-transform spectroscopy in the far infrared range. Some of the compounds were also investigated with Raman spectroscopy, medium- and near-infrared absorption spectroscopy, as well as absorption spectroscopy in the visible and ultraviolet range and by inelastic neutron scattering. Three compounds were examined by Raman spectroscopy under elevated pressure: AgO, AgF and AgF_2. The main scope of the work was to get insight into vibrational structure of the studied compounds as well as understand their pressure-induced phase transitions (wherever applicable). The second goal was to determine magnetic superexchange constant for two-dimensional AgF_2 from Raman scattering spectra, and for one-dimensional $AgFBF_4$ from NIR-absorption spectra. The auxiliary goal, dictated by the course of the experimental work, was to understand photochemical decomposition of AgF_2 and $AgSO_4$.

The work is divided to a literature review and a description of experimental results. The literature part consists of five chapters. The first describes the properties of divalent silver compounds with an emphasis on crystalline structures adopted by the compounds described in the experimental part, as well as factors affecting these structures. The second chapter summarizes the current state of knowledge on the crystal structures and spectroscopic properties of relevant silver compounds and two reference compounds: one-dimensional Sr_2CuO_3 and two-dimensional La_2CuO_4. The third provides an abridged description of physics relevant to the research methods used in experiments as well as summarizes the assumptions of the notation used to describe the experiments. The fourth chapter includes information on the magnetic ordering of materials and discussion of the selected techniques. The last chapter of literature part briefly describes the selected methods of testing substances under high pressure and sums up the current knowledge about the properties of compounds studied here in the high-pressure regime.

The experimental part consists of three chapters. The first describes the experimental setups used during the research. The next one contains a detailed description of the results.

The spectroscopic measurements of silver(II) sulphate(VI) prepared using the new electrosynthesis method in concentrated sulfuric(VI) acid showed its similarity with the product of chemical synthesis developed earlier, albeit substantial differences in reactivity to water vapor were also found. In addition, the laser-induced decomposition of $Ag^{II}SO_4$ was observed and it was shown that the decomposition product is dependent on the wavelength of the laser used. A similar photosensitivity was observed for silver(II) sulfate(VI) monohydrate. The hydrate was also characterized spectroscopically in the wide range from far-infrared to ultraviolet, which allowed determination of the orbital splitting parameters as well as has provided the supplementary evidence for the presence of water molecules in its crystal structure.

Research on silver fluoride (I) at high pressure showed the presence of several Raman bands in contrast with predictions of group theory (no Raman-active bands), some of them probably originating from color centers or overtone of the IR-active fundamental. Research on silver (II) fluoride proved its high photosensitivity to laser light. The product of laser-induced photodecomposition has been studied in the range from atmospheric pressure up to 47 GPa. It seems that photodecomposition leads to a derivative containing $Ag(II)F_4^{2-}$ anion, notably $Ag(I)_2Ag(II)F_4$, which is the first mixed-valence Ag(I)/Ag(II) fluoride known. Pressure dependence of the characteristic Raman band for this phase was measured up to 47 GPa.

In addition, using Raman scattering spectroscopy and inelastic neutron scattering, I have successfully identified and measured for the first time the bimagnon transitions in two-dimensional antiferromagnet, AgF_2, and determined the value of the intra-sheet magnetic superexchange constant, J. The large value of J=70 meV sets this compound second only to lamellar oxocuprates(II).

Fluorosilver(II) fluoroborate has been characterized by Raman scattering, inelastic neutron scattering, infrared Fourier spectroscopy and mid-infrared reflection spectroscopy. The characteristic band appearing in the NIR absorption spectra enabled me to estimate the intra-chain magnetic superexchange constant for this compound to be about 270 meV. This value is immense, and it surpasses the largest known superexchange constant ever measured (240 meV for Sr_2CuO_3).

Research on silver oxide(I, III) conducted under a high pressure showed no pressure-induced decomposition or comproportionation of this compound to no less than 74 GPa. In addition, due to the good agreement of the experimental Raman band positions with those derived from the theoretical calculations made on the AgO high-pressure models, it was possible to demonstrate the existence of two structural phase transitions in the pressure range from 0 to 74 GPa. The obtained spectroscopic results helped to confirm findings from the powder x-ray diffraction (described in Dr A. Grzelak's PhD Thesis).

The last element of the chapter is a description of the research carried out on three alkali metal fluoroargentates: $CsAgF_3$, $RbAgF_3$, and high-temperature form of $KAgF_3$. Despite clear structural differences between them, the Fourier transmission spectra in the far infrared range of all compounds show substantial similarity. Accurate assignment of bands measured in this work requires additional theoretical calculation of phonon dispersion to be performed.

The last chapter is a summary of the research carried out during the doctoral studies and presents suggestion for further research.

(PL) Streszczenie pracy

Niniejsza rozprawa doktorska opisuje badania związków srebra wykonane metodami spektroskopowymi. Główny nacisk został położony na związki srebra dwuwartościowego: fluorek srebra(II) AgF_2, siarczan(VI) srebra(II) wraz ze swoim monohydratem, tetrafluoroboran fluorosrebra(II) $(AgF)BF_4$, fluorosrebrzan(II) cezu $CsAgF_3$, rubidu $RbAgF_3$, oraz wysokotemperaturowa forma fluorosrebrzanu(II) potasu, HT-$KAgF_3$ Ponadto zbadane zostały inne związki srebra: fluorek srebra(I) (jako ważny układ referencyjny) oraz tlenek srebra(I,III) AgO. Wszystkie związki zostały zbadane za pomocą spektroskopii fourierowskiej w zakresie dalekiej podczerwieni. Część związków zbadana została również za pomocą spektroskopii ramanowskiej, spektroskopii absorpcyjnej w zakresie średniej i bliskiej podczerwieni, jak również za pomocą spektroskopii elektronowej z zakresu światła widzialnego i ultrafioletu oraz za pomocą nieelastycznego rozpraszania neutronów. Trzy związki, AgO, AgF i AgF_2 zostały zbadane metodą spektroskopii Ramana pod zwiększonym ciśnieniem. Głównym celem pracy było zrozumienie struktury oscylacyjnej badanych związków, jak też wniknięcie w naturę ich przemian strukturalnych pod wysokim ciśnieniem (dla wybranych układów). Drugim celem było oszacowanie stałej nadwymiany magnetycznej dla dwuwymiarowego AgF_2 z użyciem spektroskopii Ramana, a dla jednowymiarowego $AgFBF_4$ z użyciem spektroskopii absorpcyjnej w zakresie NIR. Celem ubocznym, który wyniknął w trakcie prowadzenia prac badawczych, było zrozumienie rozkładu fotochemicznego AgF_2 i $AgSO_4$.

Praca podzielona jest na część literaturową i część eksperymentalną. Wstęp teoretyczny składa się z pięciu rozdziałów. Pierwszy opisuje właściwości związków srebra dwuwartościowego z naciskiem na struktury krystaliczne które przyjmują związki opisane w części eksperymentalnej, jak również wpływ temperatury i ciśnienia zewnętrznego na rzeczone struktury. Drugi rozdział podsumowuje obecny stan wiedzy na temat struktur krystalicznych i właściwości spektroskopowych związków srebra i dwóch ważnych układów referencyjnych: jednowymiarowego Sr_2CuO_3 i dwuwymiarowego La_2CuO_4. Trzeci rozdział opisuje podstawy fizyczne użytych metod badawczych jak również streszcza założenia notacji użytej do opisu eksperymentów. W czwartym rozdziale znalazły się informacje dotyczące magnetycznego uporządkowania materiałów i omówienie zastosowanych technik badania owego uporządkowania. Ostatni rozdział wstępu teoretycznego opisuje zastosowane metody badania substancji pod wysokim ciśnieniem i podsumowuje dotychczasową wiedzę na temat właściwości badanych w rozprawie zwiazków w warunkach wysokiego ciśnienia.

Część eksperymentalna składa się z trzech rozdziałów. Pierwszy opisuje układy eksperymentalne zastosowane w trakcie badań. Kolejny zawiera szczegółowy opis przeprowadzonych badań. Pomiary spektroskopowe siarczanu(VI) srebra(II) zsyntezowanego nową metodą elektrolizy Ag_2SO_4 w stężonym kwasie siarkowym(VI) pokazały jego podobieństwo do produktu wcześniej opracowanej syntezy chemicznej (pomimo znacznych różnic w reaktywności obu produktów względem pary wodnej). Ponadto zaobserwowano rozkład $Ag^{II}SO_4$ wywołany światłem laserowym i pokazano, że tożsamosc chemiczna produktu rozkładu jest zależna od długości fali zastosowanego lasera. Podobną światłoczułość zaobserwowano dla monohydratu siarczanu(VI) srebra(II). Ten ostatni związek został ponadto po raz pierwszy scharakteryzowany spektroskopowo w zakresie od dalekiej podczerwieni do ultrafioletu, co pozwoliło na wyznaczenie parametrów rozszczepienia orbitalnego jak i dodatkowe potwierdzenie obecności cząsteczek wody w strukturze krystalicznej hydratu.

Badania nad fluorkiem srebra(I) pod wysokim ciśnieniem wykazały obecność większej liczby pasm ramanowskich niż przewidywana z obliczeń teorii grup (brak pasm); część z nich prawodpodobnie pochodzi od centrów barwnych lub od nadtonu aktywnego w podczerwieni drgania normalnego T_{1u}. Badania nad fluorkiem srebra(II) wykazały jego wysoką fotoczułość. Produkt indukowanego światłem laserowym fotorozkładu został zbadany w zakresie od ciśnienia atmosferycznego do 47 GPa. Wydaje się, ze rozkład fotochemiczny prowadzi do pochodnej zawierającej aniony $Ag(II)F_4^{2-}$, zapewne $Ag(I)_2Ag(II)F_4$, który jest pierwszym znanym fluorkiem srebra o mieszanej wartościowości Ag(I)/Ag(II). Wyznaczono zależność ciśnieniową charakterystycznego pasma ramanowskiego tej nowej fazy do ciśnienia 47 GPa.

Ponadto dzięki zastosowaniu spektroskopii rozproszenia ramanowskiego oraz nieelastycznego rozpraszania neutronów z powodzeniem zidentyfikowałem i zarejestrowałem po raz pierwszy przejścia bimagnonowe w dwuwymiarowym antyferromagnetyku, AgF_2, i wyznaczyłem wartość wewnątrzwarstwowej stałej nadwymiany magnetycznej, J, dla tego związku. Duża wartość J=70 meV plasuje ten związek jako jedyny, poza warstwowymi tlenkami miedzi(II), wykazujący tak silną nadwymianę magnetyczną w dwóch wymiarach.

Fluoroboran fluorosrebra(II) został scharakteryzowany za pomocą rozproszenia ramanowskiego, nieelastycznego rozproszenia neutronów, spektroskopii fourierowskiej w podczerwieni oraz spektroskopii odbiciowej w zakresie średniej podczerwieni. Charakterystyczne pasmo absorpcyjne w zakresie bliskiej podczerwieni pozwolilo na oszacowanie wewnątrzłańcuchowej stałej nadwymiany magnetycznej dla tego związku na około 270 meV, co przekracza najwyższą znaną do tej pory wartość zmierzoną dla Sr_2CuO_3 (240 meV).

Badania nad tlenkiem srebra(I,III) prowadzone w zakresie wysokich ciśnień wykazały brak indukowanego ciśnieniem rozkładu lub komproporcjonacji tego związku do nie mniej niż 74 GPa. Ponadto, z uwagi na dobrą zgodność pozycji pasm ramanowskich z obliczeniami teoretycznymi dokonanymi na modelach wysokociśnieniowych faz AgO udało się wykazać istnienie dwóch strukturalnych przejść fazowych w przedziale ciśnienia od 0 do 74 GPa, co potwierdza wyniki uzyskane z uzyciem rozpraszania promieniowania rentgenowskiego na próbkach proszkowych (rozprawa doktorska Dr A. Grzelaka).

Ostatnim elementem rozdziału jest opis badań przeprowadzonych na trzech fluorosrebrzanach(II) metali alkalicznych: HT-$KAgF_3$, $CsAgF_3$ i $RbAgF_3$. Pomimo wyraźnych różnic strukturalnych widma spektroskopii fourierowskiej w zakresie dalekiej podczerwieni tych związków wykazują bardzo duże podobieństwo. Dokładne przypisanie wszystkich pasm wymaga przeprowadzenia obliczeń teoretycznych struktury fononowej tych związków.

Ostatni rozdział stanowi podsumowanie przeprowadzonych badań i przedstawienie perspektyw dalszych badań.

(EN) Goals of this work

This thesis is a fragment of a more extensive study of divalent silver compounds as potential precursors of high-temperature superconductors which has been conducted from 2002 at the University of Warsaw. The motivation for this research comes from similarities between silver compounds (with particular emphasis on binary and ternary connections with fluorine) and copper oxides (oxocuprates).

Silver(II) fluoride is the simplest divalent silver compound containing structural motifs analogous to those found in copper oxide superconductors. It is therefore an excellent starting point for research into the family of silver(II) compounds. Because silver(II) fluoride contains corrugated layers composed of $[AgF_{4/2}]$ squares, an interesting research problem lied in determining whether the said layers under increased pressure would flatten, or rather transform to a topologically different structure. This study also attempts to understand the magnetic properties of this compound, notably to determine the intra-sheet magnetic superexchange constant, and its behavior under increased pressure, and under illumination with laser light.

Understanding the properties of silver(II) fluoride also required the examination of silver fluoride (I), which is one of the main impurities of every sample of AgF_2. In order to be able to separate the contributions to the vibrational spectra from this impurity, it was necessary to carry out a series of measurements for silver(I) fluoride reference sample.

$(AgF)BF_4$ was another interesting compound studied. This compound contains antiferromagnetic chains in which the small distance between adjacent silver(II) atoms should, according to theory, result in immensely strong antiferromagnetic interactions; this feature renders it an interesting object for research. In terms of magnetic ordering this system is a silver-fluorine equivalent of one-dimensional copper and oxygen compounds (for example Sr_2CuO_3). The research conducted in the doctoral thesis was aimed at characterizing this compound with the vibrational spectroscopy techniques and an experimental determination of the intra-chain magnetic superexchange constant using absorption spectroscopy in NIR range.

The last system containing silver and fluorine to be examined in this work was a trio of fluoroargentates(II): $CsAgF_3$, $RbAgF_3$ and high-temperature form of $KAgF_3$. Although the first two compounds have not been examined so far by vibrational spectroscopy methods,

their characterization and comparison would allow to understand the influence of the size of alkali metal cation on the properties of this class of perovskite compounds, and might serve as a starting point into future research on their properties as a function of pressure. As with the other silver(II) and fluorine compounds mentioned earlier, this is important due to their potential use as precursors of high-temperature superconductors.

The next group of substances studied in this dissertation are compounds containing silver(II) and oxygen. An important representative of this group is AgO, silver oxide (I, III). It is a mixed valence compound with silver on the first and third oxidation states. The research problem is whether AgO may undergo comproportionation under high pressure conditions *i.e.* become a genuine Ag(II) oxide. The theoretical calculations carried out in the past by various research groups came to contradictory conclusions regarding both the pressure at which phase transitions might occur, as well as the product high-pressure structures. The final solution of this problem has been obtained here from a series of Raman scattering measurements carried out in a wide pressure range. My measurements supplemented X-ray diffraction measurements conducted in parallel by Dr A. Grzelak.

The last research problem which I tackled with during this doctoral dissertation was the complete characterization of two new members of the silver(II) sulfate(II) family: a product of electrochemical synthesis in concentrated sulfuric acid (el-$AgSO_4$) and silver(II) sulfate(VI) monohydrate. The identity of both compounds was unknown at the beginning of the research, therefore my goal was to identify them via vibrational and electronic absorption spectroscopy. Their photosensitivity was also studied.

(PL) Cele pracy

Niniejsza praca stanowi fragment rozleglejszego studium związków srebra dwuwartościowego jako potencjalnych prekursorów nadprzewodników wysokotemperaturowych, prowadzonego na Uniwersytecie Warszawskim od 2002. Motywacją do tych badań jest szereg podobieństw występujących między związkami srebra (ze szczególnym uwzględnieniem połączeń dwu- i trójskładnikowych z fluorem) a tlenkami miedzi (oksokupratami).

Fluorek srebra(II) jest najprostszym związkiem dwuwartościowego srebra zawierającym motywy strukturalne analogiczne do związków opartych o tlenku miedzi. Stanowi wobec tego doskonały punkt startowy do badań nad rodziną związków srebra(II). Ponieważ fluorek srebra(II) zawiera w swej strukturze pofałdowane warstwy złożone z kwadratów [$AgF_{4/2}$], interesującym problemem badawczym było stwierdzenie, czy rzeczone warstwy ulegają pod wpływem zwiększonego ciśnienia wypłaszczeniu, czy przekształcają się w odmienną topologicznie strukturę. W niniejszej rozprawie usiłuję zrozumieć właściwości magnetyczne tego związku a w szczególności wyznaczyć stałą nadwymiany magnetycznej w warstwach, oraz jego zachowanie pod zwiększonym ciśnieniem i w warunkach naświetlania wiazką laserową.

Zrozumienie właściwości fluorku srebra(II) pod wysokim ciśnieniem wymagało również zbadania fluorku srebra(I), stanowiącego jedno z głównych zanieczyszczeń AgF_2. By móc odseparować od siebie wkłady do widm oscylacyjnych pochodzące od obu związków, niezbędne było przeprowadzenie serii pomiarów widm dla referencyjnego fluorku srebra(I).

Kolejnym obiektem zainteresowania byl $(AgF)BF_4$. Związek ten zawiera antyferromagnetyczne łańcuchy, w których ni-ewielka odległość między sąsiadującymi atomami srebra(II) powinna wg. teorii skutkować silnymi oddziaływaniami antyferromagnetycznymi. Układ ten pod względem uporządkowania magnetycznego jest fluorosrebrowym odpowiednikiem jednowymiarowych związków miedzi i tlenu (przykładowo Sr_2CuO_3). Badania przeprowadzone w doktoracie miały więc na celu scharakteryzowanie związku z użyciem technik spektroskopii oscylacyjnej wraz z eksperymentalnym wyznaczeniem wartości stałej nadwymiany z użyciem widm absorpcyjnych w zakresie bliskiej podczerwieni.

Ostatnim zbiorem układów zawierających srebro i fluor jaki został zbadany w tej pracy była trójka fluorosrebrzanów(II): $CsAgF_3$, $RbAgF_3$ oraz wysokotemperaturowa postać $KAgF_3$. Chociaż pierwsze dwa związki nie były do tej pory zbadane metodami spektroskopii oscylacyjnej, scharakteryzowanie ich i porównanie ze sobą umożliwiłoby zaobserwowanie wpływu wielkości kationu metalu

alkalicznego na właściwości tej klasy związków perowskitowych, zaś w dalszej perspektywie stanowiłoby zaczątek badań nad ich właściwościami w funkcji ciśnienia zewnetrznego. Podobnie jak w przypadku innych wymienionych wcześniej związków srebra(II) i fluoru jest to istotne z uwagi na potencjalne zastosowanie ich jako prekursorów nadprzewodników wysokotemperaturowych.

Kolejną grupą substancji zbadanych w tej rozprawie są związki zawierające srebro(II) i tlen. Ważnym przedstawicielem tej grupy jest AgO, tlenek srebra(I,III). Jest to związek o mieszanej walencyjności, w którego strukturze znaleźć można srebro na pierwszym i trzecim stopniu utlenienia. W tym wypadku problem badawczy stanowi czy pod zwiększonym ciśnieniem AgO może ulec komproporcjonacji tworząc tlenek srebra(II). Obliczenia teoretyczne przeprowadzone w przeszłości przez różne grupy badawcze dochodziły do sprzecznych wniosków zarówno odnośnie ciśnień w jakich następować mogłyby przejścia fazowa, jak i wysokociśnieniowych struktur. Problem ten został tu rostrzygnięty dzięki przeprowadzeniu serii pomiarów rozpraszania ramanowskiego w funkcji ciśnienia oraz (rownolegle prowadzonych przez dr. A. Grzelaka) pomiarach dyfrakcji rentgenowskiej na proszkach.

Ostatni problem badawczy z jakim borykałem się w trakcie wykonywanie tej rozprawy doktorskiej to możliwie kompletna charakterystyka dwóch nowych przedstawicieli rodziny siarczanu(VI) srebra(II): produktu elektrochemicznej syntezy w stężonym kwasie siarkowym (el-$AgSO_4$) oraz monohydratu siarczanu(VI) srebra(II). Tożsamość obu związków była w momencie rozpoczęcia badań nieznana, dlatego za cel postawiłem sobie identyfikację ich na podstawie pomiarów spektroskopii oscylacyjnej oraz spektroskopii elektronowej. Fotoczułość obu zwiazków także była przedmiotem badań.

Table of contents

A. Review of literature

A.1 Introduction

Silver is a group 11 element naturally occurring mostly in elemental form. Due to its relative rarity, and low chemical reactivity it was known in antiquity and used for several millennia as precious metals, e.g. for minting coins. From a chemical point of view, silver might be studied in comparison with another coinage metals, copper and gold. The most apparent difference is due to the color of copper, which is caused by ease of optical electronic transition from d band to conduction band [1]. The analogous transition in silver occurs at an energy exceeding the visible range, hence the difference in color. There are of course more distinguishing properties, and they will be described in the context of compounds, not pure elements.

The standard electrode potential of Ag(II)/Ag(I) pair in aqueous solution is equal +1.98 V (the formal oxidation potential of Ag(II)/Ag(I) in 33% oleum reaches +2.90 V[2]). Analogous copper Cu(II)/Cu(I) pair is characterized by a much lower standard potential: +0.153 V[3]. Thus, any neutral compound containing divalent silver must contain anions sufficiently resistant towards oxidation. What counterions are suitable for Ag(II) cations? It turns out that stable connections are provided by fluoride anions ($E^0(F_{2(g)} + 2e^- \rightarrow 2F^-)$ = +2.87 V [3]), or fluorine-based anions formed from more complex entities (SbF_6^-, TiF_6^{2-} among others [4–6]). There are only over a hundred [7] of different fluoride compounds containing Ag(II) known. Such harsh limitations on resistance towards oxidation do not apply to anions bound to Cu(II) cations and comparison of the two yields unsurprising result: there are over forty divalent copper compounds for every known compound of divalent silver (40:1).

The disproportion between scarcity of silver(II) and opulence of copper(II) compounds is understandable: copper has lower both the second ionization energy and a sum of first and second ionization energies (Δ(Ag, Cu) IE_2 = 112 kJ/mol, Δ(Ag, Cu) IE_{1+2} = 98 kJ/mol). The ionic radius of copper(II) ions is also smaller than the radius of silver(II) ions, which leads to a lower lattice and solvation energies. Moreover, copper is about 800 times more abundant than silver in Earth crust [3] and this, in conjunction with the ease of reduction of Cu(II) cations, led to copper being the first metal used by humans (from the native copper and chalcocite smelting).

Another reason is the emergence of high-temperature superconductors based on copper oxide ceramics [8] in 1986, which rekindled the disproportionally large interest in

compounds of divalent (as well as tri- and monovalent) copper. Web of Science query performed on 14.03.19 using the phrase “cuprate OR oxocuprate” yielded 152 results for 1945-1986 range and over 11000 results for the 1987-2018 period.

Another important difference between silver and copper compounds stems from the character of their valence electron shells. The 4d orbitals of Ag are more diffuse than 3d ones of Cu. This provides more electron density further away from the core, thus increasing the covalent character of metal-ligand bonds [9].

It is worth noting that in a typical scenario an introduction of oxygen-based ligands to Ag(II) cation causes either reduction or disproportionation of silver(II). The most notable example is AgO, which is NOT a silver(II) oxide – there are two crystallographically different sites (of different Ag-O bond lengths and coordination numbers) present in the structure of this oxide [10]. Additionally, magnetic studies indicate that this compound contains no unpaired electrons [11]. Therefore, it is more appropriate to call this oxide $Ag(I)Ag(III)O_2$, a dioxoargentate(III) of silver(I).

The scarcity of compounds containing oxoligands and Ag(II) does not mean, that there are no precedents: a most notable one seems to be $AgSO_4$. This sulfate consists of genuine Ag(II) cations connected via sulfate groups – each cation forms a square with oxygen atoms from four separate sulfate anions. The structure and properties of $AgSO_4$ and its hydrate derivative: $AgSO_4 \cdot H_2O$, are described in the further subchapters. Other examples include $[Ag(py)_4]S_2O_8$ [12] (py = pyridine), $Ag(pyz)_2S_2O_8$ [13] (pyz = pyrazine), silver(II) triflate [14,15] or silver(II) picolinate [16].

Structures adopted by silver(II) compounds can be roughly divided into several groups, depending on the connectivity of the central atom units, for example, compounds which contain isolated Ag(II) cations differ in properties from compounds that are proper coordination polymers. The consequence of different geometry of structures can be seen in magnetic, or optical properties. For example: in the structures in which the neighboring silver(II) cations are connected via a shared ligand (for example AgF_2, alkali metal fluoroargentates), the magnetic interactions between the ions tend to be strong, and ferromagnetic or antiferromagnetic ordering is easier achieved. On the other hand, the structures that contain Ag(II) cations connected via large polyatomic ligands, are often paramagnetic down to rather low temperatures [16].

A.1.1 Divalent cations of group 11 elements: Cu^{2+}, Ag^{2+}, Au^{2+}

Most of the compounds studied in this work contained divalent cations of d^9 electron configuration – either $4d^9$ for silver(II) or $3d^9$ for copper(II). Silver cations of $4d^9$ configuration are usually coordinated in a square planar or extended octahedral configuration.

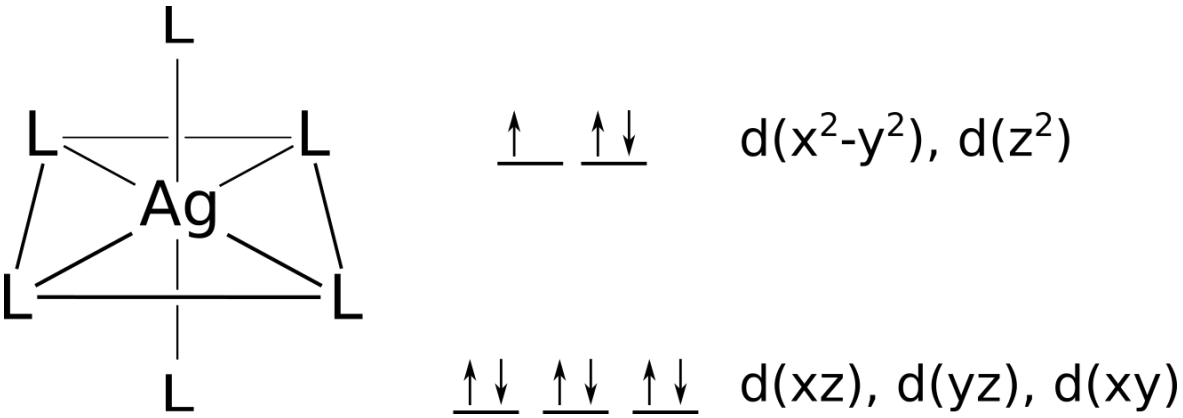

Fig. 1 - a silver(II) cation coordinated octahedrally by ligands L. The scheme on the right shows splitting of d orbital energies in the octahedral crystal field.

Fig. 1 depicts a splitting of silver(II) cation atomic orbitals in a crystal field of octahedral symmetry. The $d(x^2-y^2)$ and $d(z^2)$ orbital are degenerate and have e_g symmetry. Similarly d(xy), d(yz) and d(xy) orbitals are degenerate and have t_{2g} symmetry. The e_g orbitals contain three electrons, which means that there are two possible electronic configurations of equal energies for this d^9 cations: the d hole can occupy either $d(x^2-y^2)$ or $d(z^2)$ orbital.

A.1.2 Jahn-Teller effect

When a transition metal that adopts a degenerate ground state electronic configuration is subjected to influence from ligands, a Jahn-Teller distortion inevitably occurs[1]. The coordination neighborhood around the ion is distorted from ideal symmetry in such a way, that degeneration of electronic state of central ion is removed. Splitting of energy levels occurs so overall energy of the molecule (or of a crystal) decreases (Fig. 2).

[1] It is worth noting, that the molecule in question must be nonlinear.

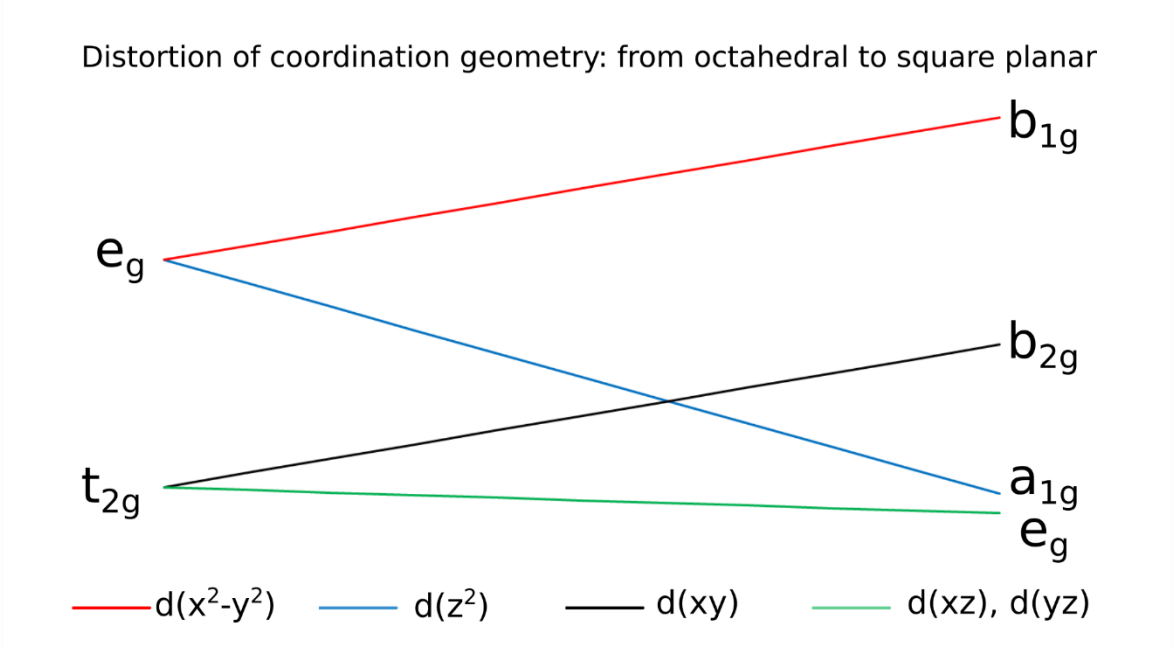

Fig. 2 – an example of -relative energies of orbitals in a continuous transition from octahedral (left) to square planar (right) geometry

The unpaired electron of the cation is placed on a molecular orbital that is built from $d(x^2-y^2)$ atomic orbital of silver (Fig. 3 below) and p(x), p(y) orbitals of fluorine ligands. This configuration decreases repulsion between crystal center and axial ligands.

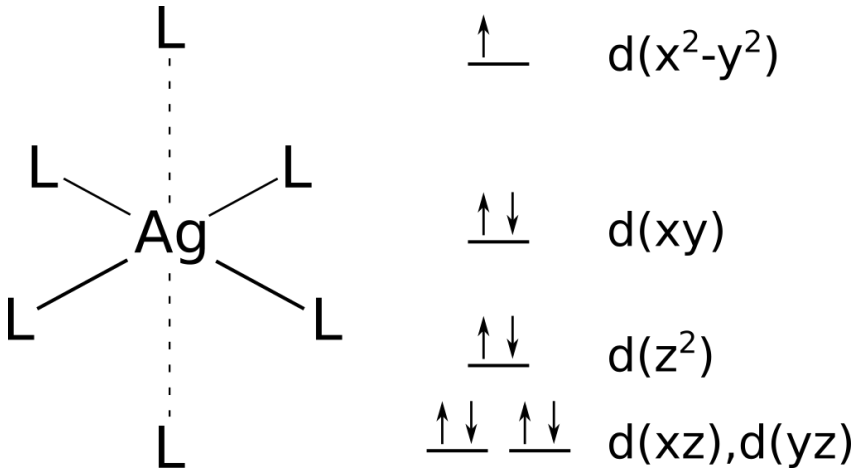

Fig. 3 - coordination geometry of d^9 cations, along with a simplified scheme of the splitting of d orbitals in the crystal field. The order of orbitals depends on the strength of the J-T effect and can be reversed for the d(xy), $d(z^2)$ pair.

Distortion of the ideal coordination around the central ion occurs only if a distorted system may decrease energy. This means that for some electronic configurations (for example high-spin d^3, high-spin d^5, high-spin d^8) of central ion in an ideal octahedral field there are no distortions possible that may decrease the overall energy of the system.

In all nonlinear molecules cases, Jahn-Teller effect lowers symmetry of coordination complex. This has a significant consequence in vibrational spectroscopy of such compounds. One of the most common coordination schemes for transition metal cations is the said octahedral coordination. A corresponding platonic solid has an inversion center right on the intersection of diagonals. Usually, the symmetry of moieties containing inversion centers imposes restrictions on possible bands appearing in IR or Raman spectra (mutual exclusion principle). However, when symmetry is lowered – for example by Jahn-Teller effect – the inversion center may be present, but some restrictions soften, and normally inactive mode might appear as allowed one in IR/Raman spectrum. This lowering of symmetry also has consequences for electronic spectra: some among formerly restricted electronic d-d transitions might become optically active after deformation of a coordination polyhedron.

In case of isolated complexes in solution, any direction of distortion (elongation/contraction of the bond between the ligand and central ion along axes x, y or z) is equally probable. Crystal lattice introduces restrictions regarding the direction of distortion – usually, only a single pattern of possible distortions with respect to crystallographic lattice vectors has the lowest free energy, which means, that crystal stabilizes in this specific geometry. This effect, which leads to a particular pattern of local distortions, is called the collective Jahn-Teller effect.

When Jahn-Teller active moieties are connected via ligands in the crystal structure, there are different ways in which neighboring coordination polyhedrons can be stacked. When distorted axes are parallel to each other, the arrangement is called a ferrodistortive one (name stems from analogy to ferromagnetic ordering, in which direction of neighboring spins is parallel). On the other hand, when the axes are perpendicular to each other, the arrangement is called antiferrodistortive (see Fig. 4 and Fig. 5).

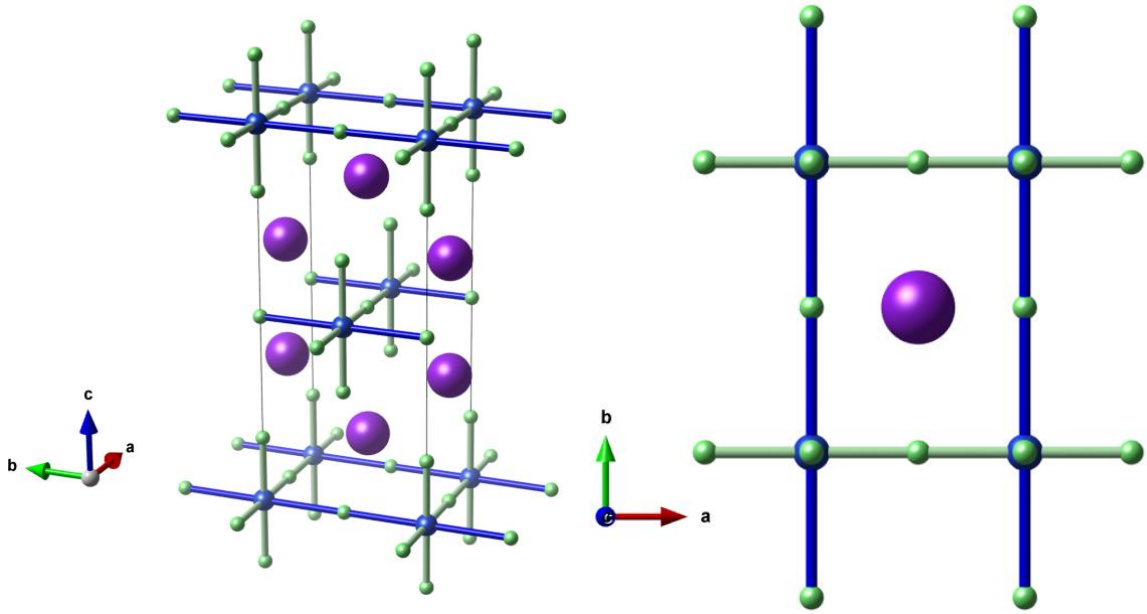

*Fig. 4 - an example of an ferrodistortive arrangement of octahedra in the high-pressure phase of K_2CuF_4 (Ammm space group). Long Ag-F bonds are depicted using blue cylinders. The figure on the left depicts a whole crystal cell, figure on the right depicts a top view of a single layer of this double perovskite. The distortion axes – long Ag-F bonds – are parallel to each other and extend along the **b** direction.*

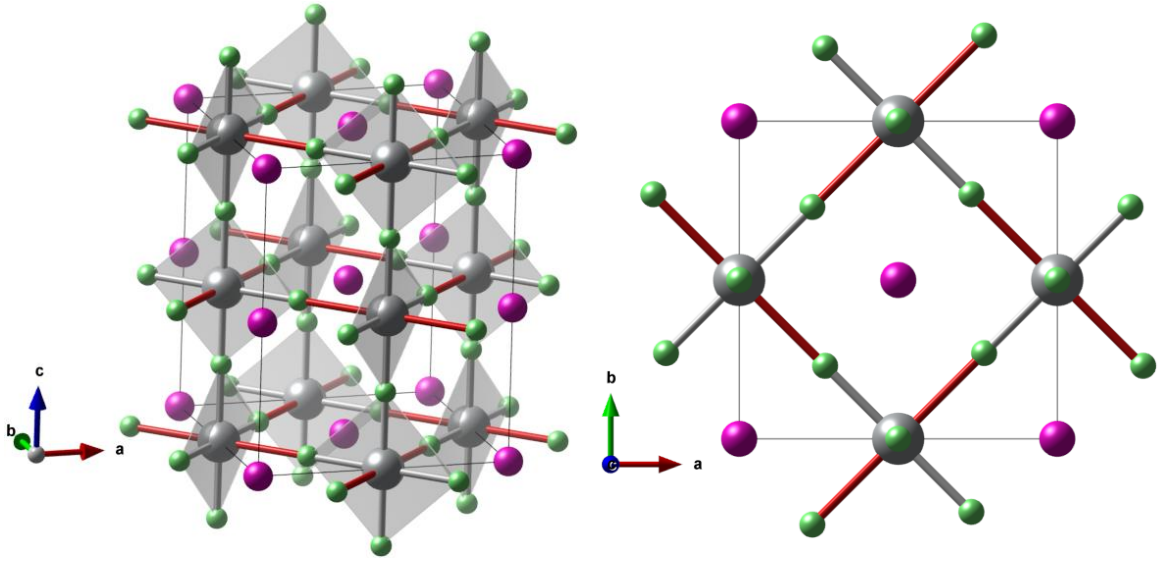

Fig. 5 - an example of antiferrodistortive arrangement of octahedra in $CsAgF_3$ (I4/mcm space group). Long Ag-F bonds are depicted using red cylinders. The figure on the left depicts a whole crystal cell, the right one depicts a top view of a single perovskite layer. The long Ag-F bonds are perpendicular to each other.

A.1.3 Structural types of selected coinage metal compounds

A.1.3.1 Cubic perovskite and related perovskite structures

Perovskite structure is adopted by compounds with ABX_3 formula, where A and B are cations, and X are anions. Typically A and B cations differ in size, with A cations being the larger of the two. The ideal perovskite structure adopts a $Pm\bar{3}m$ cubic structure where B cation is positioned at (0,0,0) and is coordinated octahedrally by six X anions at (½, ½, ½) positions [17–19]. The A cations, larger than B cations, are positioned at (½, ½, ½) points and are coordinated by twelve X anions in a cuboctahedral topology. Some perovskites

(especially those containing Jahn-Teller active B cations) diverge from ideal cubic structures due to elongation, compression and/or rotation of BX_6 octahedra. Usually, this changes the symmetry system of the compound to tetragonal or orthorhombic. The packing of strongly Jahn-Teller distorted octahedra may be increased via tilting of the octahedral axis from the direction of the cell vector. An ideal cubic perovskite structure with Z = 1 has IR-active modes 3 T_{1u} and a single silent optical mode T_{2u}[2]. Lowering symmetry increases the size of the cell, and introduces new optical modes. For example, the space group of a distorted perovskite $GdFeO_3$ is *P*nma, Z = 4. Group theory dictates, that this structure has 24 Raman-active, 25 IR-active and 8 silent optical modes.

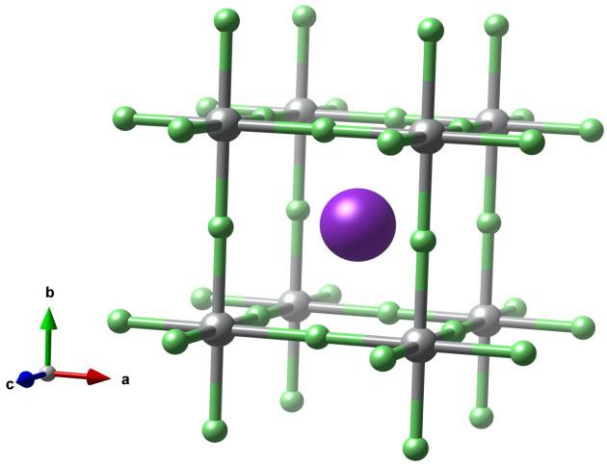

Fig. 6 - A ball-and-stick model of a cubic perovskite crystal cell, space group is $Pm\bar{3}m$, Z=1. Smaller B cations form the vertices of the cube, while the larger A cation is positioned in the middle of the cell.

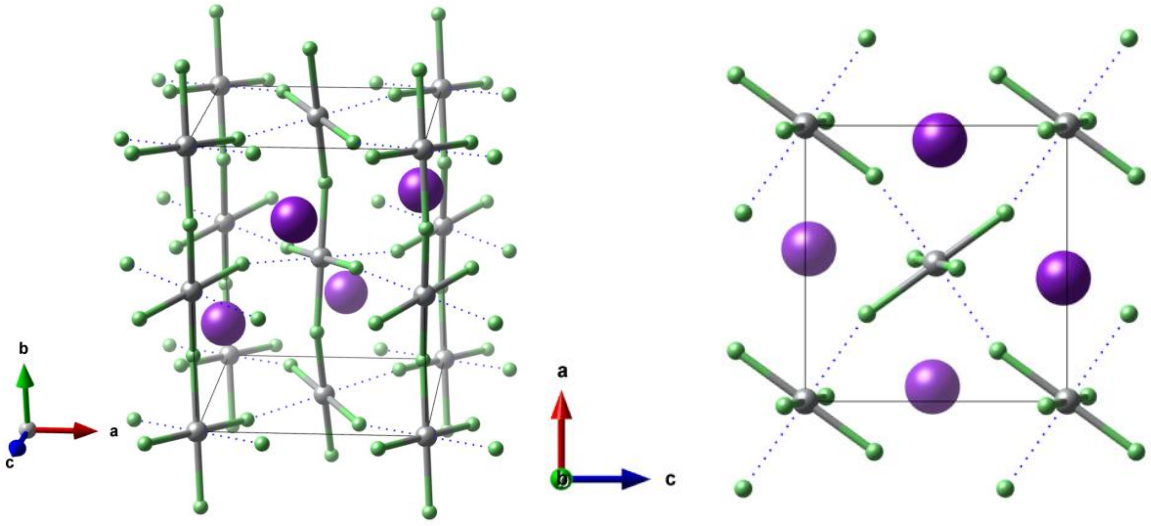

Fig. 7- A ball-and-stick model of a low-temperature phase of $KAgF_3$. The structure adopted by this fluoroargentate is a distorted perovskite, also called $GdFeO_3$ – type. The space group is Pnma, Z=4 [20]. Dashed lines indicate long Ag-F bonds. Picture on the right presents a top view of a crystal cell, presenting distortion in a clearer manner, as a rotation and elongation of octahedra forming ideal cubic perovskite.

[2] The nomenclature of vibrational spectroscopy is described in more detail in chapter A.3.1.

A.1.3.2 Double perovskite structures

Several silver and copper compounds, such as, e.g., Rb_2AgF_4, Cs_2AgF_4 [20], **La_2CuO_4** [21][3], crystallize in a perovskite-related structure, called double perovskite. The prototypical structure of A_2BX_4 might be visualized as two layers of perovskite that have been slid against each other in the [½,½, 0] direction parallel to the surface of the layers, or as an intergrowth of perovskite ABX_3 and layers of cesium chloride structure-type AX. The space group of the product of such undistorted modification is $I4/mmm$. As in the case of cubic perovskite, the high-symmetry compound can decrease its symmetry due to, e.g., Jahn-Teller effect. This can lead to two types of structure modification: ferrodistortive, when distortions of all octahedrons in a direct neighborhood align in the same direction, or antiferrodistortive, when neighboring octahedra are distorted in perpendicular directions.

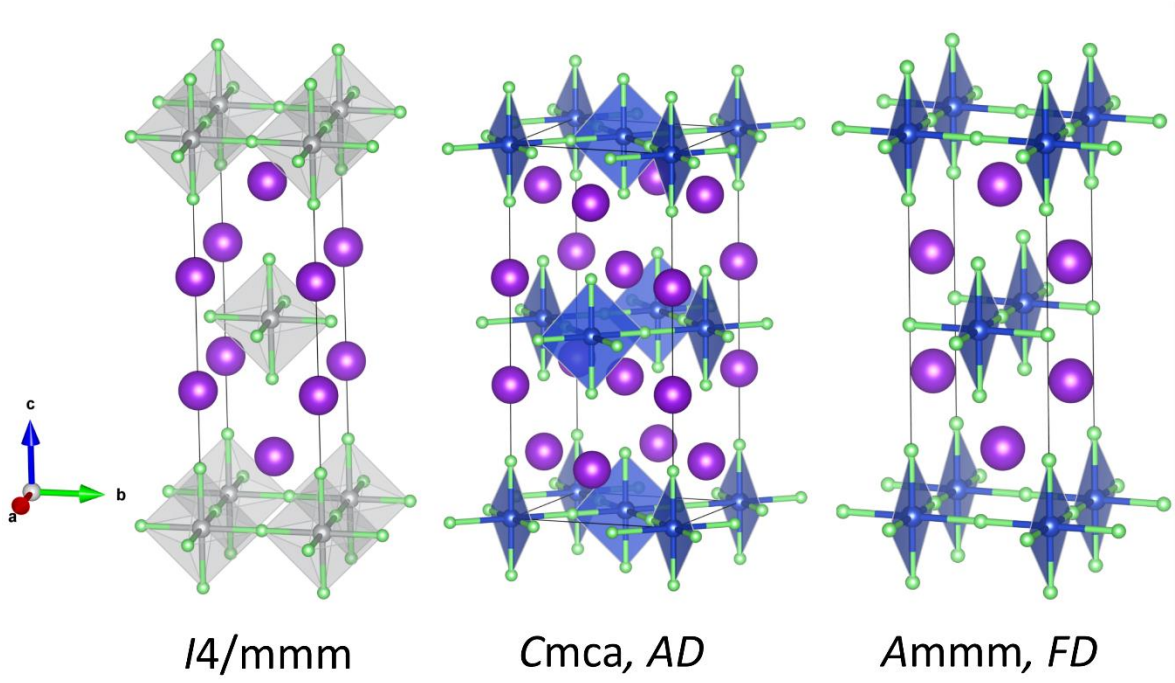

Fig. 8 - A comparison of several different types of double perovskites. From the left: K_2NiF_4 [22]*, a low-pressure antiferrodistortive phase of K_2CuF_4* [23]*, the high-pressure ferrodistortive phase of K_2CuF_4* [24]

It is worth noting that elongation or contraction of metal-ligand bonds along a selected axis is not the only possible deformation of ideal double perovskite structure present in real compounds. The coordination octahedra might be rotated in layer plane or with respect to the layer plane.

[3] Compounds indicated with **bold** font are most relevant to this thesis.

A.1.3.3 Rock-salt and cesium chloride structures

NaCl-type and CsCl-type structures are often adopted by AX compounds. Both belong to the cubic family, with NaCl-type having a $Fm\bar{3}m$ spacegroup, and and CsCl being $Pm\bar{3}m$. They are prototypical structures of binary ionic AX compounds. According to Pauling's rules, binary ionic crystals of cation-anion radius ratio between 0.414 and 0.592 should adopt NaCl structure, and those with a cation-anion radius ratio over 0.732 will adopt CsCl structure [25]. The structures differ in coordination geometry: NaCl contains cations coordinated octahedrally, whereas CsCl contains cations coordinated cubically. The CsCl type is quite well packed – hence, compression of compounds that adopt NaCl structure at ambient pressure in many cases leads to structural phase transition to CsCl structure – so-called B1-B2 transition [26–28]. Both structures are important in context of silver halides (especially **AgF**), as those compounds adopt those two structures either at ambient or elevated pressures.

A.1.3.4 Rutile structure

Rutile is one of the polymorphs of titanium dioxide. This prototypical structure is adopted by many AX_2 compounds, for example, dioxides: TiO_2 [29], RuO_2, IrO_2 [30], RhO_2 [31], MnO_2 [32], or difluorides of Mg, Ni, Co, Zn, Fe, Mn [33]. The crystal system of rutile is tetragonal; the space group is $P4_2/mnm$. Atoms denoted as A are usually divalent or tetravalent transition metal cations, that occupy (0,0,0) positions in the crystal cell. Each cation is coordinated by six anions placed at (x,x,0) and other symmetrically equivalent positions.

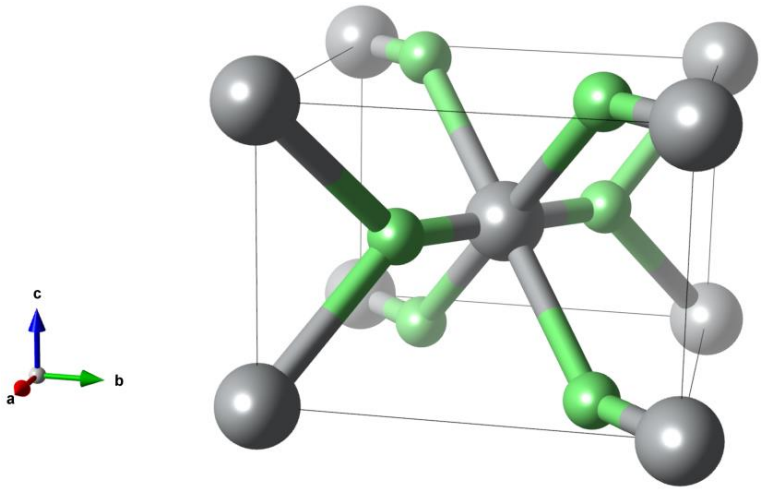

Fig. 9 - a ball-and-stick model of AX_2 rutile crystal cell. Space group is $P4/2mnm$, Z=2. Cations, denoted as A (gray balls), are octahedrally coordinated by anions X (green balls).

A.1.3.5 Fluorite structure

Fluorite structure is one of the typical structures adopted by AX_2 compounds (for example difluorides of Ca, Sr, Ba, Cd [34], as well as dioxides: ThO_2, UO_2, CeO_2, ZrO_2 [35,36]). Fluorite structure is *fcc* (face-centered cubic), the spacegroup is $Fm\bar{3}m$. Cations A are positioned on the vertexes and in the middle of faces of crystal cell. The anions on the other hand form a simple cube centered on the middle of the crystal cell. The small cubes side length equals half of the larger one. The A cations are therefore coordinated by 8 anions forming a cube. Each anion X is coordinated tetrahedrally to four cations.

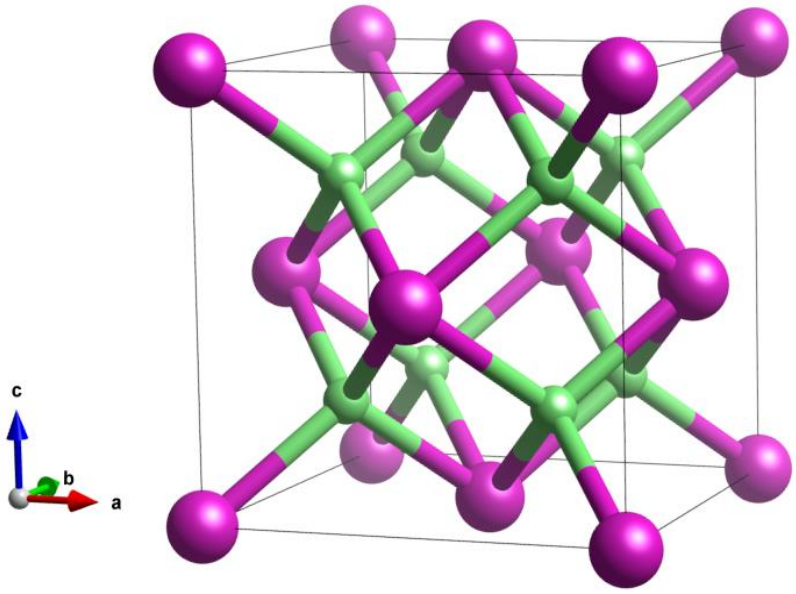

Fig. 10 - a ball-and-stick model of AX_2 fluorite-type crystal cell. Space group is $Fm\bar{3}m$, Z=4. Cations, denoted as A (pink balls) are coordinated cubically by eight anions. Each anion, denoted as X (green ball) is coordinated tetrahedrally by four cations.

A.1.3.6 Cotunnite structure

The cotunnite or α-$PbCl_2$ structure is typical for many AX_2 compounds, for example: high-pressure phases of ZrO_2, HfO_2 [37], TiO_2 [38], ambient-pressure structure of $PbCl_2$ as well as many metal difluorides (high-pressure structures of SrF_2 [39], CoF_2 [40], MgF_2 [41], and theoretically predicted high-pressure form of CuF_2 [42]). It is better packed than either rutile or fluorite: coordination number of cations A is equal 9 (while it is 6 in rutile and 8 in fluorite), whereas coordination numbers for X anion equal 4 and 5 – there are two different positions of anions in the cell. Each nine anions X from coordination neighborhoods of cations form a triangular prism with capped faces (tricapped trigonal prismatic geometry). Crystals of AX_2 compounds that under atmospheric pressure adopt those less packed structures usually transform to cotunnite upon compression.

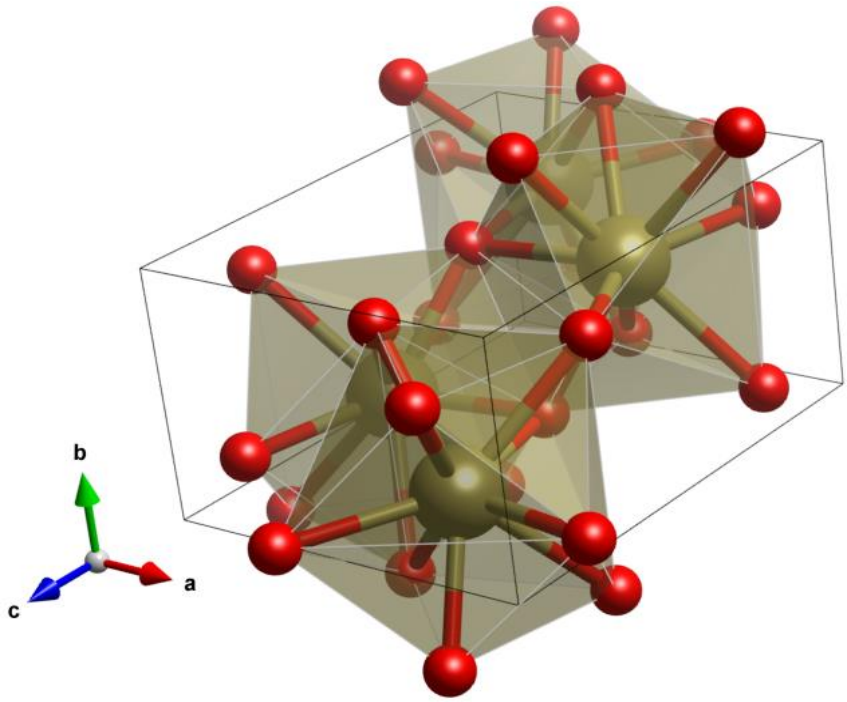

Fig. 11 - a ball-and-stick model of cotunnite-type crystal cell of an AX_2 compound. Space group is Pnma, Z=4. The golden balls are nonacoordinated cations A, whereas the red balls are anions X.

A.1.4 Optical properties of silver(II) compounds

Silver(II) cations have a $4d^9$ electronic configuration of valence electrons. One of the previous subchapters in this work describes the Jahn-Teller effect, causing deviations from ideally octahedral coordination of the Ag^{2+} cation, which removes the degeneracy of e_g orbitals. Most silver(II) compounds absorb in the UV-vis-NIR range of the electromagnetic spectrum via strongly allowed charge-transfer and weakly allowed d-d transitions (see for example [6,43]). In many cases, knowledge of these electronic transitions permits to extract the values of ligand field splitting parameters. In case of silver(I) compounds, absorption of visible light and UV may lead to a photochemical reduction of silver(I) to metallic silver. One well-known example is that of AgCl, which under visible light reacts in a process that has formed a basis of black and white photography for over 100 years. Silver(II) compounds, however, are not as light sensitive as their Ag(I) counterparts and may be stored in daylight conditions.

The absorption spectrum in the MIR and FIR region reflects the vibrations of the crystal lattice. Rarely encountered absorption bands consistent with multi-magnon and mixed phonon-multi-magnon processes will be described in more detail in the experimental part of this thesis.

A.2 Compounds of silver and selected cuprates

A.2.1 Crystal structures

A.2.1.1 Silver(I) compounds

A.2.1.1.1 AgF

Under ambient conditions silver(I) fluoride is a yellow crystalline solid, that crystallizes in *Fm-3m* space group (NaCl-type) with a = 4.936(1) Å [44,45]. A standard method of synthesis uses hydrofluoric acid in reaction with silver(I) oxide:

$$Ag_2O + 2\,HF \rightarrow 2\,AgF + H_2O$$

Usually, an excess of HF leads to the formation of colorless $AgHF_2$. This compound, however, decomposes in a vacuum, yielding pure AgF:

$$AgHF_2 \xrightarrow{vac.} AgF + HF$$

AgF is photosensitive and is prone to forming defects, therefore its samples usually are contaminated with silver clusters [46].

AgF undergoes a pressure-induced phase transition to *P*m-3m structure (B1–B2 transition, or NaCl-CsCl transition) at 2.70(2) GPa. On decompression, it adopts anti-NiAs structure between 2.7 and 0.9 GPa, and then transforms back to the NaCl type [47].

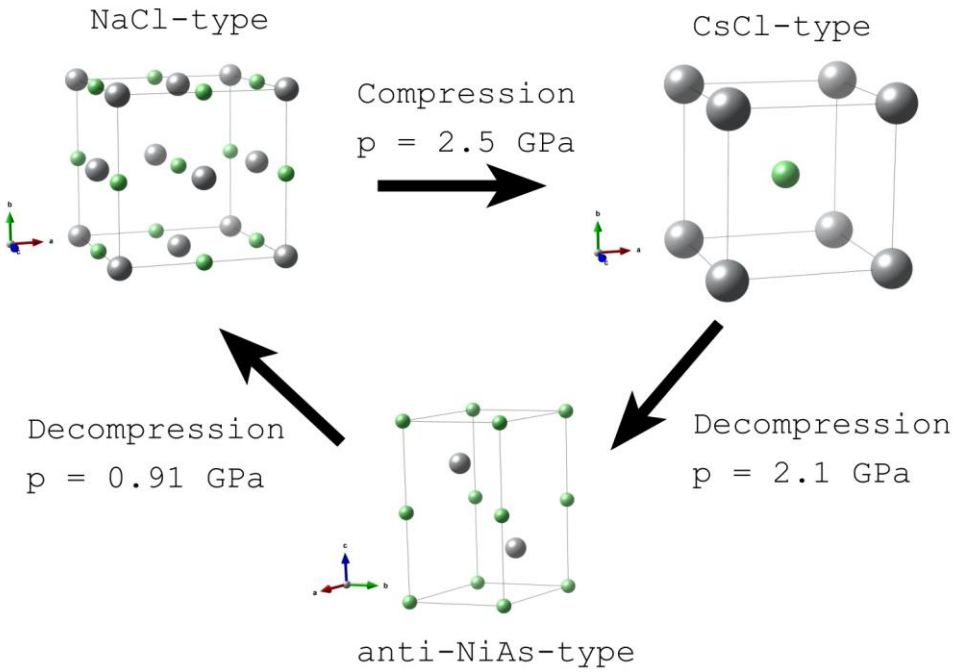

Fig. 12 - pressure-induced phase transitions occurring in AgF [47].

The symmetries of cubic phases of silver(I) fluoride, AgF-I ($Fm\bar{3}m$) and AgF-II ($Pm\bar{3}m$), do not permit the first-order Raman bands to be observed, as in both cases only IR active T_{1u} bands may be detected in the IR spectrum. In both structures second order Raman processes (overtones) in principle are permitted, as the symmetry of $T_{1u}*T_{1u}$ product is *gerade* ($A_{1g}+E_g+T_{2g}+T_{1g}$).

Electron configuration of Ag^+ in silver(I) fluoride is d^{10}, therefore it is a (closed-shell) diamagnetic, ionic system. On its own AgF right has many unusual properties – it is the only water-soluble silver(I) halide, is dark yellow while AgCl is colorless, and has a bandgap which is surprisingly difficult to predict by theory [46]. However, in this dissertation, it will be mostly studied as a product of decomposition of higher fluorides of silver, as a reference and a pressure gauge.

A.2.1.2 Silver(II) compounds

A.2.1.2.1 AgF_2

Under ambient pressure and at room temperature silver(II) fluoride is a dark brown crystalline solid. First documented synthesis of **AgF_2** took place in 1891 [48], although at the time the chemical identity of the product of the reaction of fluorine with silver was unknown. Current methods of synthesis vary depending on the starting compound. All samples used in our experiments were synthesized by fluorination of $AgNO_3$ in anhydrous HF:

$$2AgNO_3 + 2F_2 \xrightarrow{aHF} 2AgF_2 + N_2O_5 + \frac{1}{2}O_2 \qquad (1)$$

The silver(II) fluoride obtained by reaction (1) crystallizes in the comproportionated form of $Ag(II)F_2$, also called α-AgF_2. A disproportionated form of the compound, namely $Ag(I)Ag(III)F_4$ (β-AgF_2) can be obtained in the reaction of $KAgF_4$ with $AgBF_4$ in aHF at −81°C [49]:

$$KAgF_4 + AgBF_4 \xrightarrow{-81°C,\ aHF} Ag(I)Ag(III)F_4 + KBF_4$$

Obtained disproportionated compound is thermodynamically unstable – it transforms exothermically to α-AgF_2 around 0 °C.

Silver(II) fluoride is a compound that combines high oxidation potential of divalent silver (Ag^{2+}/Ag^+ pair reaches a potential of +2.9V *vs.* NHE in oleum [2]) with an ability to fluorinate a plethora of compounds. Properties of AgF_2 make it an interesting object of study

for chemists and physicists alike, although they are also responsible for technical `problems concerning its storage and handling. AgF_2 reacts with traces of water:

$$4AgF_2 + 4H_2O \rightarrow 2Ag_2O + 8HF + O_2 \quad (2)$$

Therefore, it must be stored under an inert gas atmosphere (Ar) in fluoropolymer containers.

Under ambient pressure and temperature AgF_2 adopts *Pbca* space group [50].

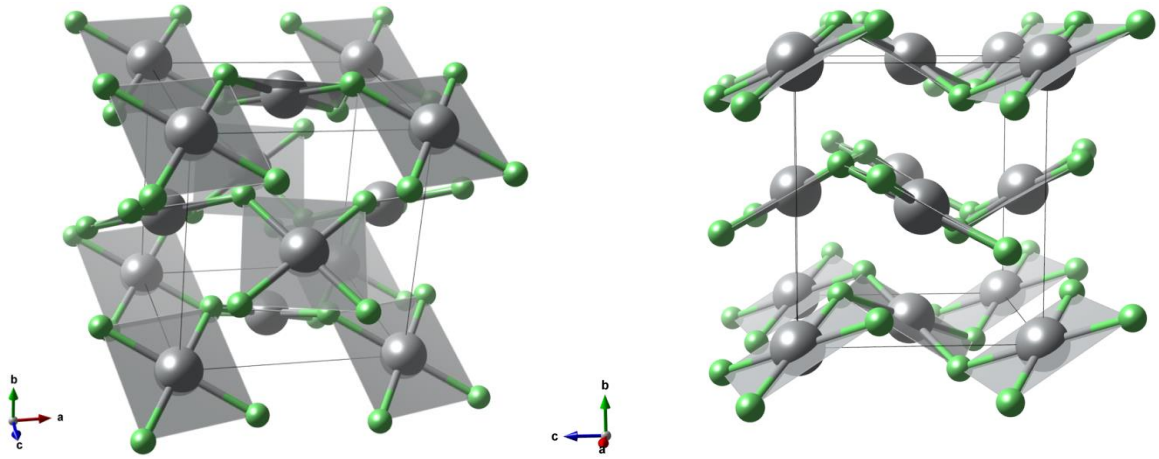

Fig. 13 – Two projections of the crystal structure of α-AgF_2

The figure above shows the model of the crystal structure of AgF_2. Gray spheres represent Ag(II) cations, and smaller green spheres represent fluoride anions. Lattice parameters of the ambient-pressure phase are a = 5.568(1) Å, b = 5.831(1) Å, c = 5.101(1) Å, Z = 4, V = 165.61(5) $Å^3$ [51,52] – these values originate from an X-ray study, but were consistent with neutron diffraction studies [50].

Initial XRD measurements of AgF_2 powder samples were not consistent with each other – authors claimed silver(II) fluoride crystallized in different space groups (see: references 6-8 in Fischer *et al.* [52]). The data was hard to interpret properly due to much higher form factors of Ag(II) cations in comparison with those of fluorine anions. More reliable results were achieved by using neutron diffraction, where the ratio of form factors is close to one [50].

It is worth noting that the neutron diffraction study was conducted at two temperatures: 4.2 K, and at room temperature. According to the authors (Fischer *et al.*), the differences between the results of measurements using neutron scattering at those two temperature points lied mostly in the presence of an additional small reflex in the low-temperature experiment, indexed as 011. This is indicative of the magnetic ordering of the sample, since this reflection is forbidden in the chemical space group. Since no other new reflexes were

found below Néel temperature, the magnetic crystal cell was found to be equal to crystal unit cell.

The crystal structure of AgF_2 is composed of corrugated sheets consisting of vertex sharing [AgF_4] squares, stacked in layers. Ag-F bond lengths inside aforementioned squares are equal to 2.086(1) Å (according to Jesih *et al.* [51]). The distance between closest silver cations in the same layer equals 3.7757(6) Å, while the distance to nearest neighbors from a separate layer is 3.8737(6) Å. The angle between diagonals of vertex sharing squares is 129.64(15)°, while F-Ag-F angles within [AgF_4] squares are equal 86.66(12)° and 93.34(12)°. DFT calculations indicate the presence of antiferromagnetic ordering mediated by superexchange through Ag-F bonds, though measurements also show a presence of weakly ferromagnetic interactions AgF_2. This additional feature is caused by a small collective deviation of spin vectors in the [001] direction [50] which is caused by Dzyaloshinskii-Moriya interaction [53,54].

A.2.1.2.2 $AgFBF_4$

Under ambient conditions, **$AgFBF_4$** is a green-blue solid (Casteel *et al*. mention also the synthesis of $AgFBF_4$ as violet single crystals and brown solid – for synthesis from $AgBF_4$ deliberately contaminated with AgF [55]). Two typical methods of synthesis use silver fluorides and boron trifluoride as reagents [56]. First, one can use silver(II) fluoride as a starting reagent:

$$AgF_2 + BF_3 \xrightarrow{aHF} AgFBF_4$$

One can also use silver(I) fluoride as a precursor, and then fluorinate the $AgBF_4$ intermediate:

$$AgF + BF_3 \xrightarrow{aHF} AgBF_4$$

$$AgBF_4 + F_2 \xrightarrow{aHF} AgFBF_4$$

$AgFBF_4$ is highly reactive. It decomposes in contact with air, yielding a black solid and pungent gas. Samples of $AgFBF_4$ must be stored in perfluorinated polymers and under an inert atmosphere.

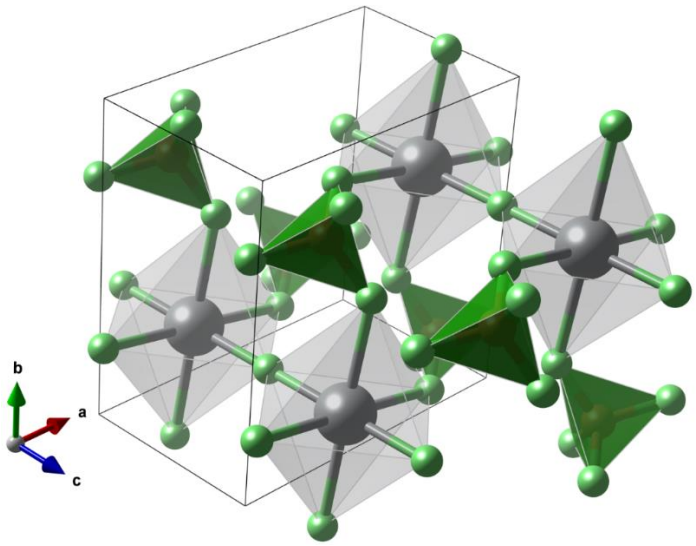

Fig. 14 - a 1x1x2 ball-and-stick model of supercell of $AgFBF_4$. Gray balls indicate positions of silver cations; green tetrahedra depict locations of $[BF_4]$– groups.

The figure above depicts a 1x1x2 supercell of $AgFBF_4$. The compound crystallizes in $P4/n$ space group with a = 6.7000(3) Å, c = 4.0113(2) Å, Z = 2, V = 180.067(16) $Å^3$. The crystal structure of $AgFBF_4$ consists of chains of compressed $[AgF_6]$ octahedra interconnected by $[BF_4]$ tetrahedra (see Fig. 15). The short axes of octahedra are lined up along the propagation direction of the AgF^+ chain, with average intrachain Ag(II)-F distance being equal 2.005(3) Å, which is one of the shortest Ag-F distances known [57]. The angles between axes of the octahedra are equal 180.0(1)°.

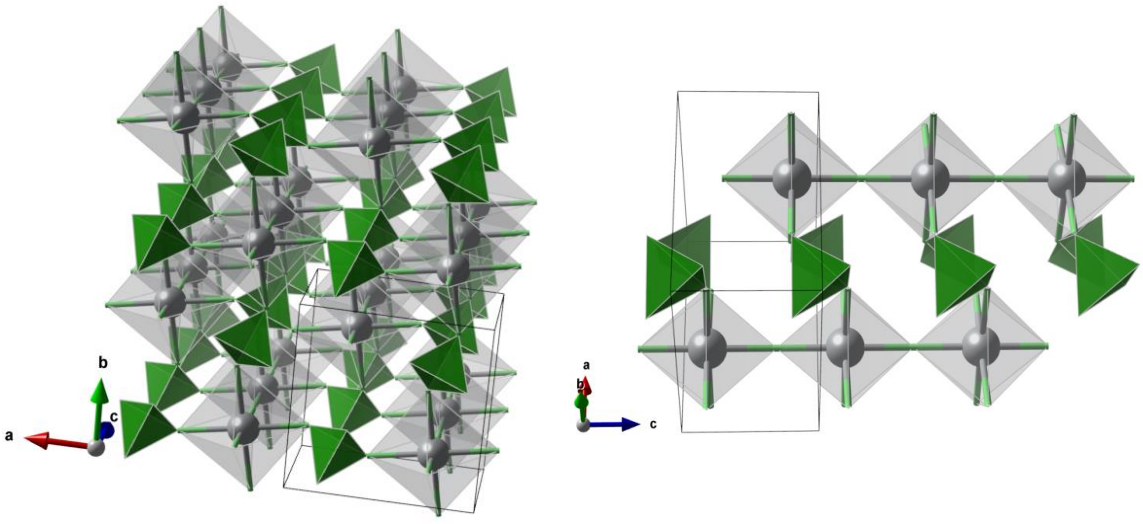

Fig. 15 – left: a 2x2x3 supercell of $AgFBF_4$. Positions of fluorine atoms were omitted for clarity. $[AgF_6]$ octahedra form chains extending in the c direction. Right: a 1x1x3 supercell of $AgFBF_4$ showing chains of $[AgF_6]$ octahedra.

A.2.1.2.3 $KAgF_3$

$KAgF_3$ is a brown solid, synthesis of which was first time documented in 1971 [58]. It can be obtained as a product of Lewis acid-base reaction of KF and AgF_2:

$$AgF_2 + KF \xrightarrow{Ar,\ V=const,\ 360°C} KAgF_3$$

via thermal decomposition under dynamic pressure of potassium Ag(III) fluoride [59]:

$$KAgF_4 \xrightarrow{vacuum,\ 440°C} KAgF_3 + ½\,F_2 \uparrow$$

The first method of synthesis yields product contaminated with other silver(II) compounds, mainly $K_3Ag_2F_7$, as well as AgF. The second method leads to a product contaminated only with diamagnetic AgF. This latter route enables magnetic measurements of Ag(II) in $KAgF_3$ without further purification of the sample.

In the 80–225 K temperature range, $KAgF_3$ crystallizes in a *P*nma space group [60]. The structure of this phase is a distorted perovskite-type, $GdFeO_3$. In 80 K the crystal cell parameters are as follows: a = 6.3815(9) Å, b = 8.254(1) Å, c = 6.0581(8) Å, V = 319.10(7) $Å^3$, Z = 4. The Ag-F-Ag angle, or an angle between elongation axes of neighboring octahedra along ***b*** direction equals 153.2(7)°. The angle between equatorial bonds of neighboring octahedra, sharing a fluoride anion, equals 157.2(8)°. The equatorial bond length is 2.121(4) Å, while the apical bond length equals 2.490(13) Å. Kurzydłowski and Grochala [61] reported the calculated magnetic superexchange coupling constants for both intrachain (along ***b*** direction, denoted J_{1D}) and interchain (denoted $J_\perp$) superexchange. The J_{1D} constant was calculated to be 1311 K (113 meV) indicating a strong antiferromagnetic coupling consistent with predictions from Goodenough-Kanamori-Anderson rules [62–64]. The experimentally determined value equals *ca.* 1160 K (100 meV). The calculations of the $J_\perp$ interchain constant yielded -58 K (-5 meV). The small negative value indicates a weak ferromagnetic coupling between the neighboring chains.

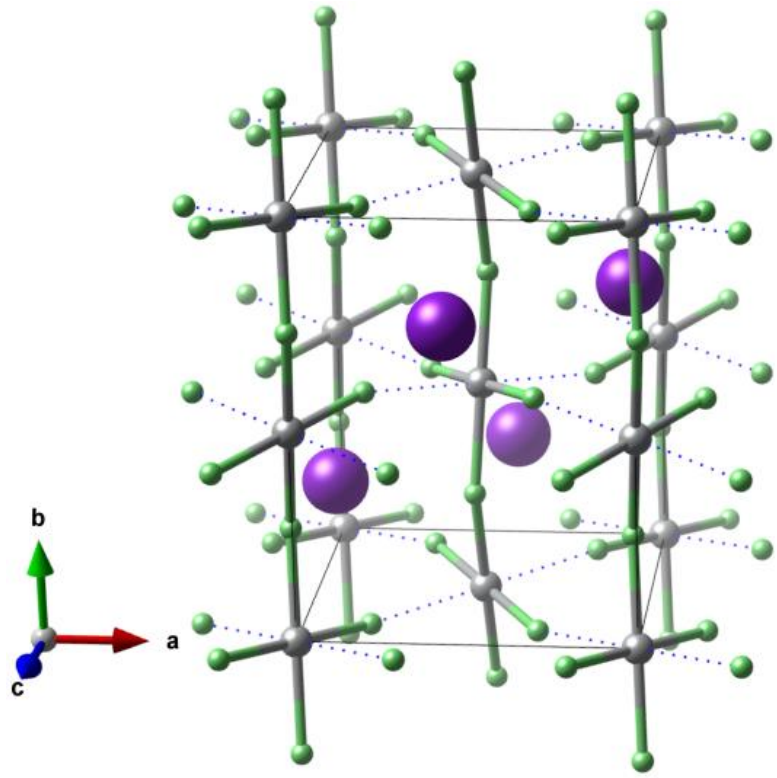

Fig. 16 - the ball-and-stick model of a low-temperature phase of $KAgF_3$ [58,60,65]. *The dashed lines indicate long Ag-F bonds (2.49 Å, while the short ones measure less than 2.1 Å).*

On heating potassium fluoroargentate(II) undergoes a structural phase transition between 225 K and 235 K to a disordered polytype [60].

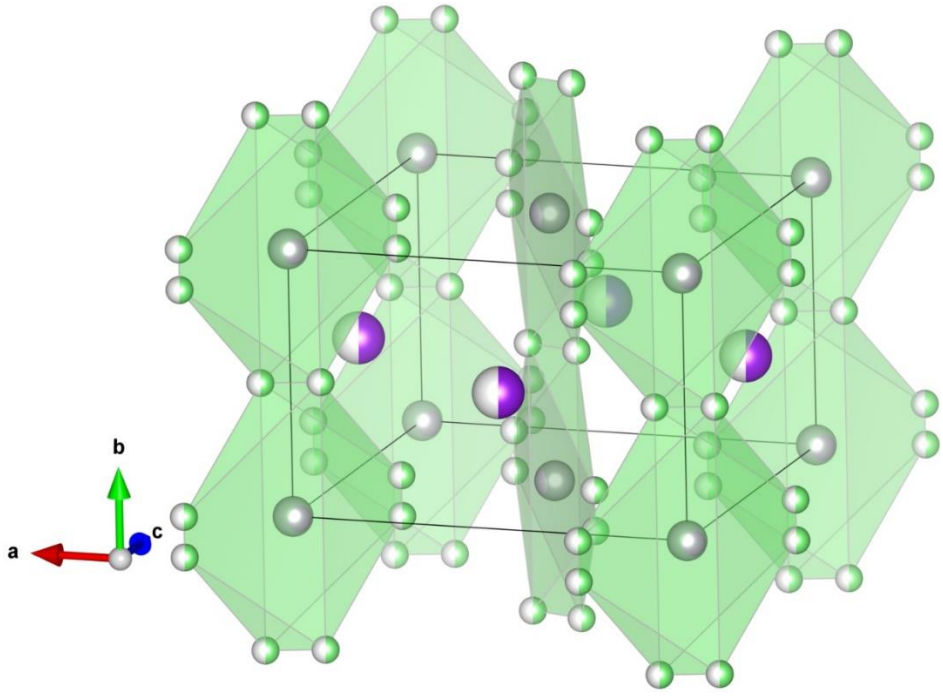

Fig. 17 - ball-and-stick model of crystal cell of a high-temperature polymorph of $KAgF_3$. Two-colored balls indicate a disorder in the position of atoms.

The figure above depicts a disordered crystal cell of HT-$KAgF_3$. At 298 K it crystallizes in *P*cma space group with cell parameters: a = 6.2685(6) Å, b = 4.1522(3) Å, c = 6.1828(5) Å, Z = 2, V 160.926(13) $Å^3$. Volume per formula unit of $KAgF_3$ is 80.46 $Å^3$ and is almost equal to the sum of volumes per f.u. of AgF_2 and KF – 79.55 $Å^3$. Each silver cation is coordinated by an elongated octahedron made of fluorine atoms. The structure of $KAgF_3$ might be interpreted as a distorted perovskite, or more precisely a $KCuF_3$ analog. One of the features distinguishing this structure from the low-temperature form is a presence of static disorder in tilting of $[AgF_6]^{4-}$ octahedra.

A.2.1.2.4 $RbAgF_3$

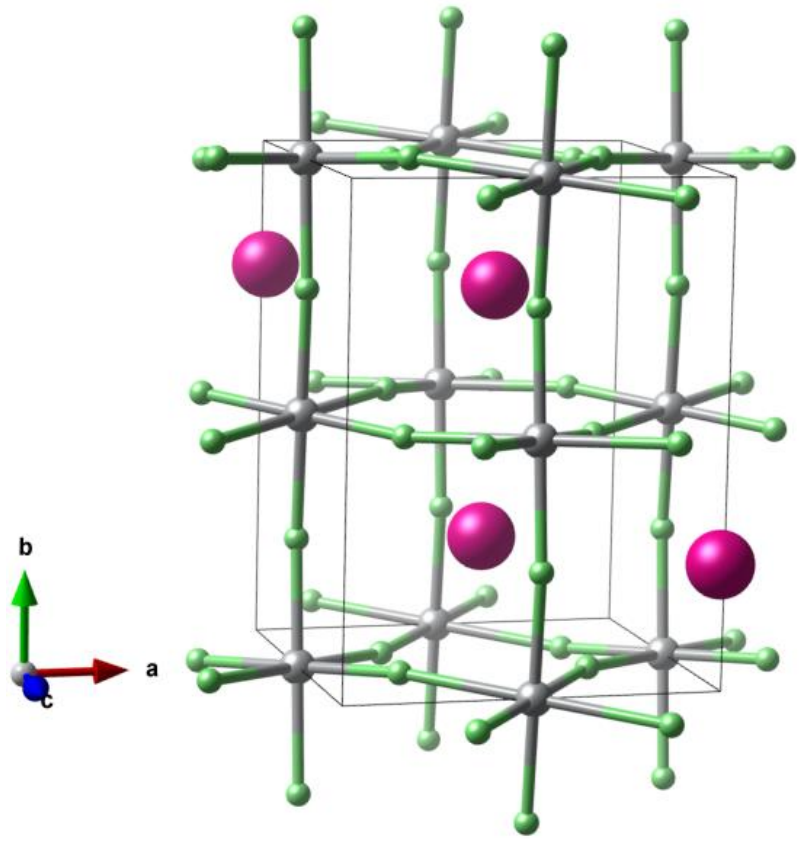

Fig. 18 - a ball-and-stick model of $RbAgF_3$ crystal cell. Pink balls mark the positions of Rb^+ cations in the structure, green balls: F^- anions, gray: Ag^{2+} cations [58].

$RbAgF_3$ is a brown solid first synthesized by Hoppe and Odenthal in 1971 [58]. This fluoroargentate was thought to crystallize in the $I4/mcm$ space group, Z = 4, although DFT+U calculations performed by Kurzydłowski [4] indicate, that the space group actually has a slightly lower symmetry: *P*nma. The crystal cell parameters of $RbAgF_3$ are: a = 6.477 Å, b = 8.620 Å, c = 6.449 Å, V = 360.06 $Å^3$. The structure consists of $[AgF_6]$ vertex-sharing distorted octahedra. The length of Ag-F bonds lying along the ***b*** direction is equal 2.1688 Å, while the bonds lying in the ***ac*** plane are 2.0927 Å and 2.4976 Å long. This

means that the structure is antiferrodistortive and consists of elongated octahedra with longer axes in the ***ac*** plane. The angles in Ag-F-Ag chains along the ***b*** direction are equal 167.06°, whereas angles Ag-F-Ag in the antiferrodistortive layers are equal 169.17°. This fluoroargentate is actually isostructural with low-temperature polymorph of $KAgF_3$.

A.2.1.2.5 $CsAgF_3$

As in the case of $RbAgF_3$, the cesium analog is a brown solid, that was first synthesized by Hoppe and Odenthal in 1971 [58]. The rubidium fluoroargentate crystallizes in $I4/mcm$ space group with cell parameters: a = 6.489 Å, c = 8.520 Å, Z = 4, V = 358.75 $Å^3$. Volume per formula unit is slightly larger than the sum of volumes per f.u. of AgF_2 and $CsAgF_3$ – 95.62 $Å^3$ *vs.* 89.69 $Å^3$.

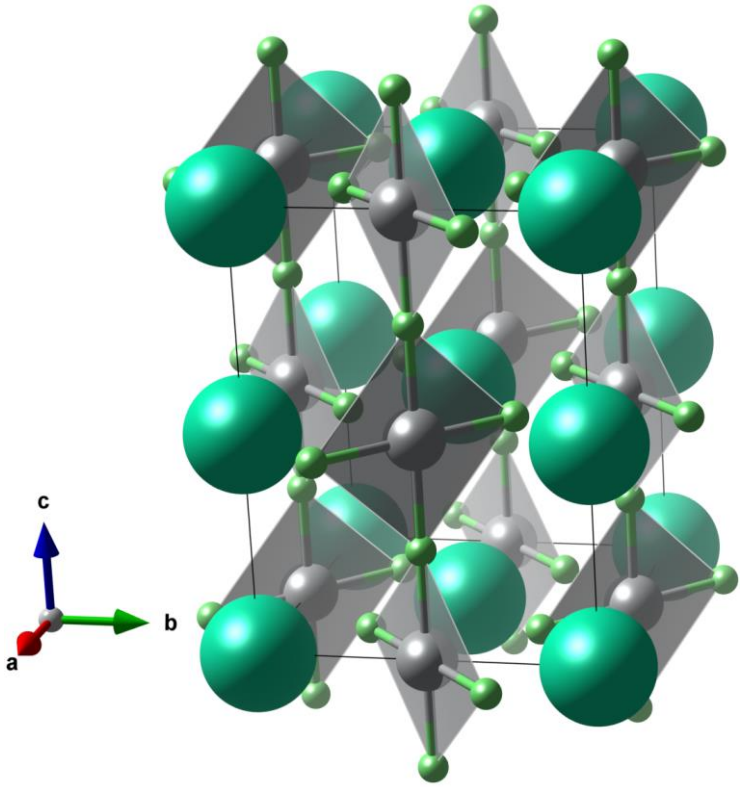

Fig. 19 - a crystal structure model of $CsAgF_3$. Large green balls represent the positions of Cs cations, small green balls represent positions of fluorine atoms, and gray balls represent positions of divalent silver [58].

Each silver cation in the crystal cell of $CsAgF_3$ is coordinated by an elongated octahedron of fluorine atoms. The long axes of neighboring polyhedrons are perpendicular to each other, which is consistent with antiferrodistortive modification of double perovskite structure. The equatorial Ag-F bonds form perfectly linear chains extending in the ***c*** direction.

A.2.1.2.6 K_2AgF_4

K_2AgF_4 is the oldest known alkali metal fluoroargentate from the M_2AgF_4 series. It was first synthesized by Odenthal *et al*. in 1971 [58] – later, the authors synthesized Cs_2AgF_4, Rb_2AgF_4 and other fluoroargentates [20,66]. Dipotassium fluoroargentate is an example of a compound that can adopt two different structures depending on the conditions during the synthesis. For some time only the high-temperature, metastable *Cmca* polymorph was characterized [58]. Further studies revealed a thermodynamically stable low-temperature post-perovskite $P2_1/c$ phase.

A.2.1.2.6.1 α-K_2AgF_4

The first known polymorph of K_2AgF_4 was the metastable α-K_2AgF_4. As mentioned earlier, first documented synthesis took place in 1971. The metastable phase was synthesized via a direct high-temperature synthesis from KF and AgF_2 in 2:1 molar ratio, yielding violet crystals:

$$2KF + AgF_2 \xrightarrow{2\ days,\ 480°C} \alpha\text{-}K_2AgF_4$$

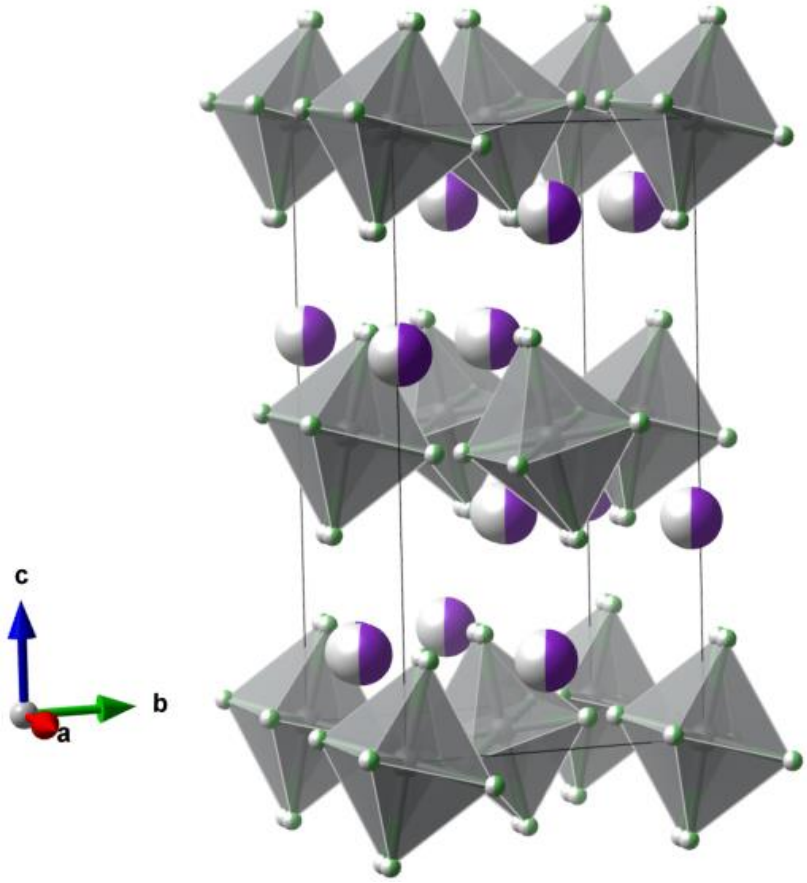

Fig. 20 - a ball-and-stick model of the crystal structure of α-K_2AgF_4. Purple/white balls indicate positions of potassium cations. The structure exhibits a disorder in the positions of fluorine anions and potassium cations [67].

Fig. 20 depicts a crystal structure of high-temperature polymorph of K_2AgF_4, measured at 200 K [66]. Models of the crystal structure proposed before contained layers of compressed vertex-sharing [AgF_6] octahedra [65]. The new correct solution corresponds to a *C*mca space group in the *B*mab setting, just like in the previous descriptions of the structure, although in contrast to earlier work the new structure is antiferrodistortive, and contains elongated octahedra as well as disorder in positions of potassium and fluorine atoms. The new structure has an improved goodness-of-fit parameters (R_{old} = 3.06%, R_{new} = 2.47%), and is structurally more similar to double perovskites containing bigger cations (Rb_2AgF_4, Cs_2AgF_4). The [AgF_6] octahedra forming the structure all tilted from the direction of ***c*** axis by roughly 13.6°.

A.2.1.2.6.2 β-K_2AgF_4

In 2010 Kurzydłowski *et al*. [68] published a study describing a new, stable polymorph of K_2AgF_4. Two synthesis methods were described. The first one used heating of α-K_2AgF_4 under 180 °C:

$$\alpha\text{-}K_2AgF_4 \xrightarrow{180\,^{\circ}C} \beta\text{-}K_2AgF_4$$

The second uses a direct route from KF and AgF_2 in a 2:1 molar ratio. The reaction is conducted at a lower temperature and for a longer time than in the synthesis of α polymorph:

$$2KF + AgF_2 \xrightarrow{2\,weeks,\ 300^{\circ}C} \beta\text{-}K_2AgF_4$$

Both methods yielded gray polycrystalline samples. Stability of the new polymorph from room temperature up to 250 °C was proved by series of TGA/DSC measurements of α-K_2AgF_4, where an exothermic peak with no mass change was observed for temperatures below 190 °C, indicating a structural phase transition from α to β form.

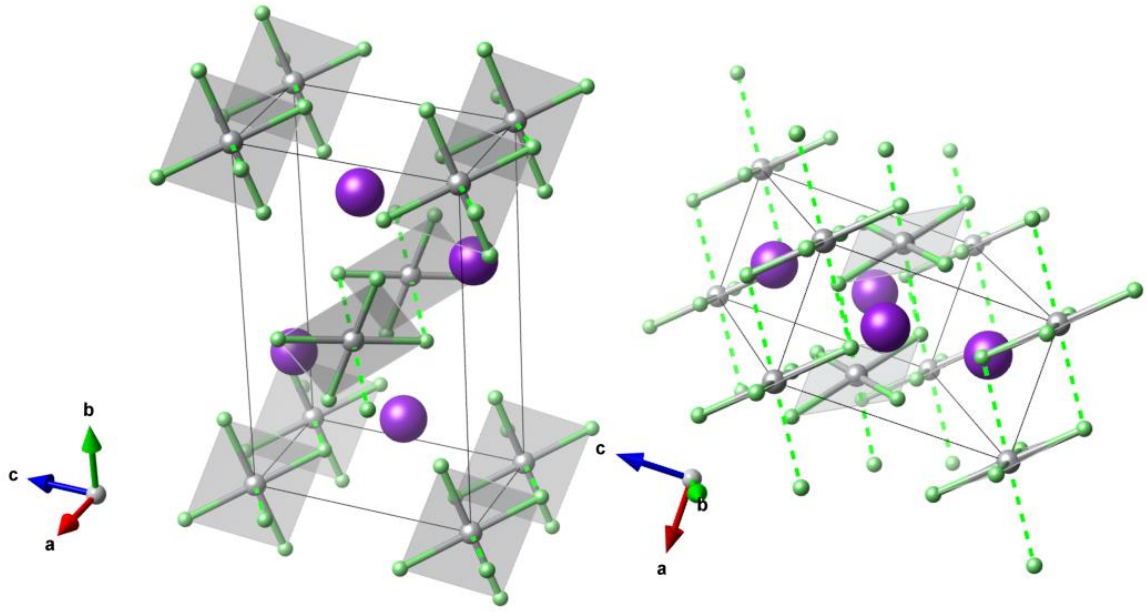

Fig. 21 – two projections of a ball-and-stick model of β-K_2AgF_4 crystal structure [68]. *The dashed lines indicate the direction of elongated Ag-F bonds.*

The β-K_2AgF_4 structure crystallizes in $P2_1/c$ space group. The cell parameters are: a = 3.7174(1) Å, b = 10.2736(2) Å, c = 6.3856(1) Å, β = 91.744(1)°, V = 243.76(1) $Å^3$, Z = 2. The figure above depicts a ball-and-stick model of the structure. The most striking difference between α and β forms lies in connectivity pattern of [AgF_6] octahedra. In the case of α polymorph, the octahedra are connected via equatorial veritces, forming two-dimensional layers. In case of the β polymorph, the neighboring octahedra are connected via the edges, forming chains extending in the ***a*** direction. Thus, the phase transition between two polymorphs also introduces a pronounced change in topology. Two-dimensional vertex-sharing layers of octahedral [AgF_6] subunits encountered in α-K_2AgF_4 are transformed into one-dimensional edge-sharing chains.

A.2.1.2.7 $AgSO_4$

$AgSO_4$ is a black solid, synthesized for the first time in 2010 [69]. Authors describe two methods of synthesis, which yield silver(II) sulfate with different contaminants. The first method uses metathesis of a highly reactive silver compound with potassium sulfate:

$$Ag(SbF_6)_2 \ + \ K_2SO_4 \xrightarrow{aHF} AgSO_4 \downarrow \ + 2KSbF_6$$

After decantation of $AgSO_4$ and several cycles of rinsing with aHF, the product was still contaminated with amorphous $KSbF_6$. The second method uses stronger, sulfuric acid, to remove weaker acid from silver compound:

$$AgF_2 \ + \ H_2SO_4 \rightarrow AgSO_4 \ + 2\,HF \uparrow$$

Despite rinsing the product with anhydrous hydrogen fluoride, the final product was still contaminated with sulfuric(VI) acid.

Crystal structure of $AgSO_4$ was initially described [68] using a triclinic $P\bar{1}$ space group with a = 4.6923(1) Å, b = 4.7535(1) Å, c = 8.0125(2) Å, α = 103.403(1)°, β = 76.478(1)°, γ = 118.078(1)°, Z = 2 and V = 151.761(6) $Å^3$. Rietveld refinement of this structure yielded R_p = 6.12% and R_{wp} = 6.26%. In 2013 [70], the structure was redetermined and described using much larger monoclinic $C2/c$ cell, after some careful DFT calculations suggested a lower enthalpy of this form of $AgSO_4$. Indeed, the Rietveld refinement of the revised cell yielded improved parameters, R_p = 2.93% and R_{wp} = 3.84%, for the following cell: a = 12.8476(2) Å, b = 13.6690(4) Å, c = 9.36678(19) Å, β = 47.5653(13)°, V = 1214.04(5) $Å^3$, with Z = 16. Difference between DFT-calculated cell parameters versus those obtained from the experiment (i.e., refined using Rietveld method) were not exceeding 1.2%, indicating a very good agreement between the two.

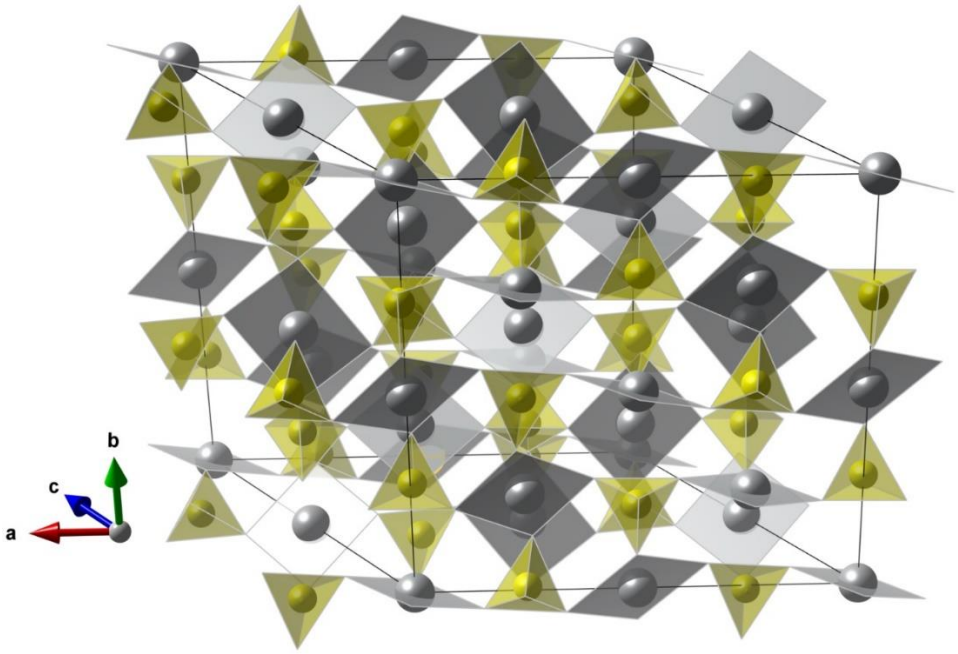

Fig. 22 - The model of the crystal structure of $AgSO_4$. Space group is $C2/c$, Z = 16.

Fig. 22 depicts the crystal structure of $AgSO_4$ $C2/c$ cell. The oxygen atoms are bridging slightly distorted [AgO_4] squares and [SO_4] tetrahedra, and they have been omitted for clarity. The structure contains four nonequivalent silver positions Ag1, Ag2, Ag3, and Ag4. Each silver cation is coordinated by four distinct sulfate groups. Average Ag(II)-O bond lengths in [AgO_4] squares occupying those positions are 2.1070 Å, 2.1262 Å, 2.0972 Å, and 2.0970 Å, respectively.

A.2.1.3 Mixed valence silver compounds

A.2.1.3.1 AgO

AgO is a mixed-valence silver oxide, containing silver(I) and silver(III) cations in equal numbers. The cations of different valency are positioned at different crystallographic sites and do not move freely between two sites. According to Robin and Day classification of mixed-valence compounds that makes AgO (or more precisely $Ag^{I}Ag^{III}O_2$) a **class I** compound [71].

Under ambient pressure AgO usually adopts a $P2_1/c$ structure with a = 5.852(1) Å, b = 3.478(1) Å, c = 5.494(1) Å, β = 107.50(1)°, Z = 4 and V = 106.6(6) $Å^3$. Ag(I) cations are coordinated linearly by two oxygen atoms with Ag(I)-O bond lengths equal to 2.158 Å. Ag(III) cations on the other hand form squares with oxygen atoms with an average Ag(III)-O bond length equal to 2.023 Å. The AgO_4 squares are connected via vertices, forming corrugated sheets extending parallel to the (100) plane. Each sheet of connected AgO_4

squares is separated from its neighbors by a layer of AgO_2 dumbbells (Fig. 24). The angle between diagonals of vertex-connected squares is equal 106.95°.

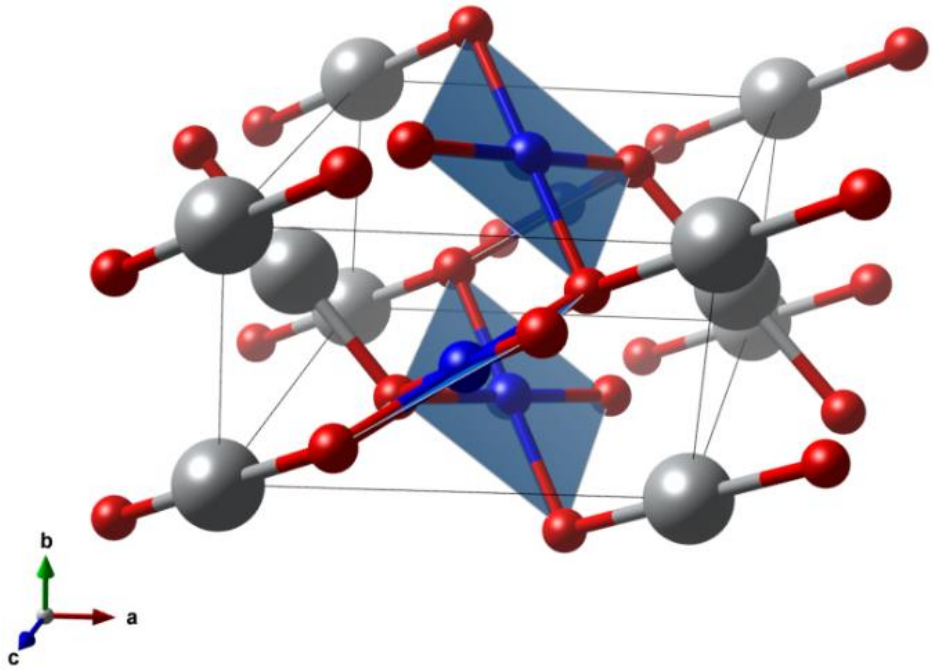

Fig. 23 - a ball-and-stick model of monoclinic Ag(I,III)O_2 structure

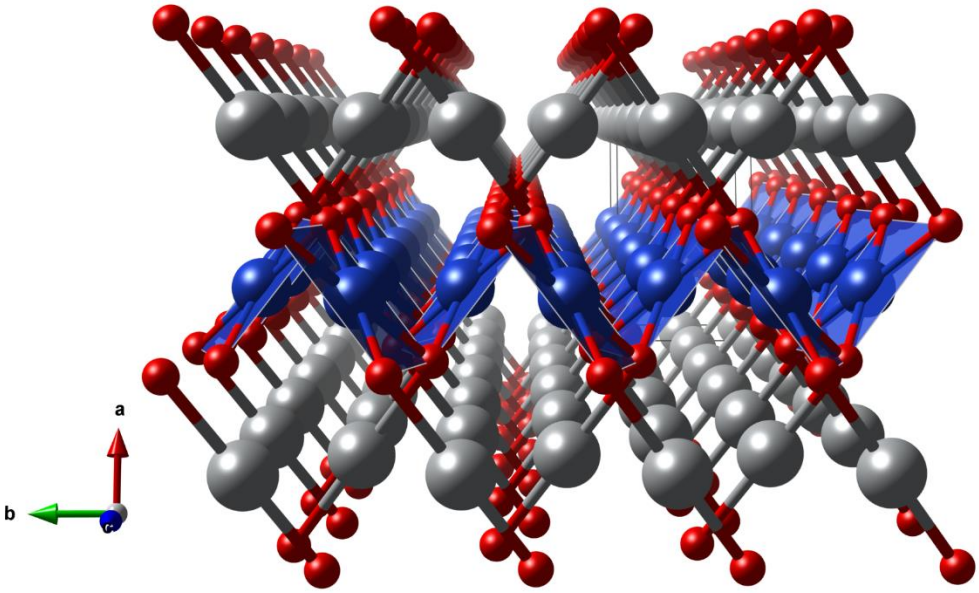

Fig. 24 - a ball-and-stick model of monoclinic Ag(I,III)O_2 structure. Notice the corrugated sheet formed from [AgO_4] squares sandwiched between layers of dumbbell-coordinated Ag(I) cations.

$Ag(I)Ag(III)O_2$ may also adopt a tetragonal $I4_1/a$ structure, with a = 6.833(3) Å, c = 9.122(4) Å, Z = 16 and V = 425.9(3) $Å^3$. Synthetic protocol leading to tetragonal form utilizes ozone to oxidize either metallic silver or Ag_2O suspension [72].

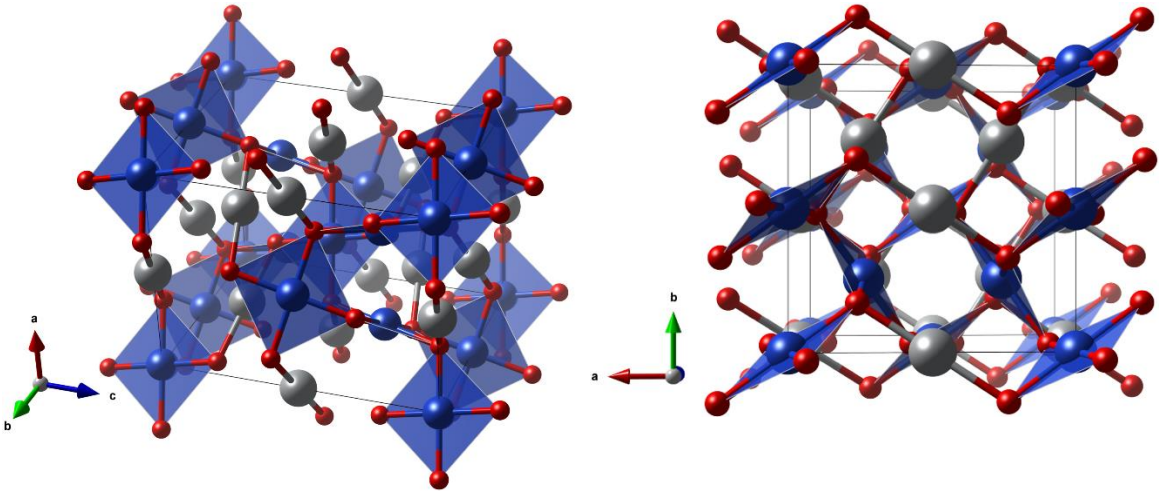

Fig. 25 - a ball-and-stick model of tetragonal $Ag(I)Ag(III)O_2$ crystal structure

In the tetragonal structure there are no distinct $[AgO_4]$ layers separated by monovalent silver cations, but rather $[AgO_4]$ squares forming puckered sheets which are connected by other $[AgO_4]$ squares and dumbbell-coordinated Ag(I) cations. Average Ag(III)-O bond length is equal to 2.023 Å, identical to that for the monoclinic polymorph. The angle between diagonals of vertex-sharing $[AgO_4]$ squares is 110.6°. Average of two Ag(I)-O bond lengths equals 2.167 Å, which is about 0.4% longer than in the monoclinic polymorph.

A.2.1.4 Compounds of copper(II) relevant to this study

A.2.1.4.1 Sr_2CuO_3

Distrontium cuprate is a black solid synthesized first time in 1969 [73]. It can be synthesized from strontium carbonate and copper oxide powders via a high-temperature sintering process. Some additional care must be applied during synthesis and handling of **Sr_2CuO_3**, due to the hygroscopic nature of this compound – it reacts with water vapor to form $Sr_2Cu(OH)_6$. The most straightforward process of calcination follows the reaction equation:

$$2\,SrCO_3 + CuO \xrightarrow{dry\ air,\ 950°C} Sr_2CuO_3 + 2\,CO_2\uparrow$$

The reaction is performed over several days. Every 24 hrs the mixture is ground to increase the yield. The process can be speeded up significantly (down to about 24h) by using higher temperature and reacting the reagents in oxygen flow:

$$2\,Sr_2CO_3 + CuO \xrightarrow{O_2,\ 1050°C} Sr_2CuO_3 + 2CO_2\uparrow$$

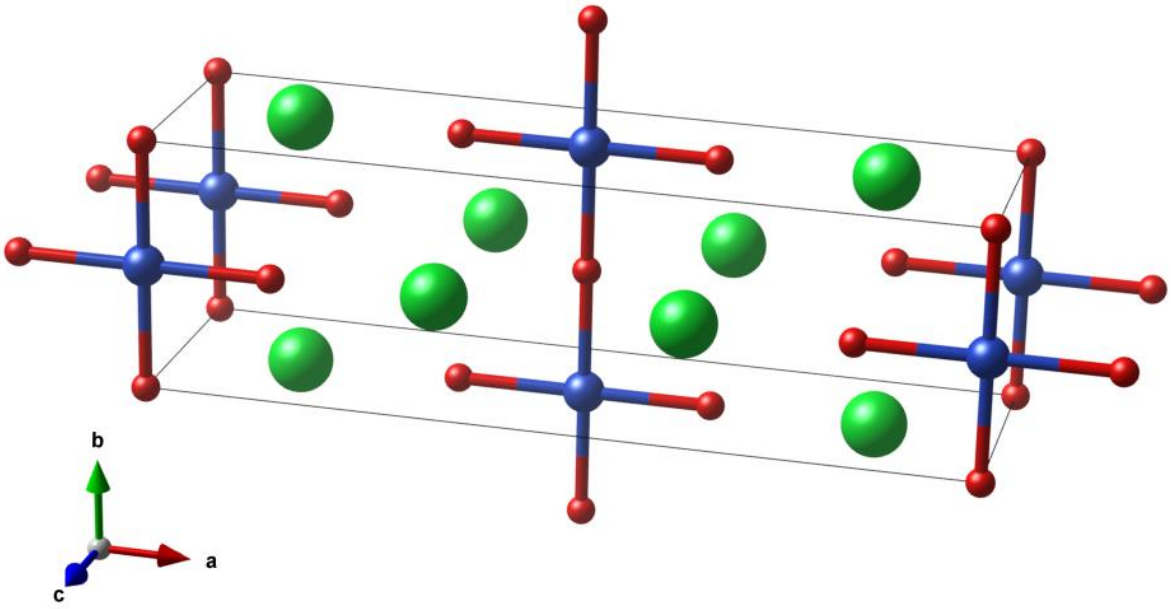

Fig. 26 - a ball-and-stick model of Sr_2CuO_3 structure [73].

Fig. 26 depicts a crystal cell of Sr_2CuO_3. Green balls represent the strontium atoms, blue – copper, red – oxygen. The copper cations are coordinated by four oxygen each, forming a chain along ***b*** direction, consisting of vertex-sharing [CuO_4] squares. The compound crystallizes in a *I*mmm space group, with cell parameters: a = 12.7024(2) Å, b = 3.91138(8) Å, c = 3.49861(6) Å, Z = 2, V = 173.82 $Å^3$.

Alignment of the Cu-O bonds in chains along the ***b*** direction (180° Cu-O-Cu angle through symmetry constraints) promotes antiferromagnetic ordering of spins via superexchange through oxygen atoms. The magnetic superexchange coupling constant J is equal to 241 meV (J_{1D}) [74], which corresponds to a record strong coupling of spins of magnetic cations along the chain. This compound is the strongest-coupled one-dimensional antiferromagnet known.

A.2.1.4.2 La_2CuO_4

Lanthanum copper oxide is a black solid, that was synthesized for the first time in 1960[4]. The simplest method of synthesis follows the equation:

$$La_2O_3 + CuO \xrightarrow{air,\ 1000-1200°C} La_2CuO_4$$

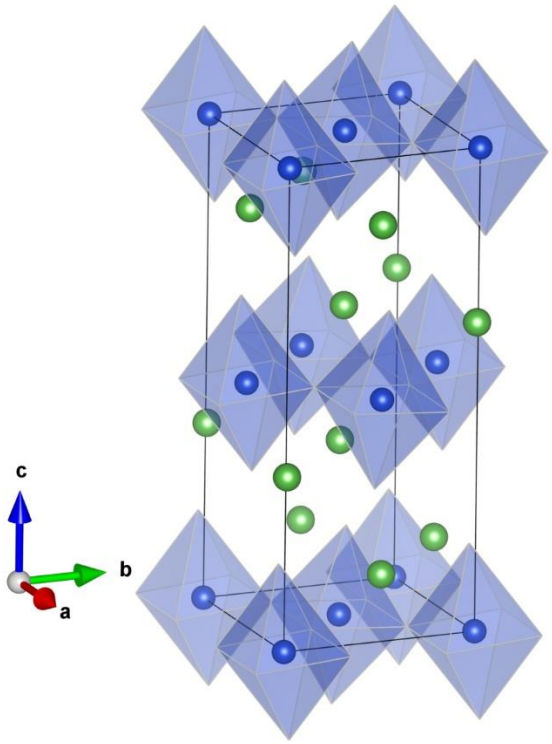

Fig. 27 - a ball-and-stick model of the La_2CuO_4 crystal structure. Positions of oxygen atoms were omitted for clarity. Blue spheres indicate positions of copper(II) cations; green spheres indicate positions of lanthanum cations.

Fig. 27 depicts a ball-and-stick crystal structure of La_2CuO_4. For clarity, the oxygen atoms positions are indicated only by vertices of coordination octahedra around copper cations.

La_2CuO_4 under ambient pressure and temperature adopts a *B*mab structure with a = 5.357 Å, b = 13.15 Å, a = 5.402 Å, Z = 4, V = 380.5 Å^3. Each copper cation is coordinated by six oxygen anions forming an elongated octahedron. The equatorial oxygen atoms are at a distance of 1.905 Å from central copper anion. Axial oxygen atoms are at a distance of 2.425 Å from the copper center. Neighboring $[CuO_4]^{6-}$ squares are slightly tilted out of the (001) plane, with the angle between their diagonals equal to 173.59°.

[4] The first paper mentioning the successful synthesis of La_2CuO_4 was written by Foex et al., *C.R. Acad. Sci.*, **1960,** 3027. Unfortunately I was not able to gain access to this publication. Nevertheless, most of the papers discussing lanthanum copper oxide indicate, that this article first mentioned this compound.

La_2CuO_4 is a ½-spin Heisenberg 2D antiferromagnet [75]. The nearest-neighbor magnetic exchange constant at 295 K is equal 138.3 meV [76], which is currently the highest known magnetic superexchange constant in a 2D layer antiferromagnet (J_{2D}) [77].

A.2.2 Vibrational spectra of selected silver compounds and oxocuprates

A.2.2.1 Group-theory predictions of the number of first-order optical modes for selected compounds

Structure type	Example	Space group	Z	Optical modes: IR-active	Optical modes: Raman-active	Optical modes: Silent	N° of normal modes
Cubic perovskite	$SrTiO_3$	$Pm\bar{3}m$	1	3 $T1_u$	-	T_{2u}	12
Distorted perovskite	**$LT\text{-}KAgF_3$, $RbAgF_3$**	$Pnma$	4	9 B_{1u}, 7 B_{2u}, 9 B_{3u}	7 A_g, 5 B_{1g}, 7 B_{2g}, 5 B_{3g}	8 A_u	57
	$HT\text{-}KAgF_3$	$Pcma$	2	7 A_g,7 B_{1g}, 5 B_{2g}, 5 B_{3g}	5 B_{1u}, 8 B_{2u}, 8 B_{3u}	6 A_u	**<u>51</u>**
	$CsAgF_3$	$I4/mcm$	4	3 A_{2u}, 6 E_u	A_{1g}, B_{1g}, 2 B_{2g}, 2E_g	A_{1u}, A_{2g}, 2 B_{1u}	27
Double perovskite	K_2NiF_4	$I4/mmm$	2	3 A_{2u}, 4 E_u	2 A_{1g}, 2E_g	B_{2u}	18
Distorted d. perovskite	**$\alpha\text{-}K_2AgF_4$**	$Cmca$	4	7 B_{1u}, 6 B_{2u}, 4 B_{3u}	5 A_g, 4 B_{1g}, 3 B_{2g}, 6 B_{3g}	4 A_u	**<u>39</u>**
	La_2CuO_4	$Bmab$	4	7 B_{1u}, 6 B_{2u}, 4 B_{3u}	5 A_g, 4 B_{1g}, 3 B_{2g}, 6 B_{3g}	4 A_u	39
	HP-K_2CuF_4	$Ammm$	2	4 B_{1u}, 4 B_{2u}, 4 B_{3u}	2 A_g, 2 B_{1g}, 2 B_{3g}	-	18
Post-perovskite	**$\beta\text{-}K_2AgF_4$**	$P2_1/c$	2	11 A_u, 10 B_u	9 A_g, 9 B_g	-	39
Rock-salt (NaCl)	**AgF**	$Fm\bar{3}m$	4	T_{1u}	-	-	3
CsCl	**HP-AgF**	$Pm\bar{3}m$	1	T_{1u}	-	-	3
Rutile	AX_2	$P4_2/mnm$	2	A_{2u}, 3 E_u	A_{1g}, B_{1g}, B_{2g}, E_g	A_{2g}, 2 B_{1u}	18
Fluorite	AX_2	$Fm\bar{3}m$	4	T_{1u}	T_{2g}	-	6
Cotunnite	AX_2	$Pnma$	4	5 B_{1u}, 2 B_{2u}, 5 B_{3u}	6 g, 3 B_{1g}, 6 B_{2g}, 3 B_{3g}	3 A_u	33
Other unique types	**AgF_2**	$Pbca$	4	5 B_{1u}, 5 B_{2u}, 5 B_{3u}	3 A_g, 3 B_{1g}, 3 B_{2g}, 3 B_{3g}	6 A_u	33
	$AgFBF_4$	$P4/n$	2	5 A_u, 5 ^1E_u, 5 ^2E_u	5 A_g, 4 B_g, 6 ^1E_g, 6 ^2E_g	3 B_u	39
	$AgSO_4$	$C2/c$	16	41 A_u, 40 B_u	30 A_g, 30 B_g	-	141
	AgO (monoclinic)	$P2_1/c$	4	8 A_u, 7 B_u	3 A_g, 3 B_g	-	21
	AgO (tetragonal)	$I4_1/a$	16	8 A_u, 8 ^1E_u, 8 ^2E_u	3 A_g, 3 B_g, 3 ^1E_g, 3 ^2E_g	9 B_u	45
	Sr_2CuO_3	$Immm$	2	3 B_{1u}, 3 B_{2u}, 3 B_{3u}	2 A_g, 2 B_{1g}, 2 B_{2g}	-	15

Tab. 1 – a group theory analysis of possible first-order optical phonon modes in compounds and structures relevant to this thesis. Underlined sums in the last column indicate structures containing disorder.

A.2.2.2 AgF

The infrared spectrum of AgF was described in a paper by Bottger and Geddes [78]. The authors measured FIR spectra of thin silver(I) fluoride films ranging from 0.1 μm to 2 μm, at 143 K and room temperature, in transmission mode or reflectivity mode (for a sample deposited on a surface of an optically flat glass plate coated with platinum). The authors found four bands in the spectrum, for which they conducted the symmetry assignments. Two bands were described as transverse optical and longitudinal optical modes at Γ point of Brillouin zone by fitting the measured positions to the known wavenumber *vs.* lattice constant function for isostructural silver(I) halides. Symmetry considerations led authors to identify the other two bands as combination modes from the edge of the first Brillouin zone [79].

Wavenumber[cm^{-1}], 300 K	Wavenumber [cm^{-1}], 143 K	Assignment
170	176	TO (Γ)
212	221	TO + TA (L)
266	273	TO + LA (L)
320	322	LO (Γ)

Tab. 2 - Positions of bands and assignment of symmetry for two measurements of IR spectra of AgF [78]

A.2.2.3 $AgFBF_4$

A.2.2.4 AgF_2

The first far-infrared and Raman spectra of solid AgF_2 under ambient pressure were reported by Mazej *et al.* [65]. The FIR study was conducted using sample smeared between HDPE plates. The Raman measurements were done on a sample closed in an inert-gas-filled quartz capillary.

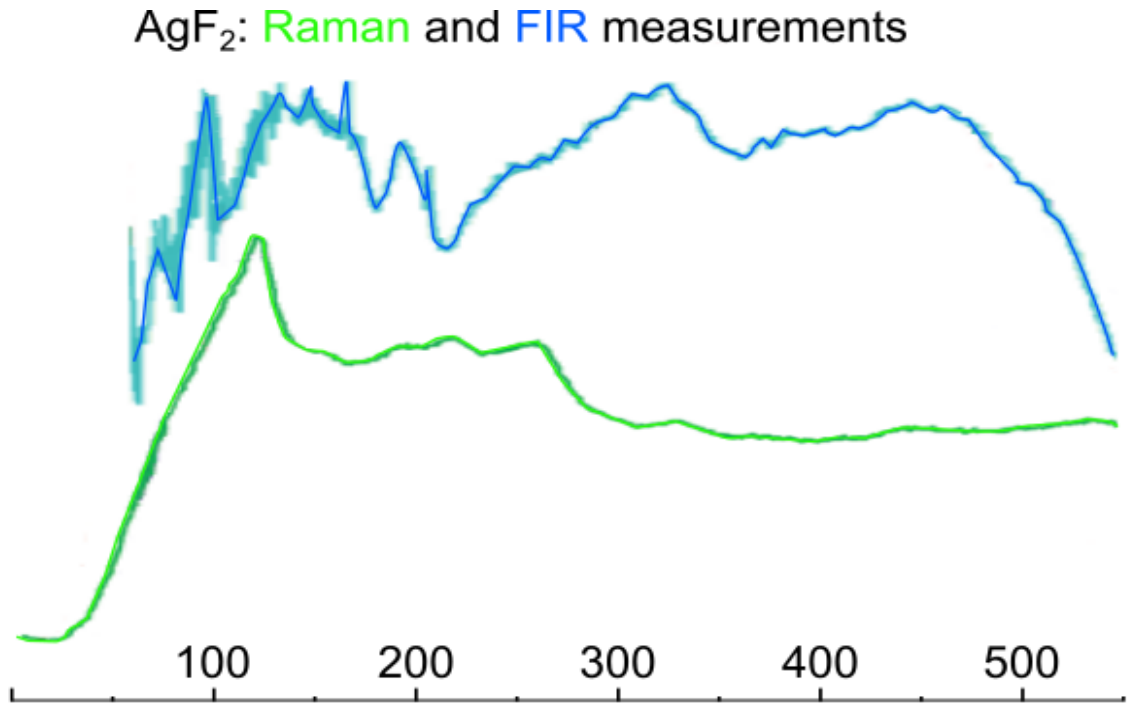

Fig. 28 - Raman (green line) and FIR (blue line) spectra of AgF_2. The spectra were published by Mazej et al. [65], *this is a digitized version of their data overlaid atop of the published spectrum.*

In the original publication [65], band positions of AgF_2 are listed in Table 3 *ibidem*. The full entry reads: 94s (IR), 139s (IR), 189m (IR), 242sh (IR), 252vs (R), 305w (R), 319vs (IR), 372vw (R), 386sh (IR), 413w (R), 445s (IR), 489m (R), 603w (R). Using vector graphic software (Inkscape), I read positions of bands from each spectrum and concluded that in the original paper there has been an error in the description of band positions.

IR dig.	**IR** [65]	**Raman dig.**	**Raman**[65]
73			
96	94 s		
		120	121 s
133	139 s		
148			
165			
192	189 m	189	
		215	
	242 sh		
			257 vs
			305 w
325	319 vs	329	
			372 vw
			413 w
	386 sh		
456		442	
	445 s		
			489 m
			603 w

Tab. 3 - Positions of vibrational bands of AgF_2 from Mazej et al. [65] *and directly read from spectra using a vector graphic program (dig).*

The positions of IR bands are correctly labeled in the original publication. On the other hand, the positions of Raman bands do not appear to describe bands seen in Fig. 28. The next subchapter describes similar errors in the same publication, related to other compounds. Moreover, the origin of these bands was not assigned to date.

A.2.2.5 $KAgF_3$, K_2AgF_4

The two known polymorphs of K_2AgF_4 along with $KAgF_3$ and KF were studied by Kurzydłowski *et al.* [68] using FIR and Raman spectroscopy. $KAgF_3$ and α-K_2AgF_4 were also studied spectroscopically by Mazej *et al.* [65].

In both studies, the FIR measurements were conducted using Vertex 80V FTIR spectrometer. Samples – solid powder – were smeared between two HDPE windows and loaded into a vacuum-tight cell. The Raman measurements were performed in sealed quartz capillaries using FT-Raman Renishaw spectrometer with HeNe laser 632.8 excitation line in backscattering geometry. In the study by Kurzydłowski *et al.* the laser power was set to 50 mW, and data was acquired in the 200–1000 cm^{-1} range relative to the excitation line. In the study by Mazej *et al.* no information regarding the laser power has been provided, the data was collected in 0–550 cm^{-1} range.

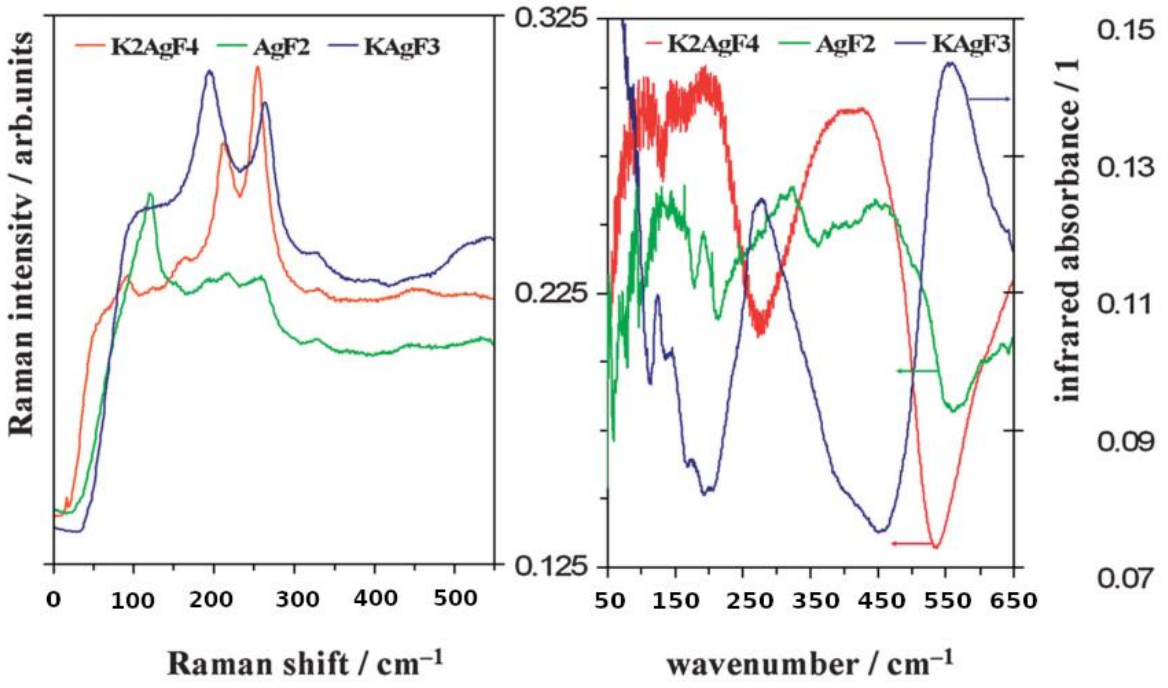

Fig. 29 - Raman and FIR spectra of AgF_2, $KAgF_3$, and α-K_2AgF_4 published by Mazej et al. [65]. *The image was edited to reverse the direction of the x-axis to keep consistency among different datasets.*

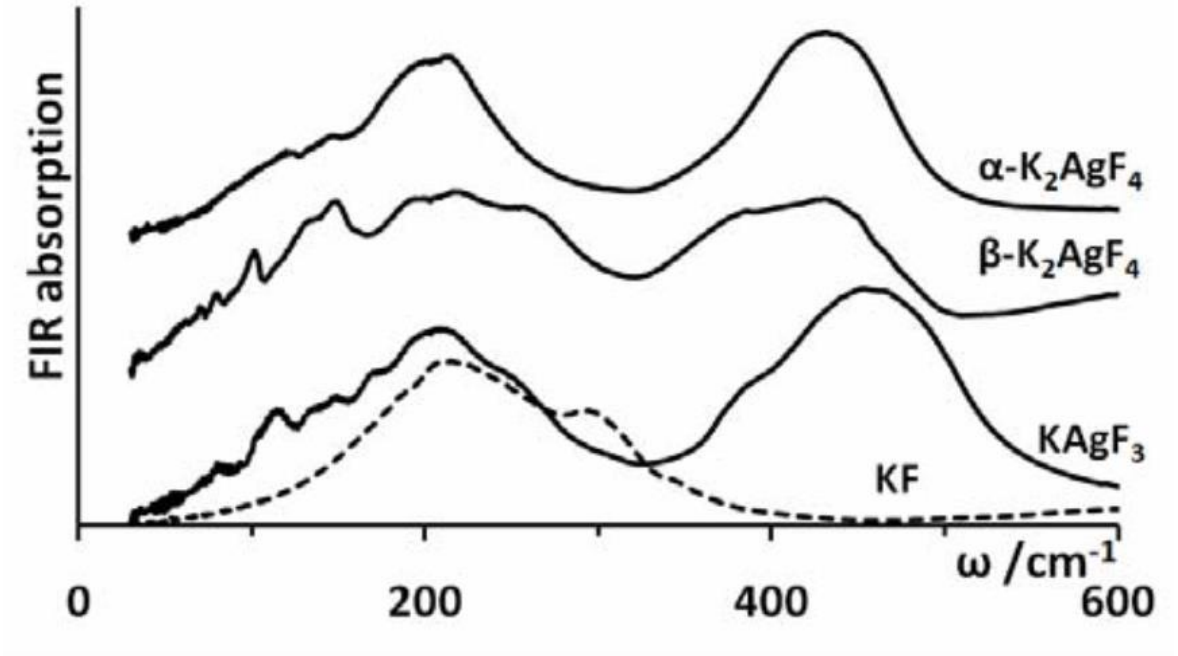

Fig. 30 - FIR absorption spectra of two polymorphs of K_2AgF_4 (α and β), $KAgF_3$ and KF as published by Kurzydłowski et al. [68].

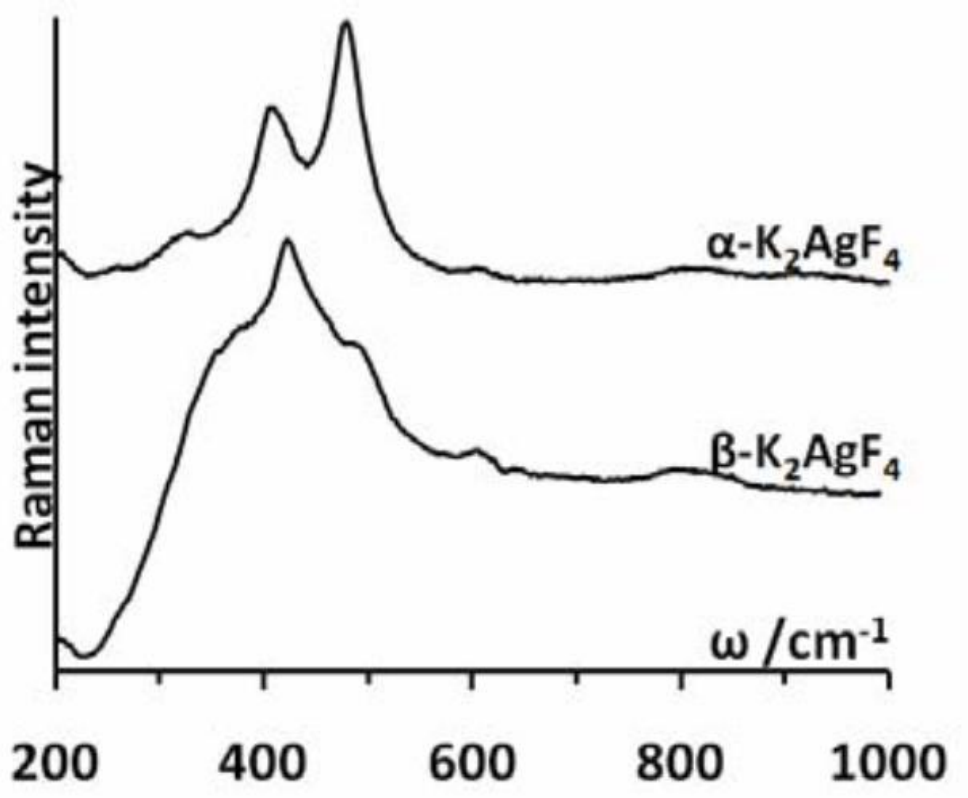

Fig. 31 - Raman scattering spectrum of two polymorphs of K_2AgF_4 as published by Kurzydłowski et al.[68].

Raman spectrum of α-K_2AgF_4 in the Mazej *et al.* paper is visually quite similar to the one obtained by Kurzydłowski *et al.* – for example, a group of three bands with intensity ratio

of about 1:4.5:7 is present in both papers – however, in [64] they are found at 164, 212 and 256 cm^{-1}, while in [68] they are at 320, 415 and 476 cm^{-1}. Similarly, higher wavenumber range in both spectra contains mostly flat background with three weak bands – one closer to the previous group, and a pair near the high-energy part of the spectrum. This strongly suggests, that despite completely different positions of wavenumbers, the spectra describe the same compound, α-K_2AgF_4. If we assume, that positions of the first group mentioned above should be equal, then we can conclude that the wavenumbers in Raman data published by Mazej *et al.* were probably erroneously scaled by a factor of ~0.5. This enabled us to correct the positions of bands in the Raman spectra of Mazej *et al.* (FIR spectra did not contain similar discrepancies; therefore they were left uncorrected).

Raman			**IR**		
α-K_2AgF_4 [65]	α-K_2AgF_4 [68]	β-K_2AgF_4 [68]	α-K_2AgF_4 [65]	α-K_2AgF_4 [68]	β-K_2AgF_4 [68]
					69
					79
105			105		101
				120	135
			147	147	149
184	205		198	196	197
				213	220
247					258
324	320				
		366	377		385
418	415	420			
			432	432	431
					450
505	476	486			
	600*	600*	595		
651					
894					

Tab. 4 - positions of bands in the FIR and Raman spectra of two polymorphs of K_2AgF_4. Data from papers by Mazej et al. [65] *and Kurzydłowski et al.*[68]. *The positions of bands in the Raman spectrum from Mazej et al. paper were corrected by scaling by the factor of 1.91. Bands indicated by an asterisk are very weak and come either from combination modes or some contamination.*

The spectral range in both experiments most likely contains all first order optical phonon modes for both polymorphs of K_2AgF_4. The 420 cm^{-1} band and 432 cm^{-1} probably do not represent the same vibrational mode, because the α structure is centrosymmetric. According to group theory, the rule of mutual exclusion forbids a single band to be optically active both in IR and Raman. To some degree that rule might be bent because of disorder in fluorine positions of both polymorphs – a possible dynamical disorder might enable a vibration to be active in both IR and Raman.

Raman	IR	
$KAgF_3$ [65]	$KAgF_3$ [68]	$KAgF_3$ [65]
	80	
	115	125
	134	
	150	146
	170	177
201	206	200
		232
	257	
		277
385	382	
		414
	460	
521		
		557
651		
793		
874		
1002		
1064		

Tab. 5 - positions of vibrational bands of $KAgF_3$ from papers by Mazej et al. and Kurzydłowski et al.

The spectra of high-temperature form of $KAgF_3$ from the two papers are quite different from each other. Both IR spectra are composed of two strong, broad bands with some additional features. Unfortunately, the positions of those bands in the two spectra do not coincide. Contrary to the Raman spectra from Mazej *et al.* [65], there does not seem to be an easy way to transform the scale in one or the other spectrum to correlate them.

A.2.2.6 $AgSO_4$

The first measurements of FTIR and Raman spectra of silver(II) sulfate were conducted by Malinowski [69]. In the FIR range, the sample measured as a thin layer deposited on HDPE windows in an enclosed measurement cell. In the MIR range, the sample was measured via the same experimental method, although using AgCl windows. The sample for Raman measurement was enclosed in a quartz capillary.

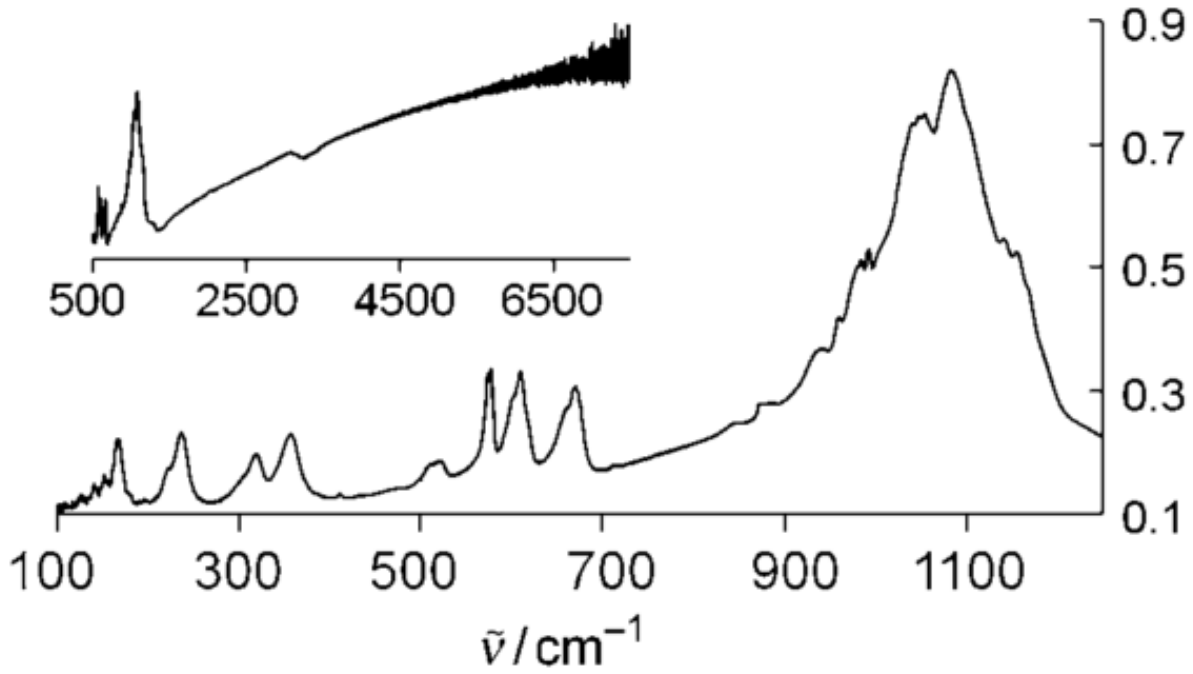

Fig. 32 - FIR and MIR spectra of $AgSO_4$ republished from Malinowski et al. [69]. *The inset depicts a +broader range of data. The direction of x-axis was reversed to keep consistency in presenting data from different papers.*

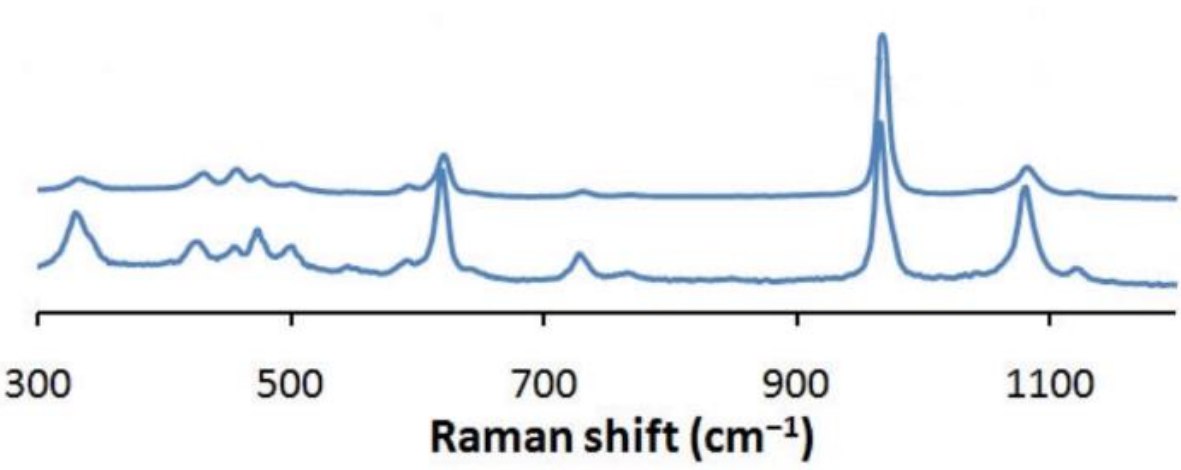

Fig. 33 - Raman spectra of $AgSO_4$ sample measured at two different spots. Data published by Malinowski et al. [69].

The table on the next page contains $AgSO_4$ band data presented in supporting information of the cited paper [69], as well as results from a later theoretical study by Derzsi [80]. Because the theoretical study was based not on the $C2/c$ group but on $P\bar{1}$ model, the assignment of modes cannot be correct (in terms of group symmetry labels).

Malinowski [69]		**Derzsi** [80]			
FTIR	**Raman**	**FTIR**	**Raman**	**DFT**	**Assignment**
1156 sh		1156 sh			Impurity or combination mode
1142 sh		1142 sh			Impurity or combination mode
	1116 w		1125 m	1076	S-O stretch A_g
1084 vs	1077 m-s*	1084 vs	1083 m	1055	S-O stretch A_u
1055 s			1063 w		Impurity or combination mode
1050 vs		1055 s		1018	S-O stretch A_u
1002 sh			1045 w	1016	S-O stretch A_g
993 sh		1050 vs		1010	S-O stretch A_u
985 sh			997 w		Impurity or combination mode
			978 s	956	S-O stretch A_g
960 sh		1002 sh		945	S-O stretch A_u
930 sh		993 sh			Impurity or combination mode
887 vw		985 sh			Impurity or combination mode
	967 vs		970 s	944	S-O stretch A_g
		960 sh			Impurity or combination mode
670 m		930 sh			Impurity or combination mode
660 sh		887 vw			Impurity or combination mode
	760 w	670 m		616	O-S-O deformation A_u
610 m	725 m*	660 sh			Impurity or combination mode
600 sh			647 m	596	O-S-O deformation A_g
		610 m		590	O-S-O deformation A_u
578 m	615 m-s	600 sh			Impurity or combination mode
575 m			622 vs	573	O-S-O deformation A_g
523 w		578 m		539	O-S-O deformation A_u
	586 w			537	O-S-O deformation A_g
		523 w	520 w	495	O-S-O deformation A_u
	494 m		503 w		Impurity or combination mode
	469 m		476 s	469	O-S-O deformation A_g
358 m	448 w			408	O-S-O deformation A_u
	419 m		425 m	389	O-S-O deformation A_g
		358 m		360	Lattice A_u
318 m			305 vw	292	Lattice A_g
237 m		318 m		332	Lattice A_u
222 sh	337 sh	237 m		253	Lattice A_u
167 m	325 m-s*		262 m	224	[AgO_4] stretching and lattice A_g
		222 sh			Impurity or combination mode
		167 m		185	Lattice A_u
			171 s	177	[AgO_4] stretching and lattice A_g
				161	Lattice A_g
		157 w		155	Lattice A_u
		152 w		142	Lattice A_u
		141 w		134	Lattice A_u
			116 w	118	Lattice A_g
			83 m	106	Lattice A_g
				90	Lattice A_u
				70	Lattice A_u

Tab. 6 - positions and strengths of $AgSO_4$ bands. The left side depicts values from the paper by Malinowski et al. [69]. *The positions marked with asterisks are indicative of decomposition of the $AgSO_4$ sample to $Ag_2S_2O_7$. The decomposition occurs because of strong absorption of the visible laser. The right side depicts values from a later study by Derzsi et al.* [80] *which consist of experimental and theoretical (DFT) mode wavenumbers assuming $P\bar{1}$ unit cell. The symmetry of modes was established by computations.*

A.2.2.7 AgO

AgO under ambient pressure has been studied thoroughly by Waterhouse *et al*. [81] using FTIR and Raman spectroscopy. Group theory dictates that the monoclinic polymorph of $Ag(I,III)O_2$ should exhibit 15 IR active (8 A_u, 7 B_u) and 6 Raman active (3 A_g, 3 B_g) modes.

The Raman spectra were collected using 514.5 nm Ar^+ laser as an excitation source. To decrease the photochemical damage from the source the sample was measured using a spin-disk method: 300 mg of oxide powder was pressed into a disc and spun. Spectra were collected in perpendicular sampling geometry.

The FTIR samples were prepared by pressing oxide powder in a press. The resulting pellet was then used in FIR and MIR measurements.

The authors identified 11 bands in the IR spectrum and six bands in the Raman spectrum that can be assigned to $Ag(I,III)O_2$ phonons. The authors assign the identity to each vibrational mode by analyzing possible deformations of two different moieties present in the crystal structure of $Ag(I,III)O_2$: dumbbell-coordinated silver(I) cations, and square-coordinated silver(III) cations. Bands below 300 cm^{-1} are attributed to low-energy lattice modes whereas bands over 600 cm^{-1} are identified as coming from combination bands.

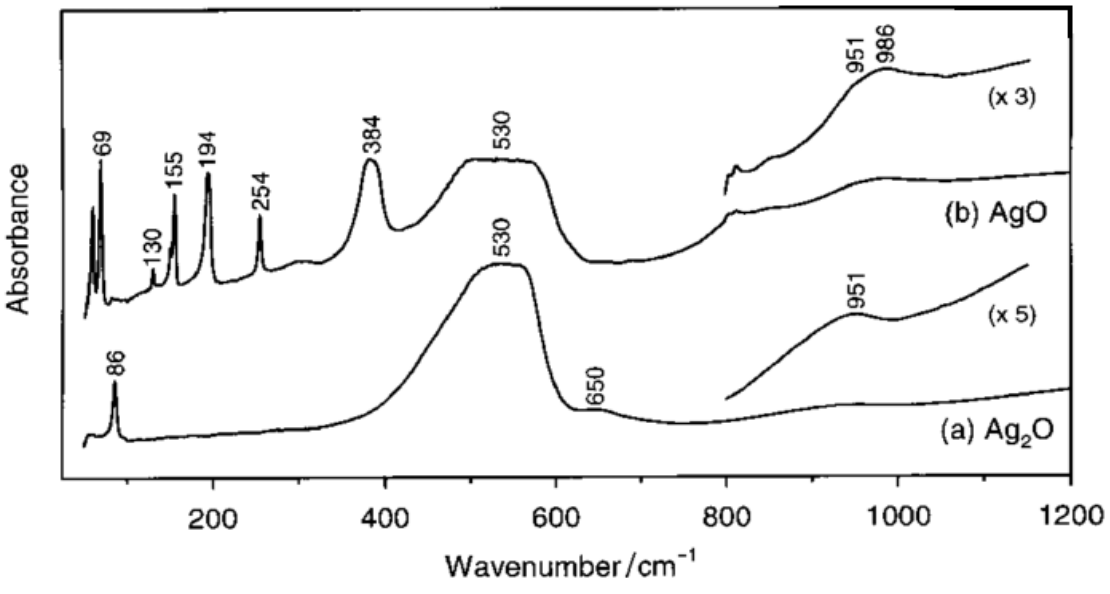

Fig. 34 - AgO and Ag_2O FTIR spectra from Waterhouse et al. [81]. *Insets depict magnified fragments of the spectra.*

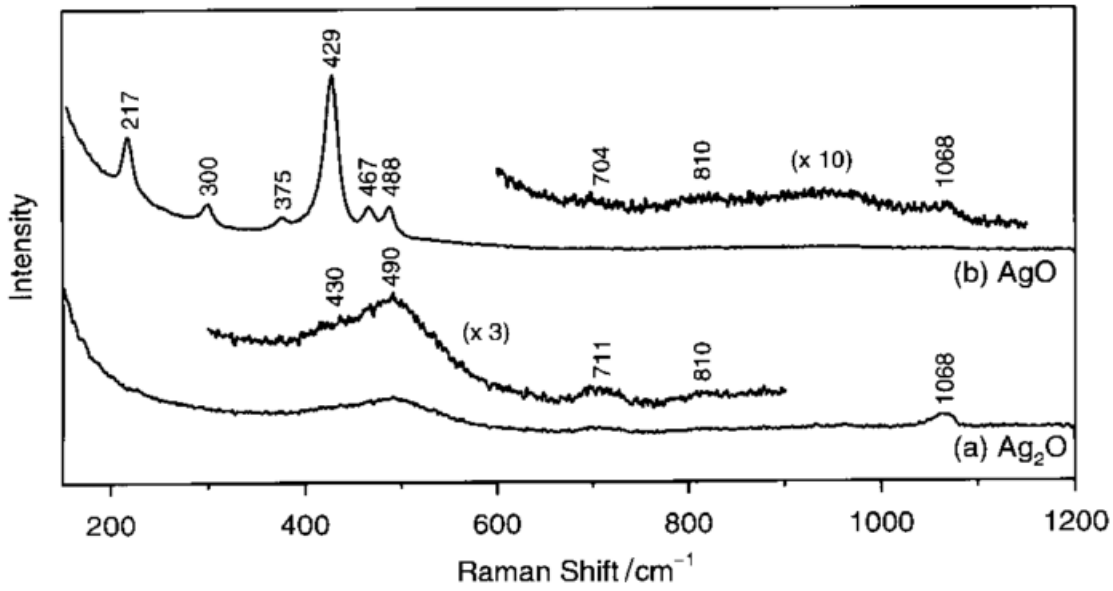

Fig. 35 - Raman spectra of AgO and Ag_2O from Waterhouse et al. [81]. *Insets depict magnified regions of spectra.*

FTIR	Raman	Assignment
986		combination of 467+530
951		combination of 429+530
530		Ag(I)-O_2 asymmetric dumbbell stretching
502		[AgO_4] deformation
	488	Ag(I)-O_2 symmetric dumbbell stretching
	467	asymmetric Ag(III)-O stretching
	429	symmetric Ag(III)-O stretching
384		[AgO_4] deformation
	375	no assignment
	300	no assignment
254		lattice mode
	217	symmetric O-Ag(III)-O bending
194		lattice mode
155		lattice mode
150		lattice mode
130		lattice mode
69		lattice mode
60		lattice mode

Tab. 7 - vibrational data and band assignments for $Ag(I,III)O_2$ [81].

The assignment has been subsequently improved by Wlodarska by including group symmetry labels [82].

A.2.2.8 Sr_2CuO_3

Under ambient pressure and at room temperature Sr_2CuO_3 (also called Sr213) adopts a *I*mmm space group. Polarization dependent IR reflectivity spectra of this oxocuprate were studied by Lee *et al.* [83]. According to group theory (see Tab. 1) authors expected 9 IR-

active optical phonon bands (3 B_{1u}, 3 B_{2u}, 3 B_{3u}) – 3 for each polarization direction parallel to the crystal cell axes. Polarized Raman spectra of Sr213 were studied by Misochko *et al.* [84] in a 10 – 300 K temperature range, using several excitation lines. The authors expected 6 Raman bands (2 A_g, 2 B_{1g}, 2 B_{2g}).

Because both mentioned groups studied Sr_2CuO_3 using polarized light, it is convenient to compare their findings using a given orientation of polarization vectors. Therefore in the following subchapter all directions of polarization are presented using Cartesian coordinate system oriented as in the next figure:

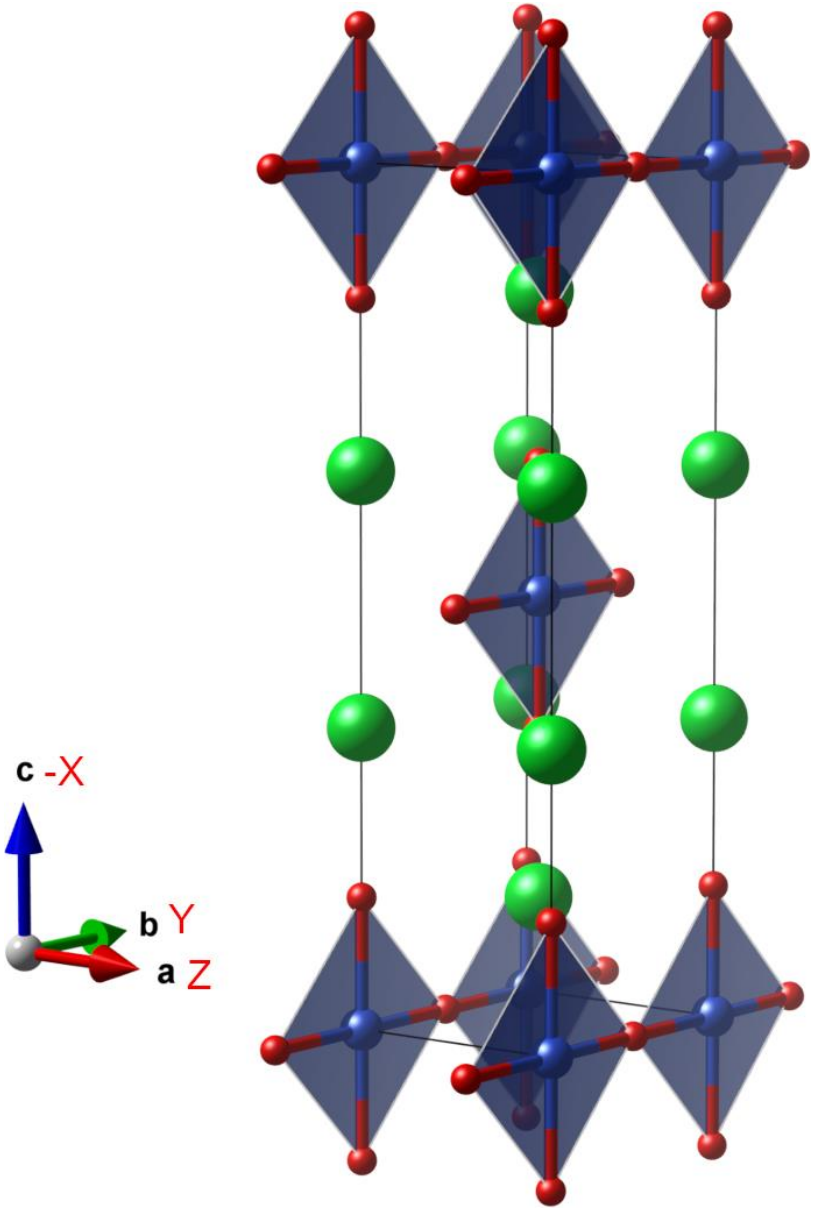

Fig. 36 - Cartesian coordinate system aligned with crystal cell directions used in studies conducted by Lee et al. [83] *and Misochko et al.* [84]. *Direction* ***y*** *is parallel to the propagation of [$CuO_{4/2}$] chains. Versor* ***z*** *is oriented along the interchain direction.*

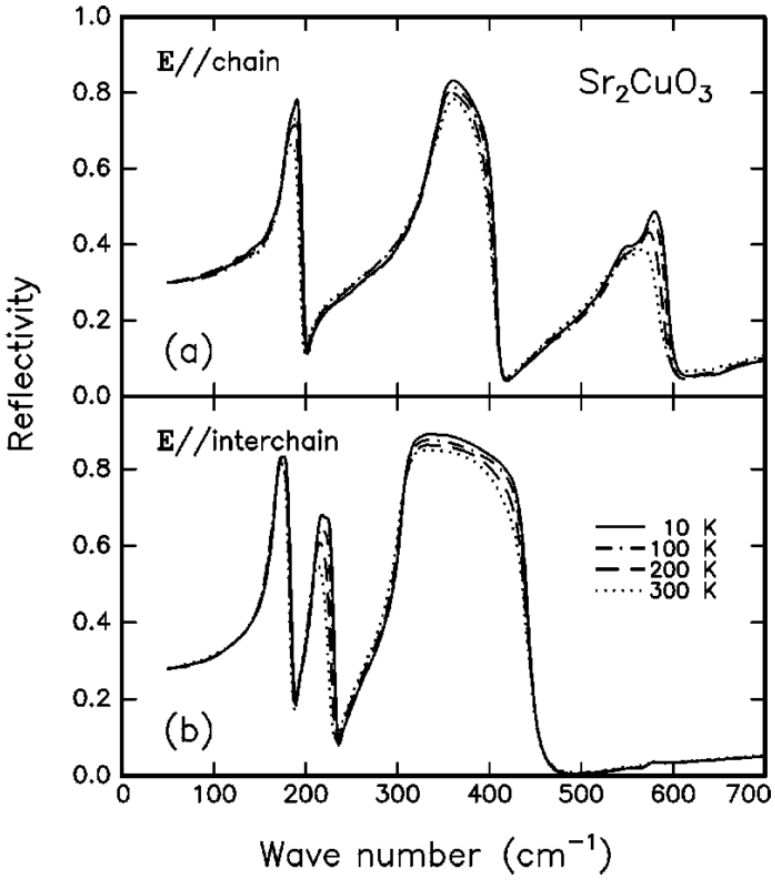

Fig. 37 - reflectivity far infrared spectra of Sr_2CuO_3 at four temperatures in the 10 – 300 K range. Two directions of polarization were used in the experiment: E //chain indicates the direction of polarization parallel to ***y****, E//interchain parallel to* ***z****. The graphs were published by Lee et al.* [83].

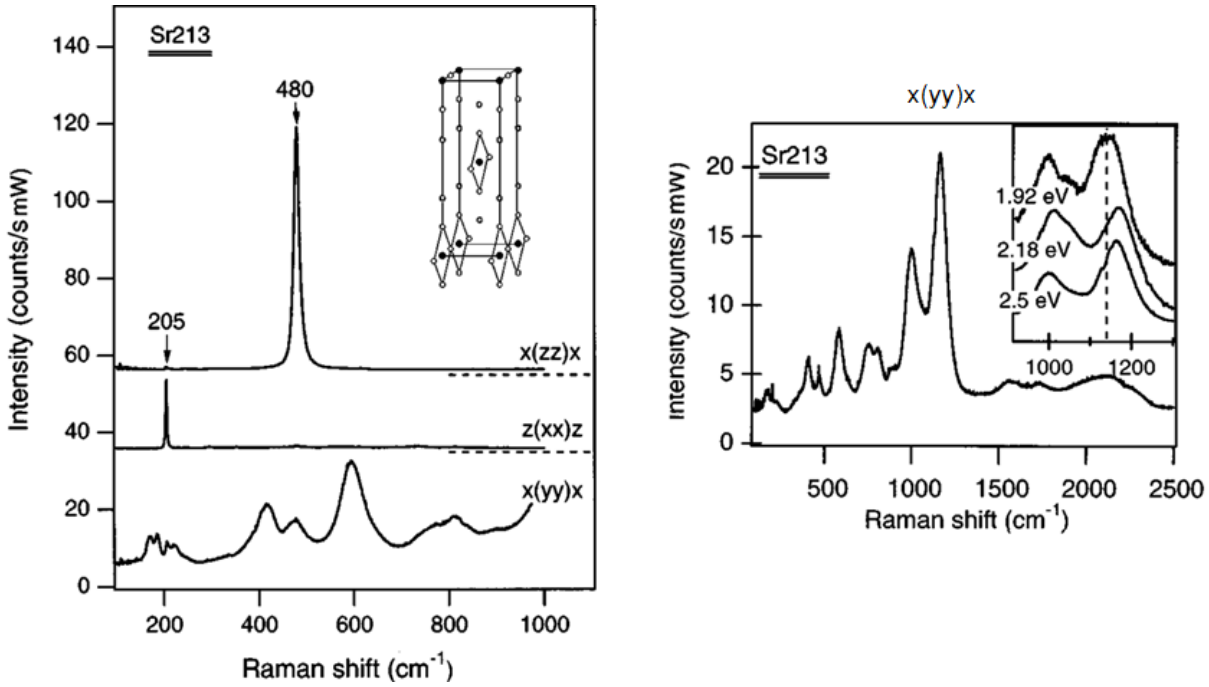

Fig. 38- Raman spectra of Sr_2CuO_3. Left side depicts measurements in X(ZZ)X, Z(XX)Z, X(YY)X polarizations. The right side depicts measurement in X(YY)X configuration in a broader range. The inset on the right picture shows the resonant character of the bands measured in X(YY)X geometry. The graphs were published by Misochko et al. [84].

Sr_2CuO_3 – positions of optical bands, [cm^{-1}] ± 10 cm^{-1}				
IR		Raman		
E ‖ y	E ‖ z	x(zz)x	z(xx)z	x(yy)x
	167			170
179				
				190
	209	205		
				220
	307			
343				
				408
			480	480
539				
558				
				580
				750
				810
				1000
				1160
				1550
				1730
				2130

Tab. 8 - positions of FIR/Raman bands in vibrational spectroscopy of Sr_2CuO_3, measured at 300 K. Compiled from articles of Lee et al. [83] *and Misochko et al.* [84].

The results of Raman measurements of the monocrystalline Sr_2CuO_3 sample are presented. Group theory dictates, that for Raman experiments conducted on Sr_2CuO_3 in A(BB)A backscattering geometry, where A≠B, A,B = {X, Y, Z}, only A_g modes are active. Therefore Raman modes at 205 cm^{-1} and 480 cm^{-1} can be easily identified as A_g. Number of modes found for –X(YY)X polarization (Tab. 8) does not follow the predictions made via group theory, which indicates that bands do not originate from a non-resonant first-order Raman scattering. Authors of the cited paper suggested a resonant mechanism as a partial explanation for the number of modes group theory exceeding expectations. The authors base this conclusion on series of Raman experiments using different excitation lines (see Fig. 38, inset on the right side) which showed that dependence of intensity is not proportional to the reciprocal fourth power of wavelength. Instead, the intensity has reached a maximum at about 2 eV, which corresponds to the energy of the charge-transfer gap in Sr_2CuO_3 [85].

The authors have assigned the 408 cm^{-1} and 580 cm^{-1} to bending and stretching modes originating from bridging oxygen atoms in [$CuO_{4/2}$] chains. This enabled identification of 750 cm^{-1} and 1160 cm^{-1} modes as their overtones and 1000 cm^{-1} mode as a combination mode. Further observations regarding Raman data will be discussed in subchapter A.2.3.1.

The FIR spectra of Sr_2CuO_3 conducted for two different polarization directions (Fig. 37) contain three bands each. The authors suggest that for the intrachain polarization (E || y) the three bands are the product of so-called external – 179 cm^{-1}, bending – 343 cm^{-1}, and stretching – 539 cm^{-1}, 558 cm^{-1} – modes[5] of the chains (see also [86]). The highest energy band obtained for light polarized parallel to the $[CuO_{4/2}]$ chains is split into two components separated by 19 cm^{-1} (maximum-to-maximum).

A.2.2.9 La_2CuO_4

Under ambient pressure and at room temperature the crystal structure of La_2CuO_4 is orthorhombic (*B*mab setting of the *C*mca group, Z=4). The expected number of vibrational modes is 39. Vibrational Raman spectra of this oxocuprate and a family of its strontium-doped analogs, $(La_{1-x}Sr_x)_2CuO_4$, were studied by Sugai [87]. The author describes the undoped compound in terms of *C*mca symmetry with 39 optical modes (18 Raman-active: 5 A_g, 3 B_{1g}, 6 B_{2g}, 4 B_{3g} and 21 IR-active: 4 A_u, 6B_{1u}, 4B_{2u}, 7B_{3u}). Experiments conducted by Sugai used a well-polished single crystal of La_2CuO_4. The measurements were conducted for a range of temperatures from 5 to 513 K (low-temperature regime measured in helium flow cryostat, the high-temperature regime in an air filled furnace) and polarization configurations. 514.5 nm Ar-ion laser excitation line was used in a backscattering geometry in most experiments, apart from a series of measurements at 30 K which probed the resonant effects in Raman spectra using three different laser excitation lines – 514.5 nm, 488.0 nm and 457.9 nm. In all experiments the Rayleigh scattered light was removed using a double monochromomator.

Sugai found that each spectrum of La_2CuO_4 can be divided into three regions: below 870 cm^{-1}, between 870 cm^{-1} and 1500 cm^{-1}, and over 1500 cm^{-1}. The first region contains 24 bands, second one contains 9 bands that are interpreted as overtones and combination bands. The third region houses the bimagnon band, which will be further described in subchapter A.2.3.2.

[5] In this case external mode corresponds to movement of Sr^{2+} cations against the $[CuO_{4/2}]$ chains, bending and stretching correspond to appropriate deformations of the chain subunits.

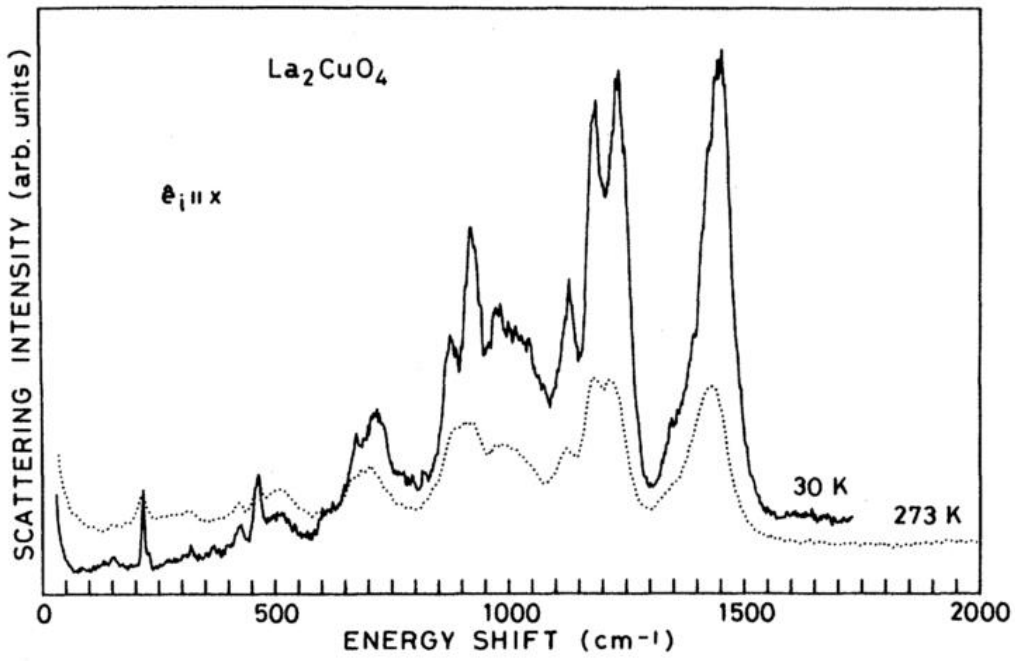

Fig. 39 - Raman spectra of La_2CuO_4 collected at two temperatures: 30 K (solid line) and 273 K (dashed line). Figure from article by Sugai [87].

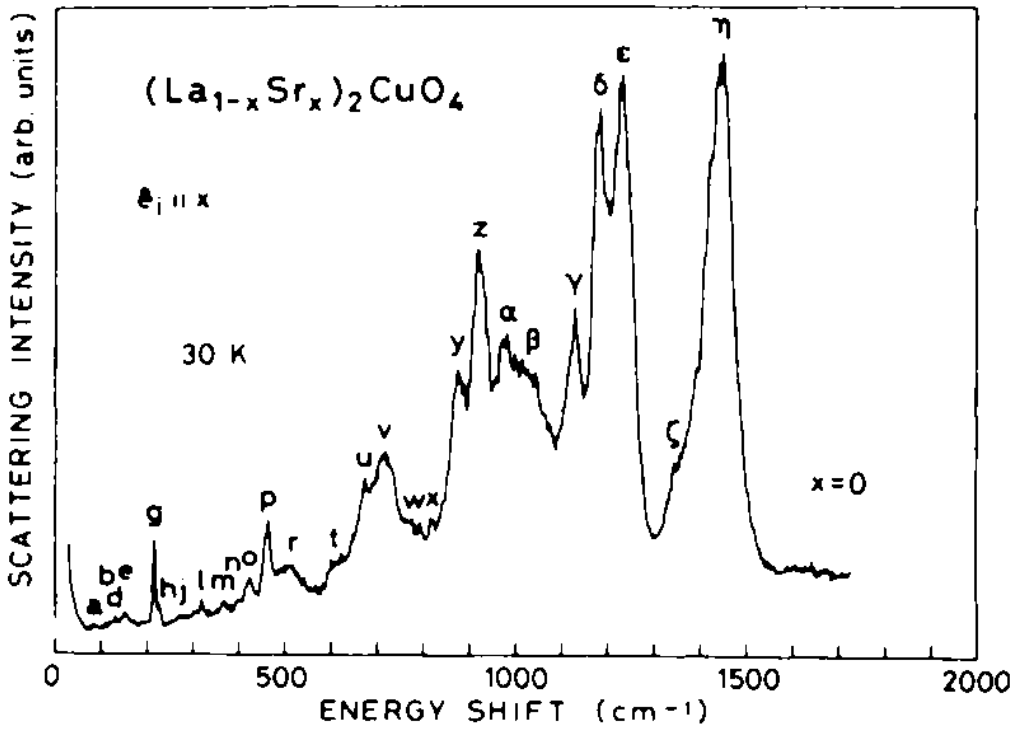

Fig. 40 - Raman spectra of La_2CuO_4 oxocuprate. Latin and Greek letters indicate positions of bands: a to x are interpreted by as single phonon bands, y to η are overtones and combination bands. Illustration is taken from an article by Sugai [87].

	(x, x+y)	(z, z)	(x, z)	rep.		(x, x+y)	(z, z)	(x, z)	rep.
a	85				y (o+p)	876 s			
b	112				z (2p)	919 s			
c		126 s		A_g	α (p+r)	976 s			
d	132				β (2r)	1023 sb			
e	152	156 s		A_g	γ (p+u)	1129 s			
g	216 s		219		δ (r+u, p+v)	1182 s			
h	227	229 s		A_g	ε (r+v)	1232 s			
j	273	273 s		A_g	ζ (2u)	1347			
l	318				η (2v)	1449 s			
m	366								
n	398								
o	424 s	426 s		A_g					
p	462 s								
r	511 sb								
t	608								
u	673 s								
v	716 sb								
w	792								
x	818								

Tab. 9 - positions of bands in La_2CuO_4 spectrum from an article by Sugai [87]*. The column headers (a, b) indicate the polarization of incoming (a) and scattered (b) light and assigned irreducible representation of the mode (rep.).*

A.2.3 Multimagnon bands in Raman and IR spectra of selected silver and copper compounds

A.2.3.1 Sr_2CuO_3

The evidence for the presence of magnetic bands in Sr_2CuO_3 was presented in the MIR measurements by Suzuura *et al.* [88]. The authors prepared a monocrystalline sample of Sr213 in the form of a thin plate, with well-developed and polished (100) face. Measurements were conducted for incoming light polarized along the [$CuO_{4/2}$] chain direction (E || ***b***) and for light polarized in the perpendicular direction (E || ***c***).

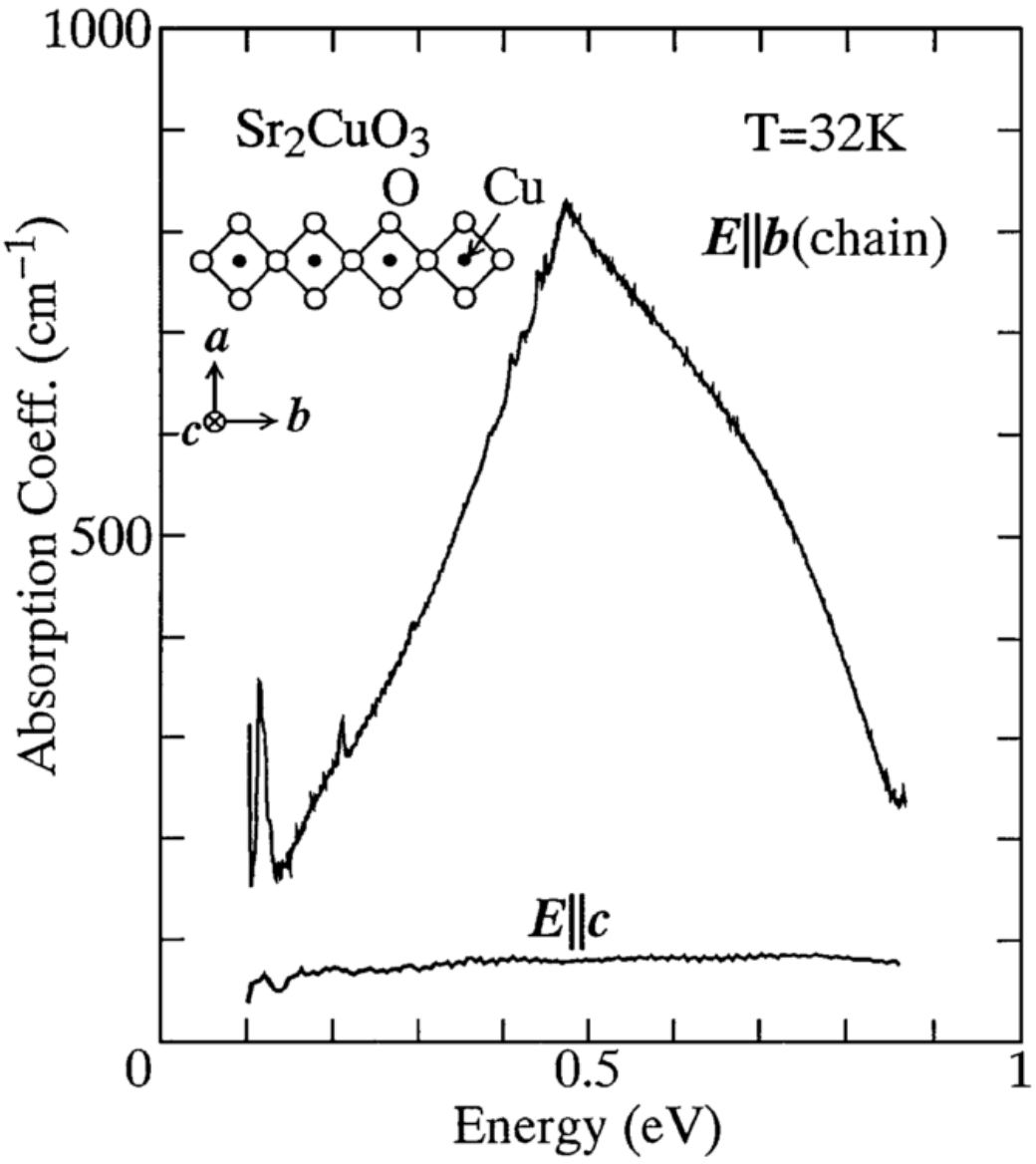

Fig. 41 – MIR spectra of Sr_2CuO_3 measured and published by Suzuura et al. [88]. *Top spectrum was obtained for incoming light polarized along the direction of [$CuO_{4/2}$] chains, the bottom one was obtained for the perpendicular direction of polarization.*

The two spectra presented in Fig. 41 differ dramatically from each other, indicating a one-dimensional character of the process responsible for the absorption line shape. The E || ***b*** spectrum consists of a very strong band that peaks just below 0.5 eV, and two smaller bands positioned at about 0.1 eV and 0.2 eV (both coming from phonons). The shape of the large band contains a sharp cusp which differs from the model described in the same year by Lorenzana *et al.* [89].

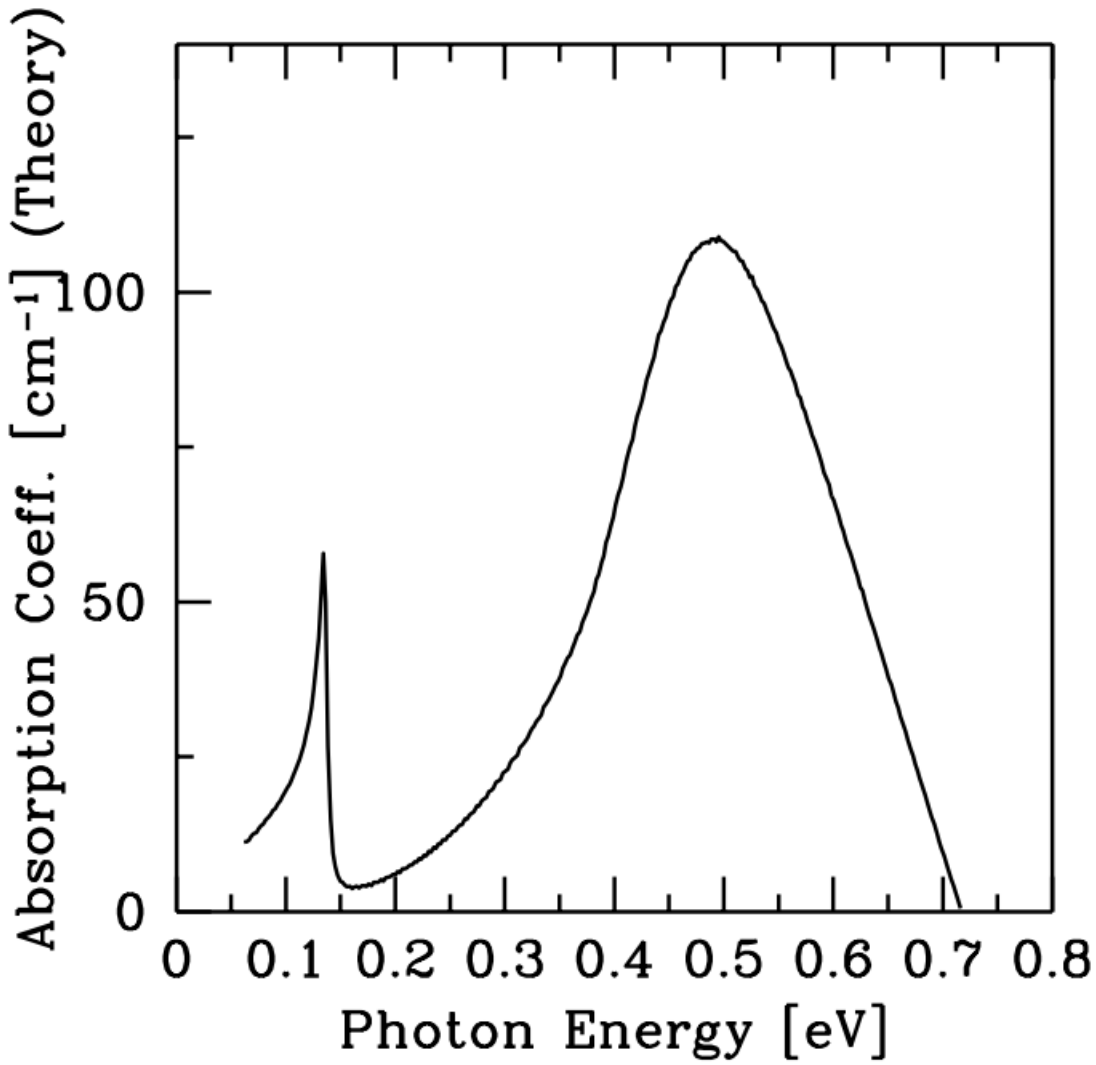

Fig. 42 – theoretical line shape of infrared absorption of 1D antiferromagnetic chain calculated and published by Lorenzana et al. [89]. *The large band at ~0.5 eV is caused by phonon-assisted two-magnon absorption. The calculations were conducted for phonon energy of 0.062 eV and antiferromagnetic superexchange constant J = 240 meV.*

The data collected by Suzuura *et al.* enabled Lorenzana and Eder to construct a better model of the one-dimensional antiferromagnetic chain [90]. The new model reproduced the experimental line shape very well and provided both insight into the processes occurring in the Sr213 and more general predictions regarding 1D AF chain compounds. One of the most important features of the model from the chemical point of view was finding a correlation between the position of the sharp cusp at the top of the experimental phonon-assisted bimagnon band and value of magnetic superexchange constant. The energy corresponding to the cusp is equal to sum: $J\frac{\pi}{2} + \omega_{||}$, where $\omega_{||}$ is the energy of the Cu-O stretching mode within the chain.

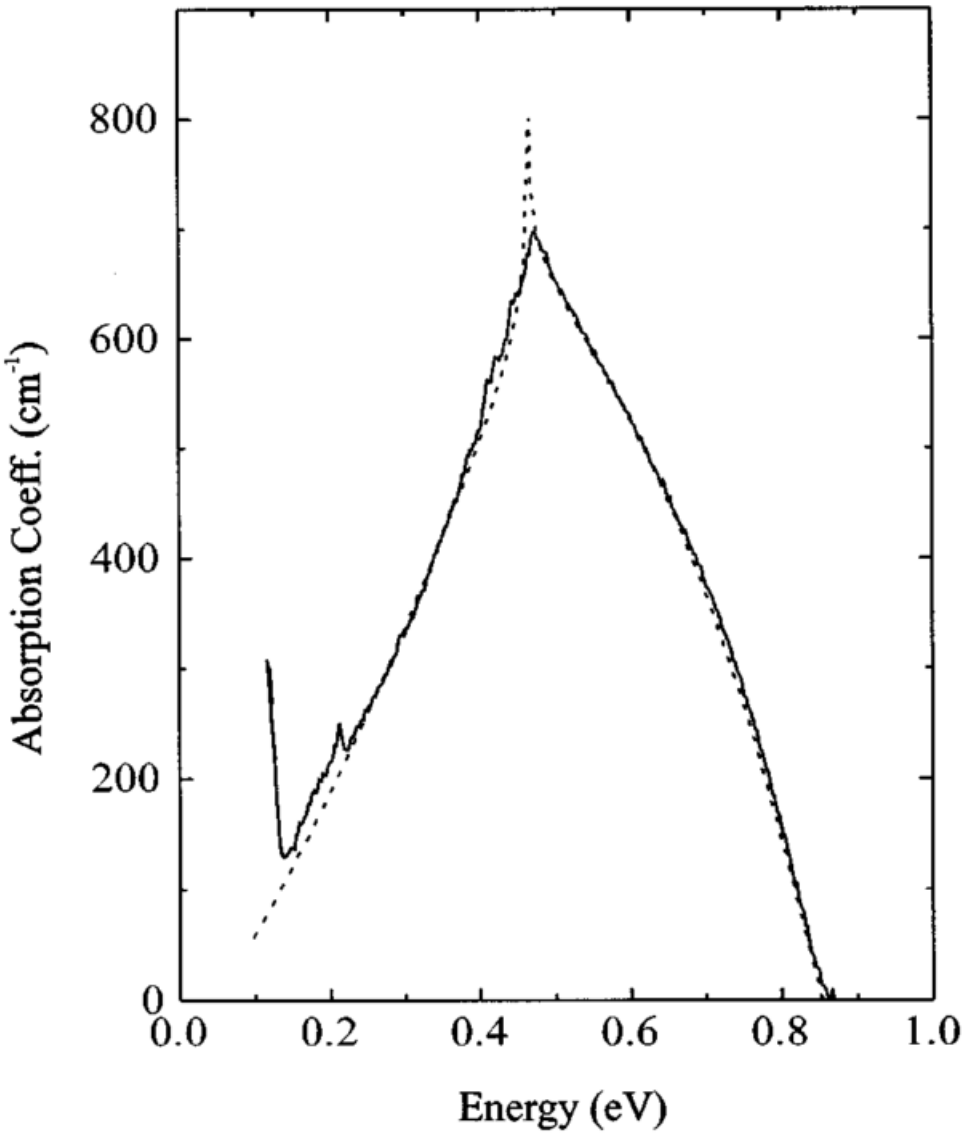

Fig. 43 - comparison of experimental IR spectrum of Sr_2CuO_3 measured by Suzuura et al. [88] *(solid line) with theoretical calculations by Lorenzana and Eder* [90] *(dashed line). The fit was obtained for J=0.246 eV, $\omega_{||}$=0.08 eV. The graph was published in the paper by Lorenzana and Eder* [90].

The experimental data and theoretical model proved to be very consistent evidence of magnetic excitation absorption bands in Sr_2CuO_3 coming from the coupling of phonon with bimagnon excitations. For one-dimensional systems, such as Sr_2CuO_3, the respective spectral feature may be observed only in absorption spectra (but not in scattering).

A.2.3.2 La_2CuO_4

Magnetic bands in the Raman spectrum of La_2CuO_4 were studied and Lyons *et al.* [91] and Sugai *et al.* [92]. Both groups used single crystals of lanthanum cuprate and Ar^+ ion laser as an excitation source.

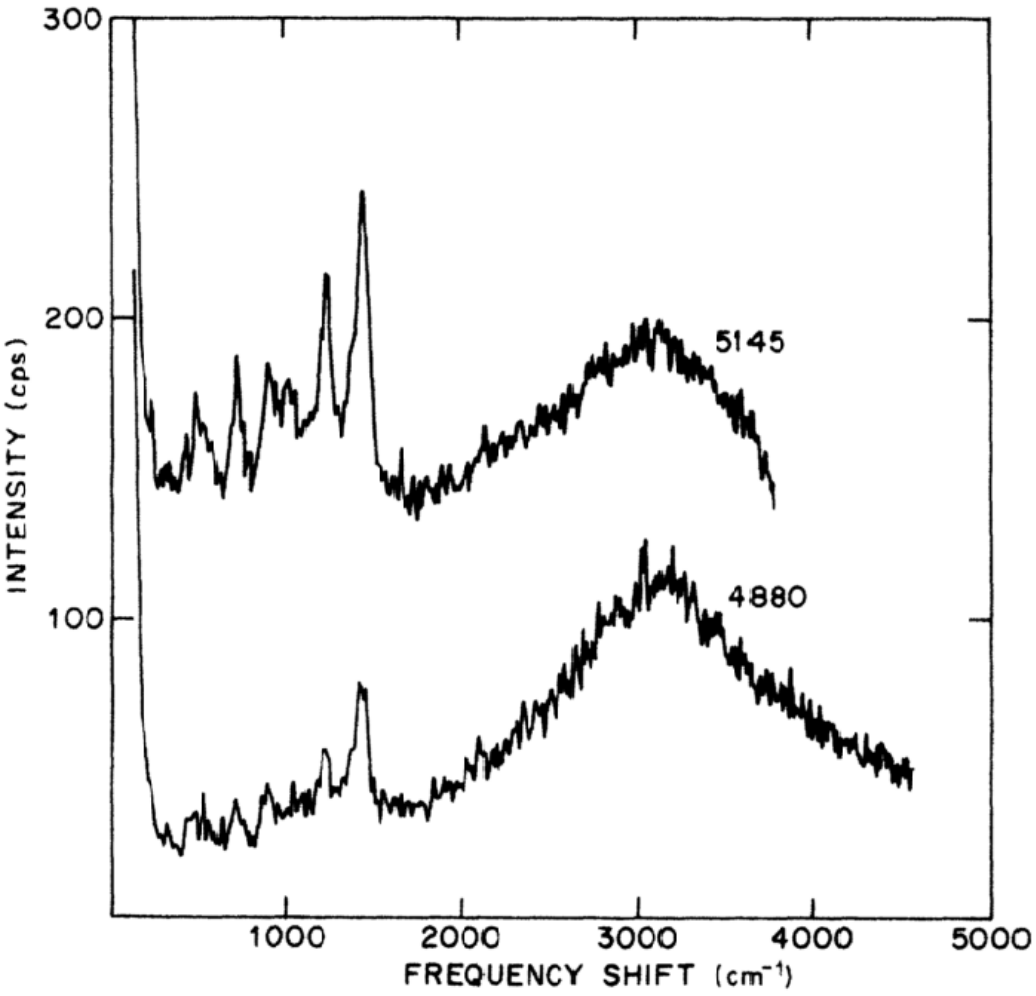

Fig. 44 - Raman spectra of La_2CuO_4 registered for two excitation lines (4880 Å and 5145 Å), published by Lyons et al. [91]. *The spectra have been moved 90 cps apart for clarity. The polarization of both incoming and scattered light was parallel to the y direction of the crystal cell. The sample was cooled in the flow of cold He gas.*

The spectra obtained by Lyons *et al.* consist of a strictly phonon part – up to about 1800 cm^{-1} – and a single strong and wide band centered at about 3200 cm^{-1}. The origin of the high-frequency band is a bimagnon scattering process which is indicated by the shape, position, dependence of intensity on temperature (not shown here). The position of maximum can be used to derive the rough value of magnetic superexchange constant in this 2D layered antiferromagnet, which yields J = (3200/3) cm^{-1} = 1067 cm^{-1} = 132 meV. For two-dimensional systems, such as La_2CuO_4, the respective spectral feature may be observed only in scattering spectra (but not in absorption).

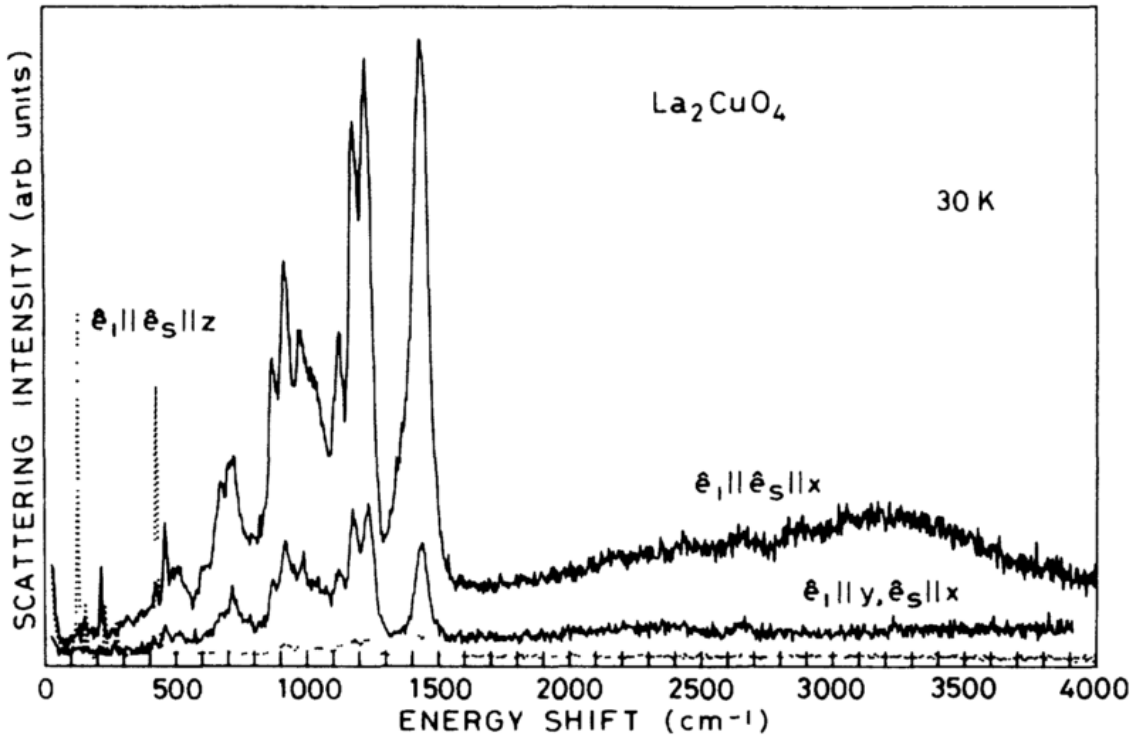

Fig. 45 - Raman spectra of La_2CuO_4 obtained by Sugai et al. [92] *for different polarization configurations. The symbol $\hat{e_I}$ indicates the direction of polarization of incoming light, whereas the symbol $\hat{e_S}$ indicates the direction of polarization for the scattered light.*

The spectra presented in a paper by Sugai *et al.* [92] cited in Fig. 45 above strongly differ from each other depending on polarization. The bimagnon band at 3200 cm^{-1} is only present in the (x, x) configuration – it is highly polarized. The (y, x) spectrum lacks the bimagnon band, although retains some intensity of the phonons. The (z, z) spectrum (dashed line) positioned just over the x-axis of Fig. 45, lacks the intensity even in the phonon part. All these observations correlate with the layered structure of La_2CuO_4.

A.3 Experimental techniques

A.3.1 Nomenclature in vibrational spectroscopy

A.3.1.1 Mulliken symbols

Mulliken symbols are used for conveying information about the symmetry of irreducible representations or optical modes in crystallography and spectroscopy. Most symbols consist of a main letter and indexes:

$$upper\ left\ index\, X_{lower\ indexes}^{upper\ right\ index}$$

In a typical scenario, the upper left index is empty – its purpose will be described further in the text. The main letter (X) represents the dimensionality of the irreducible representation and can take values of A, B – for one-dimensional representations, E – for two-dimensional representations, and T – for three-dimensional representations[6]. The choice of A or B depends on the sign of the character of rotation around the principal axis – for A it is positive, for B it is negative. In other words, representations with A as a main letter are symmetric in respect to rotation around the principal axis, whereas B are anti-symmetric.

The lower index can consist of a letter – g or u – and a number – 1, 2, or 3. The letter indicates parity in regards to inversion, letter g (*gerade* – in German: even) indicates symmetric representation. Letter u (*ungerade* – odd) means anti-symmetric representation.

The number in the lower index – for groups different than D_2 or D_{2h} – indicates whether the representation is symmetric with respect to vertical mirror plane perpendicular to the main axis (1) or not (2). In D_2 and D_{2h} groups another convention is used: the indexes express symmetry in regards to three perpendicular C_2 axes present in the group.

The upper right index may be empty or contain a single prime symbol – when representation is symmetric with respect to horizontal symmetry plane – or a double prime symbol when it is anti-symmetric.

[6] All information presented in this subchapter concerns notation used in solid-state spectroscopy. More mathematically oriented research in group theory usually requires more symbols: for example, for irreducible representations of dimensions higher than 3. Another exception comes from the realm of nanomaterials: buckmisterfullerene C_{60} has truncated icosahedral symmetry described by a point group I_h which contains 1,3,4 and 5 dimensional representations. There are other such compounds, although none of them is relevant to this thesis.

The upper left index is used to indicate elements of complex two-dimensional irreducible representations. For example, the E_u representation from the C_{4h} point group can sometimes be described as a pair of component representations ^1E_u, ^2E_u.

A.3.1.2 Porto's notation

Porto's notation is used to define the geometry of linear polarization of light interacting with the sample in the scattering process. A typical "word" in this notation looks like following: A(BC)D. Each of the four letters defines a different property in the process. The first letter before parentheses, A, defines the direction of propagation of the incoming light. The last letter, D, defines the direction of the propagation of scattered light. Letters inside the parentheses define the direction of polarization of incoming light (B) and direction of polarization of scattered light (C). An example of using Porto notation to describe a back-scattering geometry process would be -X(YY)X – this means, that both the incoming and scattered light propagate along the X-axis, and both the incoming and scattered light are polarized in the Y direction. Similarly, a typical right-angle scattering geometry can be described with a X(ZZ)Y "word". The notation is convenient in the description of polarized Raman experiments – for example on monocrystalline or thin film samples.

Another way to describe polarization is to use parentheses to define the direction of polarization filters before and after the sample. For example (x, x+y) would describe a process in which incoming light is polarized by a filter in the x direction, and the scattered light is analyzed without any polarization filter. Example of such description is given in subchapter A.2.3.2.

A.3.1.3 Description of bands

In a typical spectroscopic study, the researchers are interested not only in the position of the bands, but also in their intensity. To present the data in a convenient and easy to compare way it is useful to assign a label to each band that communicates how intense the band is in comparison with all the other bands in the spectrum. Each band receives a label that depends on the ratio of its intensity to the intensity of the strongest band in the spectrum. Bands that fall into 0.8 to 1 intensity-to-maximum-intensity range are very strong and are labeled "vs", next range (0.6 to 0.8) contains strong bands, labeled "s", then medium ("m"), weak ("w") and very weak ("vw") analogically.

Some authors also use label "sh" to indicate a band that is a shoulder of another – a weaker and not so well resolved band on the side of a much stronger band is a shoulder, especially

if its maximum is not strongly pronounced. Bands which are broad in comparison with other bands that can be detected in the same range are sometimes labeled as “br”.

A.3.2 Raman scattering spectroscopy

There are several different ways in which photons react with matter. In the case of Raman spectroscopy, the incident light wave from NIR to UV range becomes inelastically scattered during interaction with the sample. The signal measured in Raman spectroscopy corresponds to the intensity of scattered light as a function of wavelength. The difference in energy between incoming and scattered wave corresponds to the energy difference in initial and final states in the illuminated sample. Depending on the identity of the sample, this could mean change in rotational, vibrational or electronic energy levels – in case of gases and liquids – or quasiparticle excitations (for example phonon, magnon, exciton) in solid samples. Raman spectroscopy enables observation of a myriad of interesting effects in many materials. The more detailed description of this technique in the further part of this text will only depict some of the possible phenomena occurring in the solid state.

Only two photons and a scatterer are participating in the simplest version of a scattering event. An initial photon has an energy $E_i = h\nu_i$, scattered photon has an energy $E_s = h\nu_s$. If $\nu_i = \nu_s$ there is no change in photon energy:

$$E_i = E_s$$

In this case, the scattering is called elastic or Rayleigh scattering. If the energy of an incoming photon is different from the energy of the scattered photon, the scattering is inelastic. The conservation of energy principle requires balancing the energy:

$$\nu_i \neq \nu_s \Leftrightarrow E_i = E_s \pm E_n$$

The energy equation above indicates that in an inelastic scattering process (a scattering process in which energy of the scattered photon differs from an initial one) there must occur some excitation or relaxation process exchanging energy with scattering photons. The simplest process in solids providing such an energy transfer is excitation or deexcitation of a phonon. A phonon excitation taking part in the scattering process must have energy equal to $\pm E_n$, to obey the conservation of energy principle. Additionally, momentum conservation must also be obeyed. Therefore, if $\boldsymbol{k}_i$, $\boldsymbol{k}_s$, and $\boldsymbol{q}$ are wavevectors of incoming, scattered waves and phonon participating in scattering, then:

$$\boldsymbol{k}_i = \boldsymbol{k}_s \pm \boldsymbol{q}$$

Above equation might be transformed using the triangle inequality (let $|\boldsymbol{k}| = |\boldsymbol{k}_i| > |\boldsymbol{k}_s|$):

$$0 \leq |\boldsymbol{q}| \leq 2|\boldsymbol{k}|$$

For a typical laser wavelength $\lambda_i = 500$ nm, the wavenumber of incoming photon is equal $\nu = 20000\ \mathrm{cm}^{-1}$. We can therefore expect:

$$4\pi\nu \approx 2.5 \cdot 10^5\ cm^{-1} \geq |\boldsymbol{q}|$$

The wavevector of a phonon participating in scattering event must belong to the first Brillouin zone. Assuming that crystal lattice of scattering crystal is cubic and has a = 5 Å spacing, the wavevector at the edge of Brillouin zone is equal:

$$\frac{\pi}{a} = \frac{\pi}{5\text{Å}} = \frac{\pi}{5 \cdot 10^{-8}\ cm} \approx 6.3 \cdot 10^7\ cm^{-1}$$

The difference of over two orders of magnitude between $4\pi\nu$ and $\frac{\pi}{a}$ indicates that Raman scattering probes only photons with wavevectors lying rather close to the center of the first Brillouin zone. Because the dispersion relations of phonons in the close neighborhood of the center tend to be flat (gradient of dispersion approximately equal zero), the wavenumbers span a very small range. This causes sharpness of Raman bands in most crystalline solids. To probe the dispersion relation beyond the small volume around the center of the Brillouin zone, one needs to use incoming radiation of much shorter wavelengths, *e.g.*, X-ray radiation.

Due to the interaction of monochromatic[7] light source with the solid sample, we obtain elastically scattered Rayleigh band, inelastically scattered Raman bands and photoluminescence signal. To register the signal, the scattered light is first collected via a lens (e.g., from a microscope). Most Raman spectrometers that use visible lasers as an excitation source are dispersive instruments. The light gathered by a microscope is reflected, processed and then dispersed using a reflecting diffraction grate. Small, well defined spectral ranges are then registered by a detection system: a photomultiplier or a CCD camera. The signal output from the detector is, therefore, a histogram of intensity (for example number

[7] Light emitted by lasers is never strictly monochromatic, but usually the emission spectrum can be approximated sufficiently well with a narrow gaussian distribution. Also, very interesting results can be achieved by using short pulses of light – a narrow temporal pulse can be described via Fourier analysis as a set of many different modes.

of detections by pixel in CCD camera per second) versus wavenumber: absolute, or relative to the excitation source, i.e., a Raman spectrum.

If the energy of a scattered photon is smaller than the energy of the initial one, we call the scattered photons Stokes-shifted. In opposite case, we are dealing with the anti-Stokes photons. To observe anti-Stokes shifted photons, the probed material must be able to transfer energy from an excited state. Therefore anti-Stokes bands are observed mostly in high-temperature measurements – a deexcitation of a thermally pre-excited photon takes place.

Both Stokes and anti-Stokes Raman bands are much less intense than the Rayleigh band. Registering small signals together with very large signals is very inconvenient, therefore it is useful to remove Rayleigh scattered light before recording the Raman spectrum. This can be achieved either by using appropriate filters or by physically obstructing the elastically scattered light. The most commonly used filters are either band-stop (notch) filters or low-pass (edge) filters. Due to several orders of magnitude difference in intensities of Rayleigh and Raman bands, the filters must have sufficiently high attenuation factors and might be used in ensembles to remove unwanted Rayleigh signal more thoroughly.

The intensity of the Raman effect depends on the polarizability of the scattering medium. Both classical and quantum-mechanical treatments of scattering indicate, that to observe Stokes/anti-Stokes bands the change in polarizability during the vibration must not equal zero. Group-theory analysis of the QM model indicates that a vibrational mode can have non-zero Raman intensity only if its irreducible representation transforms as second-rank tensors (x^2, y^2, z^2, xy, xz, yz). This proves to be very useful in counting the number of symmetry-permitted Raman bands in solid state and assigning the group theory labels to bands present in the spectrum.

A.3.3 UV-vis-NIR electronic absorption spectroscopy

This type of UV-vis-NIR spectroscopy is based on absorption of electromagnetic radiation from near infrared to middle ultraviolet (from 8000 cm^{-1} to 50000 cm^{-1}, or 1250 nm to 200 nm, or 1.0 eV to 6.2 eV) by the studied sample. First selection rule of UV-vis-NIR spectroscopy demands that energy is absorbed only if the incoming light contains photons with energies equal to the difference in electron energy levels of the sample: $\Delta E_{B,A} = h\nu$. The causes of absorption might be d-d transitions for transition metal compounds, charge-transfer transitions between ligand and metal center, π-π^* transitions in aromatic systems, higher overtones and combination tones, but also absorption by different defects in crystal

structures. From the viewpoint of technical aspects of high-pressure studies, the last category of absorbers is most important. Most diamonds grown artificially contain some nitrogen, boron, hydrogen, nickel, cobalt or silicon defects [93–96]. Depending on the number of electrons and the atomic radius of the incorporated contaminant, the resulting defect in diamond induces different changes in the local geometry of the crystal lattice and results in high fluorescence that may potentially dominate the signal from the sample.

The selection rule used in UV-vis-NIR spectroscopy is called Laporte rule. It states that only transitions between spectroscopic terms of different parity may be permitted in crystals or molecules with the center of symmetry. Undistorted or tetragonally distorted octahedral complexes have a center of symmetry, therefore d-d transitions should be prohibited in such compounds. However, some molecular vibrations of centrosymmetric moieties lower the symmetry, enabling *vibronic* (coupled vibrational and electronic) transitions. Another factor that softens the selection rule was mentioned in the former subchapter: collective Jahn-Teller effect might decrease the symmetry of ligands-metal moiety enabling absorption in the UV-vis-NIR range.

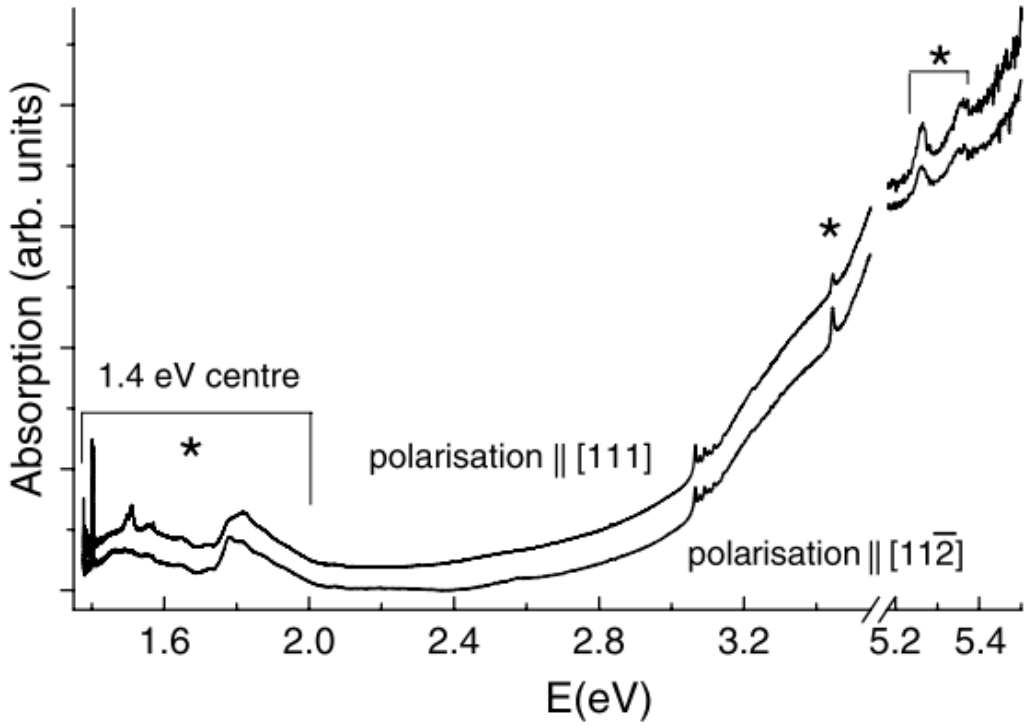

Fig. 46 - a UV-vis spectrum of Ni-rich diamond grown in the high-pressure, high-temperature process. Asterisks mark the positions of polarization-dependent bands, that are indicative of Ni-related optical centers. Published for Iakoubovskii and Collins [95].

A.3.4 Fourier-transform Infrared Spectroscopy – FTIR

The FTIR spectroscopy is based on absorption of electromagnetic radiation from far infrared to near infrared (from 10 cm^{-1} to 12500 cm^{-1}, or 1 mm to 800 nm, or 1 meV to 1.5 eV) by the studied sample. A photon of the incoming radiation is absorbed if its energy equals a difference in energy levels in the sample. The vibration induced by incoming photon also needs to have correct symmetry – the change in positions of atoms must induce changes in dipole moment of the studied molecule or the solid sample[8]. Because the orientation of molecules in liquid or gas samples is averaged in time, the polarization of the incoming light does not influence the absorption. In the case of monocrystalline, thin film or other spatially ordered samples, the direction of polarization of incoming light might also be considered. Depending on the relative orientations of the sample and direction of polarization, the absorption coefficient changes (due to a change in the projection of dipole moment).

The typical setup of an FTIR spectrometer consists of several elements. A source emits electromagnetic radiation containing waves from the infrared range. A popular source of IR radiation is *globar* – in essence, a ceramic (SiC) resistor able to withstand high temperatures required to emit needed electromagnetic radiation thermally. Radiation emitted by the source is filtered, collimated and then enters the Michelson interferometer. In the interferometer, incoming light shines on a beamsplitter, which divides it evenly into two beams: one that later reflects of a stationary mirror, and the other that reflects of a moving mirror. When the difference in path lengths between both beams is equal to multiple of one of the wavelengths included in the input beam, the constructive interference combines the divided parts back together in the output. If the difference in path lengths is equal $\frac{(2n+1)}{2}\ \lambda$, the beams interfere destructively, and the wavelength is omitted from the output. For a set difference D in path lengths, elements of the whole range of wavelengths interfere constructively or destructively depending on the what does D mod λ equal to. Moving one mirror leads to change in the path length difference, therefore changing the sets of wavelengths contained in the output. The changing sets of wavelength are absorbed by the sample and the intensity of the reflected/transmitted part of the beam is measured by the detector. The spectrum is obtained by performing Fourier Transform of the intensity versus the time function. Repeating the

[8] There are also electric quadrupole transitions, although they observation is extremely challenging, as they are very weak – so far, they have been observed mostly in O_2, N_2 or H_2. Another exception is vibronic coupling, which occurs when forbidden transition between two electronic states is made possible via coupling with some vibrational mode.

measurement many times increases the signal-to-noise ratio proportionally to the square root of the number of scans.

The beamsplitter for a given wavenumber range must be made from a material that absorbs light very weakly in the region of interest. The additional coating is also used to achieve near 50:50 reflection-to-transmission ratio for a range of interest in the experiment. For example in the 400-4000 cm^{-1} range, a most common beamsplitter is KBr coated with a layer of Ge. In the far infrared, coated Mylar foil enables measurement in the 40-600 cm^{-1} range.

The detection system may be composed of a pyroelectric material, for example DTGS: deuterated triglycine sulfate, or DLaTGS: deuterated, L-alanine doped triglycine sulfate. When such crystal is illuminated by infrared radiation, it heats up. This produces an electric potential, measured and registered by a built-in circuit board.

The selection rules for the IR spectroscopy of solids demand that absorption occurs only when the difference in energy of vibrational levels of the sample equals the energy of the incoming photon. Additionally, several other conditions must be upheld. First, the normal vibration that might increase in energy due to absorption must have an irreducible representation that transforms as versors x, y or z. In compounds that crystallize in centrosymmetric spacegroups, this has a consequence in a "rule of mutual exclusion". In such compounds, there can be no bands that are active both in IR and Raman spectroscopy. Additionally, in many space groups there are vibrational modes that are inactive in both IR and Raman spectroscopy, so-called silent modes. Fortunately, those modes may be detected using inelastic neutron scattering (INS) method.

It is worth mentioning, that besides first-order vibrational bands, sometimes second and higher order processes might be observed – IR or Raman overtones, combination bands. Irreducible representations of such processes must contain fully symmetric representation to be observed.

A.4 Magnetically ordered materials

A.4.1 Classes of materials, basic information about magnetic properties

Magnetic properties of a material result from the electronic structure of constituent atoms. In case of transition metal compounds, the configuration of the metal center is one of the crucial parameters determining the character of magnetic interactions.

In the classical view, movement of electrons induces a magnetic field. Biot-Savart law describes the magnetic field induced by electric current flowing in a conducting loop:

$$d\boldsymbol{B} = -\frac{1}{4\pi\epsilon_0 c^2} I \frac{\boldsymbol{r_l} \times d\boldsymbol{l}}{|\boldsymbol{r_l}|^3}$$

Where **B** is a magnetic field, I is current, $\mathbf{r}_l$ is vector connecting a small length of conductor d**l** with a point at which **B** is measured. Integrating d**B** over the length of the circular loop at distance x much larger than the radius of the loop gives:

$$\boldsymbol{B}(x) = -\frac{\mu_0}{4\pi} \frac{3\left(\frac{\boldsymbol{x}}{|\boldsymbol{x}|} \cdot \boldsymbol{m}\right)\frac{\boldsymbol{x}}{|\boldsymbol{x}|} - \boldsymbol{m}}{|\boldsymbol{x}|^3}$$

Where vector m is magnetic dipole moment:

$$\boldsymbol{m} = \frac{I}{2}\oint_L \boldsymbol{x}_l \times d\boldsymbol{l}$$

The magnetic dipole moment is always caused by movement of electrical charge. In the case of electrons, the magnetic moment has two contributions: orbital magnetic moment and spin magnetic moment. In case of isolated atoms or ions, contributions to magnetic moment come from all valence electrons. Magnetic properties of ions and atoms situated in crystal lattices are much more complicated, as several more variables come into play: spin-orbit coupling, the distance and interactions between magnetic neighbors, the geometry of ions and ligands, temperature. Each contribution is discussed shortly below.

The magnetic dipole may interact with external magnetic fields. The potential energy U of interaction between magnetic dipole, m, and magnetic field induction, B, -can be described by the equation:

$$U = -\boldsymbol{m} \cdot \boldsymbol{B}$$

Moreover, the force acting upon magnetic dipole is equal to the gradient of the potential energy:

$$\boldsymbol{F} = \nabla U = -\nabla (\boldsymbol{m} \cdot \boldsymbol{B})$$

In constant and uniform magnetic field a magnetic dipole precesses around the direction of the field with so-called Larmor frequency, dependent on the strength of the field:

$$\omega = -\gamma B$$

where γ is a gyromagnetic ratio. This property stems from the observation, that for constant and uniform field B, the gradient of B is equal to 0. That, along with an earlier equation, determines that net force acting on the magnetic dipole should be equal to zero. On the other hand, the B field can exert a torque on a magnetic dipole, which leads to the precession of magnetic dipole.

Magnetic moment per unit volume is called magnetization and for small fields is usually proportional to applied field H with proportionality constant χ_v, so-called magnetic susceptibility:

$$\chi_v = \frac{\boldsymbol{M}}{\boldsymbol{H}}$$

$$\boldsymbol{B} = \mu_0 (\boldsymbol{H} + \boldsymbol{M}) = \mu_0 (\boldsymbol{H} + \chi_v \boldsymbol{H}) = \mu \boldsymbol{H}$$

Diamagnetic materials react to external magnetic fields by inducing a small antiparallel internal magnetic field, and thus creating a repulsive interaction. They are repelled by the magnetic fields and have negative magnetic susceptibilities. Diamagnetic contributions to properties of the material come mostly from electrons residing in doubly occupied orbitals. In metals, valent electrons are delocalized, and a better description of their diamagnetism can be achieved either by treating them as a free electron gas or by full quantum-mechanical treatment.

Paramagnetic materials, on the other hand, always contain unpaired electrons. They react to the external magnetic field by inducing an internal magnetic field in the same direction. They are attracted into the regions of stronger magnetic fields, and their magnetic susceptibilities are positive, yet usually small.

Ferromagnetic materials react strongly to external magnetic fields by inducing a strong internal magnetic field parallel to the external field. In their case, the magnetization is no

longer linearly dependent on the applied field. In ferromagnets a better property to describe properties might be differential susceptibility:

$$\chi_{diff,ij} = \frac{\partial M_i}{\partial H_j}$$

The ferromagnetic properties stem from interactions of free electrons (spins) in a magnetically dense solid. The strong interaction between neighboring spins enables ferromagnets to retain the internal magnetic ordering even after the external field has been switched off. The internal magnetic field retained after turning off the external magnetic field is called remanent magnetization.

Antiferromagnetic materials contain magnetic atoms forming two spin lattices antiparallel to each other. In the simplest case, one can imagine two simple cubic lattices of equal sizes, translated against each other by [½, ½, ½] vector: each ion is surrounded by neighbors of antiparallel spin. There are of course numerous other possibilities of locating the antiparallel spins in space, but this example also shows clearly, that the I-centering present in the atomic crystal cell is no longer present in the magnetic crystal cell, which has a lower symmetry. This points to the frequently encountered difference in diffraction patterns conducted on an atomic crystal cell and a magnetic crystal cell (see: A.2.1.2.1).

Ferrimagnetic materials contain two sublattices of antiparallel magnetic moments – similar to antiferromagnetic ordering. However, the sublattices, in contrast to the antiferromagnetic case, contain magnetic moments of unequal strength. This enables the material to obtain spontaneous magnetization, just like in the case of a ferromagnet.

There are other possible ways of ordering the magnetic moments (among others: superparamagnetic, helimagnetic), although their description is outside the scope of this text.

Several mechanisms describe interactions between spins in solids. Depending on the distance and connectivity between magnetically active ions different mechanisms may prevail.

1) Direct exchange – when magnetically active entities (atoms, ions) are sufficiently close to each other, their wavefunctions may overlap. This leads to electronic interaction, and, via the Pauli exclusion principle, to the magnetic ordering of spin-orbitals.

2) Indirect exchange – when the distance between magnetically active entities is large, the overlap between their wavefunctions is negligible. Nevertheless, unpaired inner electrons (f or d) might still interact with delocalized electrons from the conduction band. This leads to coupling between magnetically active entities, particularly in magnetic metals.
3) Itinerant exchange – magnetic exchange between delocalized electrons forming conduction bands.
4) Superexchange – when magnetically active ions are separated by several angstroms and connected via nonmagnetic ligands, the lattice might still become magnetically ordered due to superexchange mechanism. In that process the interaction is usually mediated via doubly occupied p orbitals of diamagnetic ligand, L, connecting two magnetic ions, M_1, M_2. According to the Goodenough-Kanamori rules, strength and sign of the coupling constant J depend on the angle M_1-L-M_2. For angles close to 180°, antiferromagnetic ordering is preferred. When angles are close to 90°, ferromagnetic ordering is preferred.
5) Double exchange – mechanism behind this is similar to superexchange: the interaction between two magnetically active ions is mediated by diamagnetic ligand, L. Here the two connected ions must exhibit oxidation states differing by one, which enables the transfer of an electron from lower oxidation state metal to higher one, via the ligand. This mechanism leads to a ferromagnetic coupling between the ions.

A.4.2 Selected methods of studying magnetic properties

A.4.2.1 Neutron diffraction

Neutron diffraction is an experimental technique in which a sample is illuminated with sufficiently slow neutrons obtained from a spallation source or nuclear reactor. Slow neutrons have wavelengths on the order of angstrom, which enables their diffraction via scattering by crystal lattice.

The data obtained from scattering of neutrons is presented as in x-ray diffraction, as a diffraction pattern. The difference between techniques lies in crucial property of neutrons: despite having no charge, they have a magnetic moment. This causes them to interact with magnetic moments of electrons. For all types of magnetic ordering, this has a consequence in a strong dependence of magnetic form factor on temperature. Additionally, for antiferromagnetic or more complicated structures the magnetic cell size might be bigger than in case of the non-magnetic expreriment. Comparison of neutron diffraction with x-ray

diffraction, therefore, may yield data regarding the magnetic structure of studied compounds. This, however, requires the measurement temperature to be lower than the magnetic ordering temperature of the studied sample.

It is worth mentioning that there are techniques which use X-ray light to study magnetic structures of materials [97–99]. The magnetic contributions, however, are much weaker than in the case of neutron studies, so large intensities of radiation are needed for this.

A.4.2.2 Inelastic neutron scattering

Inelastic neutron scattering is an extension of a standard neutron diffraction. The main difference between the two techniques lies in the dimensionality of data collected in each experiment. Standard neutron diffraction is a scattering experiment in which a number of elastically scattered neutrons is counted depending on scattering vector **Q** (momentum transfer). In the case of the inelastic counterpart, the additional information regarding the energy difference between initial and scattered neutrons is collected. Neutrons that have wavelength approximately in the range of 0.34 – 4.0 Å have kinetic energies in the range of 10 – 700 meV. Such neutrons might effectively transfer part of their kinetic energy to the sample, enabling all manners of dynamic processes – lattice vibrations, magnetic transitions, or even d-d transitions. An important feature of INS spectroscopy is that in most cases it enables capture of all oscillation modes, regardless of their symmetry.

A.4.2.3 Optical spectroscopy

Optical spectroscopy of magnetic compounds stems from the scattering of photons by magnons, multi-magnons or combined phonon + multi-magnon processes. Magnetic transitions can be observed for both infrared and Raman spectroscopy[9].

Magnons are collective oscillations of spins, observed in magnetically ordered materials. They behave similarly to other collective oscillations found in solid-state: they are bosons, their energy depends on the structure of the studied material, they have dispersion. A more complete description of their properties depends strongly on the type of the system in question (a type of magnetic ordering, dimensionality). Compounds that have been studied using vibrational spectroscopy in relation to their magnetic excitations range from difluorides (MnF_2 [100], CoF_2 [101], NiF_2 [102]), oxides (NiO [103]), oxocuprates (La_2CuO_4 [104]). The robustness of optical techniques enables measurements in a wide

[9] Not exclusively: magnetic transitions are also studied using – apart from techniques already discussed in this thesis – electron scattering, X-ray scattering, or Brillouin scattering.

range of temperature and pressure [104,105], although the magnetic bands are most pronounced at temperatures lower than the characteristic ordering (Néel or Curie) temperature.

Magnetically active compounds studied in this thesis can be described as spin-½ Heisenberg antiferromagnets. To correctly calculate their properties, the Hamiltonian operator must include term quantifying the antiferromagnetic interactions. Heisenberg model uses a term:

$$H = -\sum_{\substack{i,j \\ i \neq j}} J_{ij} \boldsymbol{S}_i \cdot \boldsymbol{S}_j$$

J_{ij} is magnetic coupling constant (usually expressed in meV, cm^{-1} or K) between magnetic cation on positions i and j in the lattice. For antiferromagnets $J_{ij} < 0$, for ferromagnets $J_{ij} > 0$. For simplified calculations, the value of J_{ji} for ions i, j that are not direct neighbors, is set to 0. Let us calculate the energy of possible magnetic transitions in the ordered antiferromagnetic compound.

The energy of interaction between two neighboring spin-½ cations having antiparallel spin orientation is therefore equal:

$$-J\left(\frac{1}{2} \cdot -\frac{1}{2}\right) = \frac{1}{4} J$$

Now let us assume that neighboring spins are oriented parallel to each other, but the magnetic coupling constant is still lower than zero:

$$-J\left(\frac{1}{2} \cdot \frac{1}{2}\right) = -\frac{1}{4} J$$

This means that energy effect of changing an orientation of a single spin in a bond equals:

$$-\frac{1}{4} J - \frac{1}{4} J = -\frac{1}{2} J$$

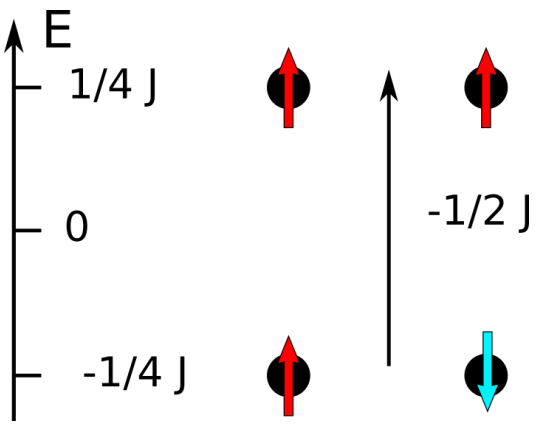

Real compounds contain many more magnetically active cations than two. Let us assume, that we are dealing with an antiferromagnetic layer that is isolated from the other layers – for example, due to a considerable distance between them. Let us also assume, that cations can interact magnetically only with their closest neighbors.

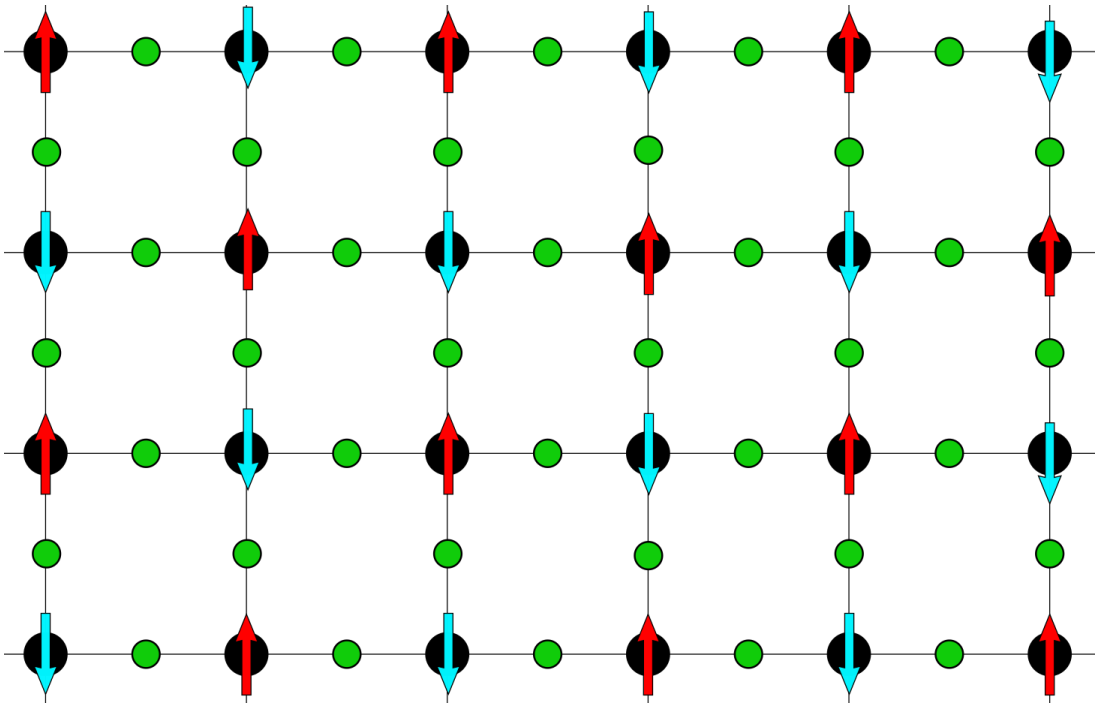

Fig. 47 - an idealized model of a two-dimensional antiferromagnetic layer

Fig. 47 depicts a model of a two-dimensional antiferromagnetic layer. Black balls depict magnetically active cations. Green balls are diamagnetic ligands, each coordinating two neighboring cations on the side of a grid. Red and blue arrows depict possible orientations of spins on cations. If one of the spins in the lattice changes its orientation, the situation changes:

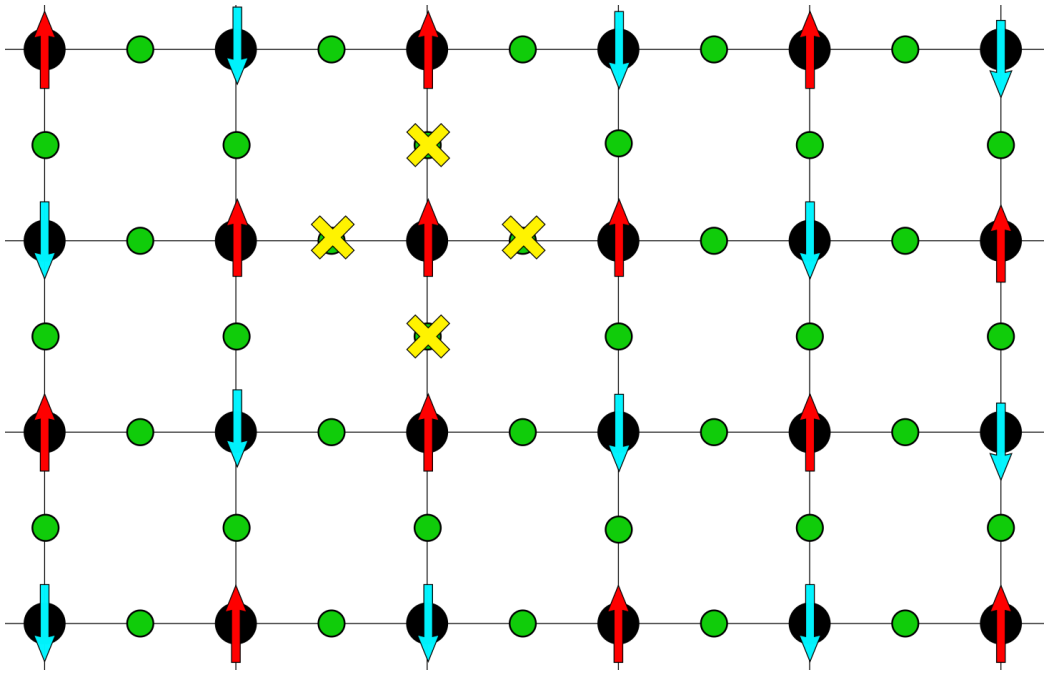

Fig. 48 - a model of antiferromagnetic lattice with a single flipped spin

Fig. 48 differs from Fig. 47 in two ways: first, a single spin in the lattice has changed orientation. Second, this change in orientation has increased the energy of the lattice due to an increase of energy of four pairs of spins – indicated by four yellow crosses. If we look at the expression describing the increase of energy in an antiferromagnetic pair of cations, we can easily calculate, that in the case of four such pairs the increase will equal:

$$4 \cdot -\frac{1}{2} J = -2 J$$

Therefore, the energy needed for a single spin flip in a 2D antiferromagnetic spin-½ lattice equals double the magnetic superexchange coupling constant. Because this transition does not change dipole moment, it cannot proceed via absorption of light – it is forbidden in IR. On the other hand, such magnon transitions can be found with Raman spectroscopy [100,106] or inelastic neutron scattering.

Another possibility of magnetic transition is to excite two spins at the same time. Depending on whether they are directly next to each other or not, we obtain two different excitations:

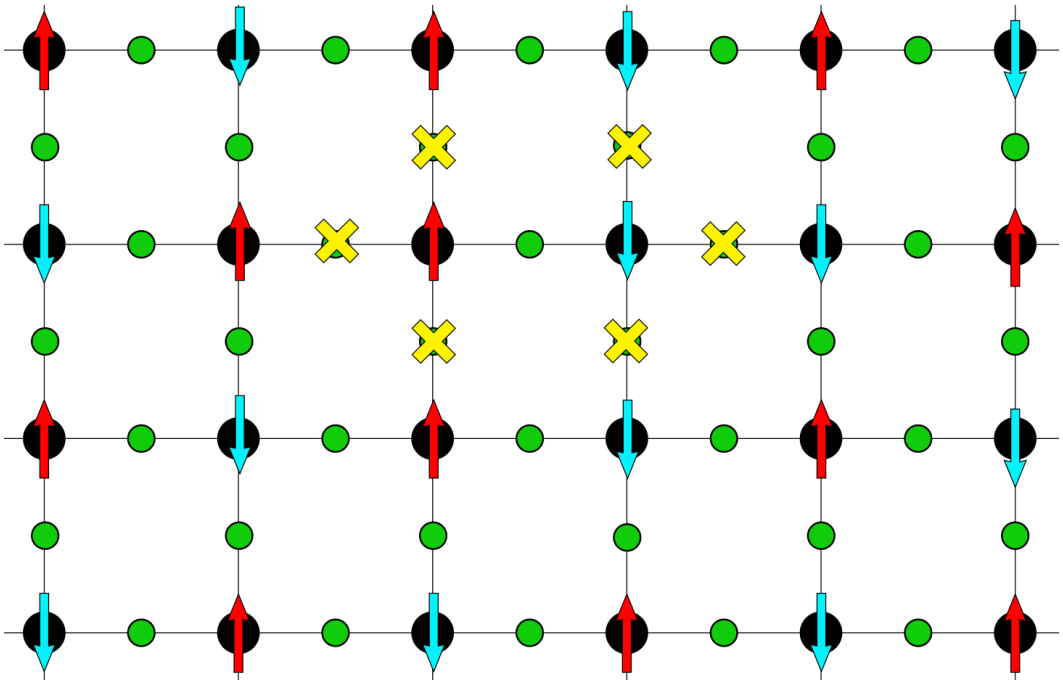

Fig. 49 - a bimagnon transition in layered antiferromagnet. The spin flips occur directly near each other.

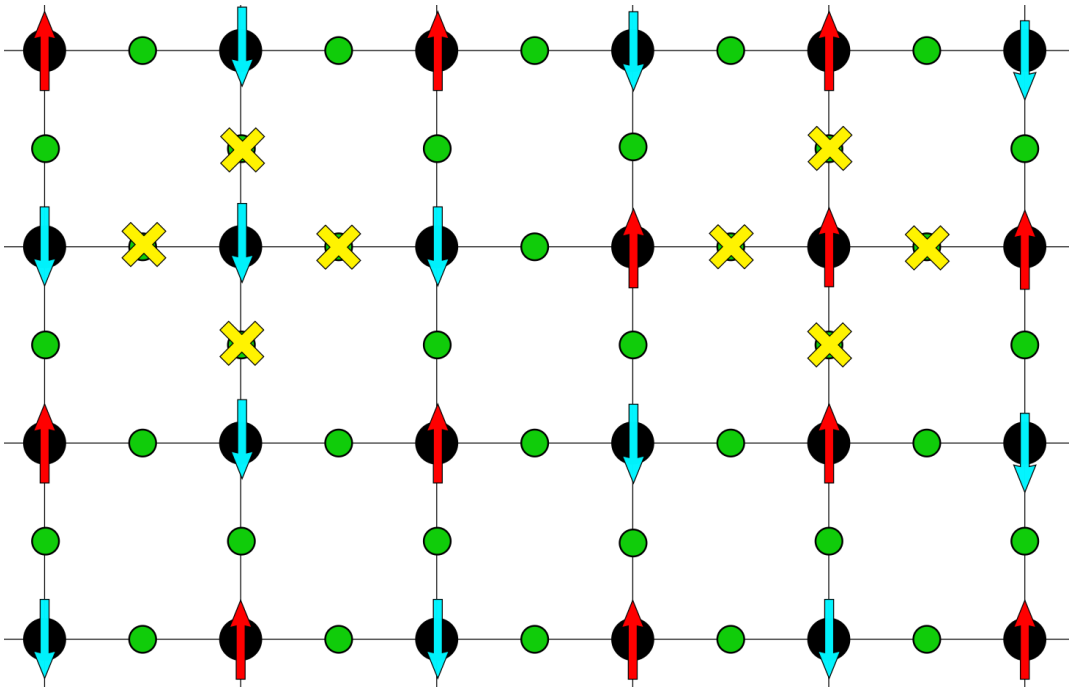

Fig. 50 - a bimagnon transition o layered antiferromagnet. The spin flips occur separated from each other.

Both Fig. 49 and Fig. 50 depict bimagnon transitions, although occurring in two different ways. In Fig. 49 the transition occurs for neighboring cations. Because of that, the number of bonds that increase in energy equals 6. Each “frustrated” bond increases the overall energy by –J/2, therefore this transition requires energy of 3J to occur. On the other hand, the bimagnon transition taking place for two isolated spins has an energy of 4J. Both transitions

do not change the local dipole moment of the lattice and therefore cannot occur during absorption processes – only during scattering.

The examples presented above introduce only a simplified version of bimagnon scattering. To correctly calculate the position of Raman bimagnon band, one must take into account magnons from the whole first Brillouin zone. This might seem unintuitive, because – as mentioned in subchapter A.3.2 – Raman spectroscopy only probes excitations from the small volume around the center of the Brillouin zone. This condition might be met during bimagnon transition if the excited magnons will have nearly equal and opposing wavevectors. Taking this into account yields a more precise value of the maximum of bimagnon Raman band: 3.38 J [107].

Processes described above are observed only during scattering events (Raman, X-Ray, neutron, electron scattering). This is a consequence of lack of change in dipole moment during the magnetic transition. In order to observe such transitions in IR, the magnetic transition must be coupled with an IR active phonon excitation. In this case, the position of the maximum of the magnetic band is at the sum of energy of the phonon coupled with the bimagnon scattering [107] (see Fig. 51).

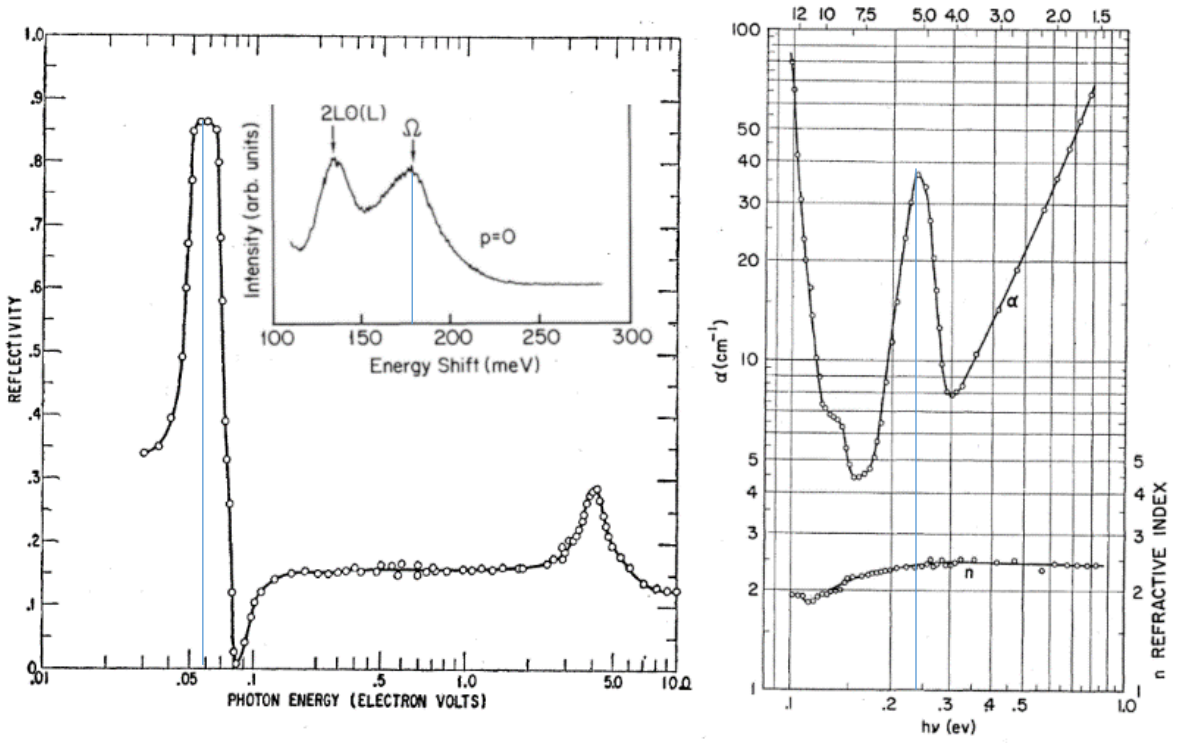

Fig. 51 - a selection of NiO spectra. Left side depicts a reflectivity spectrum of NiO presented in a paper by Newman and Chrenko [103]*. A large band at about 60 meV is a T_{1u} phonon. The inset presents data from a Raman study of NiO by Massey et al.* [108]*. The band labeled as Ω is a bimagnon band centered at about 180 meV. The graph on the right depicts an absorption spectrum of NiO (from a paper by Johnston and Cronemeyer* [109]*), where the band centered at about 245 meV – a phonon assisted bimagnon scattering band, ca. 60+180 meV – can be seen.*

It is important to note, that above considerations are quite simplified. The proper description of magnetic transitions requires the use of higher order terms, both in Hamiltonian (for example interaction with neighbors other than the nearest) and in description of light-matter interaction. Despite that, even this simplified description can yield some understanding of those processes.

A.4.2.3.1 Magnon scattering as a function of external conditions (p, T)

The position of multimagnon or phonon-assisted multimagnon bands depends on pressure [105,110–112]. The strength of magnetic interaction between the antiferromagnetic cation pairs and diamagnetic anion changes with both the bond length between subsequent cation-anion-cation triple. In the case of compounds that do not undergo drastic bond angle changes during the compression or thermal expansion, the dependence of magnetic superexchange constant, J, on the bond length d can be simply described as:

$$J = c\, d^{-q}$$

Where c is a scaling constant and exponent q usually values between 3 and 12 [113–115].

The temperature dependence of magnon bands in crystalline solids – *i.e.,* changes of bandwidth and position of the maximum – can be understood qualitatively by imagining the behavior of spins inside magnetic domains. For very high temperatures (T>J) the multimagnon bands should have a negligible intensity due to thermal excitation of the crystal and resulting paramagnetic state. Consequently, the lifetime of any magnon bands should be infinitesimal, which would increase their bandwidth to infinity. Lowering the temperature increases the magnetic correlation between the neighboring spins, which enables magnons to propagate and introduces finite bandwidth and non-zero intensity of the magnon bands. Interestingly, only local correlation is required for that, therefore magnon bands can be observed at temperatures higher than Néel or Curie temperature for a given material (as presented in following papers: [100,116–118]).

Further lowering of the temperature leads to an increase in the position of the maximum and decrease in the bandwidth. At sufficiently low temperatures (about 0.3 T_N) both position and bandwidth plateau and stop being dependent on temperature.

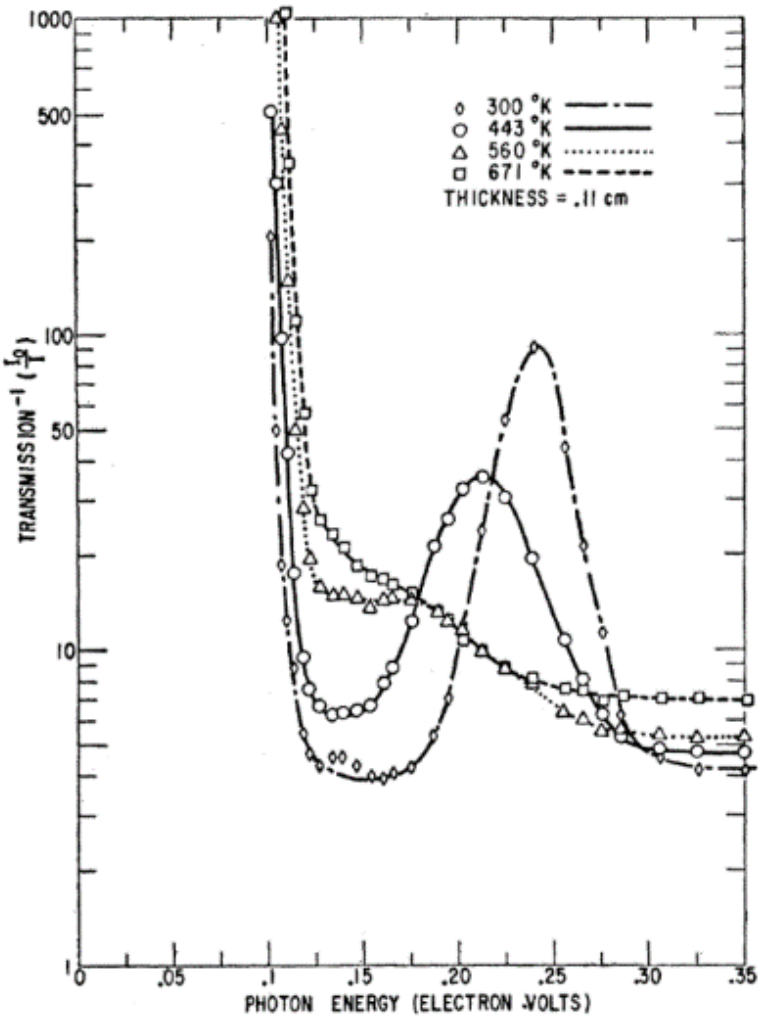

Fig. 52 - Dependence of intensity of phonon+bimagnon band on temperature. Illustration from a paper by Newman and Chrenko [103]. *Néel temperature of NiO is 525 K.*

A.4.2.4 Magnetometry

Properties of magnetic materials might be studied directly using many magnetometric methods. One of the oldest ways of measuring the magnetic properties of the samples uses the Gouy balance. This method requires a strong magnet and a precise balance. The sample is inserted into a cylindrical cell, which is then attached via a thread to the balance. Measurement of the sample weight is taken. Next, the procedure is repeated, although this time sample cell is suspended in the magnetic field. The apparent change in weight of the sample is the consequence of the interaction between the sample and a magnetic field and is proportional to the magnetic susceptibility of the sample. The temperature dependent measurements are in principle possible, using this method.

In some of the magnetometric methods (VSM[10], SQUID[11]), the sample is vibrated in a very precisely defined and controlled magnetic field. The moving sample induces changes in a local magnetic field near pick-up coils. The magnitude of changes in the magnetic field depends on the materials magnetic properties. The changes in the magnetic field induce voltage difference in pick-up coils which can be measured and translated to magnetization and magnetic susceptibility.

SQUID devices are more sensitive than VSMs due to their detection system containing a superconducting Josephson junction. They can detect magnetic flux on the order of single fluxons – quanta of magnetic flux. This enables them to precisely measure even very weak magnetic phenomena or small amounts of samples – they are successfully used in magnetoencephalography for mapping brain activity [119].

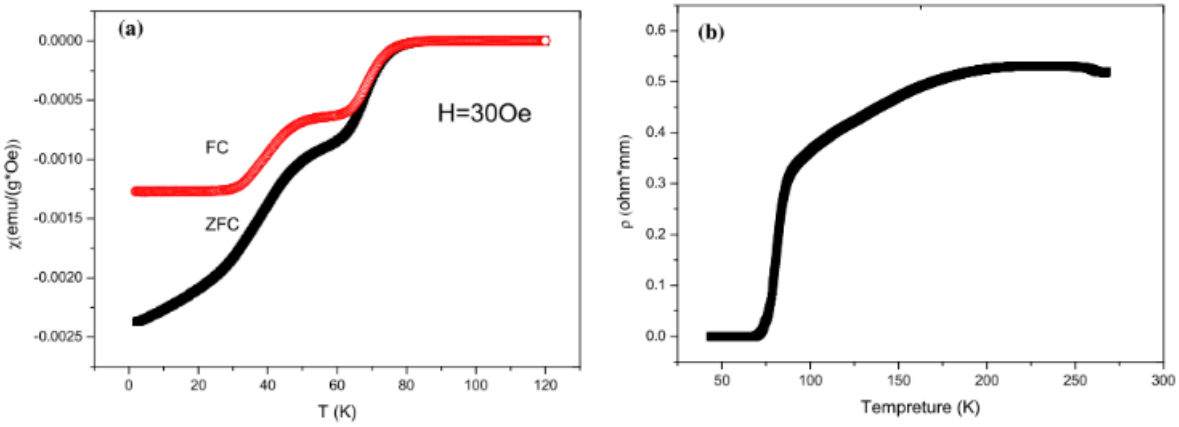

Fig. 53 – a diagram published for Liu et al. [120] *depicts a measurement conducted using a SQUID magnetometer. (left) Magnetic susceptibility of a $Sr_2CuO_{3,4}$ sample as a function of temperature in zero-field-cooled and field-cooled conditions. The two drops in susceptibility indicate presence of two magnetic (superconducting) phase transitions. (right) Curve of resistivity vs. temperature of the same sample. Drop of resistivity to zero near 75 K is indicative of phase transition to superconductive state. This coincides with the magnetic measurement on the left.*

A.4.2.5 Heat capacity measurements

Measurement of heat capacity under constant volume/pressure in a range of temperatures is yet another method of characterization of magnetic phase transition. The transition between states with different magnetic ordering is always accompanied by a change in entropy caused by a change in spin orientation. Therefore, for each possible transition (for example from an antiferromagnetic to a paramagnetic at Néel temperature, from a ferromagnetic to a paramagnetic at Curie temperature, from superconducting to normal state transition at

[10] VSM – Vibrating Sample Magnetometry – measurement method in which a sample oscillates inside a constant magnetic field and thus induces voltage changes in pick-up coils. The signal measured in VSM depends on magnetic properties of the measured sample.
[11] SQUID – superconducting quantum interference device – a device that very precisely measures changes in magnetic flux by monitoring the voltage along the Josephson junction.

critical temperature for type I superconductors) the heat effect is in principle detectable by differential scanning calorimetry, using Physical Property Measurement System or other methods of heat capacity measurement.

The figure below shows the heat capacity of an AgF_2 sample as a function of temperature. The experimental curve contains three signals – a small positive peak at about 90 K, a small negative peak at about 220 K and a lambda-shaped signal at about 160 K. The small signals are artifacts. The lambda-shaped one is evidence of the magnetic transition between the antiferromagnetic and paramagnetic states. The temperature at which signal blends back into the background – 165 K – is a Néel temperature for AgF_2.

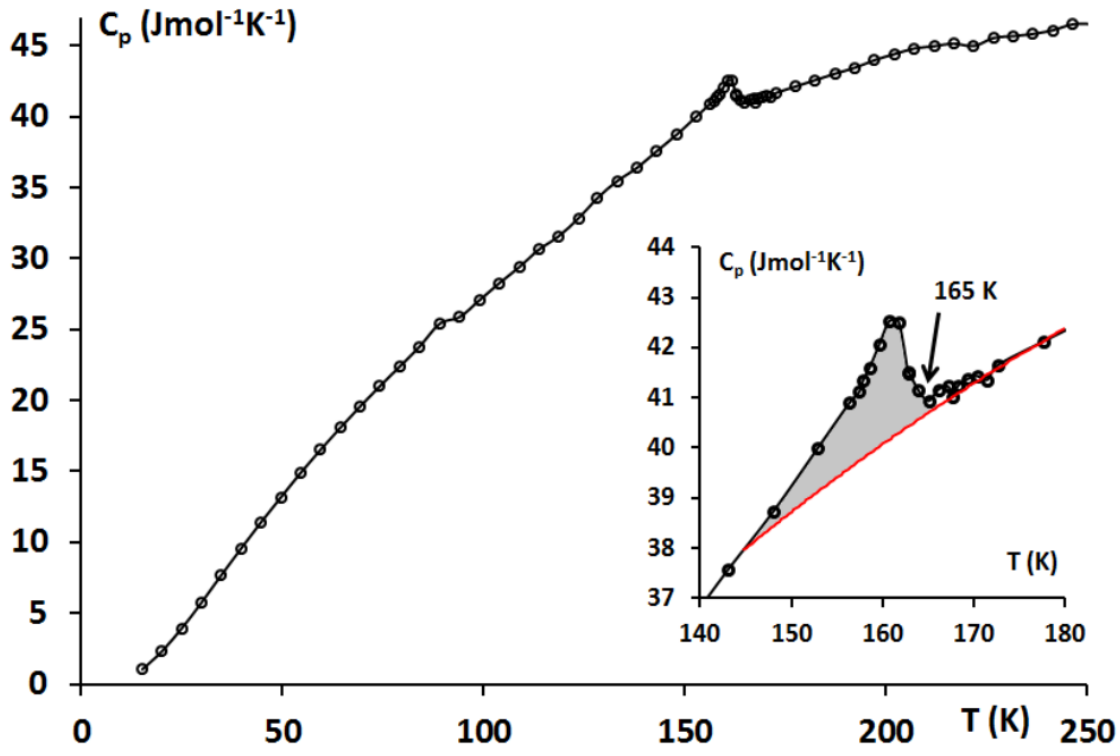

Fig. 54 - a graph of heat capacity under constant pressure as a function of temperature, measured for AgF_2 sample by Dr. Tomasz Jaroń [59]. *The inset presents more clearly the change of heat capacity during the phase transition, i.e. at Néel temperature.*

A.5 Experimental science at high pressure

A.5.1 Justification of studying compounds in the high-pressure regime

The equation of state (EOS) is a thermodynamic equation describing a state of a system depending on some external physical conditions. One of the most well-known examples of EOS is the ideal gas law, which describes the state of an ideal gas (composed of noninteracting point molecules) as a function of pressure, volume of the container and

temperature of the system. The state of a solid is usually described as a function of pressure, temperature and, sometimes, external magnetic and electric fields.

Depending on how fast the pressure is applied to the system, the compression is described as static, or dynamic (for a very short time scales, the term "shock compression" is used). Shock compression studies are outside the scope of this thesis, therefore will not be discussed further.

One of the equations of state used very often in static solid-state experiments is Birch-Murnaghan EOS. It describes pressure p needed to compress a solid to a volume V, if this solid has a bulk modulus B_0, a derivative of bulk modulus with regards to pressure equal $B_0^{'}$, and volume at some reference point (usually at 0 GPa) equal V_0. All parameters of the equation are described in more detail below. The equation itself is:

$$p(V) = \frac{3B_0}{2}\left[\left(\frac{V_0}{V}\right)^{\frac{7}{3}} - \left(\frac{V_0}{V}\right)^{\frac{5}{3}}\right]\left\{1 + \frac{3}{4}(B_0' - 4)\left[\left(\frac{V_0}{V}\right)^{\frac{2}{3}} - 1\right]\right\}$$

Bulk modulus, B_0 is defined as:

$$B_0 = -V\left(\frac{\partial p}{\partial V}\right)_{p=0}$$

The unit of B_0 is equal to the units of pressure. Usually, the values of B_0 are provided in GPa and range from several GPa for very soft solids or liquids, to over 400 GPa for diamond (it is important to note, that B_0 is a function of temperature). A higher value of bulk modulus indicates that a compound is more resistant to pressure – under hydrostatic pressure its volume will decrease less than for a different compound with a smaller B_0.

B_0' is the derivative of B_0 with respect to pressure. It is defined as:

$$B_0^{'} = \left(\frac{\partial B_0}{\partial p}\right)_{p=0}$$

The derivative of bulk modulus with pressure can be interpreted as a way to tell how does the solids hardness change with pressure. Structures with a high value of B_0' become hard very fast, structures with low B_0' are more compressible – due to a layered structure enabling compression of interlayer space, the presence of polarizable atoms, or voids in the structures.

V_0 is volume at a reference pressure, usually 1 atm (~0 GPa). If the substance under study undergoes a pressure-induced structural phase transition at some pressure p_1, then it is convenient to use volume at pressure p_1 as a reference.

The Birch-Murnaghan equation of state (BM-EOS) is routinely used to calculate pressure inside the sample space during HP experiments via X-ray diffraction.

A.5.2 Equipment – diamond anvil cells

The piece of scientific equipment used to statically apply high pressure to samples is called a diamond anvil cell (DAC). In essence, a diamond anvil cell consists of two polished diamonds facing each other and compressing a sample. DACs differ in construction, although many common features are present in all variations. Most DACs used in research consist of main body, seats, diamonds, and a gasket.

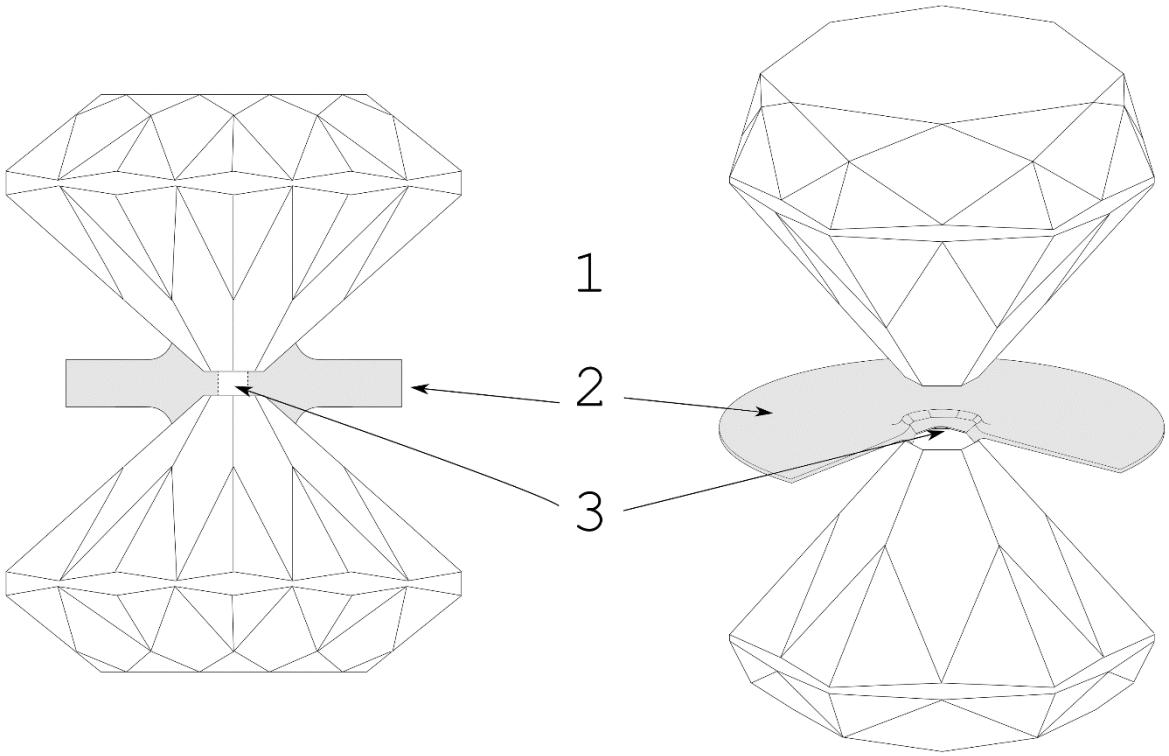

Fig. 55 - a side view and perspective view of the main elements of diamond anvil cell

Fig. 55 depicts the scheme of the DAC used typically for high-pressure experiments. The left part of the diagram shows a side view, whereas the right side shows a perspective view. A pair of diamonds (1) is pushed axially on each other while exerting pressure on a metal gasket (2). Sample chamber (3) is cut inside a gasket. The light can shine through the sample

to obtain diffraction, scattering or absorption spectra as a function of pressure and temperature.

Historically, the first “natural” diamond anvil cells were not constructed but instead synthesized by Nature. During the process of diamond crystallization in Earth mantle, some minerals might sometimes form inclusion in a diamond matrix. Pressure and temperature that the diamonds were experiencing would also be acting upon the inclusions. The diamonds that crystallized with inclusions would sustain the pressure conditions inside them even after being mined. Raman or IR spectroscopy measurements of samples contained in naturally formed DACs are therefore a way of researching geological processes occurring at depths impossible to be probed directly [121–123].

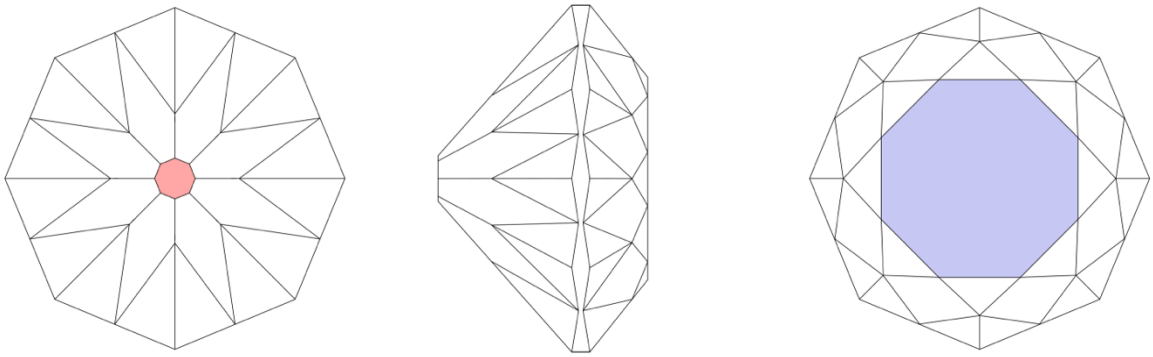

Fig. 56 - diagram depicting a brilliant cut diamond

The diamonds used in high-pressure research are cut differently than those used in jewelry. The culet – a small face, colored in red on the figure above – in contact with the sample is one of the most important aspects of the diamonds suitable to use in high-pressure experiments. The size of the culet together with its shape determines the maximum pressure that can be achieved in an experiment. The typical diameter of a culet used in experiments ranges from >1 mm to 30 um. On the opposite side of the diamond, colored blue on the figure above lies a table. Culet and table should be parallel to each other, to decrease the possibility of diamonds sliding off each other or cracking under high pressure.

Depending on specific experimental conditions the culets might be shaped in various ways, or coated with an additional layer of material – for example very thin Pt wires might be deposited on the surface of diamond for electrical measurements under high pressure. Diamonds with beveled culets can withstand higher pressures than their flat counterparts,

whereas partially perforated diamonds have increased the signal-to-noise ratio in spectroscopy measurements[124].

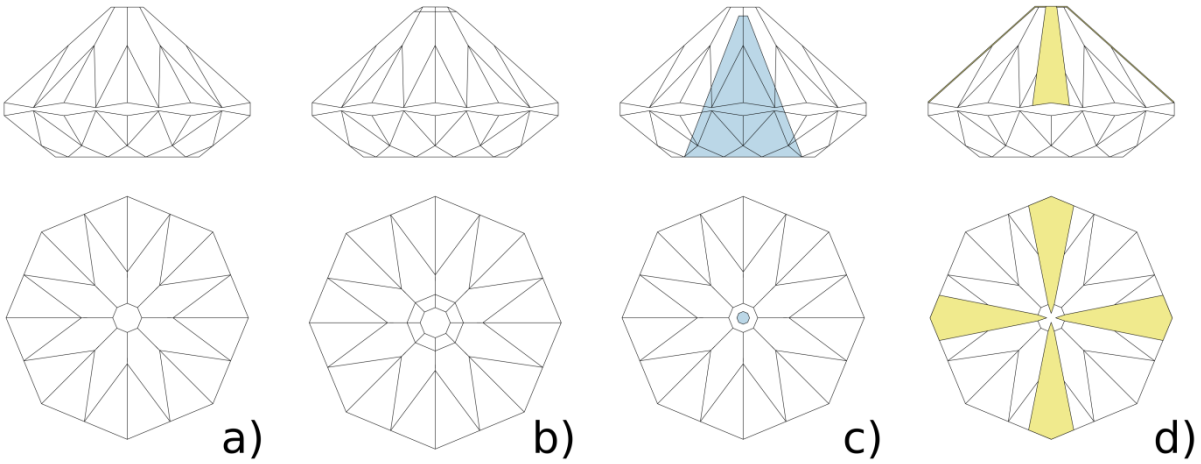

Fig. 57 - special diamond modifications. See text below for details.

Different shapes and modifications of diamonds can be introduced if such need arises (see Fig. 57). These are **a)** regular culet **b)** beveled culet, which takes into account diamond deformation during pressing ("cupping") enabling work in higher pressures **c)** partially perforated diamond – decreased amount of material along the axis improves signal-to-noise ration in spectroscopic measurements **d)** patterned diamond – gold electrodes deposited via CVD (chemical vapor deposition) or FIB (focused ion beam lithography) enable resistance measurements.

Diamonds used in high-pressure experiments are divided into several classes depending on the purity. Class I diamonds are usually contaminated with nitrogen and strongly absorb IR and UV light. Additionally, they have a strong fluorescence spectrum. This limits their use to XRD experiments, direct visual studies of samples under high pressure, or as a pressure gauge. Less contaminated class II diamonds do not contain nitrogen defects and give smaller fluorescence signal, permitting measurements with Raman or infrared spectroscopy. Both I and II class are divided into subclasses, depending on dispersion and contents of contaminants - the IIAS diamonds are of the highest purity.

There are many different designs of DAC body, which take into account working pressure range, temperature range, magnetic properties of used materials or volume of space necessary for the experiment. Regardless of the specifics of design, the body must be well fabricated to provide excellent precision and repeatability in experiments.

Extremely high compression strength of diamonds requires the use of sufficiently durable materials to safely transfer forces from external source to the tip of the diamond. This is the purpose of the so-called seat. The seats are made from stiff, tough but machinable materials – for example, silicon carbide, or tungsten carbide. To transmit light, seats should have a conical hole cut from their base to the top. The wider conical angle of the hole enables the user to access more angles in XRD experiments. On the other hand, it also increases the vulnerability of the seat.

One of the several improvements over the original design of DAC was the introduction of the gasket. Usually, it is a piece of metal foil with a small hole inside (diameter of the hole is typically between 2/3 and 2/5 of diamond diameter). The purpose of the gasket is to subject the sample to more isotropic pressure and prevent sample runaway. When the sample is placed inside the gasket hole along with a hydrostatic medium, the gasket acts as pressure container, distributing pressure in the sample chamber equally among all directions.

A.5.3 Pressure gauges and spectra measurement

In high-pressure experiments, there are two primary ways to measure the pressure inside the sample space. The first one is direct pressure measurement – by applying known force, one can approximate the pressure exerted by the diamond, provided the size of the culet is known. The second, more precise way, is to use an in-situ pressure gauge – some compound that gradually changes properties with pressure. An ideal gauge would not interact with the sample, enable easy measurement of the pressure, not obscure the signal from the sample, and not undergo any hysteresis.

Depending on the specifics of the experiment, there are always several different pressure gauges that one can use. In XRD experiments it is important to use a pressure gauge that will, on the one hand, have sufficiently high intensity in diffraction pattern and on the other hand will not obscure the pattern itself. In the Raman and IR experiments, the gauge should not emit a signal in the spectral range that is of interest to the experimenter. Depending on the pressure and temperature range probed in the experiment one can use quartz [125], ruby [126], diamond itself [127], gold [128], neon [129,130], platinum [131], Sm:YAG [132], Sm:SrB_4O_7 [133] and other compounds. Experiments described in this dissertation were pressure-calibrated using several pressure gauges, *e.g.*, XRD patterns were assigned pressure by neon pressure scale (which was also a pressure transmitting medium), or AgF diffraction.

Neon is a suitable gauge at pressures exceeding its freezing pressure, 4.8 GPa at 300 K [134]. It crystallizes in $Fm\bar{3}m$ space group, and does not undergo any phase transitions up to 240 GPa [135]. Pressure is found during the XRD data analysis stage, when positions of neon 111 and 200 diffraction reflexes are then extracted from the data. The value of pressure in a measured point of the sample can be then calculated from the known equation of state of neon. Similar technique can be used in case of other stable cubic crystals, for example, gold, platinum or copper. Neon can also serve as a pressure medium, as it retains hydrostatic conditions up to 15 GPa, with differences in pressure probed at different spots in anvil cell at 50 GPa being roughly equal to 1% [134].

Measuring ruby fluorescence is a very well-known method of determining the pressure in diamond anvil cell experiments [126,136–138]. A small ruby sphere or a sliver of crushed ruby is loaded along with the sample to the DAC. When ruby is illuminated at ambient pressure with laser light, it fluoresces two bands: R_1, R_2, at roughly 692 and 694 nm. The precise position of the fluorescence is shifted to longer wavelengths with increased pressure. Therefore, if a small ruby sphere is present in the center of the sample space of DAC, one can approximately determine under what pressure is sample by measuring the shift in fluorescence spectrum. This method is extraordinarily useful in a very wide array of studies – precise corrections have been derived for the ruby scale at various temperature and time regimes.

A last pressure scale that I would like to describe uses a diamond anvil itself. First-order Raman T_{2g} band changes shape in a well-behaved manner for a wide range of temperature and pressure. The pressure is determined by the position of minimum of derivative for the high wavenumber edge of the band. This pressure scale has been studied at ambient temperature up to 410 GPa [127].

A.5.4 Pressure studies of silver compounds at high pressure

A.5.4.1 AgF

Silver(I) fluoride has been studied under high-pressure both experimentally and theoretically. In 1970 Vaidya and Kennedy [139] studied compression and decompression of 27 halides using the piston-displacement method. In the cited paper they report one phase transition – a single discontinuity in volume versus pressure curve – for compression up to 4.5 GPa, and two phase transitions on decompression. In 1972 Halleck *et al*. [27] studied AgF using X-ray diffraction in the range of 0–125 kbar (0–12.5 GPa) and concluded that

during compression AgF transforms at about 2.5 GPa from NaCl-type structure to CsCl-type (B1-B2 transition). Several years later the same group [140] studied the compression-decompression cycle of AgF more closely and postulated that the two transitions observed during decompression most likely indicate the presence of intermediate phase of anti-NiAs symmetry. The 1998 Hull and Berastegui [47] confirmed the hypothesis using neutron diffraction of AgF sample. The resulting sequence of phases on compression-decompression cycle is:

$$NaCl \xrightarrow{2.5\ GPa,\ \ comp.} CsCl \xrightarrow{2.1\ GPa,\ \ decomp.} anti-NiAs \xrightarrow{0.91\ GPa,\ \ decomp.} NaCl$$

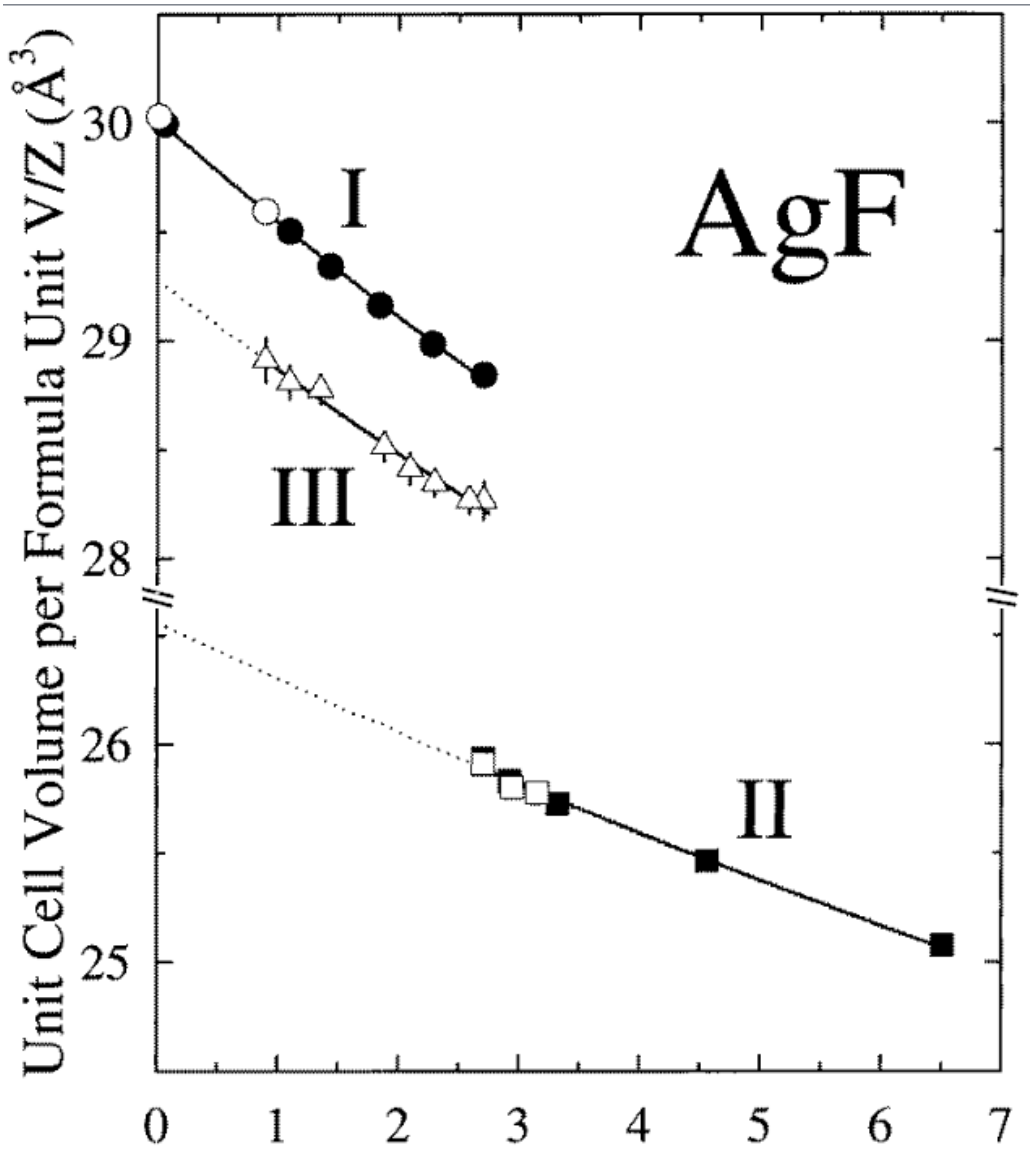

Fig. 58 – crystal cell volume as a function of pressure for three phases of AgF, taken from a paper by Hull and Berastegui [47].

A.5.4.2 AgO

The mixed-valence silver(I,III) oxide has been studied theoretically with DFT methods. Calculations using hybrid HSE06 functional were conducted by Włodarska *et al.* in 2015 [141]. The authors were able to reproduce the bandgap of ambient pressure *P2₁/c* polymorph (calculations yielded 0.94 eV, experimental value equals 1.0–1.1 eV) and observed a decrease of bandgap width with increasing external pressure. In this model at about 50 GPa the $P2_1/c$ polymorph metallizes. Due to a dynamic instability occurring before metallization, the compound was predicted to undergo a phase transition to $P\bar{1}$ form becoming a low density of states metal and preserving the disproportionated character of compound. Another theoretical study conducted by Hou *et al.* [142] predicted that at about 77 GPa AgO transforms from $P2_1/c$ to $R\bar{3}m$ structure. The trigonal structure obtained from the calculations was conproportionated. However, the authors neglected to take into account magnetic interactions between the silver cations. As Derzsi and Grochala argued in their comment [143] regarding Hou *et al.* paper, this led to an oversimplified models of the AgO structures. Introduction of magnetic interactions led to decrease in enthalpy of at least 50 meV per formula unit of $P\bar{1}$ structure in comparison to $R\bar{3}m$ structure (until reaching at least 125 GPa). It was therefore uncertain when this study commenced, what high-pressure polymorphic forms could AgO adopt, and whether they would be metallic, or not.

A.5.4.3 $AgSO_4$

In 2013 Derzsi *et al*. [70] studied compression of $AgSO_4$ in DAC. The researchers observed pressure-induced decomposition of silver(II) sulfate starting at about 23.4 GPa. The product of decomposition was found to be $Ag_2S_2O_7$ in the high-pressure structure of the K_2SO_7-type. It suggests that the decomposition reaction also yielded oxygen – either in elemental form or as a substrate in the oxidation of platinum gasket used in the experiment.

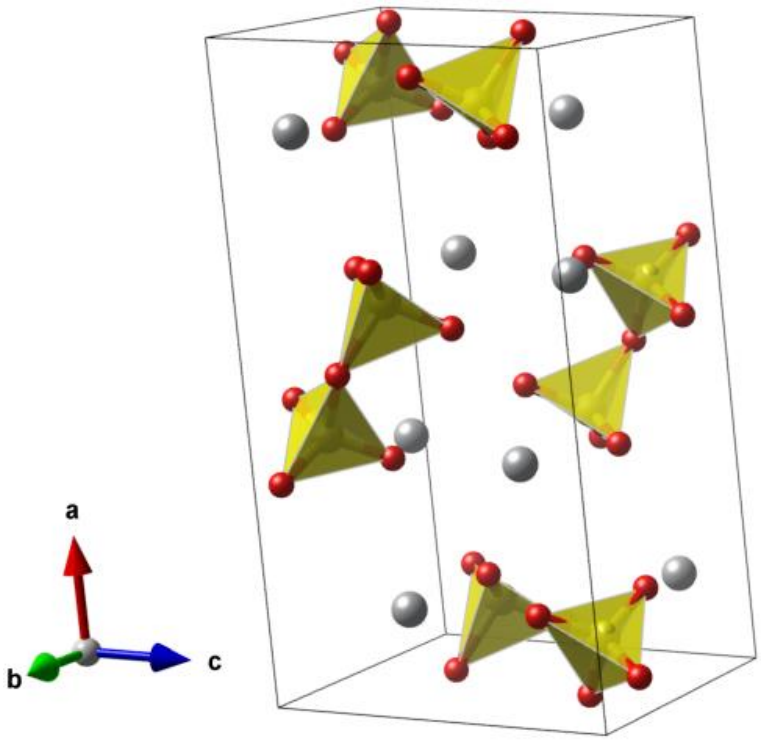

Fig. 59 - a ball-and-stick model of $Ag_2S_2O_7$ in the $K_2S_2O_7$-type structure at 23 GPa detected in experiments performed by Derzsi et al. [70].

B. Experimental work

B.1 Description of experimental setup

B.1.1 Raman spectroscopy

Most Raman spectroscopy measurements were conducted at the Laboratory of Technology of Novel Functional Materials at Center of New Technologies at University of Warsaw, using a Horiba-Yvon T64000 spectrometer. Unless specified differently, the laser used in experiments was Ar-Kr gas laser constructed by Spectra Physics. In standard measurements, a 514.5 nm excitation line was used. An aperture on the laser exit was used to cut off laser modes lacking cylindrical symmetry. The plasma lines were cut off using a diffraction grating mounted upstream from the sample. The laser provided a beam of about 400 mW power. Set of transmission filters were used to decrease the power of the beam illuminating the sample.

The laser beam was focused using a x20 apochromatic Mitutoyo lens. To increase the resolution in the z direction the scattered light was focused on a confocal aperture. The diameter of the confocal hole was about 100-150 μm. Unless specified differently, edge (low-pass) filters were used to cut off elastically scattered light. After removal of the Rayleigh and antistokes portion of the spectrum, the light was dispersed using a diffraction grating (150, 300 or 1800 l/mm) and projected onto a detector.

The detector used in the experiment was LN_2 cooled CCD consisting of array 256 x 1024 pixels. The long side of the array was parallel to the direction of images reflected off the diffraction grating (spectrometer). The spectra were obtained by binning middle 50 pixels along the short direction of the sensor array – the size of the binning area was determined by experimentally. The binning area has an optimal size − on the one hand it cannot negatively influence the quality of spectra by decreasing the signal, on the other collecting data from an arbitrarily large portion of the sensor would introduce more artifacts (space rays, etc.).

Measurements for samples at high-pressures conducted in the Geophysical Lab of Carnegie Institution of Washington used either 660 nm or 532 nm excitation lines. Rayleigh line was removed using a pair of notch filters and the filtered signal was then reflected into a Princeton Instruments spectrometer. The detector used was a LN_2 cooled CCD array.

Both Raman setups were used for high-pressure measurements in diamond anvil cells.

Some measurements also used Horiba Jobin-Yvon LabRam-HR Raman microspectrometer. A 632.8 nm He-Ne laser excitation line was used in these experiments. Dr. Zoran Mazej

from Josef Stefan Institute in Ljubljana is thanked for performing these measurements, the results of which were later analyzed by myself.

Some measurements used inVia Reflex Renishaw Raman spectrometer with 785 nm or 632.8 excitation lines. The spectrometer was coupled to a confocal microscope; the scattered light was dispersed via a diffraction grating onto a CCD detector. The elastically scattered light was removed by an edge filter. Dr. Agnieszka Kamińska-Michota from Institute for Physical Chemistry of Polish Academy of Science is thanked for enabling access to this Raman spectrometer.

Thermo NXR-FT-Raman 1064 nm spectrometer was also used in studies. It used a LN2 cooled Ge detector. The elastically scattered light was removed by a notch filter. The measurements were conducted with assistance from Prof. Wojciech Gadomski from Faculty of Chemistry (University of Warsaw), whom I would like to thank for help.

B.1.2 Infrared spectroscopy

Infrared spectra under ambient pressure were measured using Bruker Vertex 80 V FTIR spectrometer. Due to the high reactivity of the samples, the measurements were conducted using vacuum-tight solid-state sample cells (see Fig. 60). Powdered samples were spread under an inert atmosphere in a thin layer directly onto a cell window. To homogenize the layer, the windows with sample were then lightly rotated against each other, thus smearing the sample. An additional spacer of a well-defined thickness (250 μm) was placed between the cell windows after the smearing and the cell was put back and closed shut.

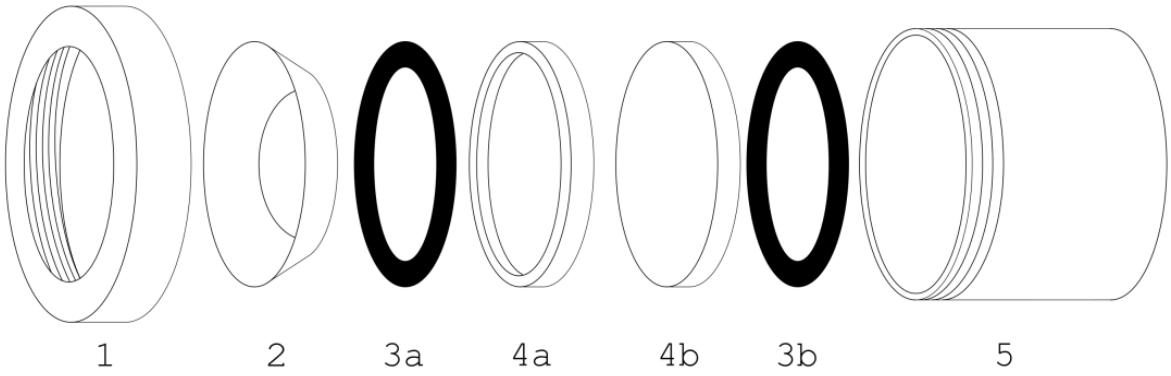

Fig. 60 - elements of vacuum-tight solid state cell. 1, 5 - main body and cap, 2 – coned-disc steel gasket, 3a, 3b – rubber o-rings, 4a, 4b – windows.

Each measurement region required a different configuration of the spectrometer. The measurements in the far infrared region (roughly 40-700 cm^{-1}) were made using a Mylar beamsplitter, Globar light source and HDPE windows. MIR studies (400-4000 cm^{-1})

required KBr beamsplitter, Globar light source and CaF_2 windows. Prevalent methods sample preparation methods: pressing a sample dispersed in KBr matrix into a pellet, dispersing sample in nujol oil or smearing it on the surface of AgCl windows cannot be applied to the most compounds in this study due to their extreme reactivity.

The procedure of measuring the FTIR spectra was independent on the probed region. First, a background spectrum of a solid-state cell without a sample was collected – the empty cell was properly assembled and positioned in the sample chamber. To decrease the signals from water vapor, CO_2 and other possible contaminants, the spectrometer has been evacuated for at least 15 min. Because of the construction of the spectrometer, the optics (interferometer chamber, detectors, etc.) can be evacuated separately from the sample chamber. This decreases the period between sample changes because smaller volume has to be evacuated each time. After the background has been collected, the cell was transferred to a glovebox, and loaded with a sample using the previously described method. The tightly closed cell was then transferred back to the sample chamber which was evacuated immediately after. Spectra were collected with 1 cm^{-1} resolution.

B.1.3 UV-vis-NIR spectroscopy

UV-vis-NIR spectroscopy measurements were conducted using Bruker 80 V spectrometer equipped with GaP, Si and DLaTGS detectors, using halogen lamp (vis, NIR) and deuterium lamp (UV) sources. CaF_2 beamsplitter was used in the whole measurement range – it retains a very good transmittance at least down to 1000 cm^{-1} and up to 80000 cm^{-1} (125 nm)[12].

Because compounds in the study are for all intents and purposes insoluble in any known solvent, their spectra must be measured using techniques appropriate for the samples in the solid state. As the size of crystallites in studied compounds is on the order of several to several tens of micrometers, scattering may introduce spurious signals.

B.1.4 High-pressure experiments

High-pressure experiments were conducted in symmetric Mao-Bell type DACs. The diamonds used in experiments were of IIAS quality (low-fluorescence suitable for Raman experiments), with diameters in the 200-300 μm range. To decrease the chance of reaction between the studied compounds and the experimental equipment, 250 μm thick rhenium gaskets were used. The diameters of the holes drilled in the gaskets were at most 0.6 of the

[12] This is an approximate value, the range in which transmittance exceeds 90% depends on the thickness of CaF_2 slab.

diamonds diameters. Before proper experiment phase each gasket was preindented[13] twice using an empty DAC – to about 10 GPa in the first step, and about 20 GPa in the second step. Gasket holes were drilled either with pulsed Nd:YAG laser drill, or with electric discharge machine (EDM). Samples were loaded under a microscope in an inert gas atmosphere in a glovebox. An inert pressure medium – neon – was loaded at about 20 MPa in a loading chamber at the collaborating institution of the Geophysical Laboratory at Carnegie Institution of Washington. A diamond anvil prepared in such a way proved to be a suitable vessel for carrying sample between the laboratories (no change in sample appearance or Raman spectrum was detected after the transport).

[13] The preindentation is a technique of compressing the gasket before drilling and further processing. A gasket is squeezed between the diamonds with a small speck of ruby for approximate pressure control. The point of doing that is threefold: first, the diamonds shapes are embedded in gasket during its plastic deformation. That simplifies the loading process, as the gasket does not move that easily from its position. Secondly, the diamonds pressing firmly into the surface of the gasket can create a very tight seal that prevents loss of contents of sample volume during further compression. Lastly, the gasket work-hardens during the preindentation stage, which decreases the amount of plastic flow during the real experiment – the sample space shrinks less than in a non-preindented case.

B.2 Own results

B.2.1 $AgSO_4$

A new method of $AgSO_4$ synthesis that used Ag_2SO_4 electrolysis in 100% H_2SO_4 was devised in 2016 by Połczyński *et al.* [144]:

$$Ag_2SO_4 + H_2SO_4 \xrightarrow{electrolysis\ in\ 100\%\ H_2SO_4} AgSO_4 + H_2\uparrow$$

Rinsing the product several times with aHF yields $AgSO_4$ of very high purity. Comparison of particle sizes between chemically (later described here as ch-$AgSO_4$) and electrochemically (later described here as el-$AgSO_4$) synthesized $AgSO_4$ was conducted using SEM imaging. Compared to the typical size of the ch-$AgSO_4$ crystals (less than a micron in diameter), the el-$AgSO_4$ crystals were much larger – several tens of microns, up to 250 x 60 μm. This indicates a slower crystallization process, but in effect yields crystals that are easier to analyze using Raman spectroscopy, or other single crystal based methods.

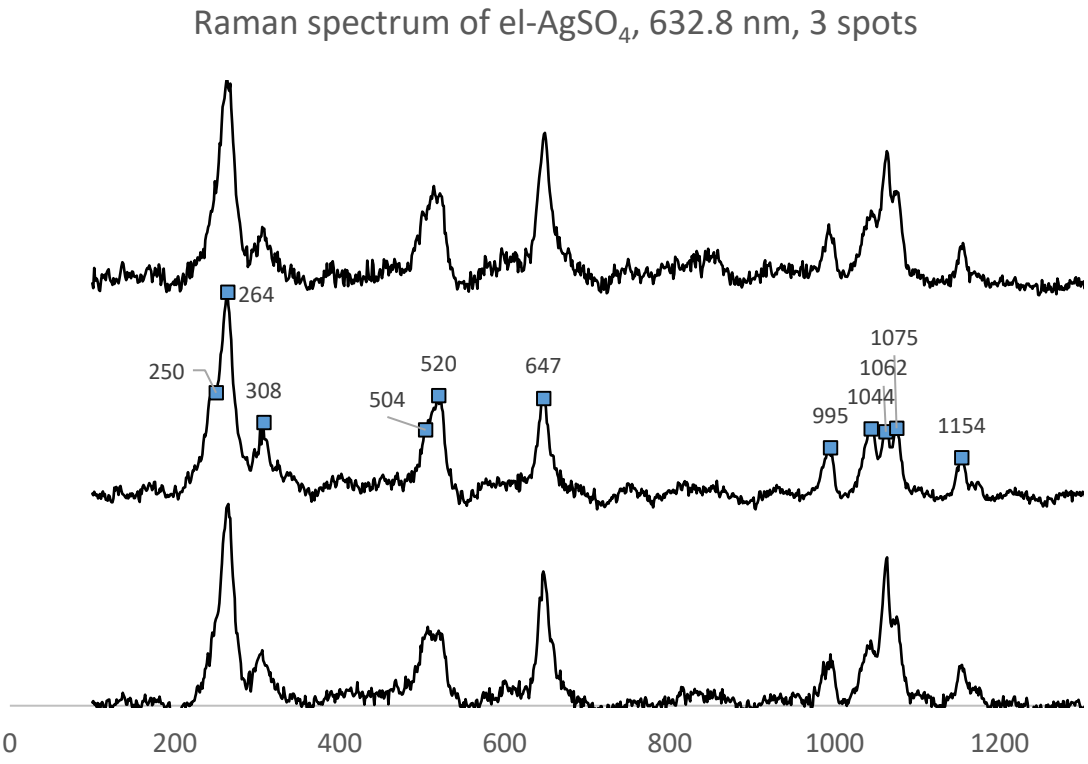

Fig. 61 - Raman spectra of el-$AgSO_4$, measured using an 632.8 nm excitation line. The spectra were captured at three different spots on the surface of sample. Abscissa is Raman shift in cm^{-1}, ordinate is intensity in arbitrary units.

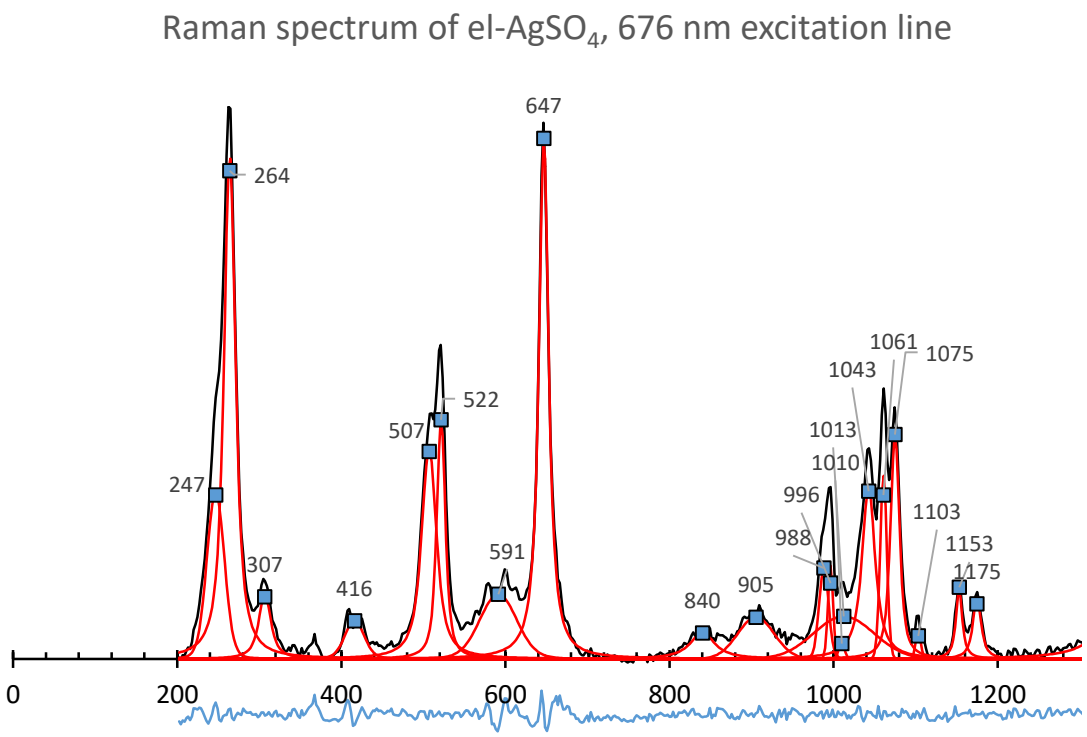

Fig. 62 - Raman spectrum of el-AgSO₄ at 676 nm excitation line.

Fig. 61 and Fig. 62 depict spectra of el-$AgSO_4$ captured by me at different sample spots and using either 632.8 nm (measured by Dr. Mazej) or 676 nm (measured by myself) excitation lines. The spectra differ slightly between another, although most band positions and are equal between the measurements. To compare the product of electrochemical with a known product of chemical synthesis the sample of fresh ch-$AgSO_4$ was measured once again.

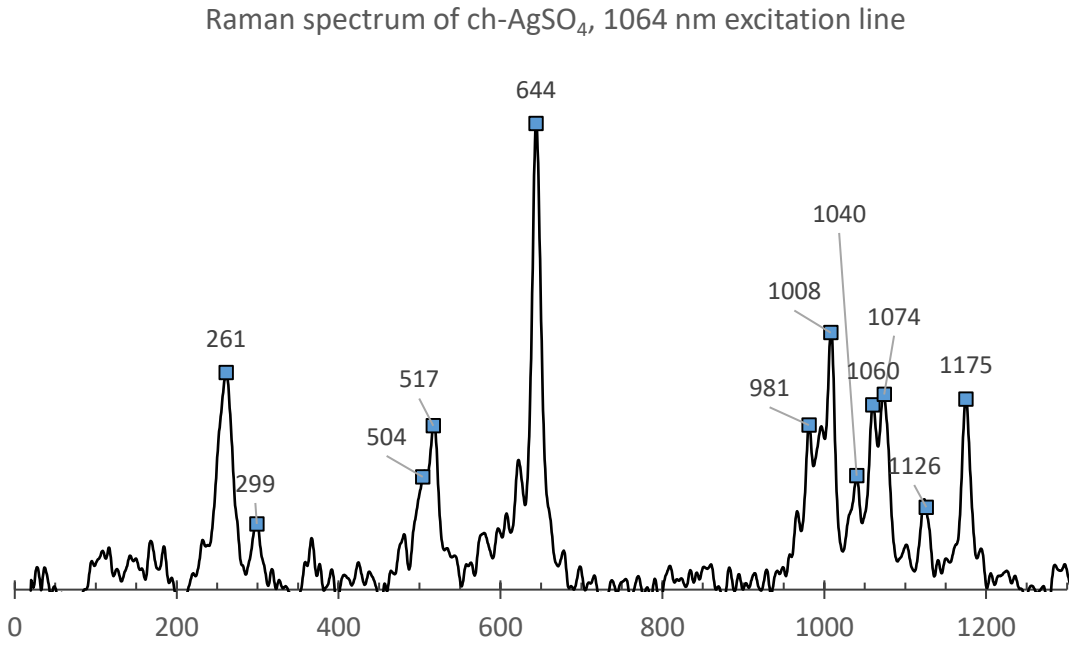

Fig. 63 - Raman spectrum of ch-$AgSO_4$ at 1064 nm excitation line (10 mW)

Most of the bands from the both samples repeat in all spectra. The most discernible difference between the two samples are in presence of bands 247 cm^{-1}, 416 cm^{-1} (most likely O-S-O A_g deformation) and 1153 cm^{-1} in el-$AgSO_4$ spectrum and 1126 cm^{-1} in the ch-$AgSO_4$ spectrum. These differences are not immense, though, and they may stem from the effects of orientation of small single crystals in the laser beam.

My own analyses of the Raman spectra of $AgSO_4$ samples revealed also their sensitivity to incoming light. The spectra shown in Fig. 64 were collected using Horiba Jobin Yvon LabRam-HR Raman microspectrometer with 632.8 nm He-Ne excitation line. Each spectrum was obtained from the same spot on the sample of ch-$AgSO_4$. Subsequent spectra were collected for longer illumination times to observe the effect of photochemical decomposition of $AgSO_4$. With increasing time, the bands attributed to $AgSO_4$ lost intensity, and new bands appeared and grew in intensity at 83, 169, 425, 476, 622, 970 cm^{-1}. The product of the photochemical reaction could not be identified, but the new bands are not characteristic of any known $Ag_xS_yO_z$ compound.

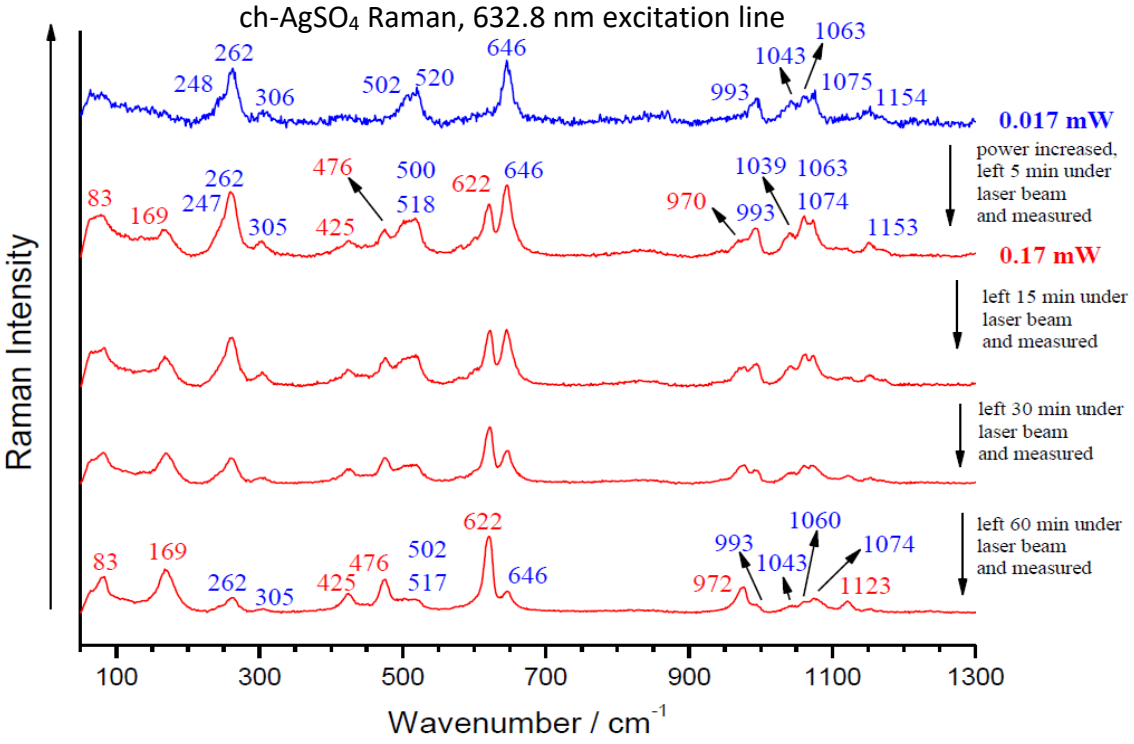

Fig. 64 – series of Raman spectra of ch-$AgSO_4$ measured at a single spot. Increased illumination time and power leads to appearance of new bands (83, 169, 425, 476, 622, 970 cm^{-1}) and decrease in intensity of old ones. These measurements were conducted by Dr. Zoran Mazej.

To better understand the photodecomposition, Raman spectra of ch-$AgSO_4$ have also been collected using a strong beam at a longer, near infrared wavelength. It could be hypothesized, based on the narrowness of electronic band gap of $AgSO_4$ [144] that such excitation would lead to a thermal decomposition of black sulfate, as opposed to a photochemical decomposition occurring with red light. Additional measurements were done using strong 1064 nm excitation with 0.1 W and 0.5 W laser power (see Fig. 65). Indeed, illumination of the sample using strong NIR light had a different outcome than using a red light and led to the formation of $Ag_2S_2O_7$ via thermal decomposition:

$$2AgSO_4 \xrightarrow{hv\ (NIR),\ \ high\ power} Ag_2S_2O_7 + \frac{1}{2}O_2$$

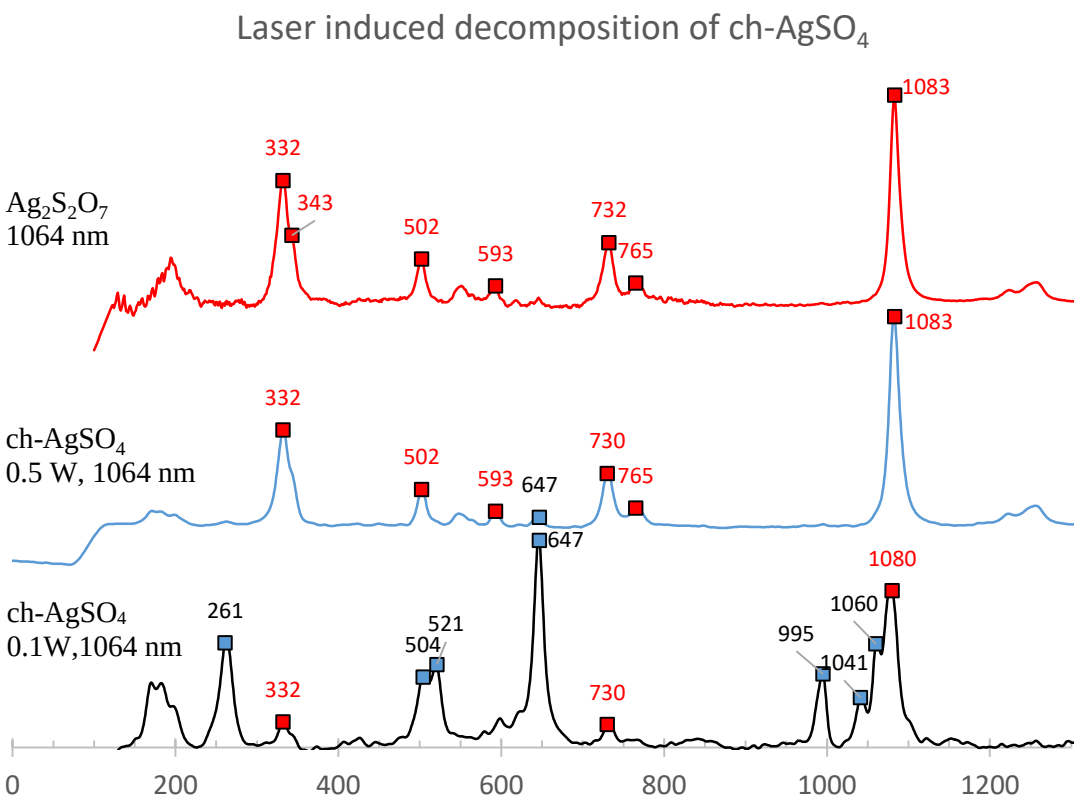

Fig. 65 – All spectra in the set were collected using a 1064 nm excitation line. The middle spectrum and the bottom one were collected for samples of ch-$AgSO_4$.Those two measurements differed only in the incident laser power. The spectrum measured using higher laser power, i.e. 0.5 W, is very similar to the $Ag_2S_2O_7$ spectrum (top one), indicating that thermal decomposition of silver(II) sulfate took place.

Clearly, a product of photochemical decomposition of $AgSO_4$ using red laser beam is different from $Ag_2S_2O_7$. One possible candidate for the photochemical product is $Ag^{1+}Ag^{3+}(SO_4)_2$. Another one could be $(Ag^{1+})_2(S_2O_8)$ [145]. These suggestions are speculative, but not wild, as those hypothetical products correspond to intervalence charge transfer (IVCT) or metal-ligand charge transfer (MLCT) and such absorptions, as we will see, fall in the visible region of this black compound.

I measured the FT-UV-vis-NIR spectrum of $AgSO_4$ using Vertex 80V spectrometer with CaF_2 beamsplitter. In the visible and near infrared range a halogen lamp was used as an illumination source, whereas in the UV range a deuterium arc lamp provided a better intensity. A solid sample cell with infrasil windows was used in the whole measurement range.

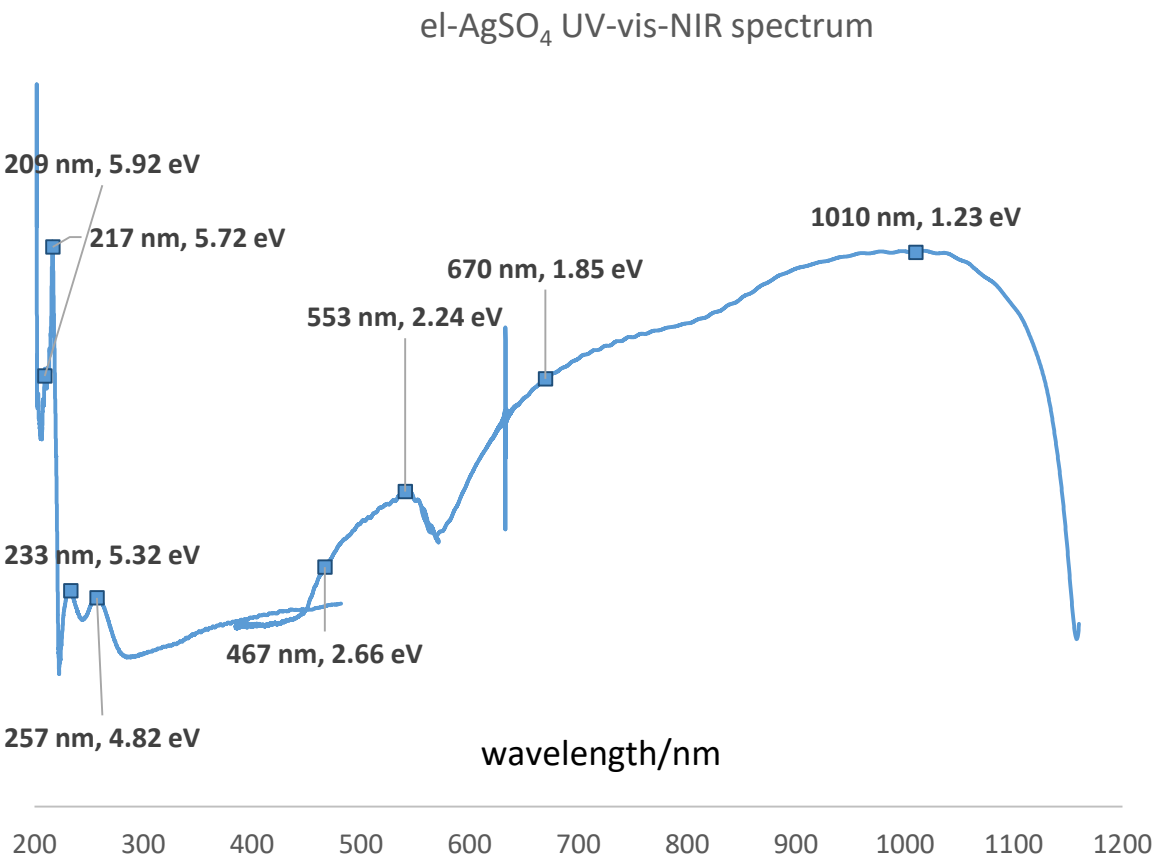

Fig. 66 - a combined UV-vis-NIR spectrum of $AgSO_4$. Published in paper by Gilewski et al. [146].

The spectrum of el-$AgSO_4$ contains eight bands (or shoulders) in 200-1150 nm range. Because Ag(II) cations in the structure of $AgSO_4$ are coordinated by an planar square of oxygen atoms[14] (Fig. 22) due to the Jahn-Teller effect, splitting is observed of molecular orbitals coming from different d orbitals of silver.

[14] The differences in axial and equatorial bond lengths are significant enough that the formally 4+2 coordination might be better described as a square.

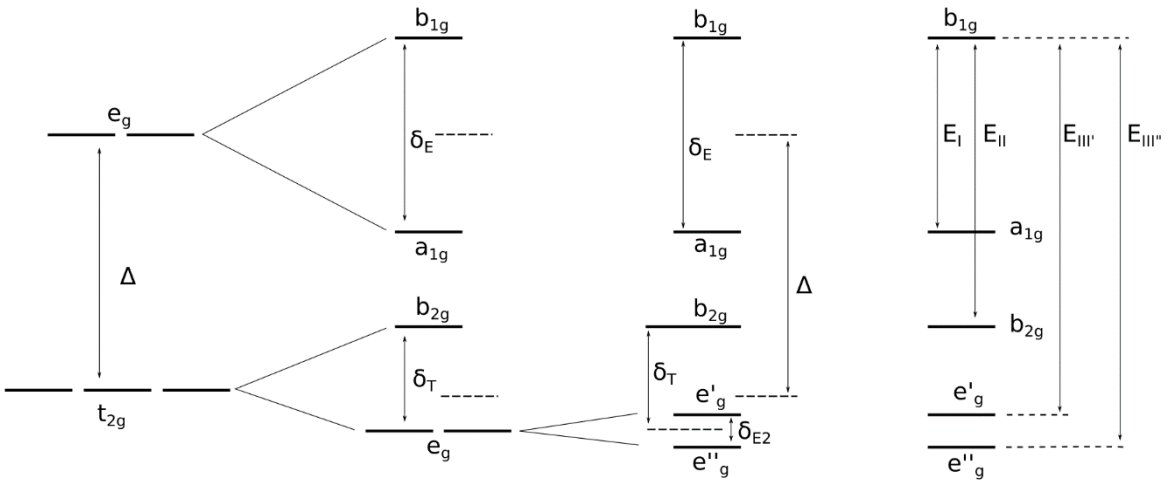

Fig. 67 - electron energy levels in Ag^{2+} cation – from the left: spherical field, crystal field with square coordination, square coordination with rhombic distortion. δ_i symbols indicate splitting between different energy levels. The diagram on the far right shows different possible transitions between Ag^{2+} orbitals.

The above scheme indicates that electronic spectrum of $AgSO_4$ should contain 4 different electronic transitions, in increasing energy order: $a_{1g}\rightarrow b_{1g}$, $b_{2g}\rightarrow b_{1g}$, $e'_g\rightarrow b_{1g}$, $e''_g\rightarrow b_{1g}$. Additional electronic transitions can come from metal to ligand charge transfers, which can be described using MO formalism.

Band	Position	Energy	Assignment
I	1010 nm	1.23 eV	$a_{1g}\rightarrow b_{1g}$
II	670 nm	1.85 eV	$b_{2g}\rightarrow b_{1g}$
III'	553 nm	2.24 eV	$e'_g\rightarrow b_{1g}$ (CT $O_{ax}\rightarrow$ Ag)
III''	467 nm	2.66 eV	$e''_g\rightarrow b_{1g}$ (CT $O_{ax}\rightarrow$ Ag)
CT1	257 nm	4.82 eV	CT, $O_{eq}\rightarrow$Ag(II)
CT2	233 nm	5.32 eV	CT, $O_{eq}\rightarrow$Ag(II)
CT3	217 nm	5.72 eV	CT, $O_{eq}\rightarrow$Ag(II)
CT4	209 nm	5.92 eV	CT, $O_{eq}\rightarrow$Ag(II)

Tab. 10 - band positions and assignments from UV-vis-NIR spectrum of $AgSO_4$.

I used band assignments shown in Tab. 10 to calculate standard splitting energies: in ^2E_g, $^2T_{2g}$ groups (δ_1, δ_2, δ_3) and between them (Δ).

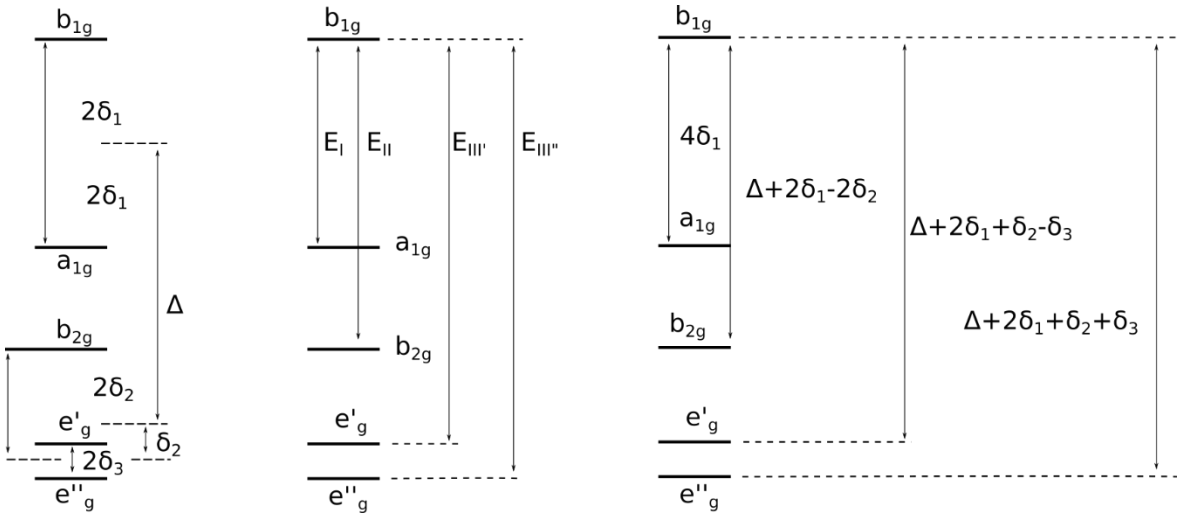

Fig. 68 - diagram of electronic transitions in $AgSO_4$. The rightmost diagram depicts energies of transitions as a functions of splitting parameters using convention adopted by Friebel and Reinen [6].

$$E_{III}^{''} - E_{III}^{'} = 2\delta_3 = 2.65\ eV - 2.24\ eV = 0.41\ eV = 3331\ cm^{-1}$$

$$E_I = 4\delta_1 = 1.23\ eV = 9900\ cm^{-1}$$

$$\frac{1}{2}\left(E_{III}^{''} + E_{III}^{'} - 2E_{II}\right) = \frac{1}{2}(2\Delta + 4\delta_1 + 2\delta_2 - 2\Delta - 4\delta_1 + 4\delta_2) = 3\delta_2$$

$$= \frac{1}{2}(2.65\ eV + 2.24\ eV - 2 * 1.85\ eV) = 0.60\ eV = 4819\ cm^{-1}$$

$$E_{III}'' - 2\delta_1 - \delta_2 - \delta_3 = \Delta = 2.65\ eV - \frac{1}{2} * 1.23\ eV - \frac{1}{3} * 0.60\ eV - \frac{1}{2} * 0.41\ eV$$

$$= 1.63\ eV = 13197\ cm^{-1}$$

Therefore Δ = 13197 cm^{-1}, δ_1 = 2475 cm^{-1}, δ_2 = 1606 cm^{-1}, δ_3 = 1665 cm^{-1}. The nomenclature used is consistent with the one used in a paper by Friebel and Reinen [6]. The large width of bands in the visible region is consistent with a very dark gray/black color of $AgSO_4$. The splitting energy Δ is higher than in the compounds containing fluorine-coordinated silver(II) cation (about 13 thousand cm^{-1} *vs.* about 9-12 thousand cm^{-1} in ternary fluorides [6]). This is a consequence of coordinating with a stronger field dianionic ligand (sulfate *vs.* fluoride).

The new method of synthesis of $AgSO_4$ proved to be a reliant source of a high purity product. The measurements and data analysis carried out here confirmed the identity of el-$AgSO_4$ but also indicated its photochemical sensitivity. The electrosynthesized $AgSO_4$ had also novel

chemical properties, as has been observed after exposing its sample to atmospheric water vapor (next chapter).

B.2.2 $AgSO_4 \cdot H_2O$

Monohydrate of silver(II) sulfate(VI) was first reported in 2016 by Gilewski *et al*. [146]. The compound was synthesized from pure $AgSO_4$ (from electrochemical synthesis) by letting it come in contact with atmospheric water vapor. The progress of the reaction occurring on the surface of $AgSO_4$ crystals was estimated by comparing the brilliance of the sample with the brilliance of the pure $AgSO_4$. Interestingly, reaction between chemically synthesized $AgSO_4$ and water vapour or water, leads to decomposition of samples yielding Ag(I) salts. The difference in reactivity likely originates from a very different specific surface of both sample types, as well as presence of small amount of hygroscopic $KSbF_6$ in chemically prepared specimen.

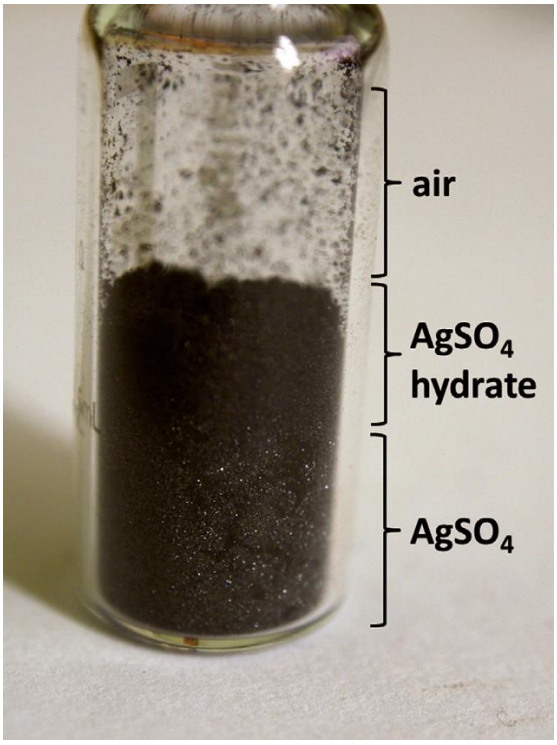

Fig. 69 - a photo of a glass vial containing freshly formed $AgSO_4$ hydrate on top of $AgSO_4$.

Fig. 69 depicts a small vial filled with two solids layered on top of each other. The top layer consists of an *in situ* formed silver(II) sulfate(VI) hydrate, the bottom one is made of pure $AgSO_4$. Both compounds are black, but hydrate crystals are noticeably less shiny.

As determined by Gilewski *et al.* [146], $AgSO_4 \cdot H_2O$ crystallizes in a triclinic $P\bar{1}$ group, with $a = 5.1189(2)$ Å, $b = 5.3878(2)$ Å, $c = 7.8526(3)$ Å, $\alpha = 107.2827(6)°$, $\beta = 105.1489(7)°$, $\gamma = 92.3864(7)°$, $Z = 2$ and $V = 197.928(14)$ Å^3. The volume per functional unit of silver(II) sulfate hydrate is about 9% smaller than the sum of volumes of one f.u. of ice I_h (hexagonal ambient pressure form of ice) and one f.u. of $AgSO_4$.

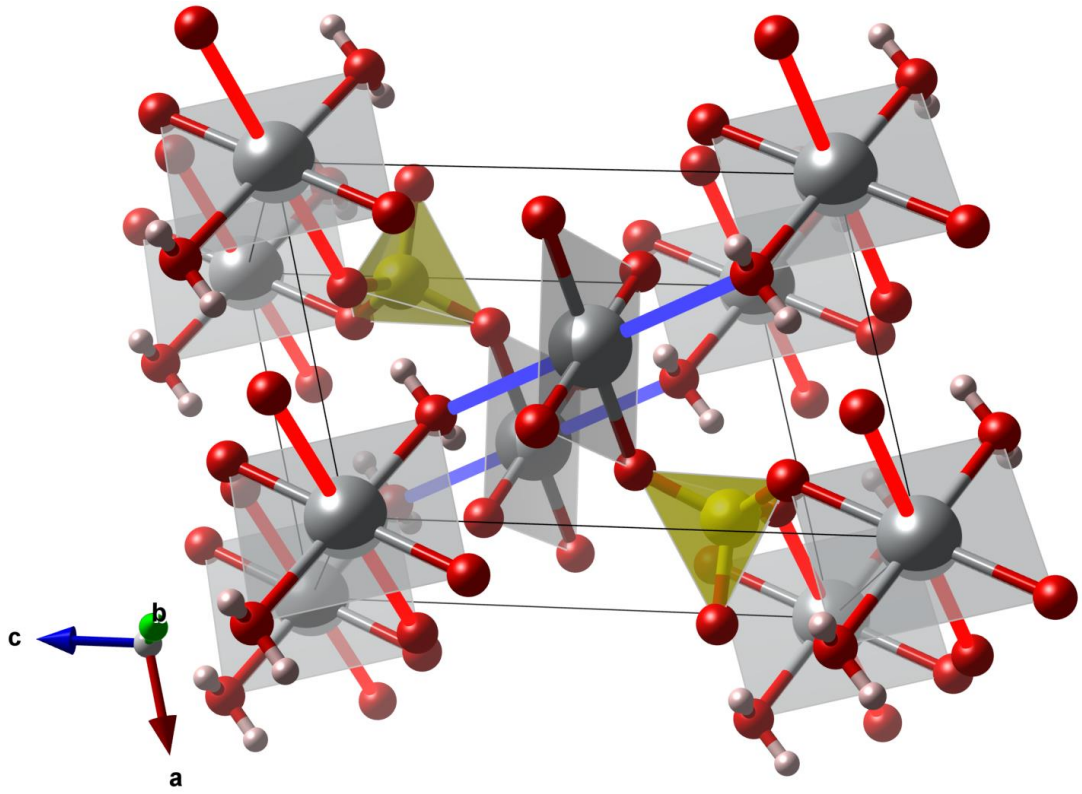

Fig. 70 - a ball-and-stick model of the crystal cell of silver(II) sulfate monohydrate

Fig. 70 depicts a crystal cell of silver(II) sulfate monohydrate. Two distinct silver(II) cations are present in the structure. The first one – Ag1 – is coordinated by 4 atoms from sulfate group, forming a square. Average Ag(II)-O bond length equals 2.112(5) Å. There are also longer, axial contacts present, at bond length Ag(II)-O = 2.652(11) Å, indicated by blue cylinders in Fig. 70. They are introduced by axially positioned oxygens belonging to water molecules. The second silver cation – Ag2 – is also coordinated by 4 oxygen atoms forming a square, but in the contrast with the first cation, two of those atoms belong to sulfate group, and two others belong to water molecules. The average Ag(II)-O bond length in this moiety equals 2.102(5) Å. The longer contacts for this cation are formed with neighboring sulfate group at Ag(II)-O distance equal to 2.642(11) Å. Therefore, both types of silver cations adopt deformed elongated octahedral coordination.

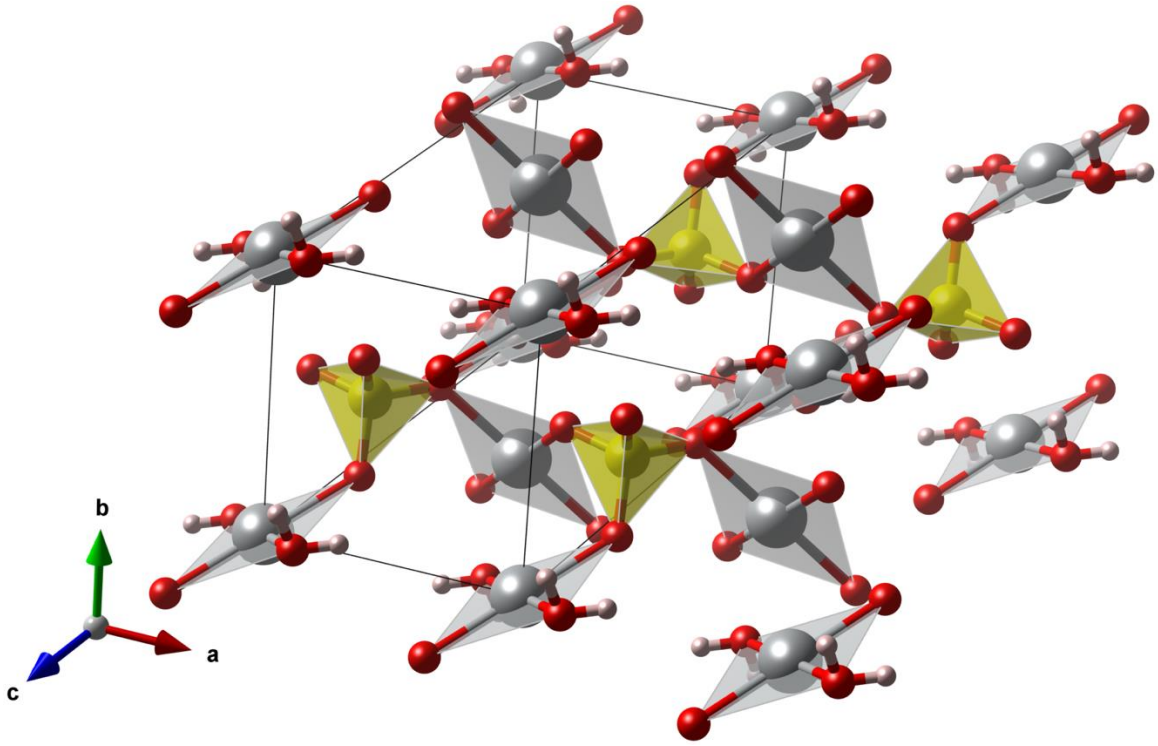

Fig. 71 - a ball-and-stick model of a 2x1x1 supercell of silver(II) sulfate monohydrate.

Fig. 71 depicts a 2x1x1 supercell of $AgSO_4 \bullet H_2O$. Ag1 cations form chains extending in **a** direction. S-O-Ag angles in chains alternate between 128.1(8)° and 131.9(6)° degrees. Each chain is connected to its neighbors in the (010) plane via two sulfate groups joined by an Ag2 cation. None of the oxygen anions of the sulfate group are terminal, three in each group coordinate Ag cations via short contacts, the last one coordinates Ag2 cation via a long contact.

B.2.2.1 Spectroscopy of $AgSO_4 \bullet H_2O$

I have performed the measurements of FTIR spectra using the previously described procedure applied to anhydrous $AgSO_4$. FIR range was measured using HDPE windows, while the MIR region was measured using BaF_2 windows.

The Raman measurements proved to be more difficult. The compound in the study is black, therefore strong absorption of laser light was expected – just like in the case of the anhydrous $AgSO_4$. Avoiding the thermal decomposition of $AgSO_4 \bullet H_2O$ required careful optimization of incoming laser power and measurement time. Power exceeding 0.17 mW of 632.8 nm line resulted in decomposition, therefore smaller power was used, which led to a rather noisy spectrum. Nevertheless, reasonable quality data was obtained.

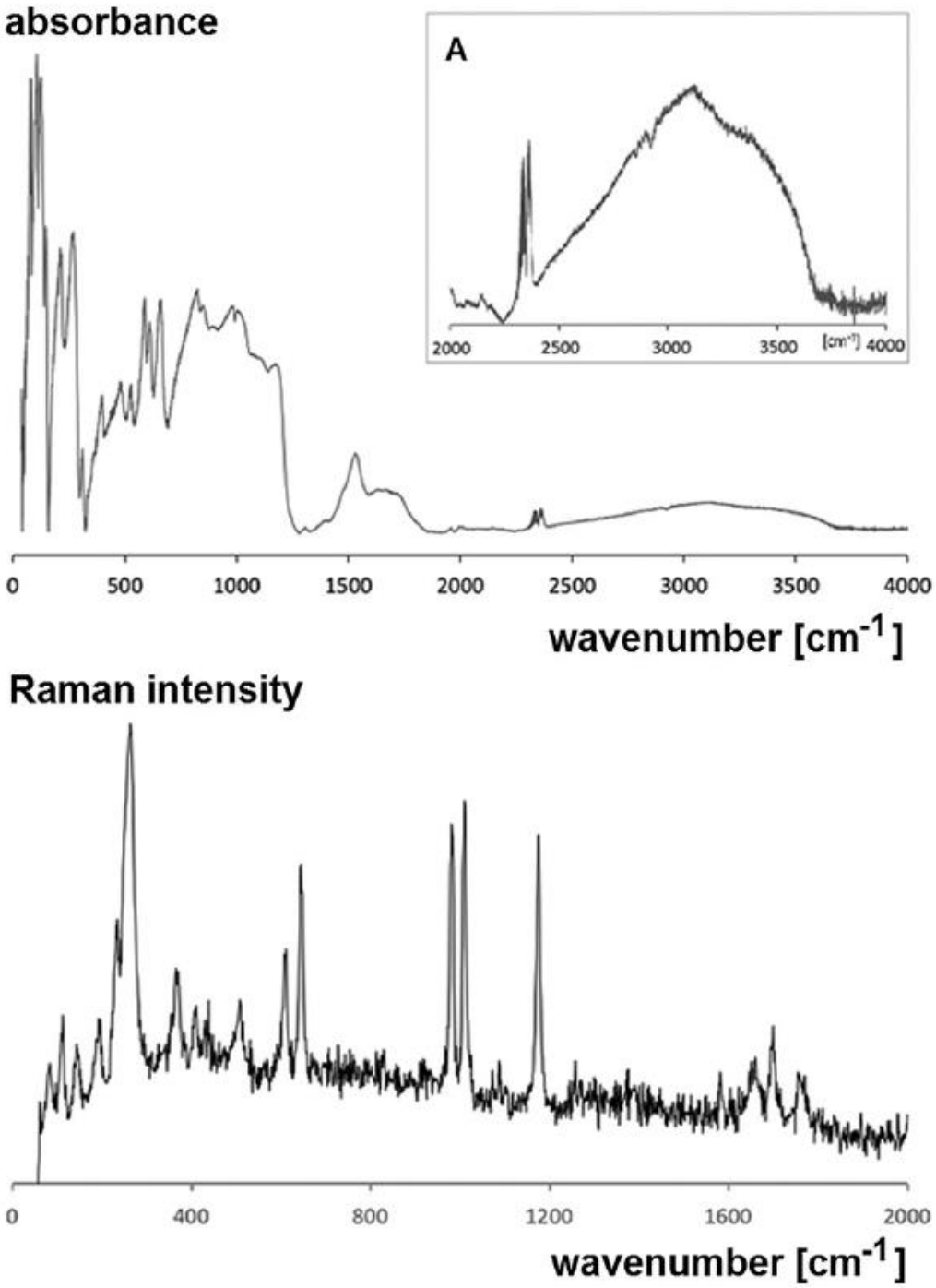

Fig. 72 - FTIR and Raman spectra of $AgSO_4$ monohydrate. The inset labeled A is a blown-up fragment of absorption spectra depicting more closely region of stretching O-H vibrations. The characteristic doublet at about 2350 cm^{-1} in FTIR spectrum comes from atmospheric CO_2.

IR	Raman	Symmetry	Assignment
3384 w br		A_u	ν(O−H)
3313 w br		A_u	
1994 vw		A_u	impurity, overtone or combination mode
1958 vw		A_u	
	1762 w	A_g	
1718 w		A_u	
	1699 m	A_g	
1675 w		A_u	
	1657 w	A_g	δ(H−O−H)
1631 w		A_u	
	1582 w	A_g	
1532 m		A_u	
1476 sh		A_u	
1402 w		A_u	impurity, overtone or combination mode
1307 vw		A_u	
1175 m	1175 s	A_u	
1112 m		A_u	
	1087 vw	A_g	
	1010 s	A_g	
1006 m		A_u	ν(S−O)
983 m		A_u	
	982 s	A_g	
896 w		A_u	
852 sh		A_u	
822 m		A_u	
660 m		A_u	
	644 m	A_g	
611 m		A_u	
	609 m	A_g	
587 m		A_u	δ(O−S−O)
525 w		A_u	
	508 w	A_g	
482 w		A_u	
	409 w	A_g	
398 w		A_u	lattice modes
	367 m	A_g	
310 w		A_u	
267 m		A_u	
	261 s	A_g	ν[AgO_4]
	233 m	A_g	
212 m		A_u	
	191 w	A_g	
147 m		A_u	
	144 w	A_g	
123 s		A_u	Hindered rotations of H_2O molecules and lattice modes
	111 w	A_g	
106 s		A_u	
82 vs		A_u	
	83 w	A_g	
77 vs		A_u	

Tab. 11 - $AgSO_4 \cdot H_2O$ vibrational modes with their intensity, symmetry and assigned identity. Symbol δ indicates deformation; symbol ν stands for stretching. Other symbols are used in accordance with their description in subchapter A.3.1.3.

Group theory analysis provided information about the number and type of first-order optical modes active for the $P\bar{1}$ $AgSO_4$ monohydrate structure. Those modes are 27 IR-active modes of A_u symmetry, and 24 Raman-active of A_g symmetry. Additionally, there are three acoustic A_u modes.

DFT calculations were conducted by Dr. Mariana Derzsi D.Sc. on different antiferromagnetic supercells of $AgSO_4 \bullet H_2O$. The one with the lowest energy was later used in computations, which led to the determination of its vibrational structure. As the magnetic supercell was based on 1x2x1 crystal cell, the number of vibrational modes obtained from calculations equaled 105 (Z = 4, therefore 9*3*4 = 108, 105 optically active and three acoustic modes).

The band positions calculated using DFT+U method were exceeding in number the band positions obtained from the experiment, hence theoretical values were selected from a broader set. To compare both datasets, the theoretical wavenumbers were scaled by a factor of 1.081. This procedure yielded an excellent agreement between selected data points from the theoretical set and experimental data collected by myself – see Fig. 73.

The experimental data and theoretical calculations, via presence and assignment of bands originating from water (stretching of O-H, bending of H-O-H) confirmed the presence of water molecules in the crystal structure of monohydrate.

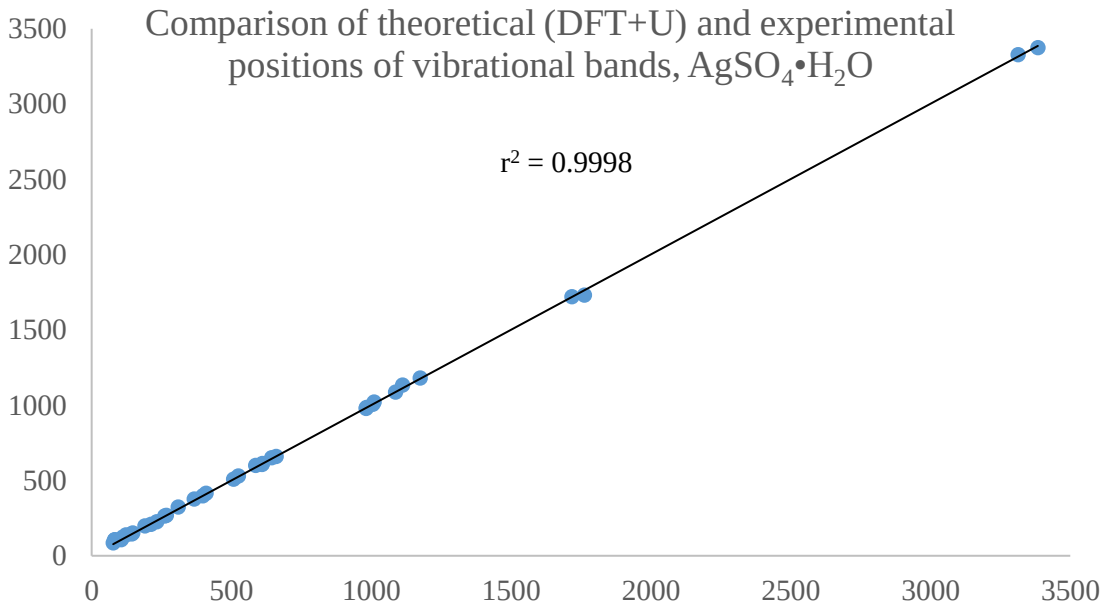

Fig. 73 - comparison of band positions between theoretical and experimental vibrational spectroscopy data for $AgSO_4 \bullet H_2O$. Theoretical positions have been scaled by a factor of 1.081.

The sample of $AgSO_4 \cdot H_2O$ was also studied using UV-vis-NIR spectroscopy.

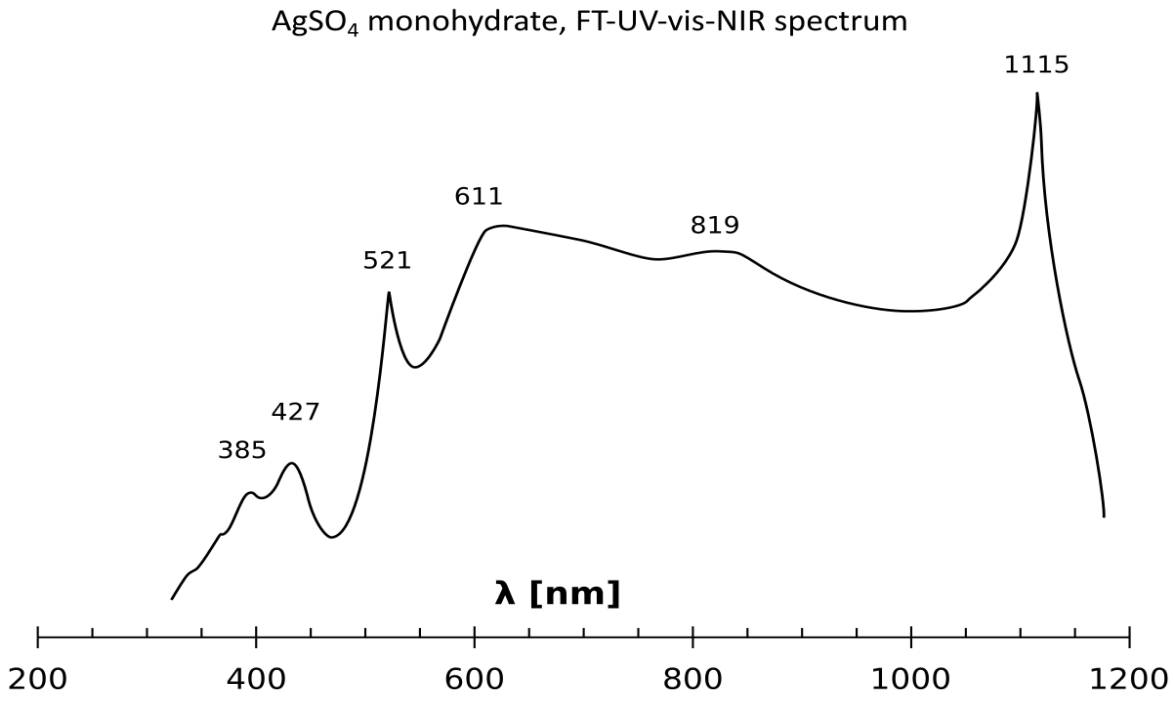

Fig. 74 - FT-UV-vis-NIR spectrum of $AgSO_4$ monohydrate.

The spectrum of monohydrate of $AgSO_4$ differs from that for the neat sulfate. Two bands (1115 nm, 521 nm) are sharper than bands present in the same spectral range in the spectrum of anhydrous sulfate. The coordination of $AgSO_4 \cdot H_2O$ is close to square planar (difference in lengths of equatorial Ag-O bonds does not exceed 1.5%). A difference in coordination geometry between two sites in the structure of hydrate leads to splitting of the charge-transfer band from axial oxygen.

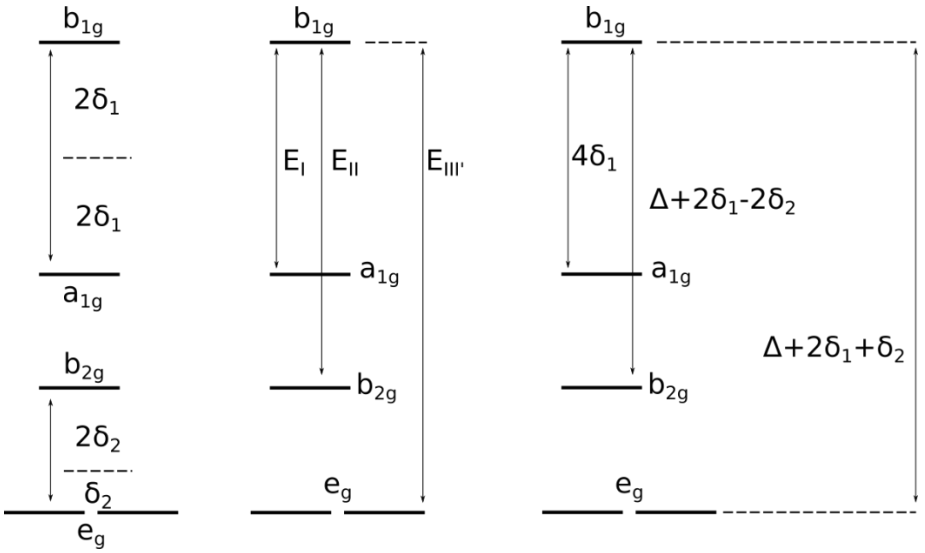

Fig. 75 - diagram of energy level splitting in $AgSO_4$ monohydrate.

Band	Position	Energy	Assignment
I	1115 nm	1.11 eV	$a_{1g}\rightarrow b_{1g}$
II	819 nm	1.51 eV	$b_{2g}\rightarrow b_{1g}$
II’	611 nm	2.03 eV	$b_{2g}\rightarrow b_{1g}$
III	521 nm	2.38 eV	$e_g\rightarrow b_{1g}$
CT1	427 nm	2.9 eV	CT $O_{ax}\rightarrow Ag$
CT2	385 nm	3.22 eV	CT $O_{ax}\rightarrow Ag$

Tab. 12 - positions, energy and assignment of UV-vis-NIR bands in $AgSO_4$•H_2O

Tab. 12 contains positions, energies and assignments of electronic transition bands found in UV-vis-NIR spectrum of $AgSO_4$ monohydrate (Fig. 74). The I, III and CT bands are self-explanatory. Presence of two $b_{2g}\rightarrow b_{1g}$ bands (II and II’) rather than one is a consequence of different local coordination geometry for two silver(II) cations in the structure of $AgSO_4 \cdot H_2O$.

	$AgSO_4$•H_2O		$AgSO_4$		
Band	Position	Energy	Position	Energy	Assignment
I	1115 nm	1.11 eV	1010 nm	1.23 eV	$a_{1g}\rightarrow b_{1g}$
II	819 nm	1.51 eV	670 nm	1.85 eV	$b_{2g}\rightarrow b_{1g}$
II’	611 nm	2.03 eV			$b_{2g}\rightarrow b_{1g}$
III	521 nm	2.38 eV			$e_g\rightarrow b_{1g}$
III’			553 nm	2.24 eV	$e'_g\rightarrow b_{1g}$
III’’			467 nm	2.66 eV	$e''_g\rightarrow b_{1g}$
CT1’	427 nm	2.9 eV			CT $O_{ax}\rightarrow A_g$
CT2’	385 nm	3.22 eV			CT $O_{ax}\rightarrow A_g$
CT1			257 nm	4.82 eV	CT $O_{eq}\rightarrow$Ag(II)
CT2			233 nm	5.32 eV	CT $O_{eq}\rightarrow$Ag(II)
CT3			217 nm	5.72 eV	CT $O_{eq}\rightarrow$Ag(II)
CT4			209 nm	5.92 eV	CT $O_{eq}\rightarrow$Ag(II)

Tab. 13 - comparison of UV-vis-NR bands between neat $AgSO_4$ and its monohydrate, and their assignment

Tab. 13 contains positions, energies and assignments of all bands found in the FT-UV-vis-NIR spectra of $AgSO_4$ and $AgSO_4 \cdot H_2O$.

Energy level splitting [cm^{-1}]		
	$AgSO_4$	$AgSO_4 \cdot H_2O$
δ_1	2475	2238
δ_2	1606	941 – 2339; aver. 1640
δ_3	1665	NA
Δ	13197	13779 – 12381; aver. 13080

Tab. 14 - comparison of splitting parameters between monohydrate and neat $AgSO_4$.

Tab. 14 contains the different splitting parameters calculated for $AgSO_4$ and $AgSO_4 \cdot H_2O$. The δ_1 splitting parameter is higher by 237 cm^{-1} (ca. 10%) than for the anhydrous sulfate. The δ_2 splitting parameters are quite different for the two compounds – because of the difference in coordination geometry of two silver(II) cations in the structure of $AgSO_4 \cdot H_2O$ mentioned before. However, an average value of δ_2 is only slightly larger for monohydrate than for the anhydrous form (1640 cm^{-1} *vs.* 1606 cm^{-1}). Because monohydrate does not undergo an additional rhombic distortion, there is no splitting between the e_g levels in its electronic structure. The value of Δ is also different for both compounds, and as in the case of δ_2 we can obtain two different splitting parameters Δ for the monohydrate. The average value of Δ for monohydrate is 117 cm^{-1} (ca. 1%) smaller than for the anhydrous form.

In conclusion of this this section, I have carried out spectroscopic measurements of both anhydrous and monohydrate forms of silver(II) sulfate(VI). The measurements provided both evidence regarding their structure and a description of physicochemical properties important in their further studies [147].

B.2.3 AgF

The silver(I) fluoride is a common product of chemical decomposition of fluoroargentates. As described earlier, this compound does not undergo structural phase transitions in the 2.7-75 GPa pressure range, and retains its bcc cell. Minute quantities of AgF may form during short exposition of divalent silver compounds samples, *e.g.*, M_2AgF_4 or $MAgF_3$, or AgF_2 to atmospheric conditions – for example during loading or transferring the sample from the inert atmosphere. Hence it was studied here as an important reference sample.

Bulk modulus and isothermic derivative of the bulk modulus were derived for all AgF phases (NaCl, CsCl, and anti-NiAs on decompression) in 0–6.5 GPa range in an earlier paper [47]. Studies conducted on AgF_2 samples, containing AgF as a product of decomposition, increased the data range to ~75 GPa, which enabled more precise derivation of B_0 and B_0' for the high-pressure CsCl phase [148]. With rederived B_0 (87.1(2) GPa) and B_0' (5.26(3)) parameters, the equation of state of this high-symmetry phase became usable as a pressure gauge [148].

A sample of commercially available AgF purchased from Sigma Aldrich (≥99.9% purity) was used here in the high-pressure Raman experiment. The diamond culet used in the experiment was 250 μm wide. A rhenium gasket 250 μm thick was preindented along with a speck of ruby (first to ~10 GPa, then to ~20 GPa). A 140 μm wide hole was cut out using

the laser cutter. The sample was loaded under an inert gas atmosphere, using an argon-filled glovebox. After loading the sample space was filled with compressed Ar reaching 180 MPa.

The experimental Raman setup used a 660 nm excitation line. The Rayleigh band was removed by two notch filters. Two sets of diffraction gratings were used (600 l/mm, 1200 l/mm). The pressure was measured using the high-frequency edge of the first-order Raman band of diamond [127]. Additionally, an ambient pressure spectrum was captured for a different sample of AgF.

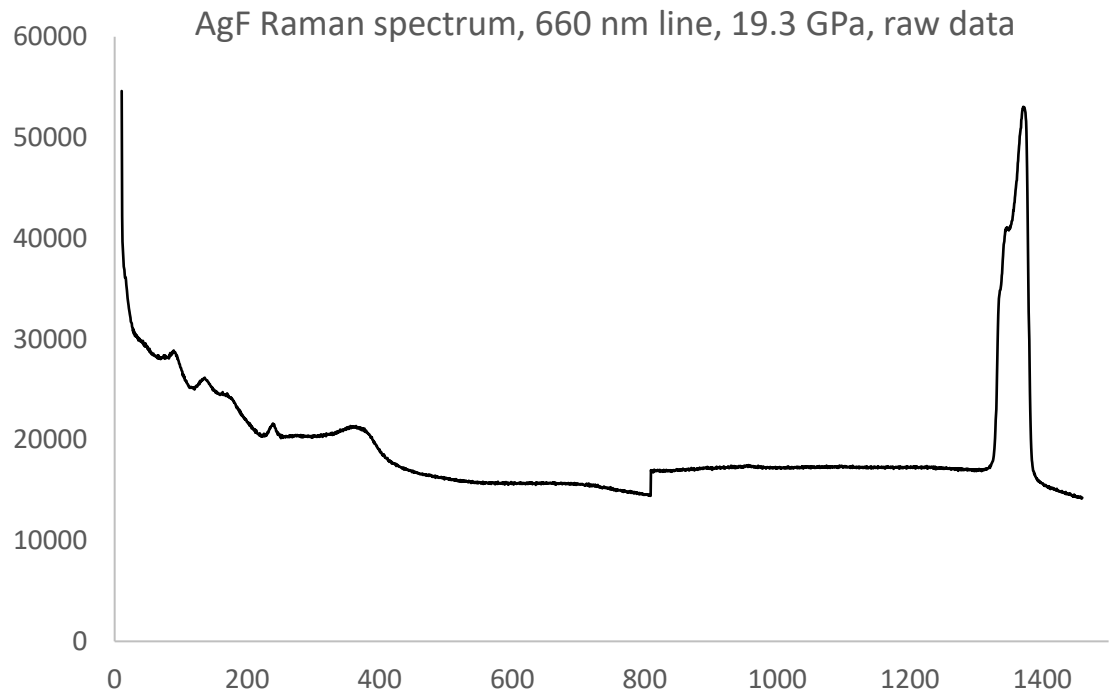

Fig. 76 - a raw (not corrected) AgF Raman spectrum, measured at 19.3 GPa.

Fig. 76 depicts a Raman spectrum of AgF measured at room temperature and at 19.3 GPa inside a diamond anvil cell. The most noticeable properties of this spectrum – an artifactual step in baseline nearby 800 cm^{-1}, small intensity of bands – are also present in the other high-pressure spectra of AgF. Region from 1300 cm^{-1} is mostly dominated by first-order diamond Raman signal. The analysis of the spectra was concentrated on 0-800 cm^{-1} range.

To compare the spectra between the measurements I cut off the baseline (smooth sum of splines) and normalized according to the area of the highest band. In individual cases some additional cleaning was applied. Obtained spectra, which were offset for clarity, can be seen on Fig. 77.

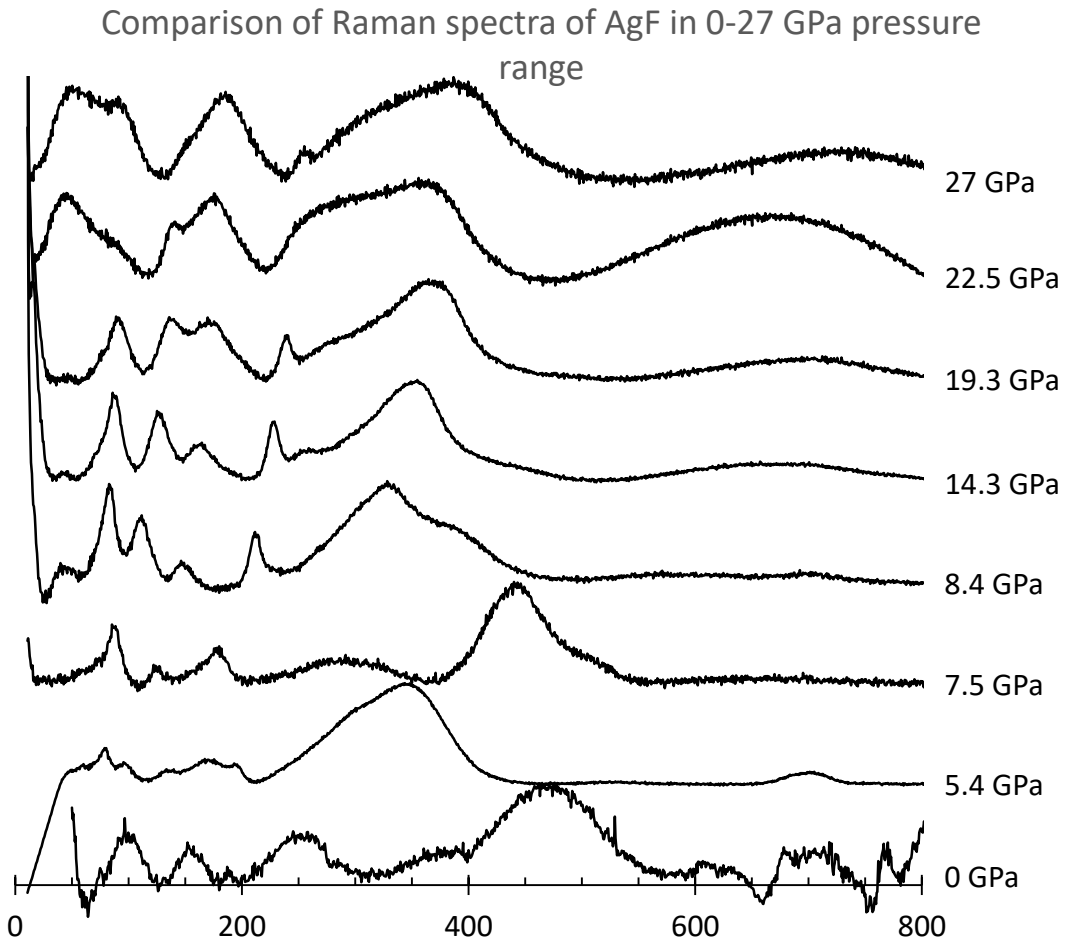

Fig. 77 - Comparison of spectra of AgF in 0-27 GPa pressure range. Note, the NaCl→CsCl-type phase transition occurs at ca. 2 GPa.

As mentioned in an earlier subchapter, AgF Raman spectrum should not contain any first-order Raman bands in both NaCl and CsCl phases (sic!). This seems to contrast with a rather rich spectra obtained in measurements. The reason for that seems to be twofold: first, the sample might be contaminated with products of reaction of gasket with sample. Second, AgF is photochemically sensitive and quite prone towards formation of crystal defects (so called color centers). Their presence in the sample might introduce additional bands. Additionally, intensity of signals is small in comparison with the background level (see Fig. 76). These factors increase the difficulty of interpretation of spectra. Nevertheless, careful deconvolution yielded some information regarding AgF under high pressure.

The deconvolutions presented on the next several pages are presented in following way: black color denotes spectra of AgF after cleaning. Blue color indicates a difference between the experimental spectrum and the constructed model. Pink, cyan, yellow and green indicate bands that have been selected for comparison – because of their presence in nearly all

spectra. Red color denotes other deconvoluted bands. All bands used in the deconvolution were Voigt functions.

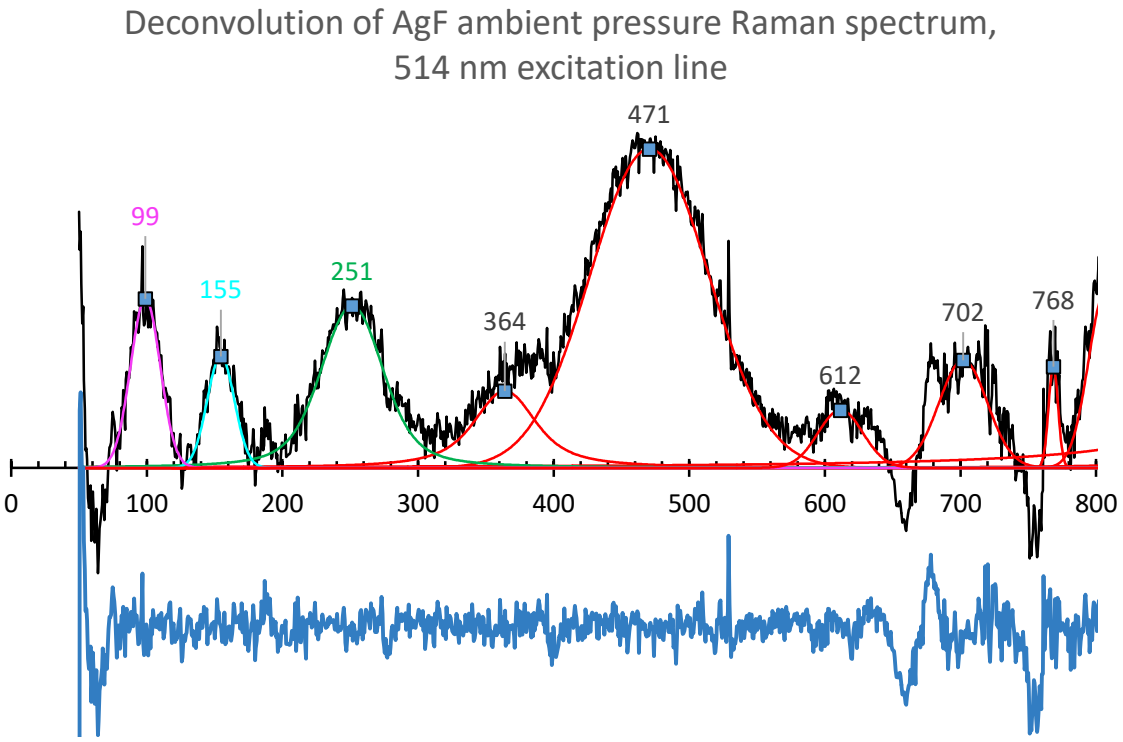

Fig. 78- deconvolution of ambient pressure Raman spectrum of AgF (514 nm excitation line)

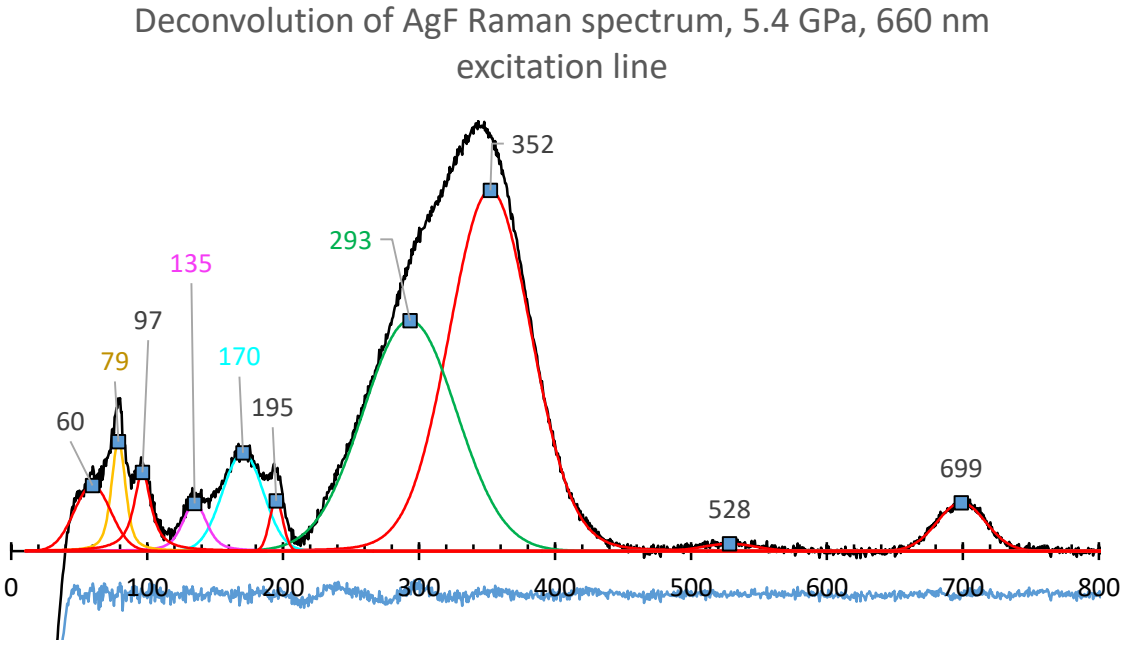

Fig. 79 - deconvolution of Raman spectrum of AgF at 5.4 GPa (660 nm excitation line)

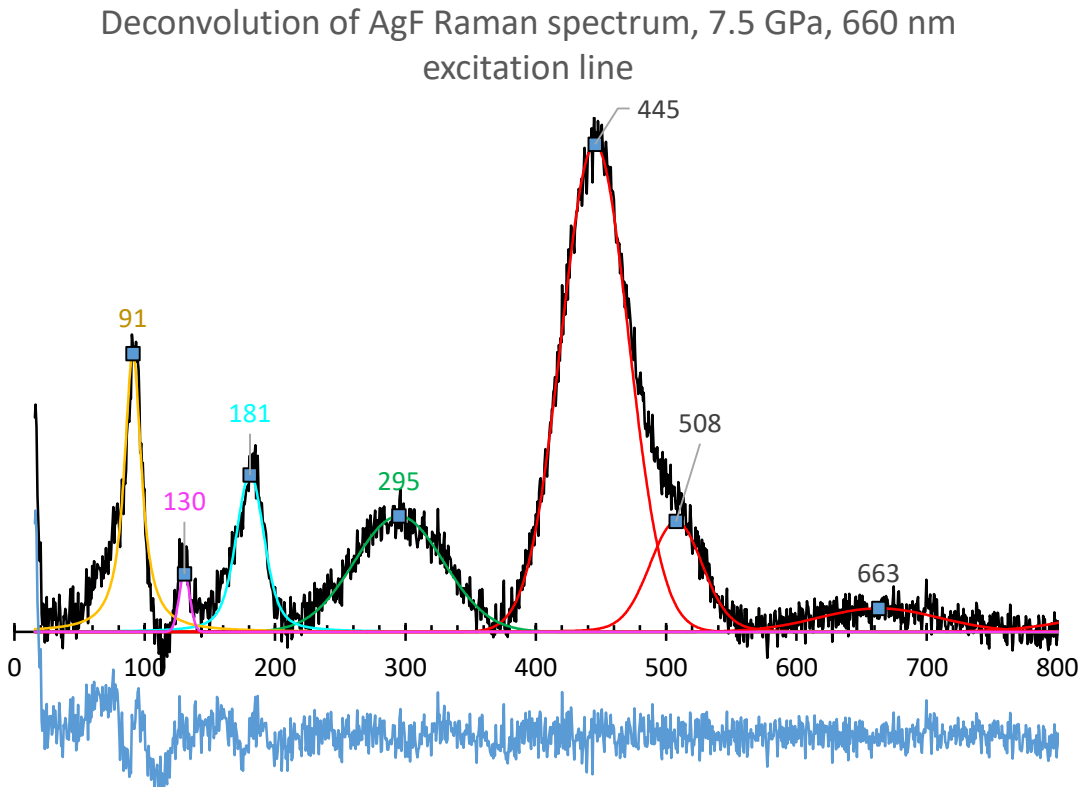

Fig. 80 - deconvolution of Raman spectrum of AgF at 7.5 GPa (660 nm excitation line)

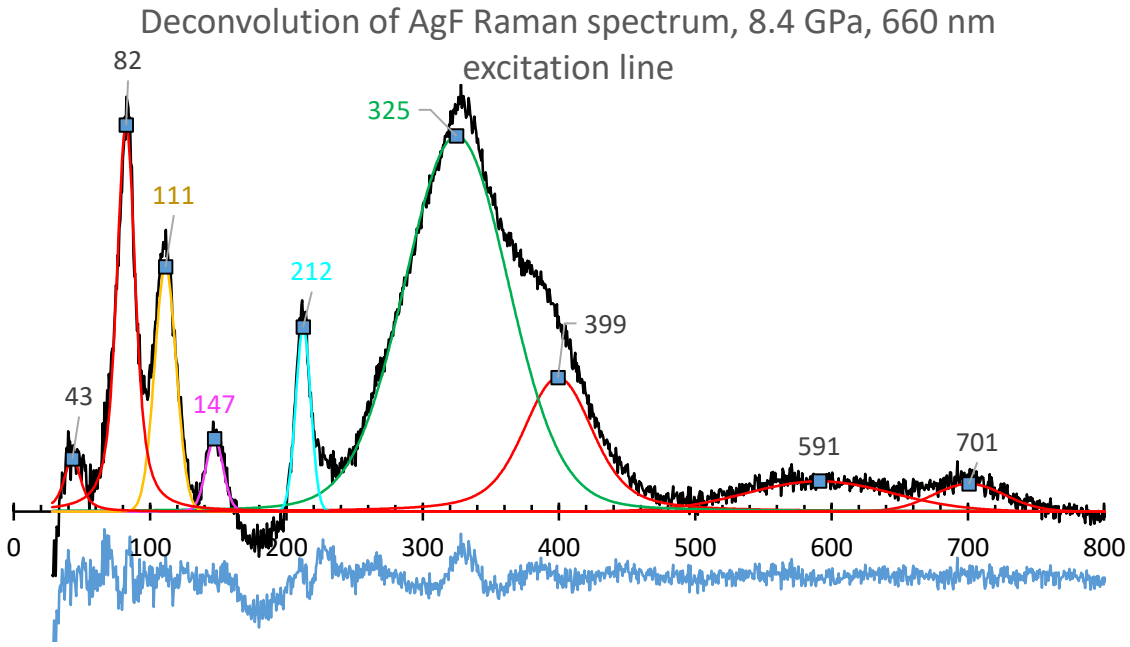

Fig. 81 - deconvolution of Raman spectrum of AgF at 8.4 GPa (660 nm excitation line)

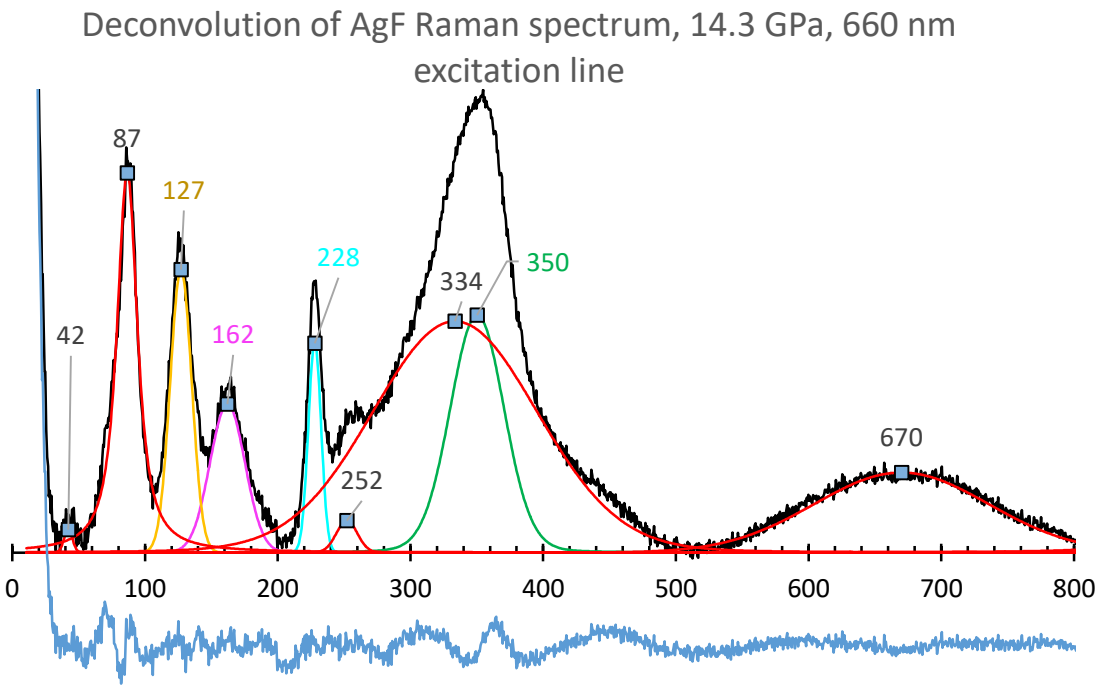

Fig. 82 - deconvolution of Raman spectrum of AgF at 14.3 GPa (660 nm excitation line)

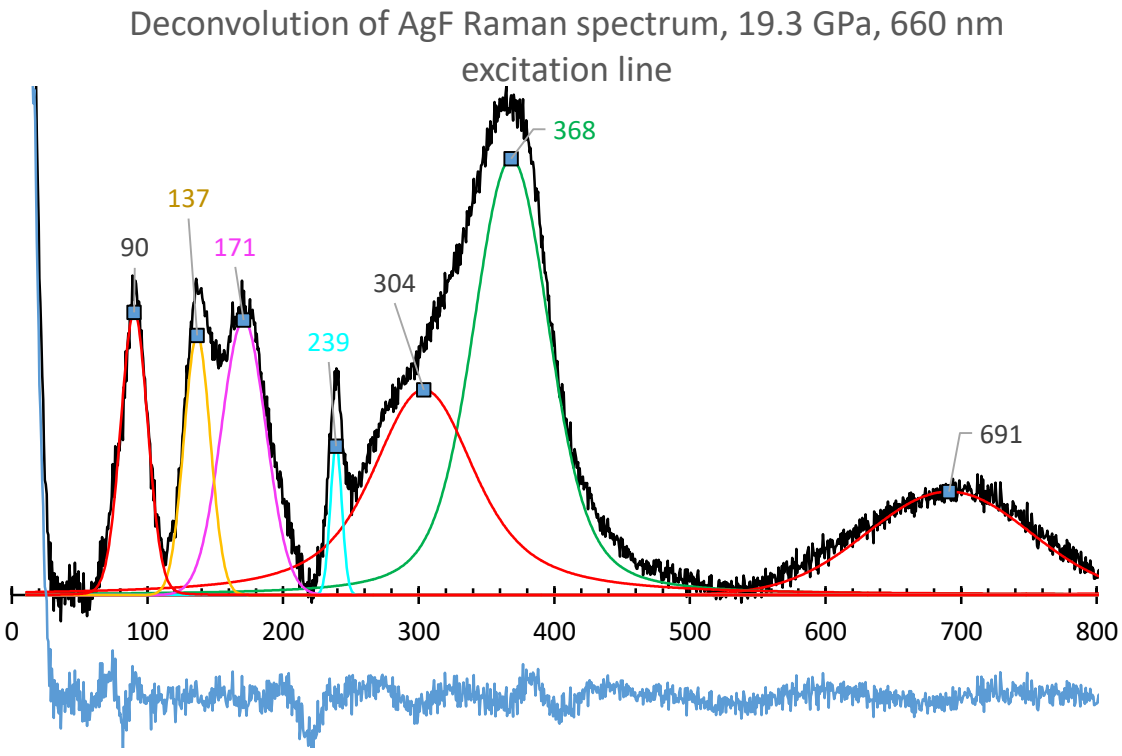

Fig. 83 - deconvolution of Raman spectrum of AgF at 19.3 GPa (660 nm excitation line)

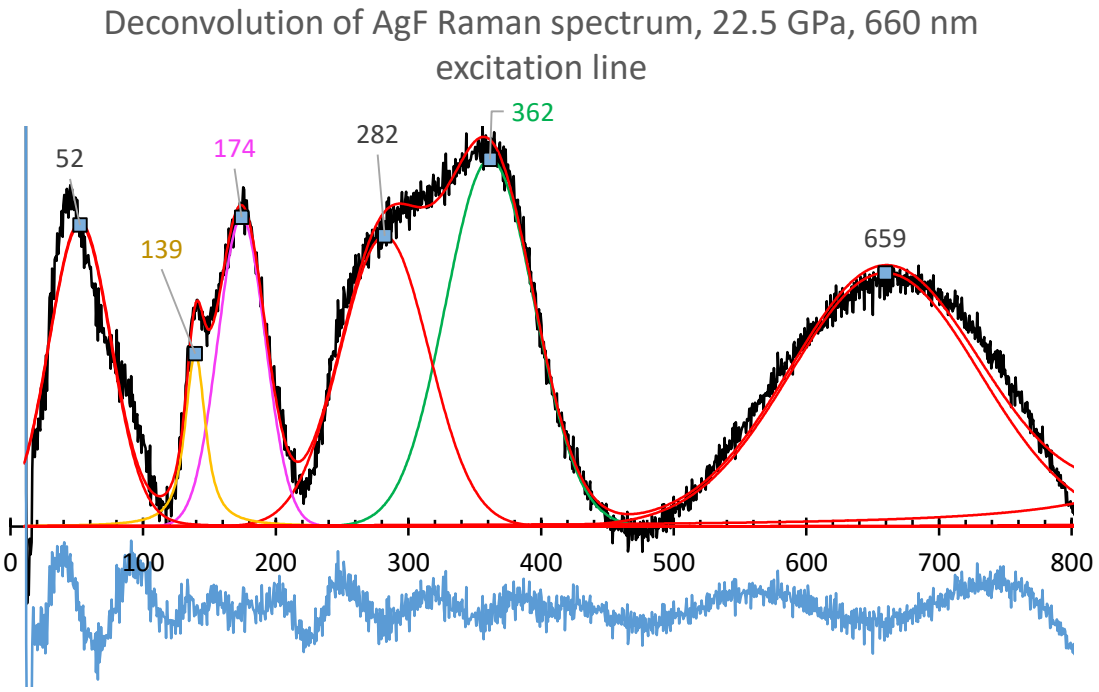

Fig. 84 - deconvolution of Raman spectrum of AgF at 22.5 GPa (660 nm excitation line)

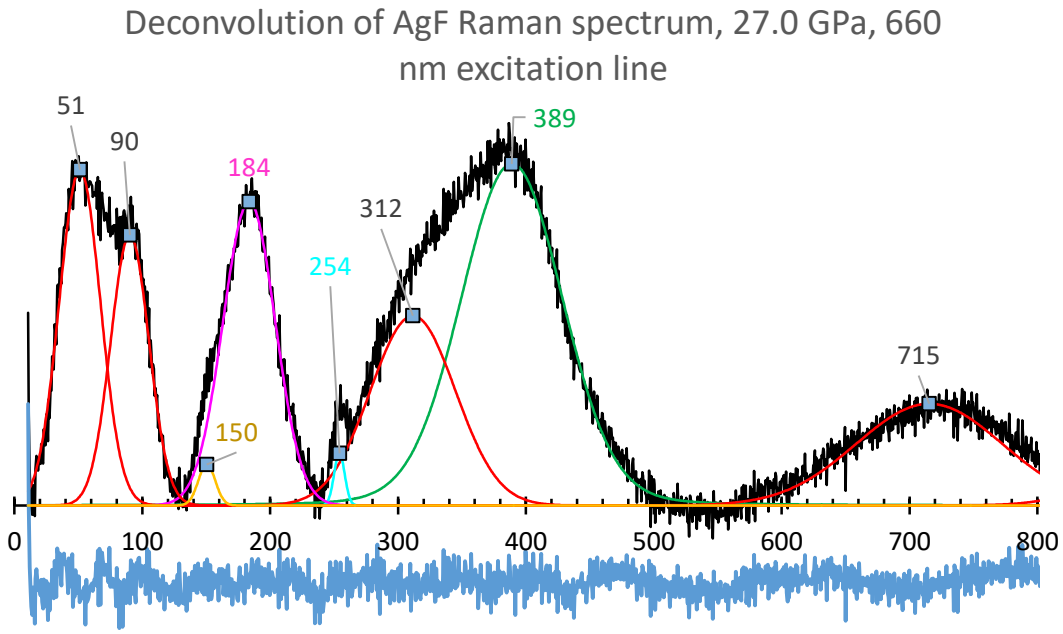

Fig. 85 - deconvolution of Raman spectrum of AgF at 27.0 GPa (660 nm excitation line)

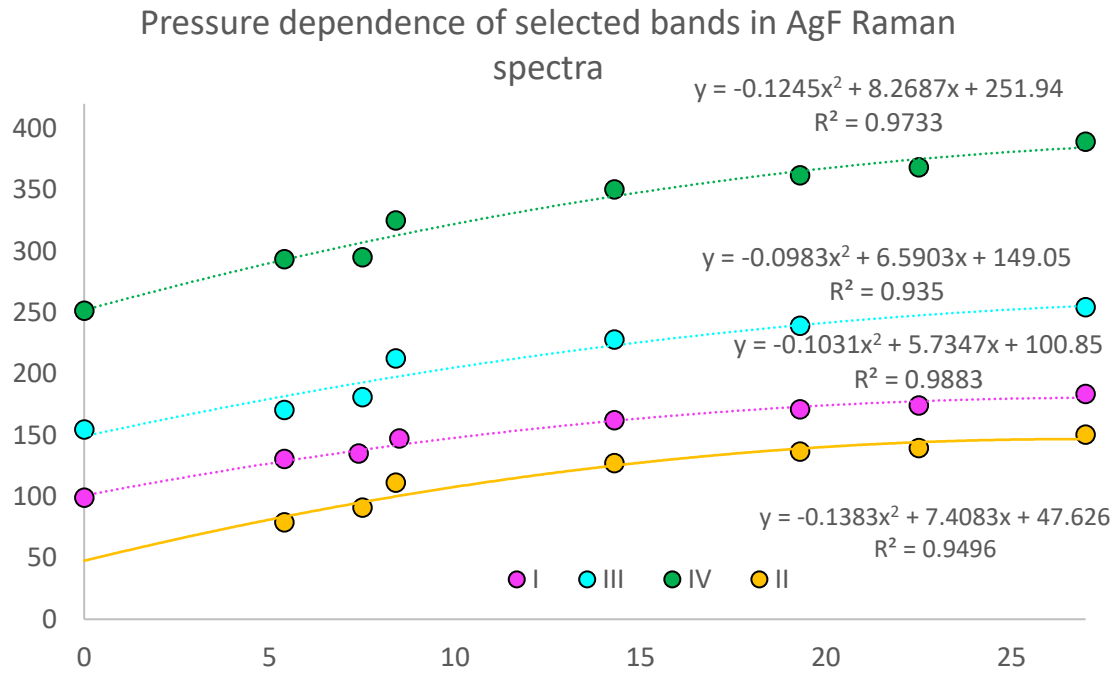

Fig. 86 - pressure dependence of selected bands in Raman spectra of AgF

The pressure dependence of the bands selected for comparison was described using quadratic functions:

$$f_i(x) = a_{0,i}x^2 + a_{1,i}\,x + a_{2,i}$$

The polynomials were used because of their robustness and qualitatively good description of band behavior at low pressure [149]. Both the $a_{0,i}$ and $a_{1,i}$ coefficients are within 1.2 standard deviations from their respective average values, which indicates that bands behave similarly in response to pressure. This suggests that no pressure-induced phase transition is present in the measurement range. Some unusual behavior can be seen at 5.4 GPa and 7.5 GPa measurements – band IV gains a neighbor to lose it again a pressure step later. The reason for that is not clear, and might be caused by a change in measurement spot – at lower pressures the sample and gasket tend to change more in response to pressure than at higher pressures, therefore replicating an exact position in each measurement is harder to achieve.

At ambient pressure three of the analyzed bands (I, III, IV) can be found (and despite the phase transition at *ca.* 2 GPa). Because ambient pressure spectrum was registered for a different sample than the high-pressure set, those bands are possibly genuine bands typical of commercial AgF, and not originate from reaction of gasket material with AgF at elevated pressure. The origin of these bands is currently uncertain (they may stem from color centers or overtone of IR-active T_{1u} fundamental, or an unknown impurity).

Concluding, I have studied silver(I) fluoride under ambient and elevated pressure and observed surprisingly rich Raman spectra of this compound. The proper characterization of AgF spectra at high pressure proved to be very useful in further studies on AgF_2.

B.2.4 AgF_2

Silver(II) fluoride has been studied using Raman spectroscopy as a part of two distinct projects. The first one was done in collaboration with Dr Adam Grzelak and Dr Mariana Derzsi. AgF_2 was studied in the high-pressure regime via XRD powder diffraction, Raman spectroscopy, FTIR spectroscopy, as well as by theoretical DFT+U calculations (*cf.* subsequent subchapters for results and analysis). The project led to (i) full assignment of vibrational spectra of AgF_2 (Table B.2.4.1), (ii) identification of two structural phase transitions occurring at increased pressures, and (iii) serendipitous observation of photochemical sensitivity of AgF_2, which led to formation of a new compound. The new high-pressure polymorphs of AgF_2 exhibited unusual structural features and physicochemical properties which will most likely lead to further future studies.

The second project was conducted in a larger, multinational team. It focused on probing the magnetic properties of AgF_2 under ambient pressure, using Raman scattering and inelastic neutron scattering. Similar studies have been conducted in the past for several metal difluorides [102,150] and other magnetically ordered compounds, especially oxocuprates [92,151,152], although never before for silver(II) fluoride.

B.2.4.1 Position and symmetry assignment of AgF_2 vibrational modes from experiment and theoretical calculations

No.	Exp IR	Exp Raman	DFT+U	HSE06	symmetry	activity	comment
1			27	38	B_{2u}	IR	range not measured
2		57	59	65	A_g	Raman	
3			73	72	A_u	silent	
4	93 w		90	92	B_{1u}	IR	
5	93 w		94	93	B_{3u}	IR	
6			98	101	A_u	silent	
7		109.5	115	118	B_{1g}	Raman	
8		125	132	140	B_{3g}	Raman	
9		138				Raman	73+73 first overtone (A_u * A_u contains A_g)
10	139 sh		134	136	B_{2u}	IR	
11			143	146	B_{1u}	IR	
12	159 w		156	161	B_{2u}	IR	
13			162	170	A_u	silent	
14	168 m		163	175	B_{3u}	IR	
15		168	171	183	B_{2g}	Raman	
16			183	200	A_u	silent	
17	193 m		185	195	B_{1u}	IR	
18	193 m		186	199	B_{2u}	IR	
19		233	227	232	A_g	Raman	
20		244	249	250	B_{3g}	Raman	
21		258	253	257	B_{2g}	Raman	Ag-F stretching => formation of quasi-1D kinked-chain structure (AgF+)(F-)
22		291	296	307	B_{1g}	Raman	
23		312	309	323	A_g	Raman	
24	307 m		310	317	B_{1u}	IR	
25	307 m		312	317	B_{2u}	IR	
26			323	325	A_u	silent	
27		337	329	340	B_{1g}	Raman	
28	341 sh		350	356	B_{3u}	IR	
29		373					193+168 combination (B_{1g}) and/or 193 first overtone
30		416					341+73 combination (B_{3g}) & photochemical product
31			441	478	B_{3g}	Raman	
32	441 vs		441	459	B_{3u}	IR	Ag-F stretching, local deformation of the [AgF_4] square towards the (2+2) bent cis-[F2...AgF_2] unit
33		446	443	481	B_{2g}	Raman	
34			453	468	B_{1u}	IR	
35			455	470	B_{2u}	IR	
36			461	477	A_u	silent	
37		482.5					257+232 combination (B_{2g}) and/or 481 Raman B_{2g} (HSE06)
38	497 sh						441+59 combination (B_{3u}) and/or 470 IR B_{2u} (HSE06)

Tab. 15 - position and symmetry assignment of AgF_2 vibrational modes from experiment and theoretical calculations, published in SI of Gawraczyński et al. [153]

B.2.4.2 High-pressure study of AgF_2

The first project mentioned in the introduction to subchapter B.2.4 aimed to understand high-pressure structural phase transitions occurring in AgF_2. The ambient pressure structure of this fluoride consists of corrugated sheets composed of [AgF_4] vertex sharing squares. As mentioned earlier, the silver(II) cations are antiferromagnetically ordered in layers. According to Goodenough-Kanamori rules, the value of magnetic superexchange constant would be higher if the layers would be flat, as suggested in preliminary DFT calculations by Romiszewski *et al.* [154]. The motivation behind the study was, therefore, to find out whether it would be possible to flatten the [$AgF_{4/2}$] layers by increasing pressure.

4

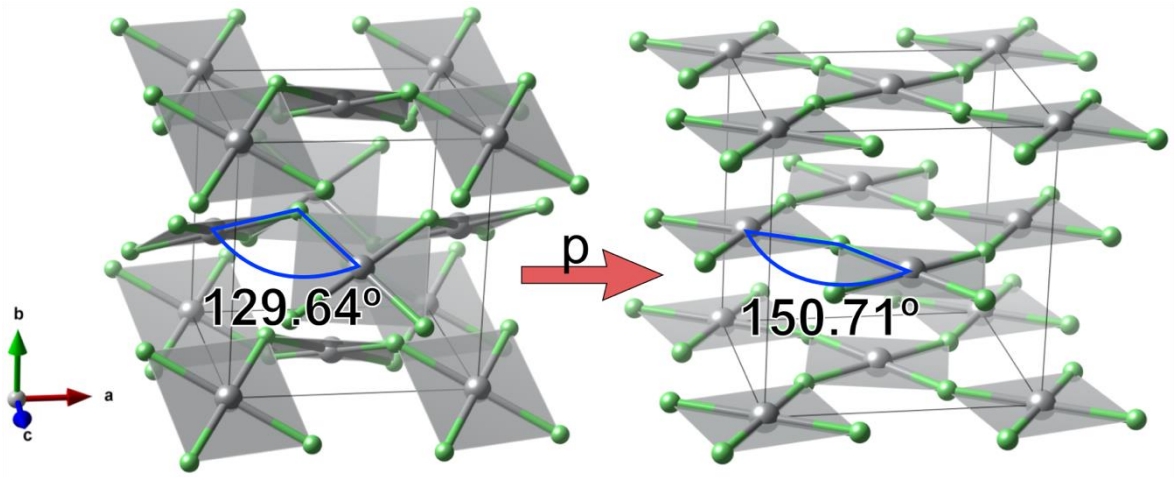

Fig. 87 - a simplified view of theoretical prediction of flattening of the layers in AgF_2 structure with pressure. The phase on the right was first described as δ-AgF_2 in a theoretical paper by Romiszewski et al. [154]

Fig. 87 depicts flattening the corrugated layers in AgF_2. Rotating the [AgF_4] squares would increase the angle Ag-F-Ag between neighboring Ag cations by about 20 degrees. As a consequence, the strength of magnetic superexchange constant would increase dramatically, as it is proportional to squared cosine of angle between the magnetic centers in antiferromagnetic materials. The J constant for flat layers in this picture would be therefore twice the constant for corrugated sheets ($\cos^2(150.71°)/\cos^2(129.64°)\approx 2$). Additional straightening of the Ag-F-Ag angles to 180° would lead to further increase of J.

The first part of the study required collection of structural data on AgF_2 in broad range of pressure. To obtain the needed information, the sample was studied by both Raman spectroscopy (by myself) and XRD diffraction with Dr Adam Grzelak leading the XRD study (with me as an auxiliary investigator). The complete XRD data were described in Dr.

Grzelak's PhD thesis [155], but the outcome of this research must be briefly described here for providing background for understanding of my spectroscopic studies.

Two samples of powder AgF_2 were loaded under an inert gas atmosphere along with a small piece of gold wire to a diamond anvil cell. The rhenium gasket was used to enclose the sample space. High-pressure neon gas was loaded into the cells to serve as a pressure medium and a pressure gauge. The DACs containing the samples were afterwards transported to the Argonne National Laboratory facility and two series of measurements spanning 0–40 GPa range were recorded using the Advanced Photon Source synchrotron. The diffraction patterns were analyzed leading to identification of two low angle reflexes: first appearing between 8.5 and 10.0 GPa and second between 13.7 and 20.6 GPa. Due to high width of reflexes in the diffraction patterns, a conclusive indexing procedure could not be carried out. Appearance of new reflex in previously empty region of diffraction pattern might on the other hand indicate a phase-transition. With that in mind, a first attempt to solve the structure of samples was undertaken. A couple of known high-pressure difluoride and dioxide structures were used as starting models in the Le Bail refinement process, but the results did not provide a full explanation of observed diffraction patterns.

The experiments were supplemented by theoretical calculations conducted by Dr Mariana Derzsi. Hybrid (spin-polarized) DFT calculations were performed for a several points in the 0-40 GPa range using VASP package. 520 eV cut-off and k-spacing of 0.2 $Å^{-1}$ were used in the optimization of structural models. A denser k spacing (0.11 $Å^{-1}$) was used in total energy calculations. In both cases antiferromagnetic interactions of Ag^{2+} cations were taken into account. Lattice dynamics were performed in PHONOPY for supercells of obtained structures, achieving force constants convergence of 0.00001 eV $Å^{-1}$. Details regarding the calculations can be found in paper by Grzelak, Gawraczyński *et al.* [148].

The theoretical calculations delivered some new candidates for high-pressure structures of AgF_2. The procedure required calculating phonon dispersion curves for a range of pressures of α-AgF_2 (the ambient pressure polymorph). For a most stable polymorph at any pressure point the phonon dispersion curves should contain phonons of energy equal or higher than zero in entire Brillouin zone. Presence of negative energy phonon in the calculations indicates a dynamic instability in the structure suggesting an existence of a lower enthalpy polymorph. The more stable structure can be then calculated by following the deformation (normal mode coordinate) corresponding to the imaginary phonon. A lower enthalpy

structure can then be optimized and the procedure continues until a structure with no imaginary phonons is found. The next step requires optimizing geometry, calculating enthalpy and phonon-dispersion curves for the newfound structure at different pressure points. Following this procedure enabled Dr Derzsi to find two candidates for high-pressure polymorphs: HP-I AgF_2 and HP-II AgF_2. The calculated phase transition pressures were consistent with the preliminary analysis of the AgF_2 diffraction patterns.

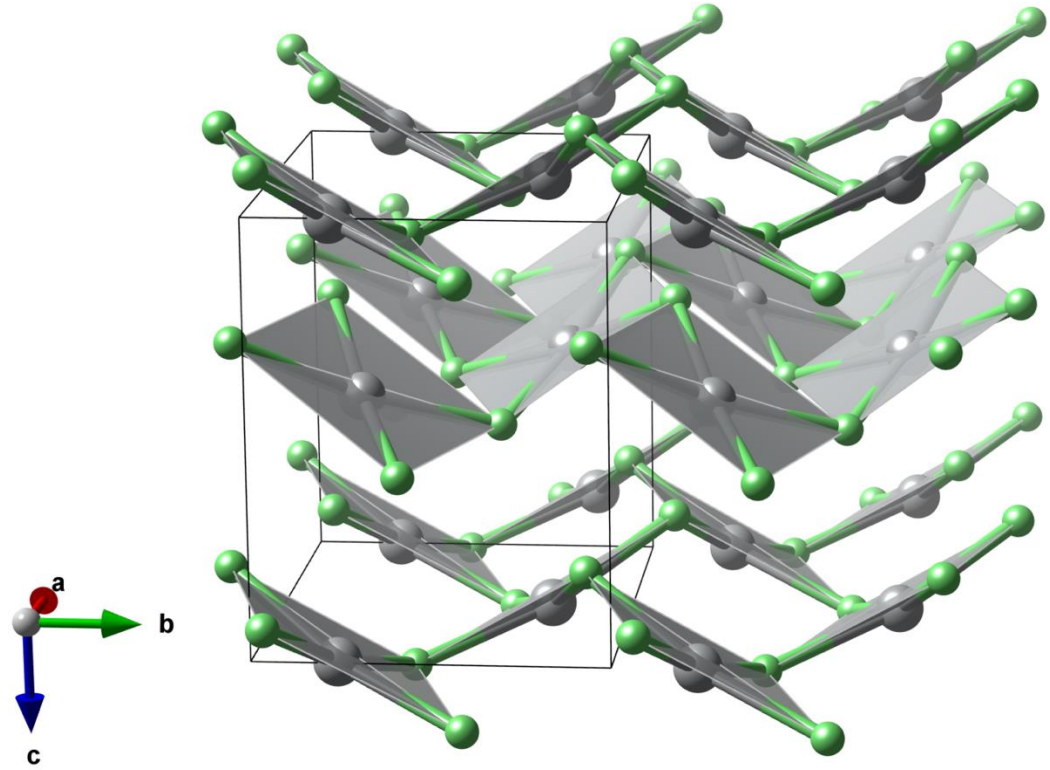

Fig. 88 - a ball-and-stick model of crystal structure of HP-I AgF_2 polymorph at 11.7 GPa.

The HP-I polymorph crystallizes in $P2_1/c$ space group. It differs from the ambient pressure phase because of a higher corrugation of layers, made by rotating [AgF_4] squares. For example, the angle between vertex sharing edges of neighboring squares decreased from 66.9° to 57.6°. The Ag-F-Ag angle between fluorine sharing neighboring cations decreases and splits from 129.6° to 128.4° and 116.8°. Another feature of the HP-I structure is differentiation of the bond length in [AgF_4] squares: at 11.7 GPa it spans four different values from 2.089 Å to 1.999 Å. This causes a loss of inversion center in the squares – therefore they are rather irregular "squares".

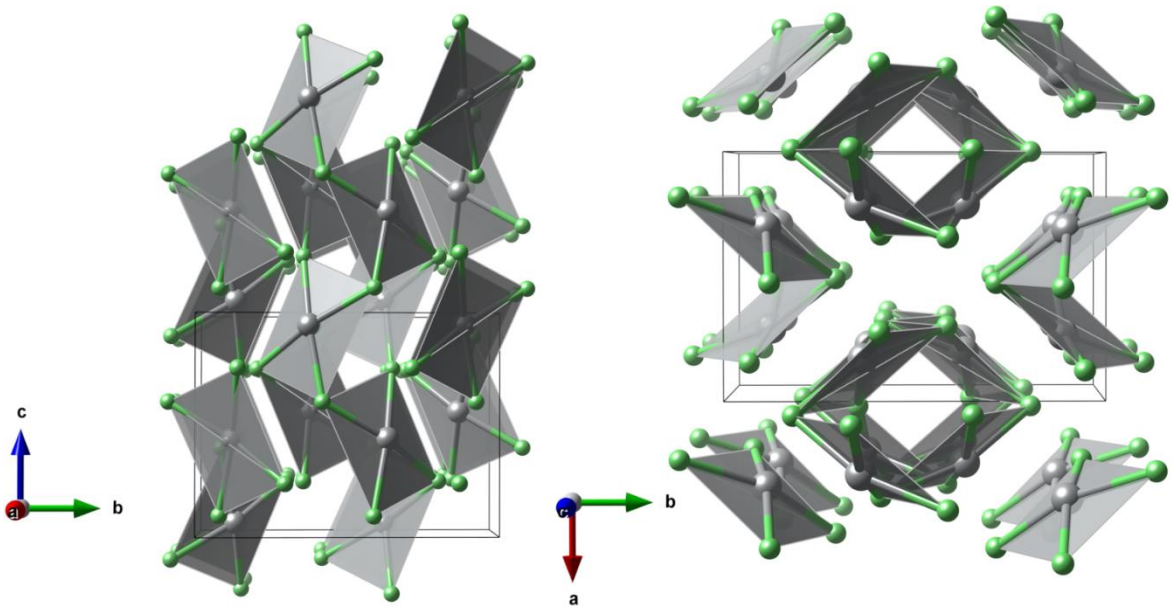

Fig. 89 - two views at a ball-and-stick model of crystal structure of HP-II AgF_2.

The HP-II polymorph crystallizes in *P*bcn space group. The structure consists of wires (or channels) formed by [AgF_4] contracted squares. Size of the channel is insufficient for intercalation of any chemical moiety, even with He atoms.

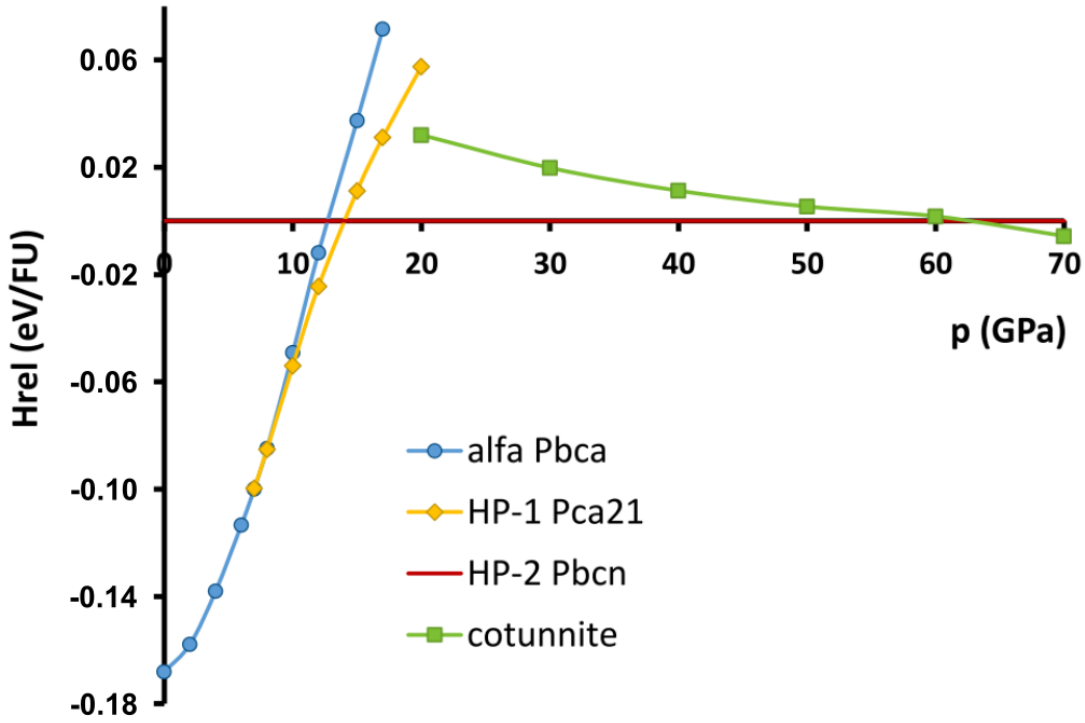

Fig. 90 – a graph of calculated enthalpy per formula unit for several polymorphs of AgF_2 as a function of pressure. Data is presented relative to the enthalpy of HP-II polymorph for a range of pressure between 0 and 70 GPa. Chart cited from paper by Grzelak, Gawraczyński et al. [148]

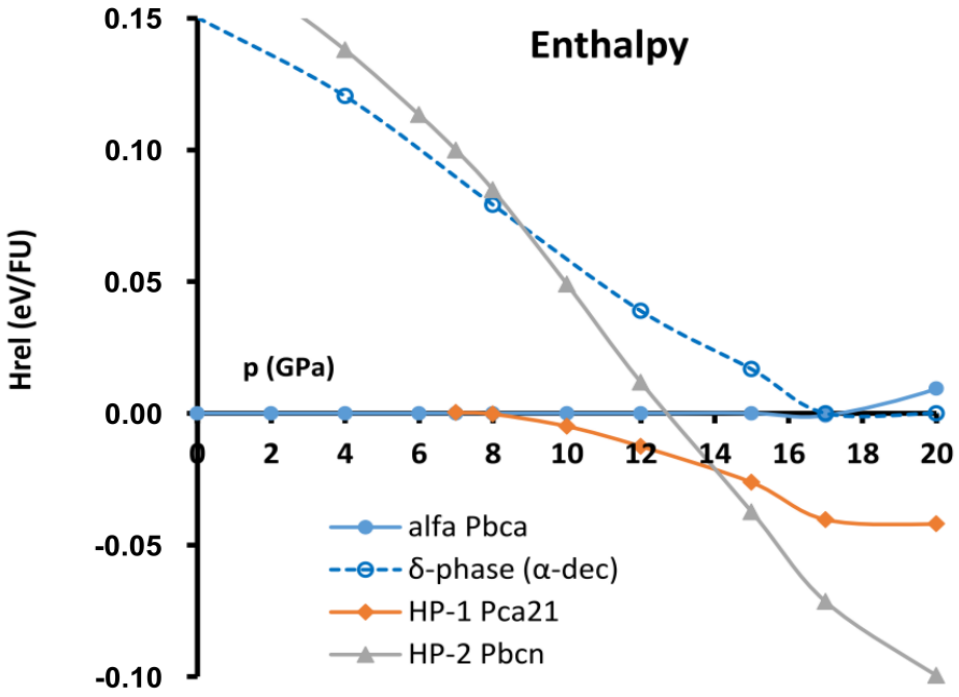

Fig. 91 - a graph of calculated enthalpy per f.u. for several polymorphs of AgF_2 as a function of pressure. Data is presented relative to the enthalpy of α polymorph. The δ-phase is a hypothetical polymorph with flat $[AgF_{4/2}]$ layers. [148]

Results of calculations presented in Fig. 90 and Fig. 91 indicate that AgF_2 under compression undergoes two phase transitions in the 0–60 GPa range: first α-AgF_2 transforms to HP-I phase between 7 and 10 GPa, and then HP-I AgF_2 transforms to HP-II AgF_2 between 12 and 15 GPa.

The Raman measurements were conducted by me in 7–47 GPa and 22–40 GPa ranges. Unfortunately, after the measurements I have found out that the 532 nm laser light used as an excitation line in Raman spectroscopy of studied AgF_2 samples always initiates a decomposition reaction (see subchapters B.2.4.3 and B.2.4.4). I found it impossible to obtain usable Raman spectra of LP, HP-I and HP-II phases of AgF_2 free from decomposition product (this probably comes from the fact that the sample studied inside diamond anvil cell is very small and high intensity of light needed to collect Raman spectrum, inevitably destroys the sample). Therefore, I could not provide supplementary proofs of the said pressure-induced phase transitions. However, the product of photochemical decomposition could be studied together with pressure dependence of its most characteristic Raman bands.

B.2.4.3 Photochemical/thermal decomposition of AgF_2 at ambient pressure

Some Raman measurements of the AgF_2 samples yielded spectra containing a peculiar band at *ca.* 420 cm^{-1}. A similar band is present in spectra of two ambient pressure polymorphs of

K_2AgF_4 (see Tab. 4). Because the band is not present in all measurements of AgF_2, its identity was most likely connected to some unknown impurity. On the other hand, much care was used in handling of the samples, therefore the amount of possible contaminants should be rather small. Additionally, most common compound introduced during improper handling of AgF_2 is AgF, which does not yield a strong Raman signal and – under ambient pressure – does not contain a band at this wavenumber (see Tab. 2 and Fig. 78). This strongly suggested that the source of contamination might not be improper handling of silver(II) fluoride, but rather a factual photochemical/thermal decomposition of the compound during Raman measurements.

The hypothesis was tested by collecting Raman spectra of AgF_2 closed in a sealed quartz capillary at 1 atm. In a glovebox filled with argon, a small portion of silver(II) fluoride powder was packed into a 1 mm diameter crystallographic quartz capillary, filling about 3 cm in length. A small amount of plasticine was used to close off the remaining end of the capillary. The capillary was then removed from a glovebox, and flame-sealed using a butane-oxygen torch. During the process, the flame did not come closer than 1.5 cm to either plasticine or layer of AgF_2. This ensured that fluoride was properly sealed. Quartz capillary can be held at that distance with bare hands during the sealing – the temperature in this area does not increase higher than about body temperature.

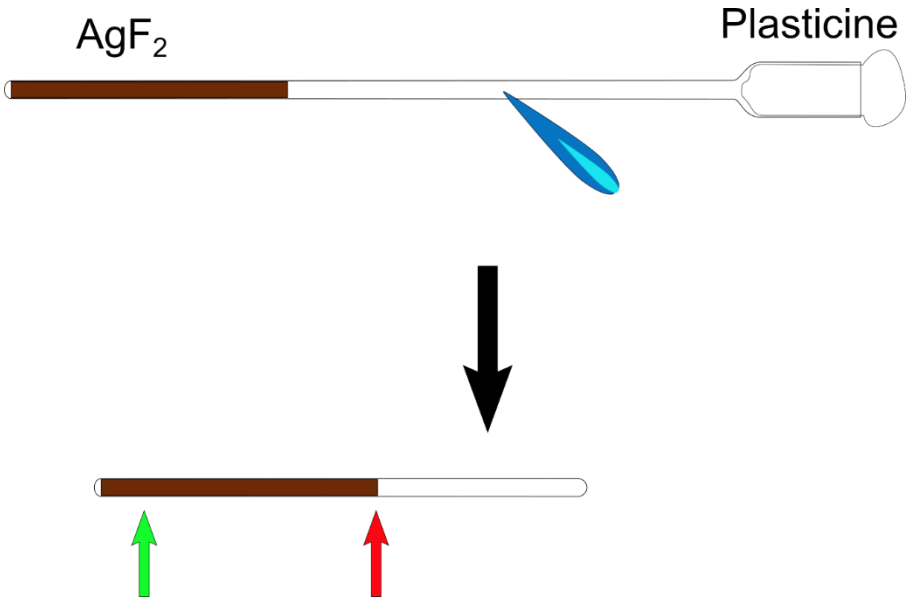

Fig. 92 - a sketch explaining the procedure of flame-sealing the quartz capillaries containing highly reactive samples. A layer of reactive compound is packed into a quartz capillary under an inert atmosphere. Capillary is temporarily closed with a thick layer of plasticine. The flame from a butane-oxygen torch is then used to melt quartz in the part of the capillary free of sample or plasticine. The red arrow indicates a part of the sample that directly "sees" the melted area. The green arrow indicates a portion of the sample from which a Raman spectrum can be collected.

Flame-sealing requires a very hot torch to properly melt quartz in a small area (melting point of quartz is about 1722 °C [3]). Apart from the intense heat, which is mostly localized to the small volume near the flame-capillary contact, the process also produces very bright light which can decompose photosensitive material. To make sure, that at least part of the sample is left in pristine condition after sealing the capillary, it is useful to fill the capillary with a layer of sample that should not be fully penetrated by emitted light (see Fig. 92). Part of the sample far away from the seal should be left untouched by the process.

The sample of AgF_2 closed using the method described above was studied using Raman spectroscopy. A single spot on the sample was illuminated using about 5 mW 514 nm line in four accumulation frames, each lasting 120 seconds. The results confirmed that AgF_2 is indeed sensitive to green light. The ratio of intensities of the bands changed and previously strongest band positioned at 250 cm^{-1} in intensity with increasing illumination time, while a previously weak 420 cm^{-1} band now grew much stronger (see Fig. 93).

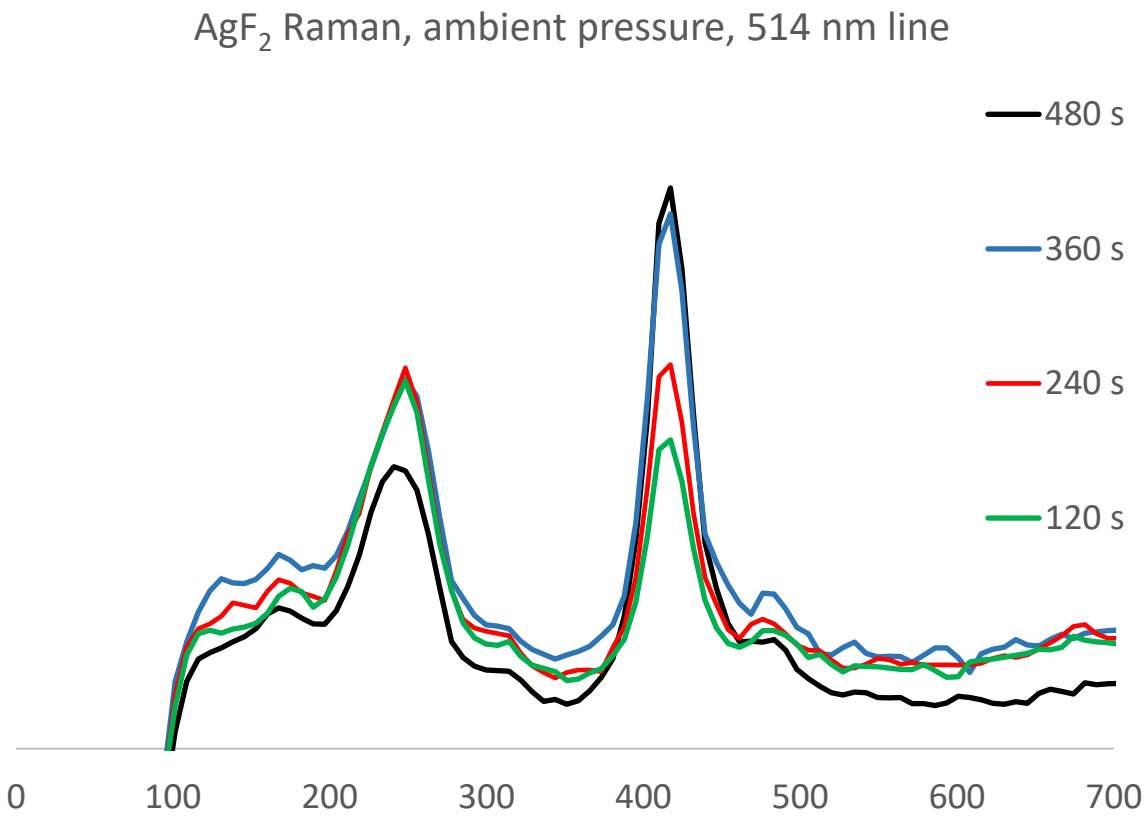

Fig. 93 - set of Raman spectra of AgF_2 under ambient pressure. All measurements were conducted in the same spot on the sample, accumulating signal for 120 s. The cumulative illumination time is presented in the legend.

This change in intensity ratio suggests that AgF_2 undergoes some reaction – possibly photochemical decomposition, as the effect is much less pronounced when using longer

wavelengths for illumination. On the other hand, in two experimental procedures used in measurements – Raman spectroscopy at ambient and high-pressure – there is a problem with dissipating heat from a light source. The sample at ambient pressure has a poor thermal contact with a metal plate under the microscope, because it must be enclosed in a quart capillary. The sample in a DAC has a contact with diamonds, which are known for their excellent heat conduction. On the other hand, its small size means that energy from the excitation line might not dissipate as easily as expected.

The chemical identity of decomposition product is yet unknown. Presence of ~420 cm^{-1} band suggests similarity to other compounds containing [AgF_4^{2-}] moieties – *e.g.* K_2AgF_4 or Na_2AgF_4 [67]. Therefore the unknown product might be a mixed valence fluoride $Ag(I)_2Ag(II)F_4$. Ionic radius of Ag^+ ions is equal 1.15 Å, which is intermediate between those of Na^+ (1.02 Å) and K^+ (1.38 Å) [3]. One could therefore expect formation of similar structure to those exhibited by alkali metal cations. A hypothetical decomposition process leading to synthesis of this product could follow such equations:

$$3AgF_2 \xrightarrow{\Delta T/h\nu} Ag_2AgF_4 + F_2 \uparrow$$

$$3AgF_2 \xrightarrow{\Delta T/h\nu} Ag_2AgF_4 + [2F]$$

where [2F] indicates source of fluorine atoms for fluorination of capillary rather than formation of F_2 molecules. In both cases, fluorine species could react with walls of the quartz capillary. Indeed, after several days of contact with the AgF_2 samples most quartz capillaries lose their transparency even in regions that do not come directly in contact with the AgF_2 (this suggests formation of F_2 gas and supports the hypothesis of photochemical decomposition of AgF_2). Glass etching is most likely an effect of reaction with fluorine (or traces of hydrofluoric acid formed from F_2 and traces of moisture), similar to acid etching process used in production of frosted glass.

B.2.4.4 High-pressure Raman spectroscopy of photochemical/thermal decomposition product of AgF_2

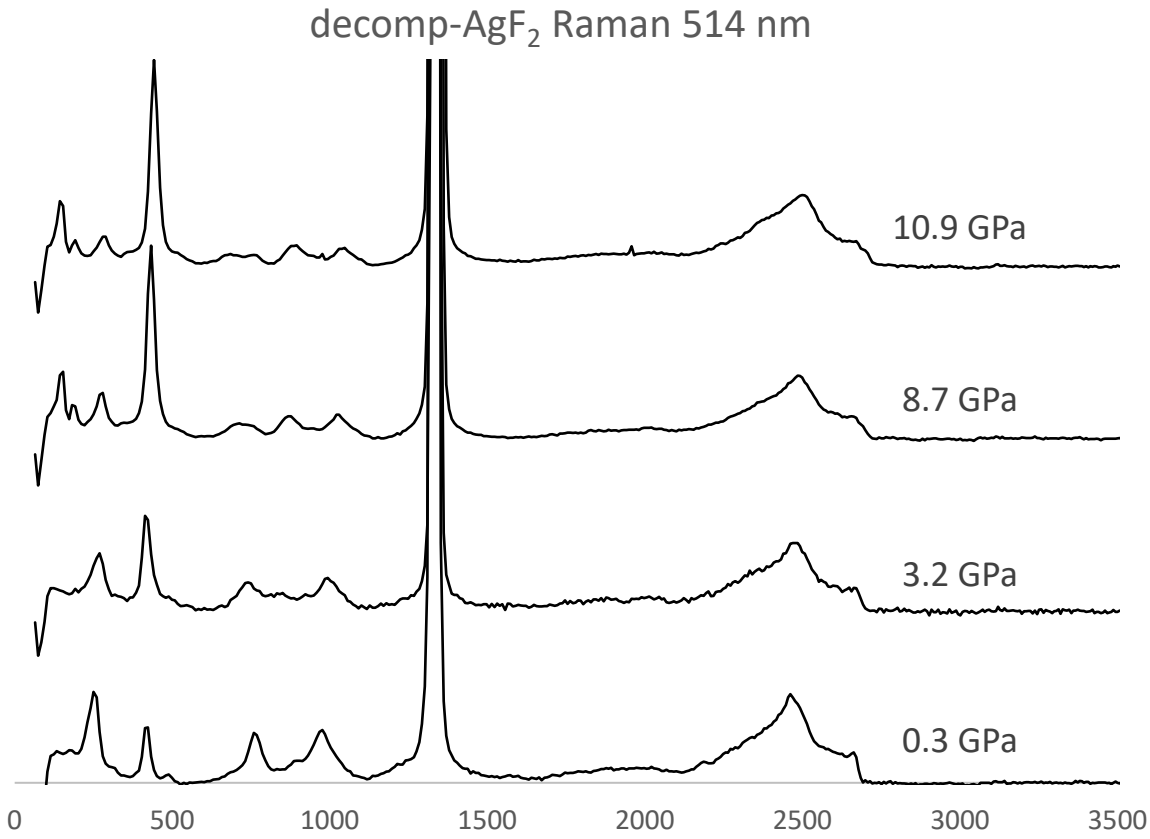

Fig. 94 - Raman spectra for four different pressure points registered for a sample of laser-decomposed AgF_2 (decomp-AgF_2). Backgrounds (four point splines) have been removed.

Fig. 94 depicts Raman spectra of laser-decomposed AgF_2 sample registered at four different pressure points. The sample (AgF_2) was loaded in a 400 μm culet diamond with 300 μm diameter sample space cut out in rhenium gasket. A sliver of ruby was loaded with the sample to serve as a pressure gauge. No pressure medium was loaded.

The very strong band appearing at about 1330 cm^{-1} is the first-order Raman active mode of diamond. Bands at lower wavenumbers belong to the sample. Deconvolution of spectra to sum of Voigt profiles was conducted for the 100-1200 cm^{-1} range. The following graphs − Fig. 95, Fig. 96, Fig. 97, Fig. 98 − contain the best fit for each spectrum. Black curves denote the experimental spectrum, red Voigt functions – deconvoluted bands, dark blue line below the x-axis is a difference curve for each fit.

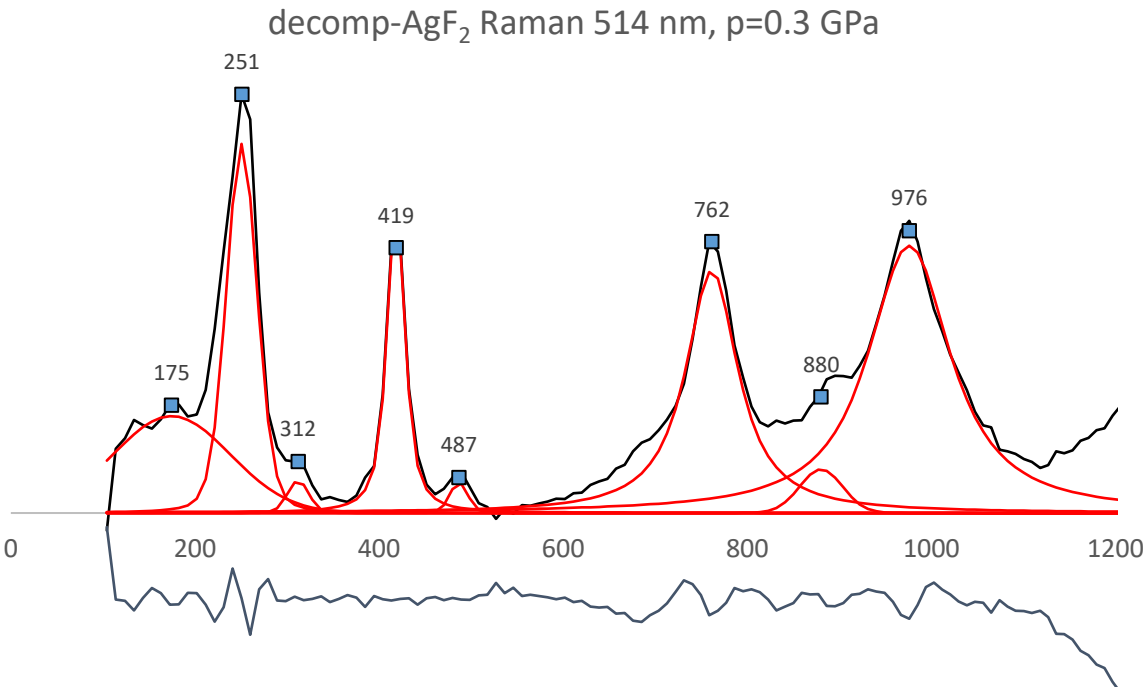

Fig. 95 - deconvolution of decomp-AgF_2 Raman spectrum at 0.3 GPa.

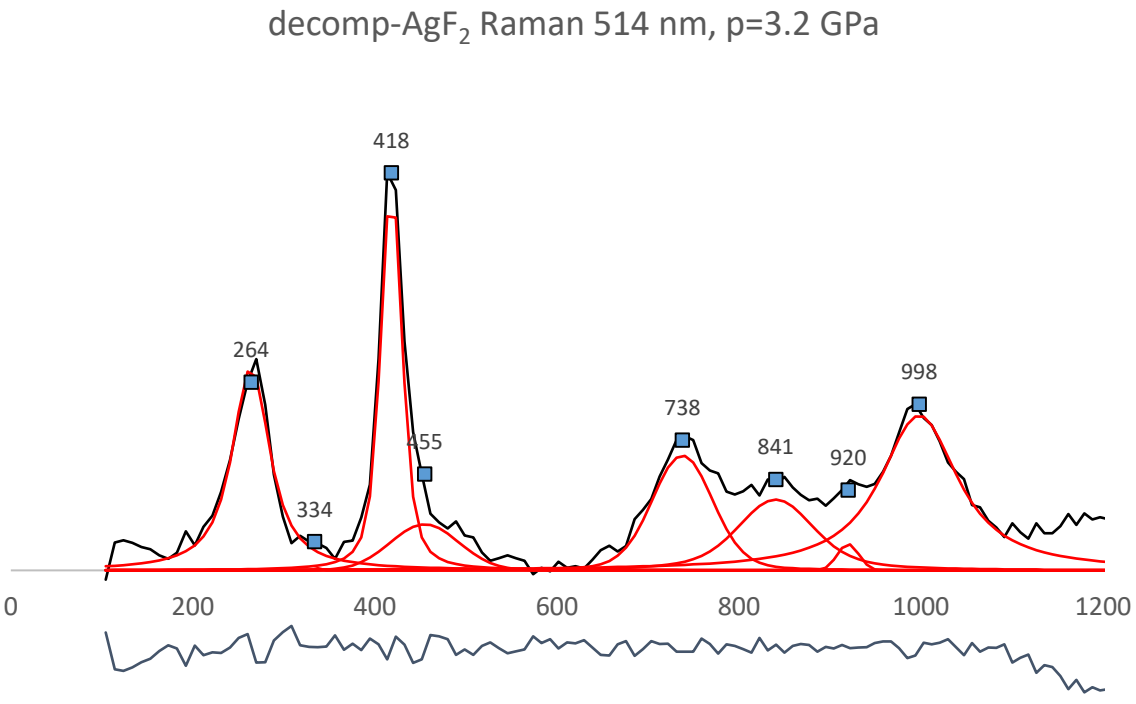

Fig. 96 - deconvolution of decomp-AgF_2 Raman spectrum at 3.2 GPa.

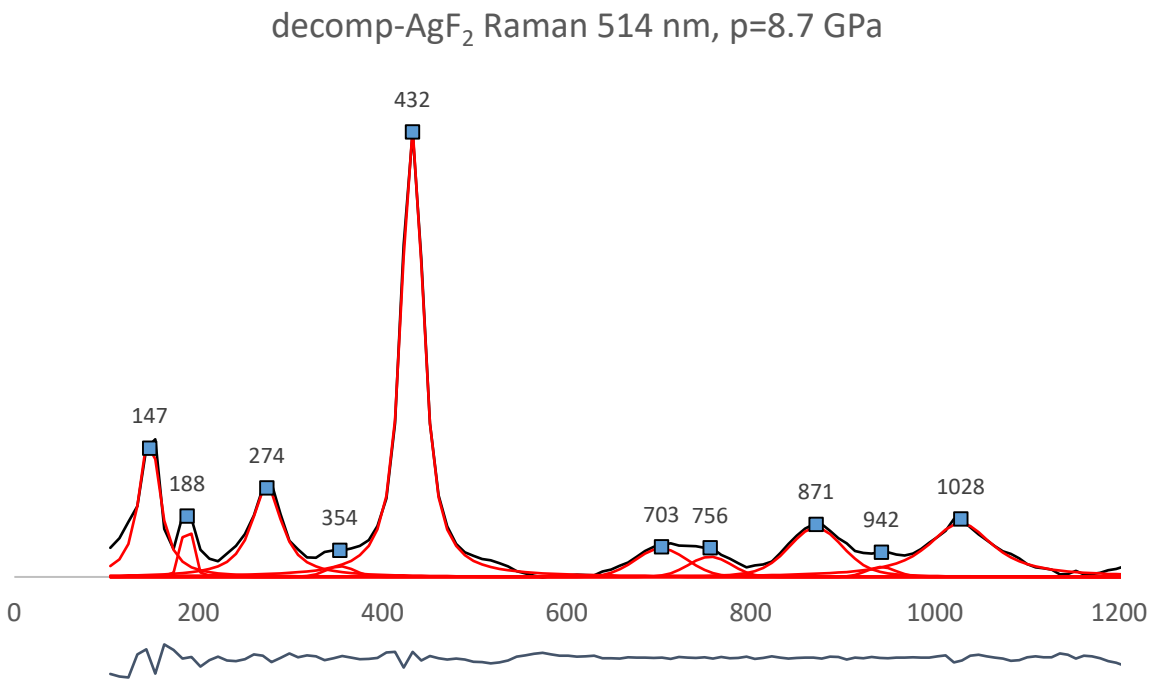

Fig. 97 - deconvolution of decomp-AgF2 Raman spectrum at 8.7 GPa.

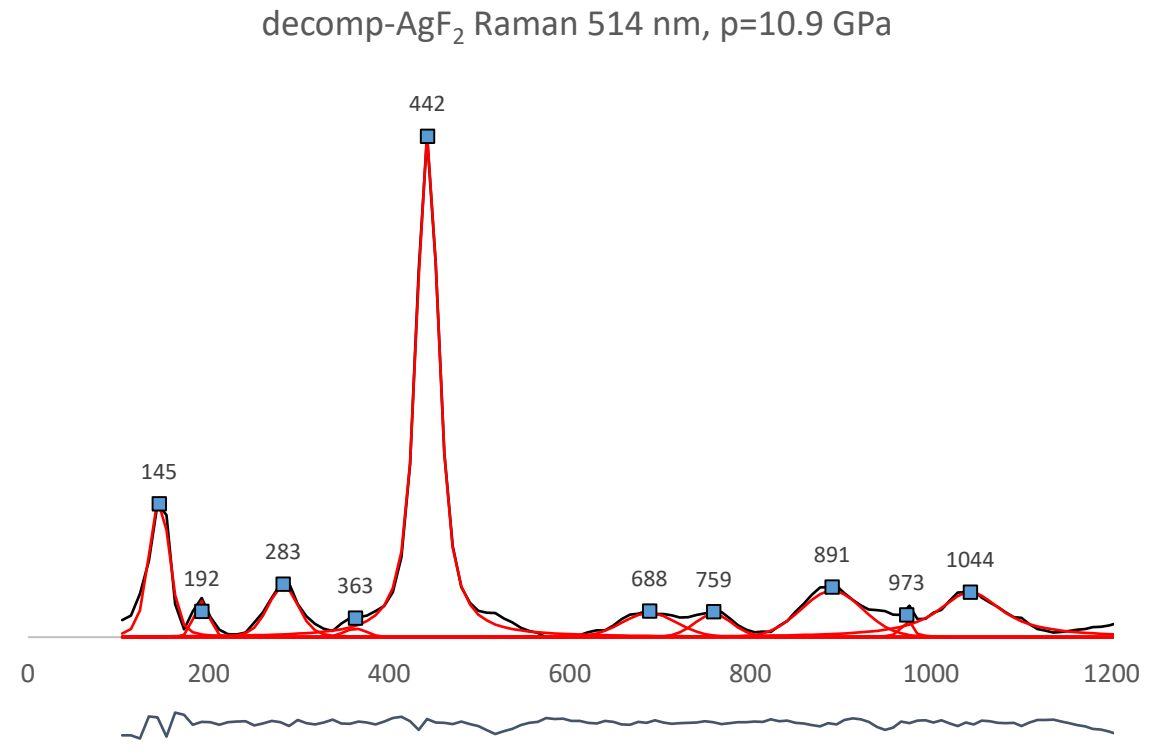

Fig. 98 - deconvolution of decomp-AgF2 Raman spectrum at 10.9 GPa.

Each deconvolution was conducted using a smallest number of functions that could reconstruct the measurement spectrum reasonably well. The method used in the fitting process was Levenberg-Marquardt algorithm implemented in FITYK [156].

Each spectrum in the set can be divided into two regions: below 600 cm^{-1} and over 600 cm^{-1}. The first region contains mostly first-order bands or low lying second-order bands. The second region contains exclusively second and possibly higher order bands. Most striking feature of the first region are bands positioned at about 250 cm^{-1} and 420 cm^{-1}. As expected, with increasing pressure both bands move to higher wavenumbers. Spectra measured at higher pressures also differ in intensity ratio of those two bands, but similar effect was observed for an increase in exposure time (Fig. 93).

Between 3.2 and 8.7 GPa, which is a pressure range in which the α to HP-I phase transition occurs in AgF_2, two new bands appear: 147 cm^{-1} and 188 cm^{-1}. No trace of this pair can be seen at lower pressures. If some amount of AgF_2 is still present in the DAC – which seems likely, considering the volume of sample illuminated with the strongest part of the laser beam should be small – the new bands might be indicative of the HP-I phase of AgF_2 or a high-pressure phase of decomposition product (presumed to be Ag_2AgF_4). A weak band at about 313 cm^{-1} and a stronger band at *ca.* 250 cm^{-1} are present in all spectra from the set, as well as some 0 GPa measurements – this strengthens the hypothesis of some portion of AgF_2 surviving the measurement.

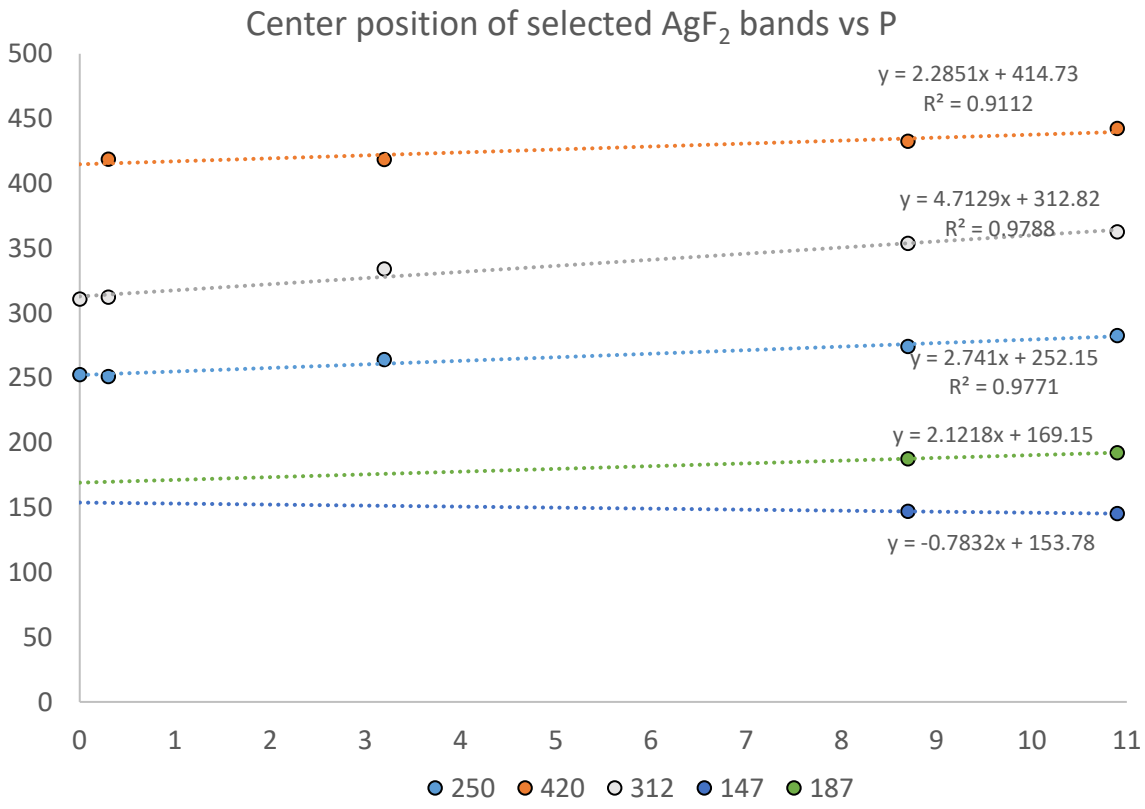

Fig. 99 - the positions of AgF Raman bands in the high pressure, experiment with no pressure medium, 0-500 cm^{-1}

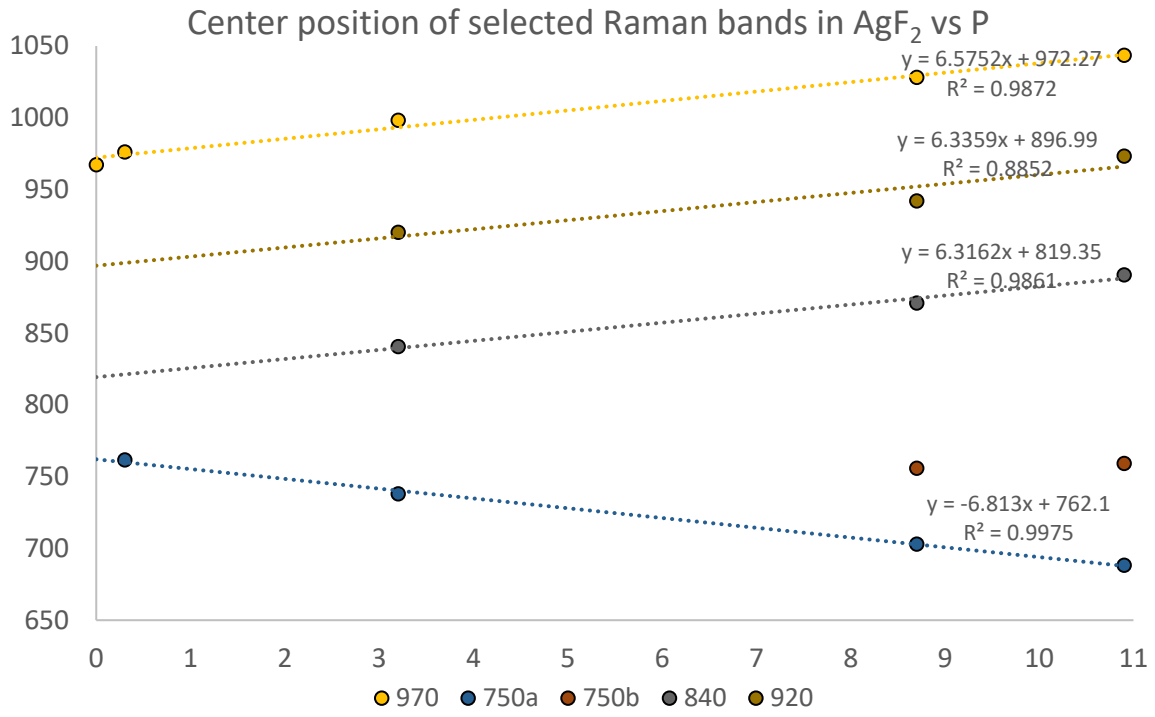

Fig. 100 - the positions of AgF Raman bands in the high pressure, experiment with no pressure medium, 650-1050 cm^{-1}

The bands positioned over 600 cm^{-1} at ambient pressure behave consistently. Bands 970, 920 and 840 cm^{-1} change position with pressure at a rate of roughly 6 cm^{-1}/GPa. Seeing as band at 250 cm^{-1} changes position at about twice slower rate, it seems likely that the 970, 920, and 840 cm^{-1} bands are of second order. The band positioned at 750 cm^{-1} at pressure between 3.2 and 8.7 GPa seems to split into two (750a and 750b in Fig.100), and one of the bands moves to the lower wavenumber with increasing pressure. This might indicate a decrease of local symmetry with some bond alternating length around Ag^{2+} in decomp-AgF_2.

The results obtained from this simple experiment proved to be interesting enough, that I prepared a new sample of AgF_2 for a high-pressure study. Neon gas loaded at about 22 MPa was used as the hydrostatic medium. Diamond band edge method was used to determine the pressure inside the measurement space. Raman spectra of the sample were measured using 660 nm excitation line.

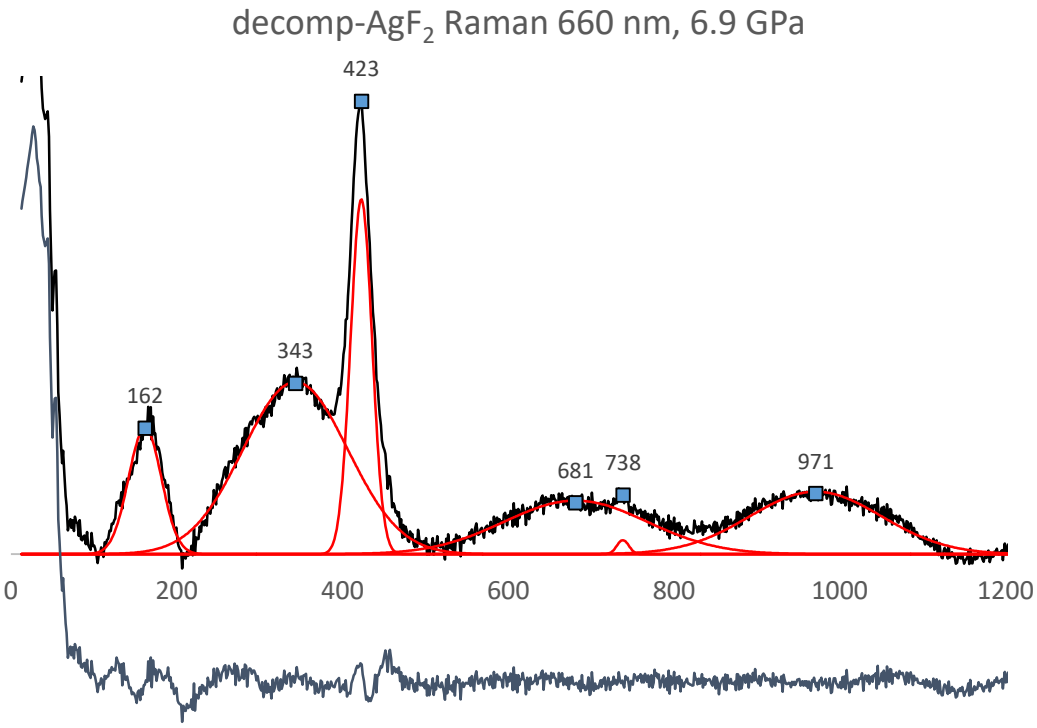

Fig. 101 - Raman spectrum of decomp-AgF_2 measured using 660 nm excitation line, 6.9 GPa.

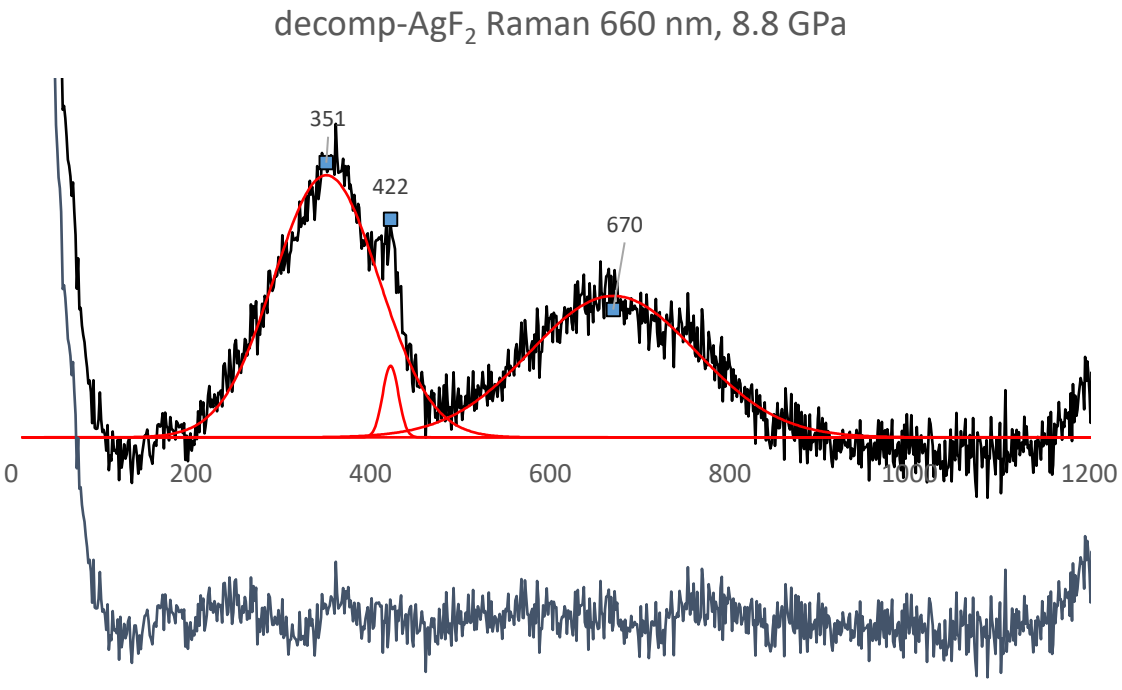

Fig. 102 - Raman spectrum of decomp-AgF_2 measured using 660 nm excitation line, 8.8 GPa.

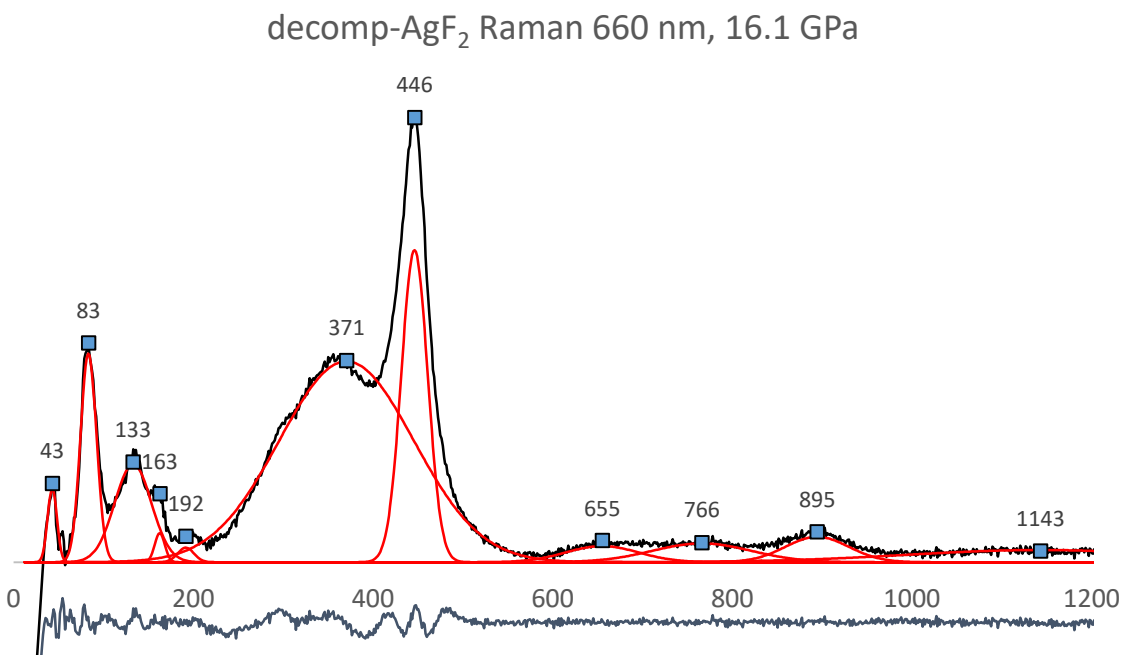

Fig. 103 - Raman spectrum of decomp-AgF_2 measured using 660 nm excitation line, 16.1 GPa.

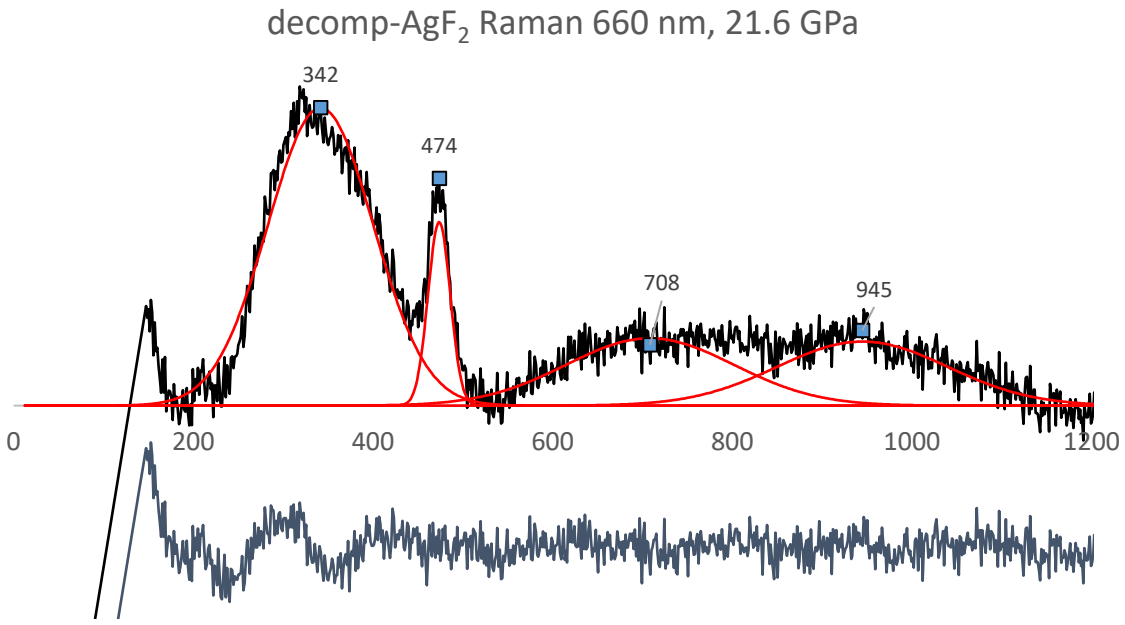

Fig. 104 - Raman spectrum of decomp-AgF_2 measured using 660 nm excitation line, 21.6 GPa.

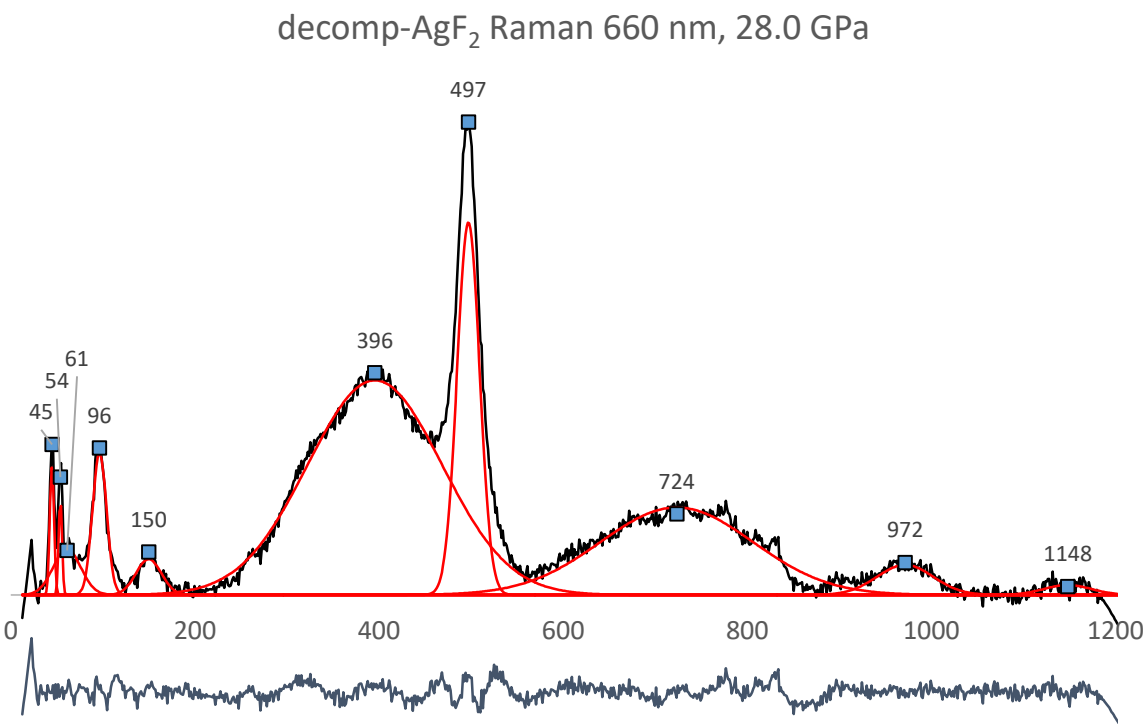

Fig. 105 - Raman spectrum of decomp-AgF2 measured using 660 nm excitation line, 28.0 GPa.

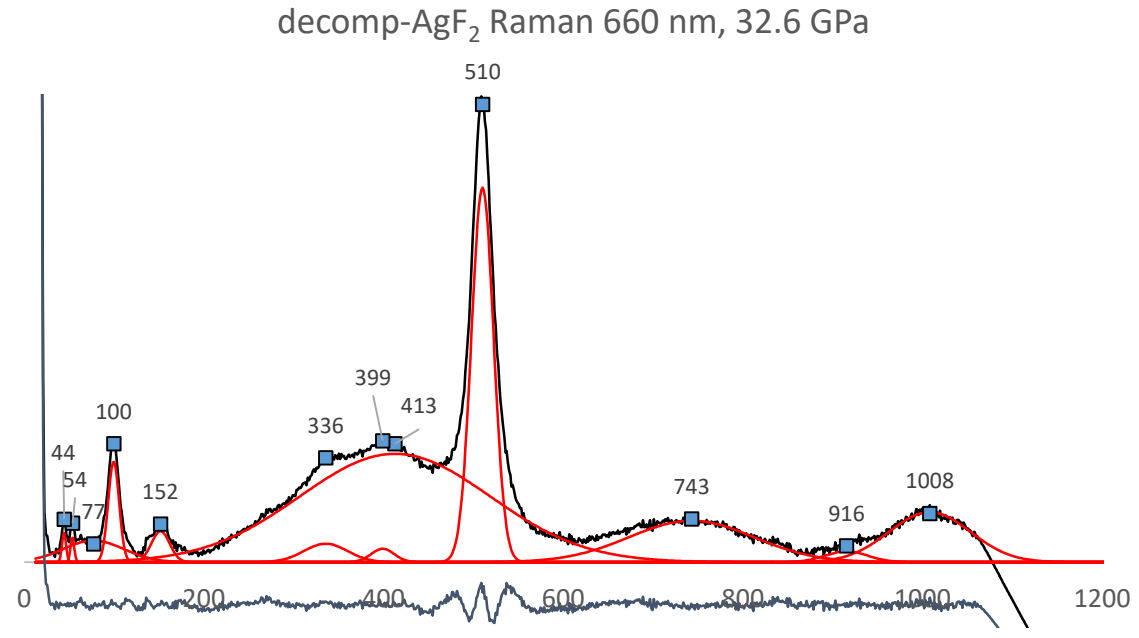

Fig. 106 - Raman spectrum of decomp-AgF2 measured using 660 nm excitation line, 32.6 GPa.

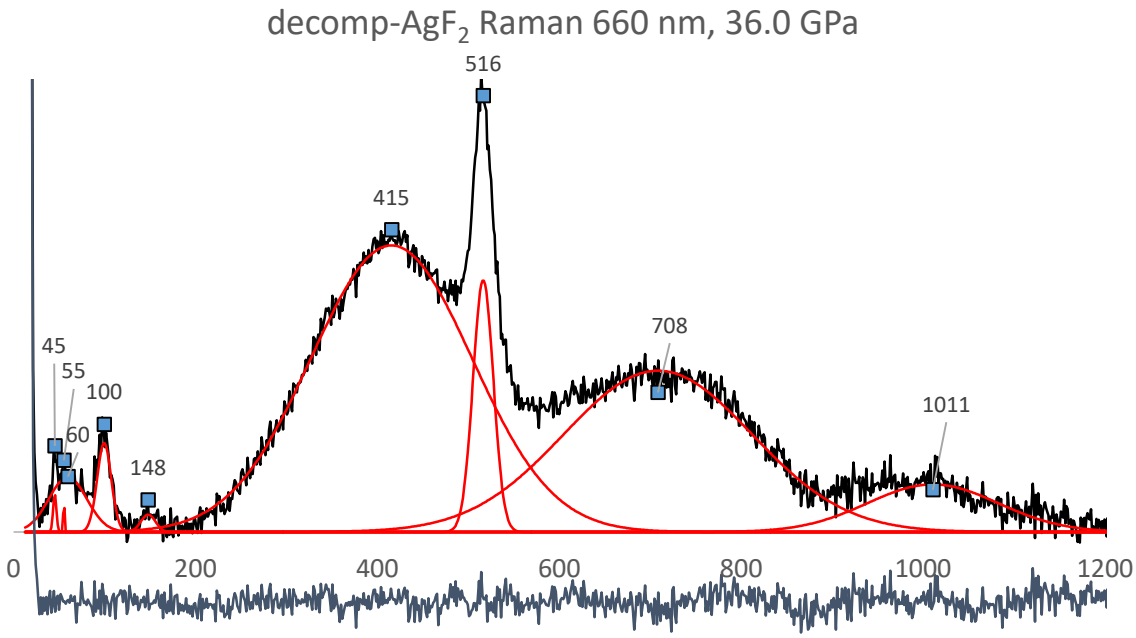

Fig. 107 - Raman spectrum of decomp-AgF2 measured using 660 nm excitation line, 36.0 GPa.

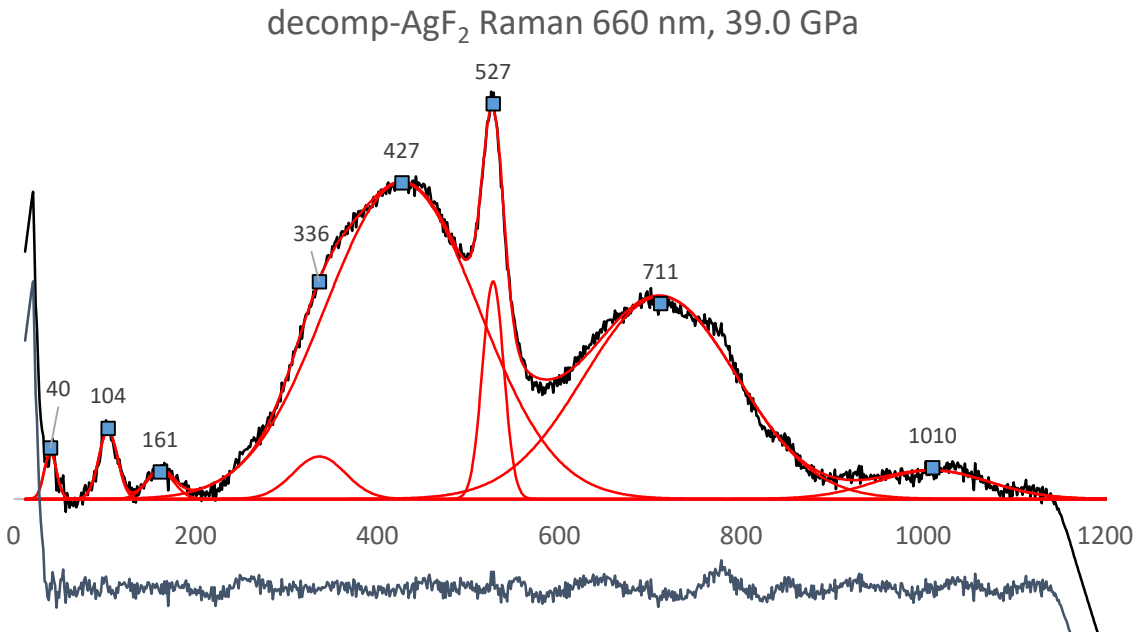

Fig. 108 - Raman spectrum of decomp-AgF2 measured using 660 nm excitation line, 39.0 GPa.

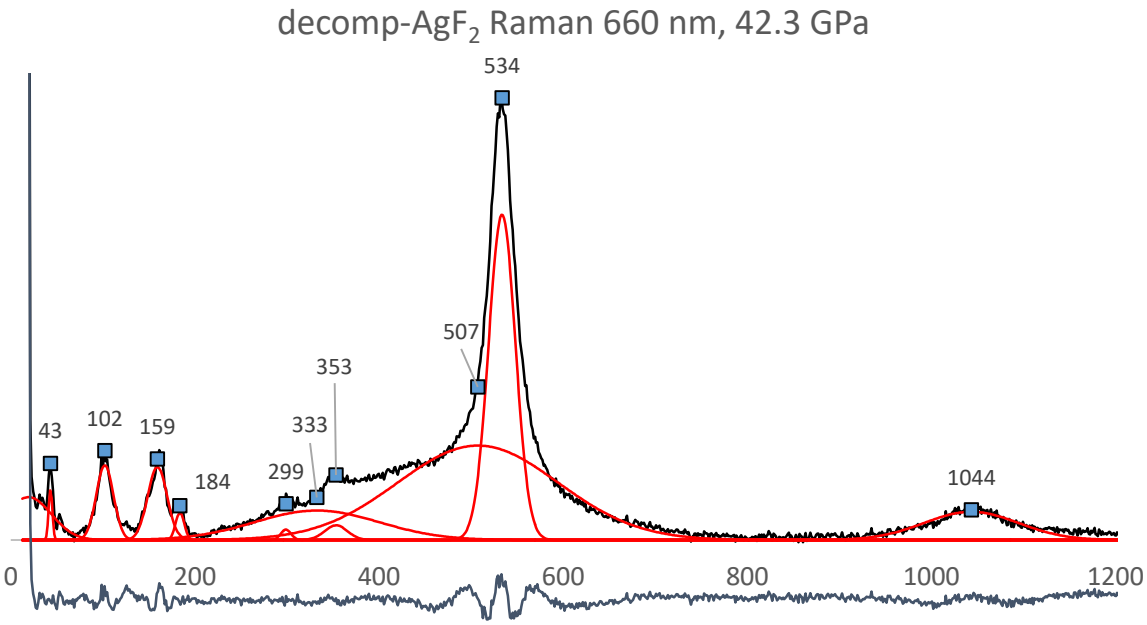

Fig. 109 - Raman spectrum of decomp-AgF_2 measured using 660 nm excitation line, 42.3 GPa.

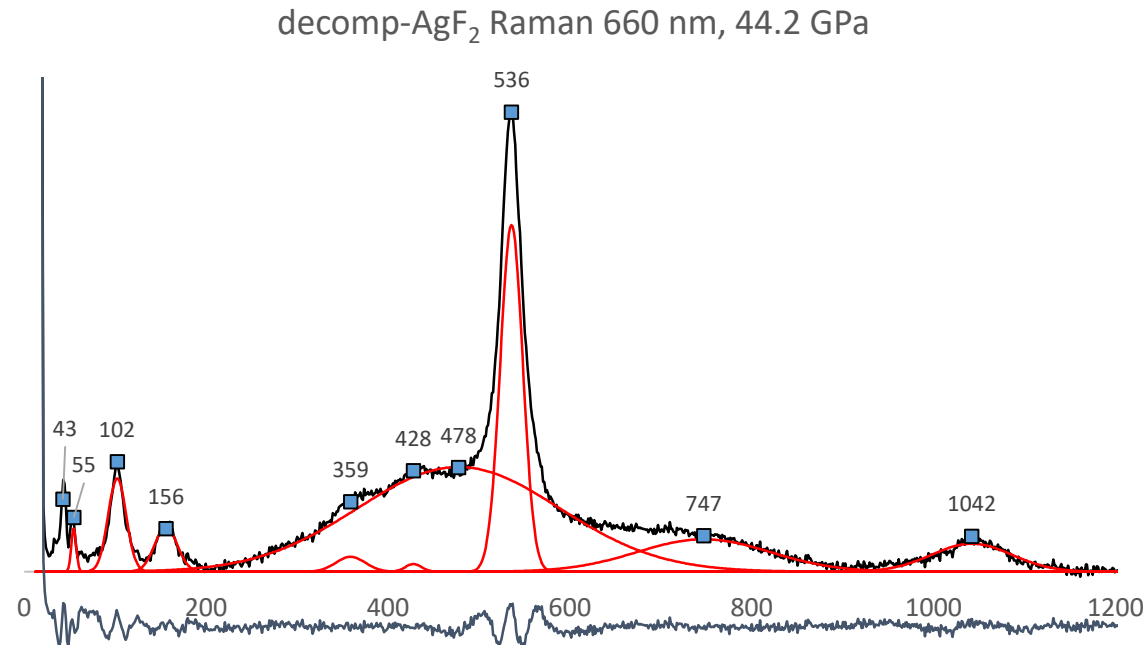

Fig. 110 - Raman spectrum of decomp-AgF_2 measured using 660 nm excitation line, 6.9 GPa.

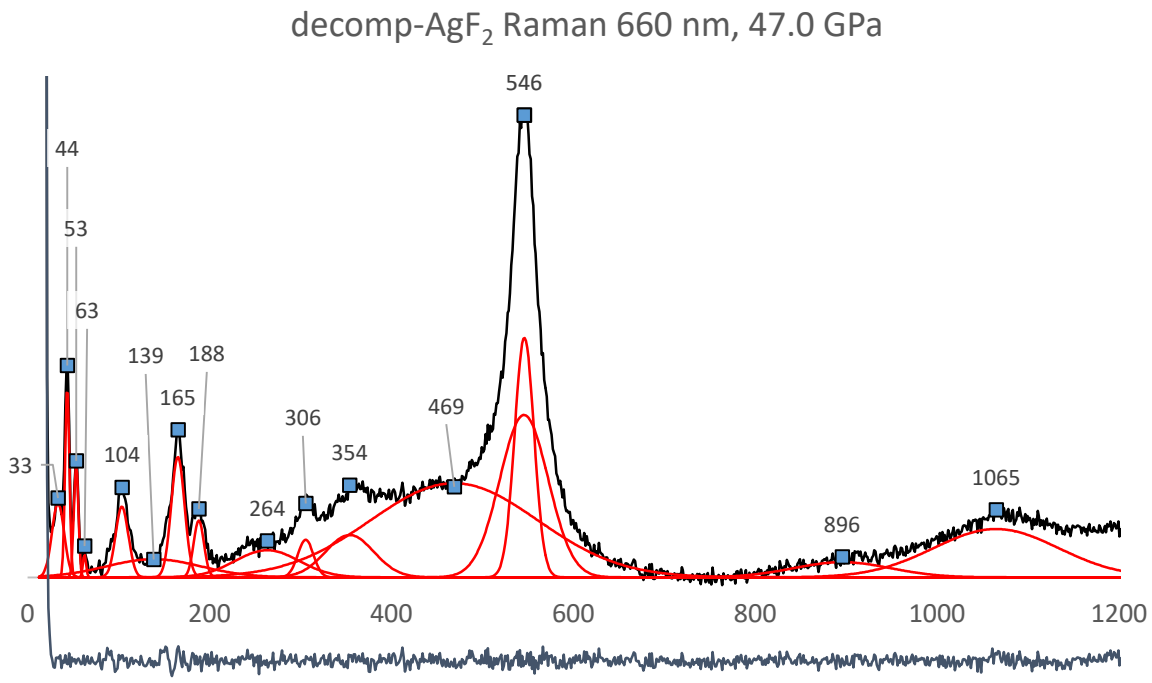

Fig. 111 - Raman spectrum of decomp-AgF_2 measured using 660 nm excitation line, 47.0 GPa.

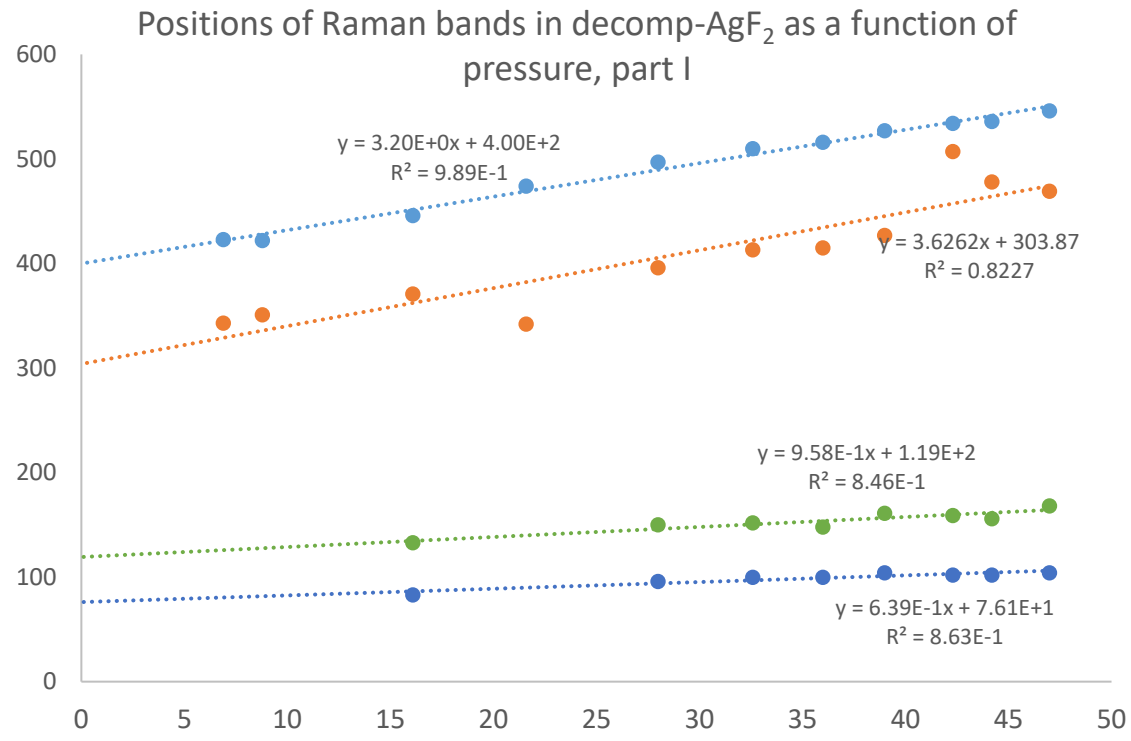

Fig. 112 - positions of bands in the decomp-AgF_2 Raman spectra as a function of pressure, 0-600 cm^{-1} range

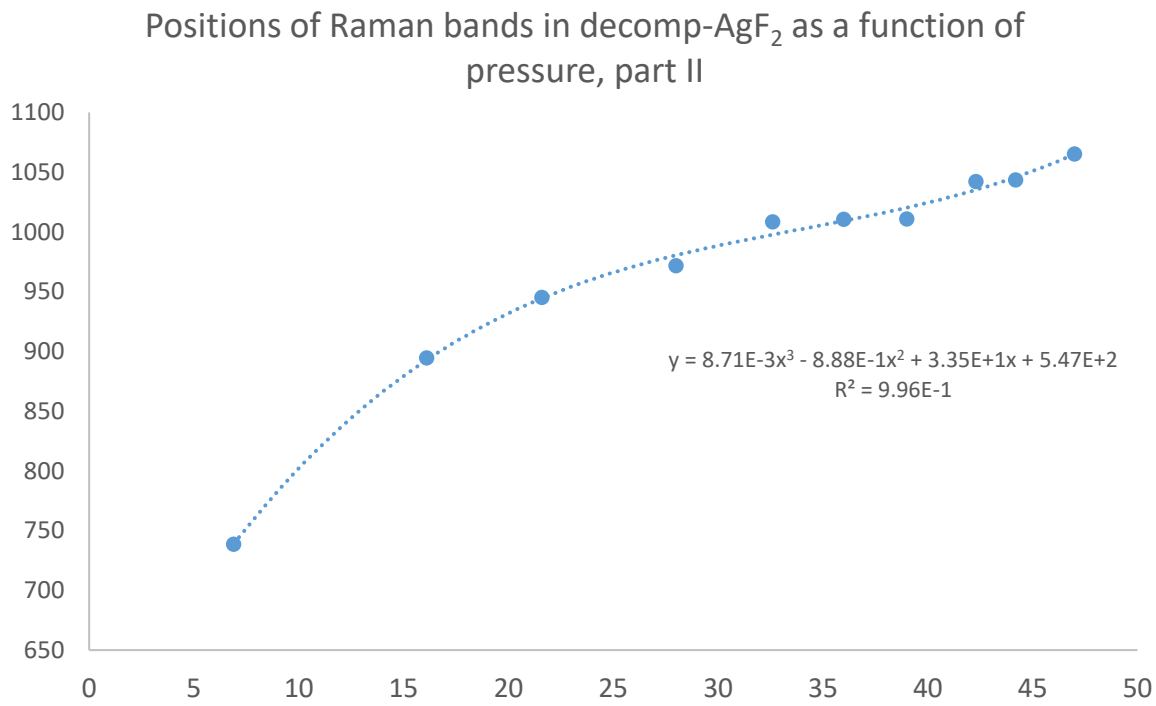

Fig. 113 - positions of bands in the decomp-AgF_2 Raman spectra as a function of pressure, 650-1100 cm^{-1} range

The two experiments – with and without hydrostatic medium[15] – differ in results. Characteristic, strongest band of pristine AgF_2, positioned at about 250 cm^{-1} at 0 GPa is present in all spectra in the experiment without hydrostatic medium. In contrast, the experiment with hydrostatic medium lacks the characteristic band even at the lowest pressure. This might indicate, that the smaller sample (in the hydrostatic conditions experiment) decomposes faster than the larger one (in experiment lacking hydrostatic conditions), and the amount of the pristine AgF_2 left after measurements is much smaller – If any. This also suggests, that the sample studied in nonhydrostatic conditions must be more representative of the decomp-AgF_2.

The band at about 420 cm^{-1} (ambient pressure value) is present, however, in both sets of spectra, and – as ambient pressure measurements indicate – is indicative of decomp-AgF_2. This statement is strengthened by the strong dependence of band position *vs.* pressure (Fig. 112). The linear regression parameters differ slightly between the experiments, although it is important to remember, that they were obtained for data in different pressure ranges, therefore different compressibility. The pressure dependence may be used in the future to

[15] Of course the Ne used as a medium in the experiment stops being hydrostatic at about 15 GPa. For the sake of simplicity I will use the names "hydrostatic experiment conditions" and "nonhydrostatic experiment conditions" to tell those two experiments apart.

confirm the chemical identity of decomp-AgF_2 in a combined theoretical – experimental study.

The other band that might be indicative of the decomp-AgF_2 is the 304 cm^{-1} band. A linear regression carried out on position *vs.* pressure data from hydrostatic sample yielded similar slope value as in the 420 cm^{-1} band (~3.6 and ~3.2 cm^{-1}/GPa). On the other hand, the situation in nonhydrostatic conditions was slightly different, as the slopes were much less similar (2.3 cm^{-1}/GPa for 420 cm^{-1} and 4.7 cm^{-1}/GPa for 312 cm^{-1}). Additionally, the intensity of the 312/304 cm^{-1} band was much lower in the nonhydrostatic conditions.

Some bands, most notably in the hydrostatic experiment, seemed too broad to come from regular phonon transitions. The experimental conditions – close to hydrostatic – should decrease the width of the bands usually caused by pressure gradient in DAC. Because the bands are so wide, their exact nature is at this moment unclear.

To summarize this section: the experiments yielded complementary results with some important differences. The hydrostatically compressed sample contained most likely only decomp-AgF_2, while in the nonhydrostatically compressed sample some pristine AgF_2 did survive up to about 11 GPa. Spectra of the second sample might contain bands from the high-pressure (HP-I) phase of AgF_2, appearing in the 140–200 cm^{-1} region between 3.2 GPa and 8.7 GPa. Spectra of the first sample on the other hand contain mostly some borad, non phononic bands of unknown origin, as well as a 420 cm^{-1} band (ambient pressure value) indicative of the decomposition product. The ambient pressure position of this band suggests, that the decomposition product is supposedly a silver(I) fluoroargentate(II): $Ag^{I}_2Ag^{II}F_4$, as very similar bands are present in the ambient pressure Raman spectra of two polymorphs of K_2AgF_4 (see Tab. 4 on page 48). An XRD study coupled with theoretical calculations is needed to confirm that assumption, and possibly will be carried out as a part of future research. It is important to note that during x-ray diffraction studies on AgF_2 at high pressure, a set of diffractograms was collected which did not match at all those for the other two sets (corresponding to mixture of AgF_2 and AgF). This third set of data might indeed correspond to decomposition product and it should be reanalyzed, while taking into account different polymorphic forms of $Ag^{I}_2Ag^{II}F_4$. This compound, Ag_3F_4, would be the first mixed-valence Ag(I)/Ag(II) quasi-binary fluoride known.

B.2.4.5 FTIR study of AgF_2

FTIR study of AgF_2 comprised of measurements in the FIR and MIR region. Since AgF_2 does not react easily with HDPE, it can be used as windows in FIR measurements. The measurements in the MIR range are more demanding: AgF_2 can react with materials used as windows or matrices in ordinary procedures. Therefore, I decided to measure the spectrum of AgF_2 using a pellet method with NaF as a dispersing medium. In the glovebox, about 2 mg of AgF_2 was added to about 198 mg of finely ground NaF and ground together using an agate mortar and pestle, until uniform in color and grain size powder was obtained. The mixture was transferred to the pellet maker and pressed into 13 mm pellet, which was quickly placed in the sample holder and transferred into a sample chamber. After evacuating the sample chamber for a quarter of an hour, a spectrum was collected.

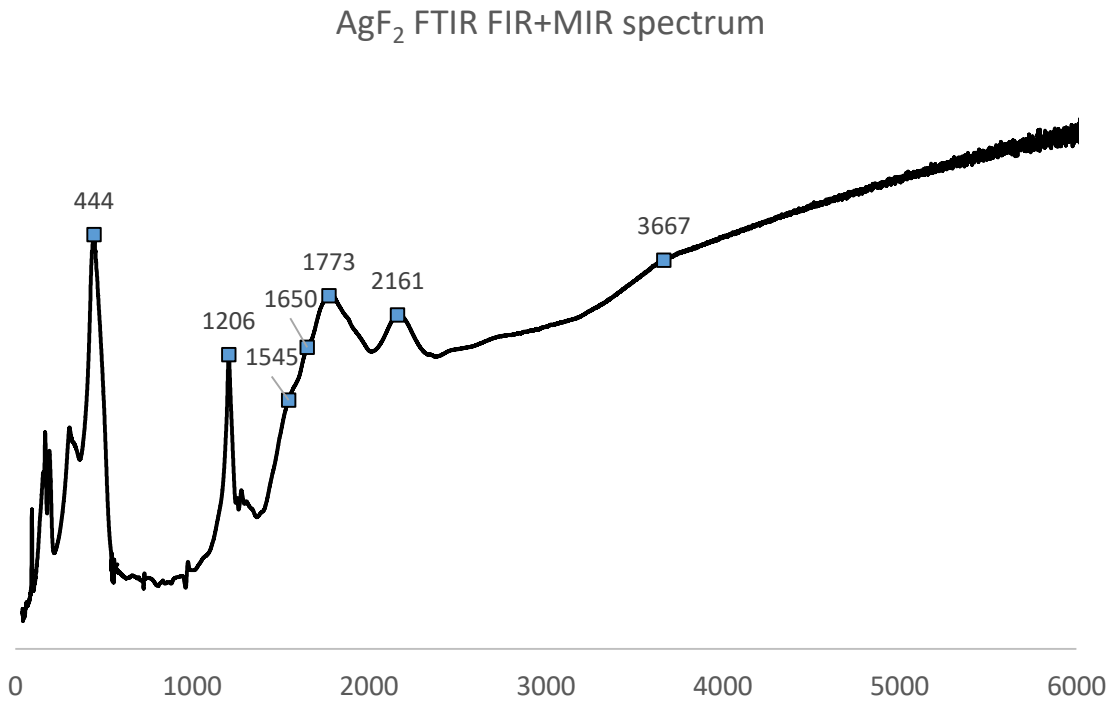

Fig. 114 - merged FTIR (FIR + MIR) spectra of AgF_2. Positions of the strongest band in the FIR region, and bands in the MIR region were marked with blue squares.

Analysis of the MIR part of the spectrum is not straightforward and it will be skipped here.

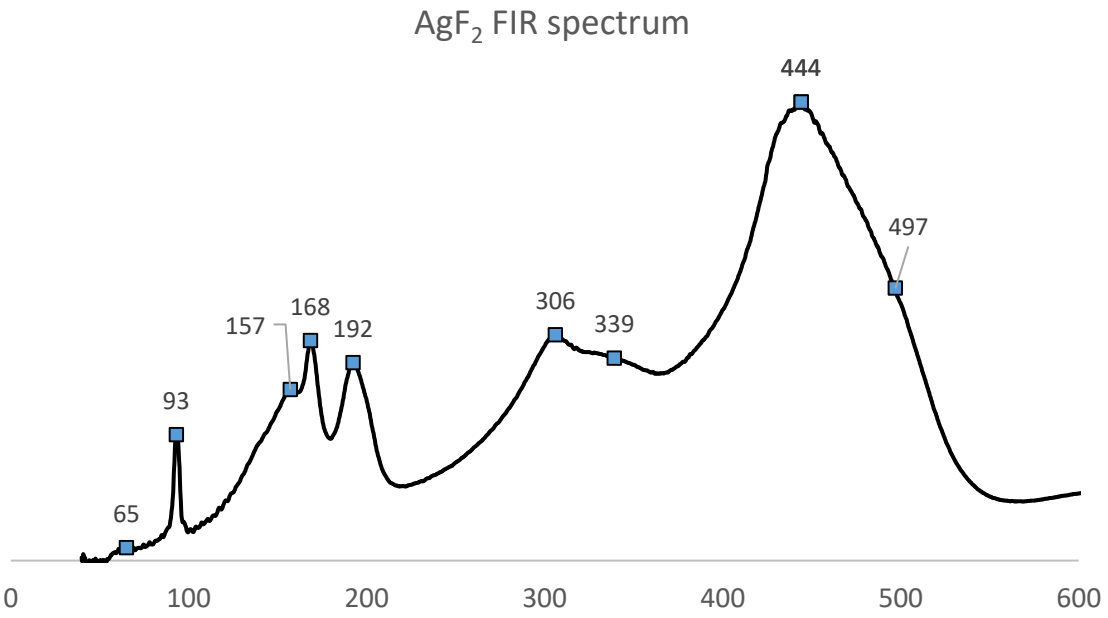

Fig. 115 - FIR spectrum of AgF_2 published in Gawraczyński et al. [153].

The FIR spectrum, which according to DFT+U calculations contained all the first-order IR active bands, has been analyzed using FITYK [156]. The procedure started with removal of the background, which has been described using a spline passing through points (49.9; -0.007), (267.7; -0.002), (575.7; 0.144), (673.8; 0.304). Next, local maxima were found and in each of their position a Gaussian function was placed. Several Gaussians were also placed at points corresponding to positions of shoulder bands (497 cm^{-1}, 135 cm^{-1}). The remaining intensity was supplemented with two broad bands (143 cm^{-1} and 355 cm^{-1}). Ready for optimization model contained 12 bands, which is less than the 15 expected from group theory. The model parameters were then fitted to data using Levenberg-Marquardt method.

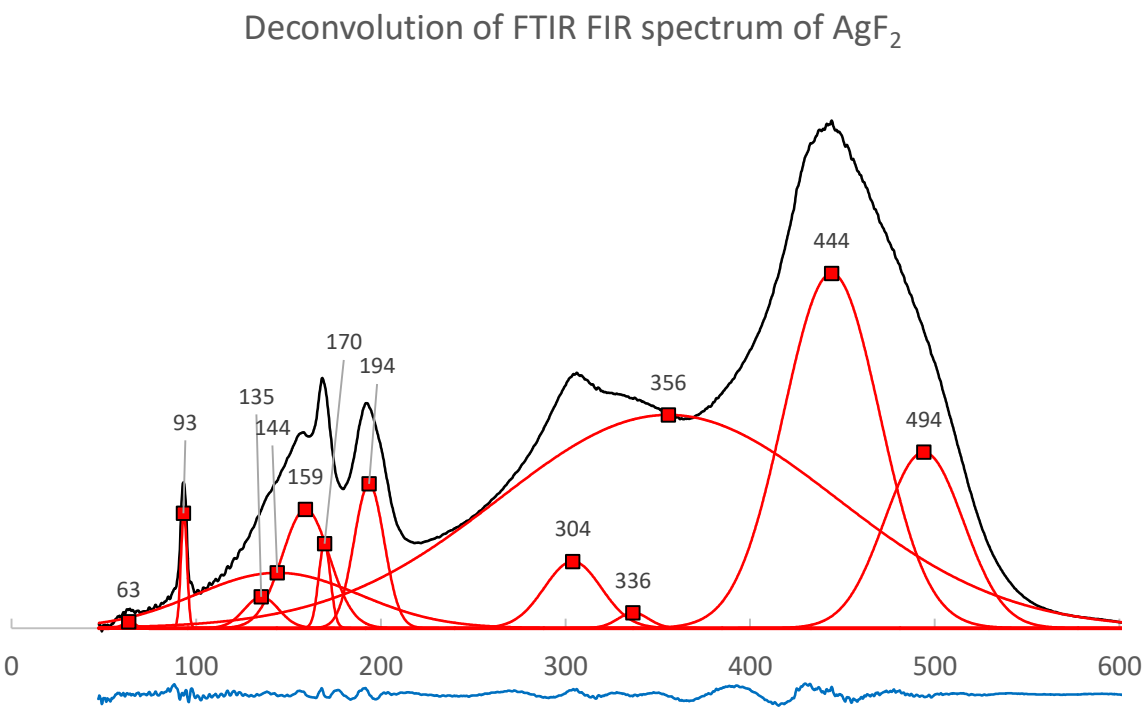

Fig. 116 - Deconvolution of the FTIR FIR spectrum of AgF_2. Black line is AgF_2 FIR spectrum after removing the background. Gaussian functions modelling the positions of bands are red. Blue colored line is a difference between the model and the measurement data.

Fig. 116 depicts the final result of deconvolution. The model (a sum of red Gaussian curves) describes the measurement data (black line) properly. The blue line, which is a difference between the measurement and model (residual), does not contain any features that would strongly suggest incorrect deconvolution. Model constructed using similar starting points but Lorentzian functions achieved worse fit – the sum of square residuals was equal 2.877. This suggests that the amount of Lorentzian admixture to the Gaussian functions is small, and the final positions of bands are most likely correct. The experimental deconvoluted bands have been compared to theoretical calculations from Tab. 15. The result of this comparison is presented in the Tab. 16.

The combined experimental – theoretical study alowed to assign all bands appearing in FTIR absorption spectra of AgF_2.

exp	DFT+U	HSE06
63	Artifact or contaminant	
93	90 (B_{1u}), 94 (B_{3u})	92 (B_{1u}), 93 (B_{3u})
135	134 (B_{2u})	136 (B_{2u})
144	143 (B_{1u})	146 (B_{1u})
159	156 (B_{2u})	161 (B_{2u})
170	163 (B_{3u})	175 (B_{3u})
194	186 (B_{2u})	199 (B_{2u})
304	310 (B_{1u}), 312 (B_{2u})	317 (B_{1u}), 317 (B_{2u})
336	27+309 ($B_{2u} * A_g = B_{2u}$)	38+307 ($B_{2u} * B_{1g} = B_{3u}$)
356	350 (B_{3u})	356 (B_{3u})
444	441 (B_{3u})	459 (B_{3u})
494	441+59 ($B_{3u} * A_g = B_{3u}$)	470 (B_{3u})

Tab. 16 - band assignment for FIR spectrum of AgF_2. Comparison of experimental band positions with those obtained through DFT+U and HSE06 calculations.

B.2.5 Spectroscopic study of magnetic excitations in AgF_2 and $AgFBF_4$

One distinct line of my studies concentrated on magnetic properties of two silver(II) compounds: AgF_2 and $AgFBF_4$. Both compounds were studied using Raman scattering spectroscopy[16], NIR absorption spectroscopy, and inelastic neutron scattering, and both were studied theoretically.

The theory summarized very briefly in subchapter A.4.2.3 on page 77 shows how light interacts with an antiferromagnetically ordered lattice of spins yielding either additional bands in Raman or IR spectra. Such bands were found in high-temperature superconductors, and their presence indicates a possibility of obtaining a completely novel family of superconductors via careful doping and/or application of external pressure in silver(II) compounds.

B.2.5.1 AgF_2

Raman spectra of silver(II) fluoride were collected using different Raman setups to ensure that the observed phenomena were not an artifact of a specific spectrometer. Additionally, the measurements at several excitation lines were conducted at different temperatures since the multimagnon bands intensity is highly dependent on the sample temperature.

[16] As it will become clearer in a later paragraphs, the procedure used in optomagnetic studies of AgF_2 is more sophisticated than the one used commonly for vibrational studies.

Because multimagnon bands decrease in intensity at temperatures higher than 0.3 T_N, and usually are rather weak or indiscernible from background noise at room temperature, the optomagnetic measurements require either a high-intensity excitation line, a long exposition, or low-temperatures. A high-intensity excitation is incompatible with AgF_2 due to its laser-induced decomposition. Low-temperature conditions always introduce some inconvenience to any measurement procedure because of possible atmospheric gases condensation, necessity to use cryogenic liquids and other minor problems. Therefore, a room-temperature procedure has been envisaged and successfully applied.

The first step of the measurement procedure was obtaining recognizable AgF_2 Raman spectra in a very broad range at the lowest power possible during 3 minutes scan. The 250 cm^{-1} band must have been clearly present at intensity exceeding three average widths of the noise to proof that the sample studied has not decomposed. This is a somewhat arbitrary condition, but it yielded good results. If the spectrum contained the 420 cm^{-1} band, the laser power was decreased and a new spot on the sample surface was selected. After achieving the goal mentioned above, the scan was repeated for a much longer time. This ensured that the spectra were collected at quality sufficient for analysis, and that no substantial decomposition occurred. A typical measurement conducted for 514 nm excitation line in the 100-5000 cm^{-1} range using a 300 l/mm grating required two spectral windows, each measured for 300 times in 120 s long scans.

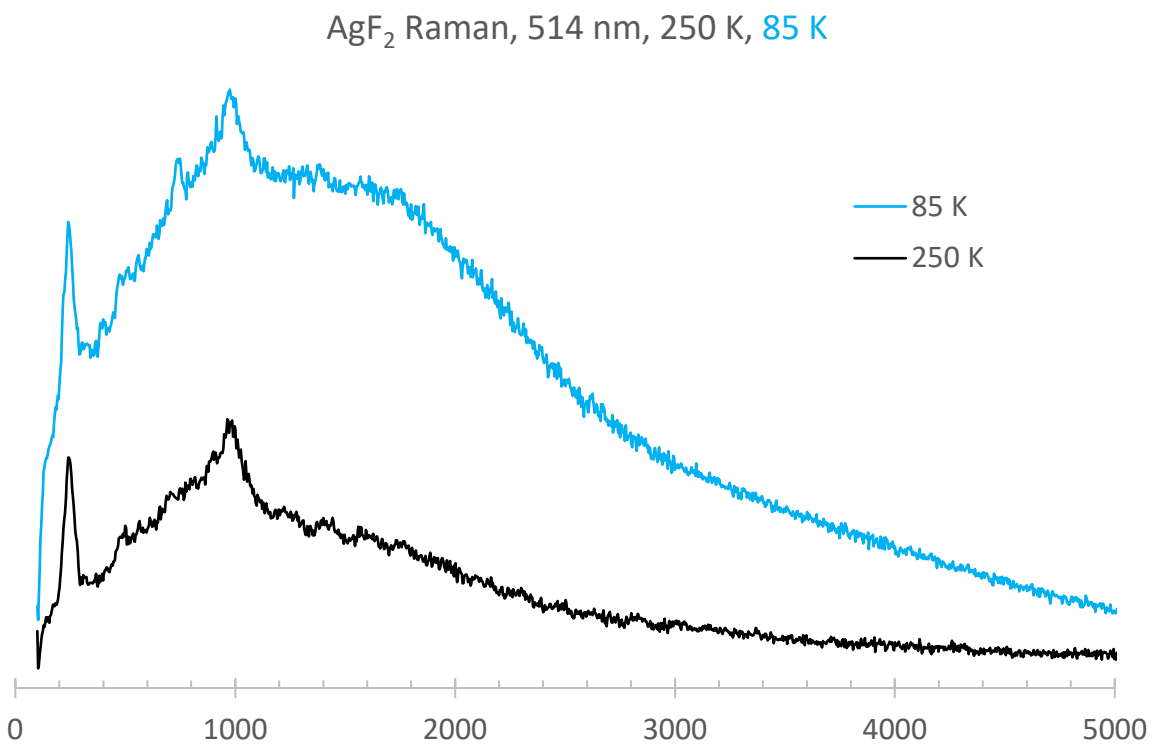

Fig. 117 - Raman spectra of AgF_2 at 250 K and 85 K, excitation line 514 nm

Since bimagnon transitions in Raman spectra are immensely temperature-dependent, especially given the relatively low Néel point of AgF_2 (165 K), the need arose of collecting spectra at low temperature. The measurements conducted in the Trzebiatowski Institute of Low Temperature Research in Wrocław with help from Dr. Maciej Ptak, used Raman spectrometer equipped with mini-cryostat, but they did not yield satisfactory results. Therefore, I have constructed a simplistic setup for measurement at a single low temperature point. Low-temperature measurement presented on Fig. 117 above were conducted for an AgF_2 sample closed in a quartz capillary. The sample was cooled in a lab-made flow cryostat (see Fig. 118). An argon gas cylinder was connected to a coiled FEP tube. The tube was held securely in place with a laboratory stand to remove possibility of even small movements on the sample end. A dewar filled with liquid nitrogen had been placed on a laboratory jack. A shift in the position of the jack changed the area of contact between LN2 bath and coiled part of the FEP tube, thereby varying the temperature of the flowing gas. A small hole was cut out near the end of the FEP tube. Sample was placed in the hole and secured by plasticine. A light from an excitation line illuminated the sample through the cut-out hole – the scattered light was collected via microscope in the backscattering geometry. The gas escaping the FEP tube at the end flowed around a thermometer, allowing an approximate measurement of the temperature in the sample – at higher temperature this method yielded about 250 K. Below

the measurement range of the thermometer, the temperature could still be approximated near the melting (about 83.8 K) and boiling (about 87.3 K) point of the Ar. When the position of the dewar was set at such height, that liquid Ar was expelled from the FEP tube, the temperature must have been in the (83.8 K, 87.3.K) range. This enabled an approximate measurement of sample temperatures as seen on Fig. 117 Despite the simple design, the cryostat proved to be suitable for low-temperature Raman measurements of the sample.

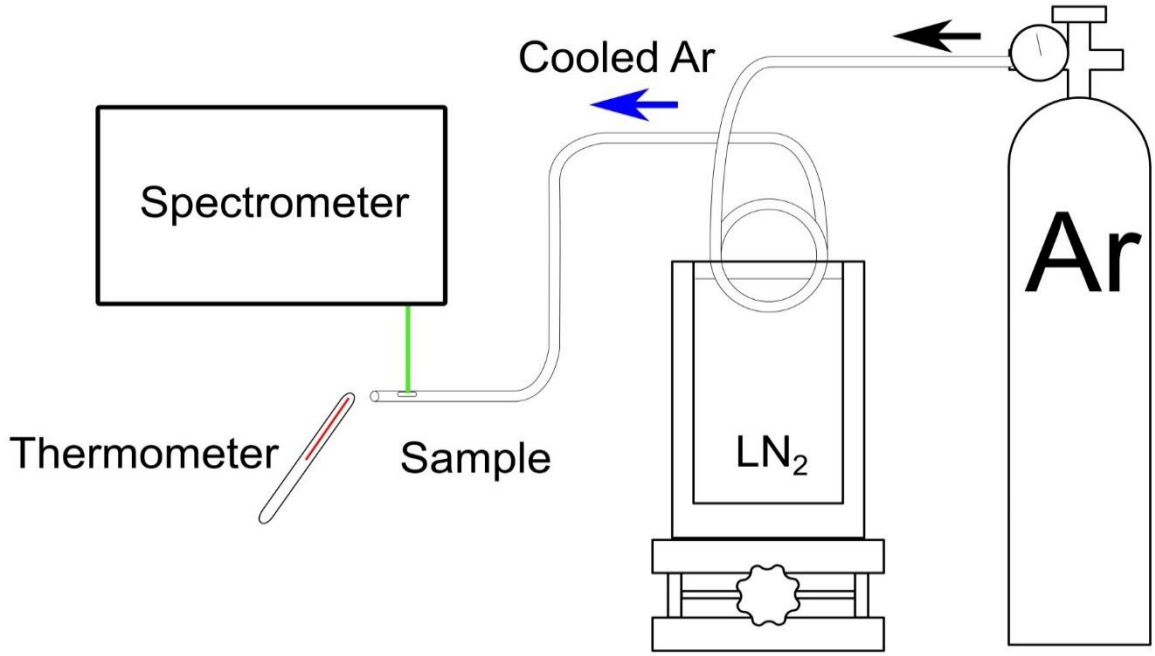

Fig. 118 – a simplified plan of a constructed flow cryostat.

The data presented on Fig. 117 was collected using a 0.3 mW (power measured directly after an attenuating filter) 514 nm excitation line. 300 l/mm grating and x20 microscope were used in the setup. Each dataset was collected for an hour in 30 two-minute acquisition steps.

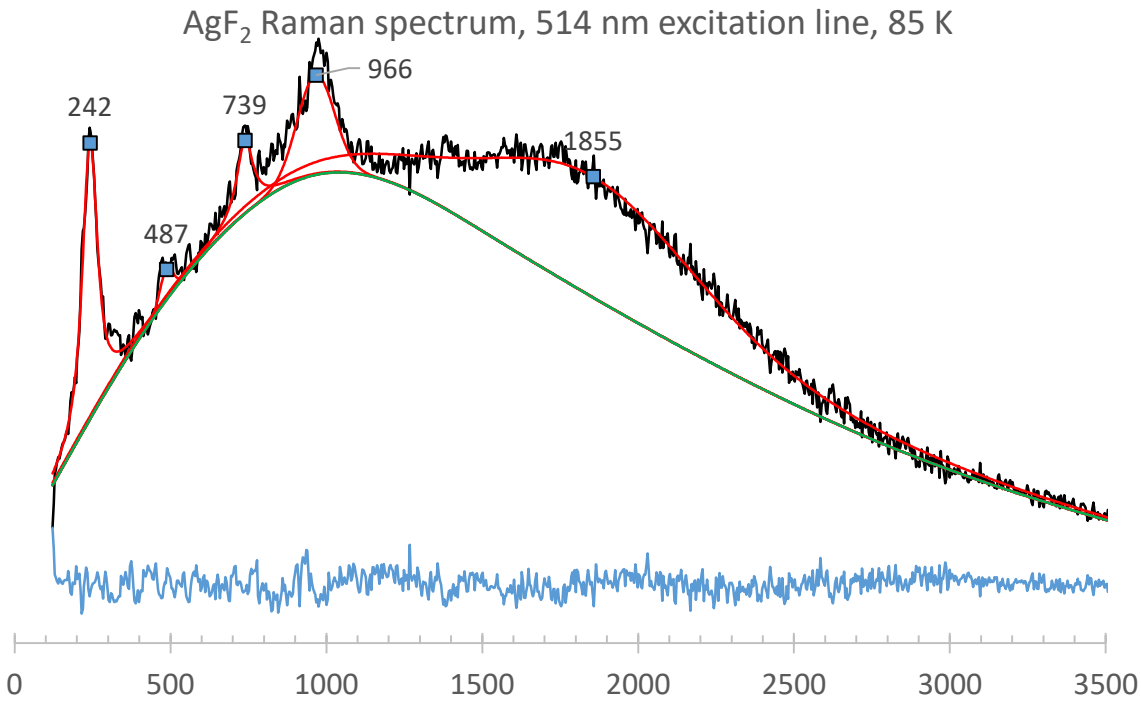

Fig. 119 - AgF_2 Raman spectrum, 514 nm excitation, 85 K

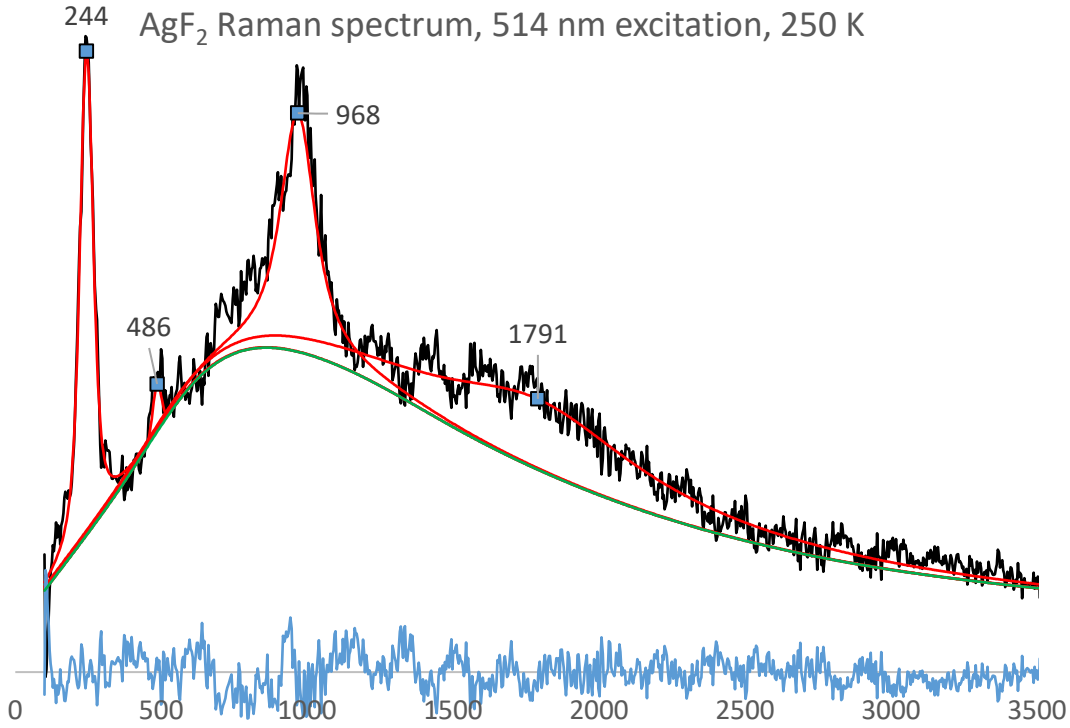

Fig. 120 - AgF_2 Raman spectrum, 514 nm excitation line, 250 K

The Raman spectra of AgF_2 in Fig. 119 and Fig. 120 are presented in following way: blue color is used to depict difference between the model (sum of a somewhat arbitrary baseline and the bands) and experimental data. The green color is assigned to baseline, and the red color is used to depict bands. This deconvolution was performed using Voigt functions.

The spectra do not contain strong 420 cm^{-1} line, indicative of decomp-AgF_2, which indicates that little or no decomposition occurred. Two strong bands are present in both spectra: the first one at about 243 cm^{-1} and the second one at 970 cm^{-1}. Both of them can be found in other Raman spectra of AgF_2. The first one is assigned to B_{2g} Ag-F stretching mode. The second one is a sum of several overtones: of Raman active modes at 478 cm^{-1} (B_{3g}), 481 cm^{-1} (B_{2g}), IR active modes at 470 cm^{-1} (B_{1u}), 468 cm^{-1} (B_{2u}), and a silent mode 477 cm^{-1} (A_u). The representations of first overtones of those modes contain a fully symmetric A_g representation, they are therefore Raman active. The 970 cm^{-1} band is also most likely resonance-enhanced at 514 nm excitation line.

Additionally, lower temperature measurement contains a 750 cm^{-1} band. Because the calculations of vibrational structure of AgF_2 do not predict any first-order Raman bands over 500 cm^{-1}, the bands positioned in the 500–1000 cm^{-1} correspond to higher order phonon bands *i.e.* overtones or combination bands.

Both spectra contain a very broad band resembling fluorescence centered at about 1820 cm^{-1} (1855 cm^{-1} at 85 K, 1791 cm^{-1} at 250 K). The intensity of the band is higher at the lower temperature, which is consistent with the behavior of magnetic bands. Additionally, the band shifts to higher energies at low temperature. This led to further measurements at different excitation lines to exclude the possibility of 1800 cm^{-1} being a fluorescence band or an experimental artifact.

The subsequent studies of the bimagnon band focused on the dependence of the signal on excitation line. The former studies for oxocuprates showed that bimagnon bands are strongly dependent on electronic resonance processes, notably when the exciting wavelength approaches absorption due to the charge-transfer gap [87]. The first line chosen for this study was the common 1064 nm line of the Nd:YAG laser.

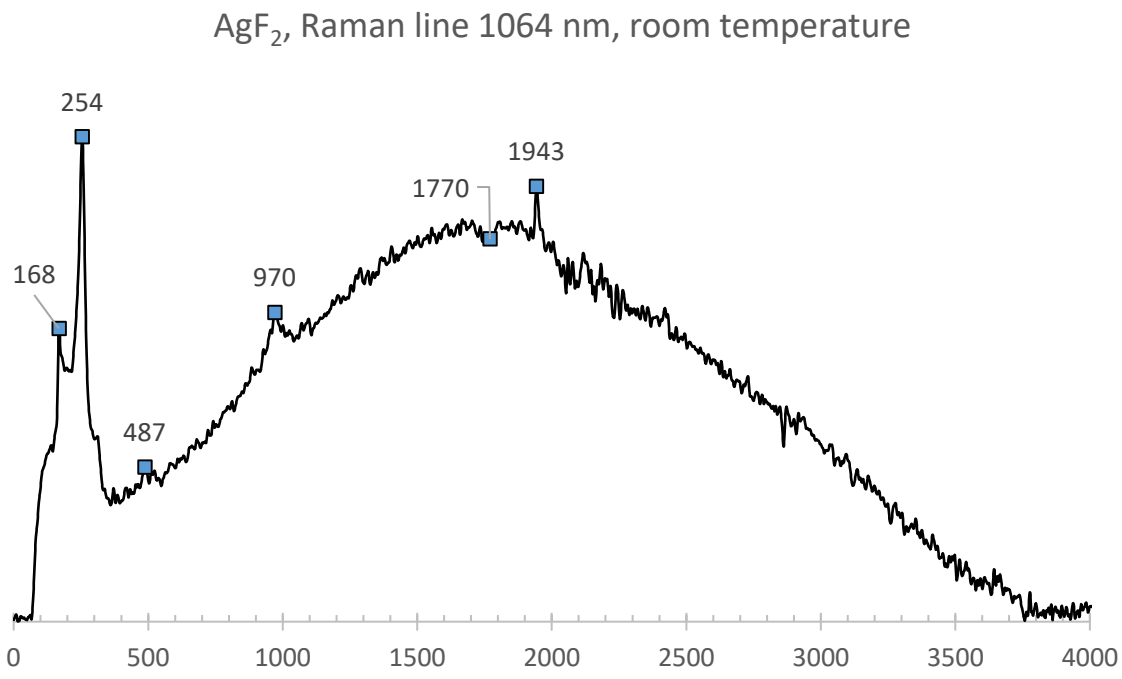

Fig. 121 - Raman spectrum of AgF_2 at room temperature, excitation line 1064 nm.

The spectrum at Fig. 121 was collected using a Thermo NXR-FT-Raman spectrometer. The sample was enclosed in a quartz capillary. To decrease the possibility of sample thermal decomposition, the laser power was set to minimum and attenuated using a set of filters until it dropped down to several mW. The spectrum seen above is averaged out of 40000 scans.

Six bands can be recognized in the measured spectrum. The bands at 168 cm^{-1} and 250 cm^{-1} were predicted in theoretical calculations and are either both of B_{2g} symmetry, or the lower wavenumber band is B_{2g} and higher wavenumber is of B_{3g} symmetry. Their high intenstiy confirms the presence of non-decomposed AgF_2. The band at 970 cm^{-1} can be observed in other AgF_2 spectra and is a second order Raman band. The presence of band positioned at 487 cm^{-1} is questionable due to its very small intensity, although calculations predict existence of such band in the spectrum (see Tab. 15, page 129). Additionally, the band is present at the low-pressure in high-pressure decomp-AgF_2 experiment (Fig. 95). The identity of band at 1943 cm^{-1} is currently unknown. The last band in the spectrum is very broad and positioned in roughly the same place as in the measurements conducted using 514 nm excitation line, at 1770 cm^{-1}. Its intensity in maximum is now comparable to the strongest phonon, and its integrated intensity is by the factor of 100 larger than that of a phonon, which clearly indicates the resonance character of the bimagnon band. It is currently unclear which physical process (absorption across fundamental bandgap, exciton, other) is responsible for the resonance.

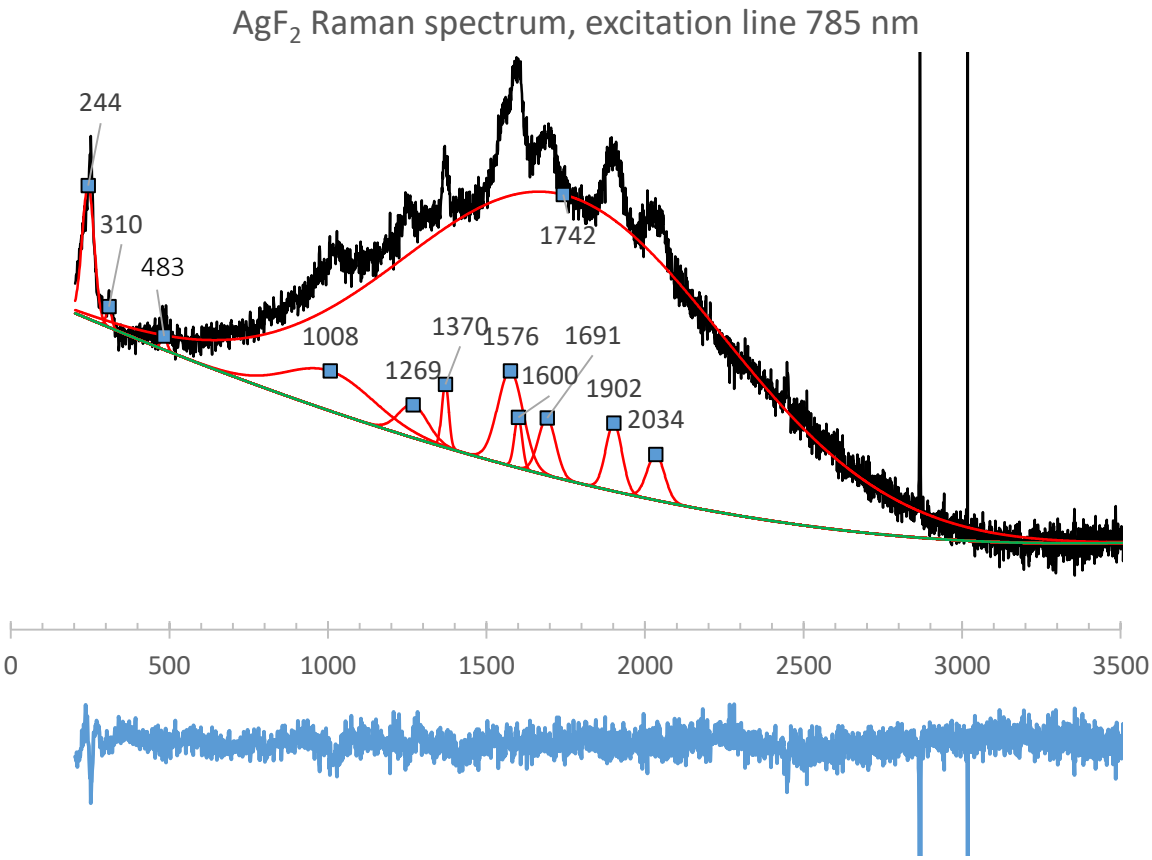

Fig. 122 – deconvoluted Raman spectrum of AgF_2 at room temperature, excitation line 785 nm

Another spectrum of AgF_2 was collected using inVia Reflex Renishaw system with confocal microscope and 785 nm excitation line. The deconvolution using Gaussians (red bands on Fig. 122) was performed on the data. Baseline, drawn with green color on the spectrum, was modelled with spline functions. The difference between the model and experimental spectrum was drawn with blue line.

The spectrum contains three bands in the low-wavenumber part of the spectrum. Band 244 cm^{-1} is present in all other AgF_2 spectra, therefore its presence is not a surprise as it confirms the presence of AgF_2. Bands 310 cm^{-1} and 483 cm^{-1} were predicted by theoretical calculations, the latter also appears in Raman spectra with excitation lines 1064 nm and 514 nm. The group of bands in the 1000-2020 cm^{-1} range stacked atop a very broad band centered at 1742 cm^{-1} are not observed in other experiments, which suggests another resonant character of the process responsible for their appearance. Their origin is currently unknown.

The broadest band in this measurement is centered at 1742 cm^{-1}. The width together with its position suggest that it is the same band that was at 1800 cm^{-1} and 1770 cm^{-1} in previously

described spectra. This convinced me that further studies of this broad bimagnon band are worth pursuing.

To further confirm the origin of the 1800 cm^{-1} band, a sample has been studied using Raman spectroscopy with 1064 nm excitation in a genuine cryostatic sample chamber. The measurements were conducted in Bolonia by dr. Giampiero Ruani and dr. Ilaria Bergenti on samples loaded by me into a prefluorinated capillary. Two spectra were collected: at 85 K and 115 K.

To compare different AgF_2 spectra to each other and to Raman spectra of other 2D antiferromagnets, the spectrometers used in measurements were calibrated using standard light sources (cavity blackbody lamp or internal standard sources). A result of the comparison can be seen on Fig. 123. An inset depicts the part of the AgF_2 spectra containing the strong 250 cm^{-1} phonon. Different AgF_2 datasets were normalized according to intensity of this band. The bimagnon band positioned at about 1800 cm^{-1} changes height with temperature as expected from a magnetic band, increasing with lowering temperature. The line shape also changes in accordance with expectations, becoming narrower at lower temperatures. Center of the band shifts to the higher wavenumbers with cooling. Comparison with bimagnon band of $EuBa_2Cu_3O_6$ (EBCO) measured at 11 K is presented to further illustrate the point.

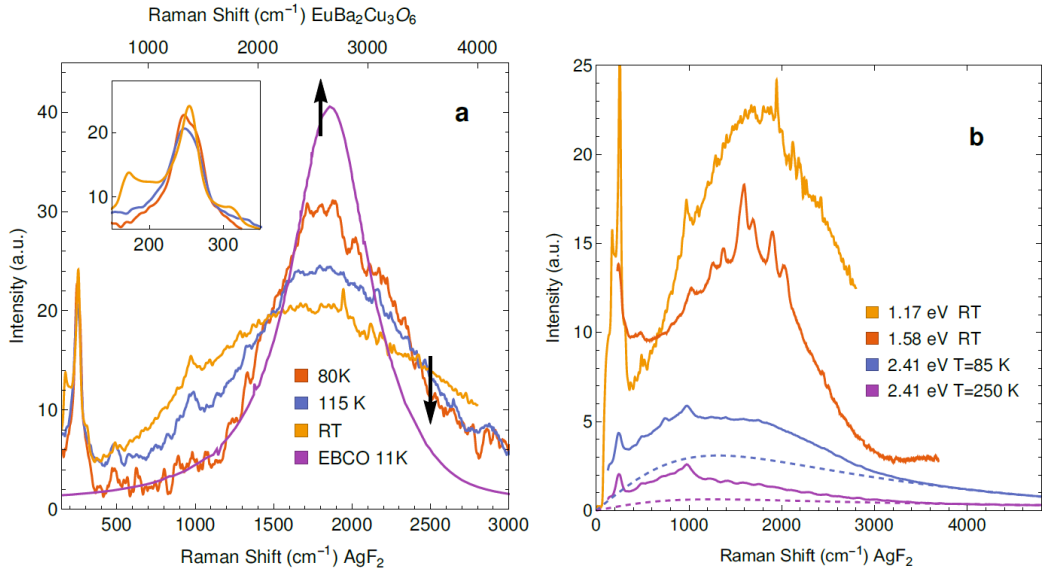

Fig. 123 - a) set of AgF_2 Raman spectra (excitation line 1.17 eV) at different temperatures compared with two-magnon line from Raman spectrum of $EuBa_2Cu_3O_6$ (EBCO, cited from Knoll et al. [157]*). Lower scale corresponds to AgF_2 spectra, while the upper one corresponds to EBCO.*
b) comparison of four AgF_2 Raman spectra at various excitation lines. Measurements with 2.41 eV excitation were conducted at two different temperatures, and were presented earlier in Fig. 117.

Using the EBCO data from paper by Knoll *et al.* [157], it is possible to calculate an approximate value of magnetic superexchange constant in AgF_2, as the ratio of J to bimagnon band position in cm^{-1} can be assumed equal in both cases. Using this assumption, we obtain:

$$\frac{J_{AgF_2}}{\nu_{AgF_2}} = \frac{J_{EBCO}}{\nu_{EBCO}} = \frac{100\ meV}{2600\ cm^{-1}}$$

$$J_{AgF_2} = 100\ meV * \frac{1800}{2600} = 70\ meV$$

The value of J = 70 meV is very large, since only undoped copper(II) oxides exhibit larger values of J, as exemplified here by EBCO.

To strengthen and confirm the spectroscopic results, the value of J should be obtained by a different method. One of complementary methods of obtaining superexchange constants is inelastic neutron diffraction (see subchapter A.4.2.2). IHence, prepared a sample suitable for measurements: about 150 grams of AgF_2 powder were packed inside an Al sample holder and sent to ISIS spallation neutron source for "Xpress access" measurement.

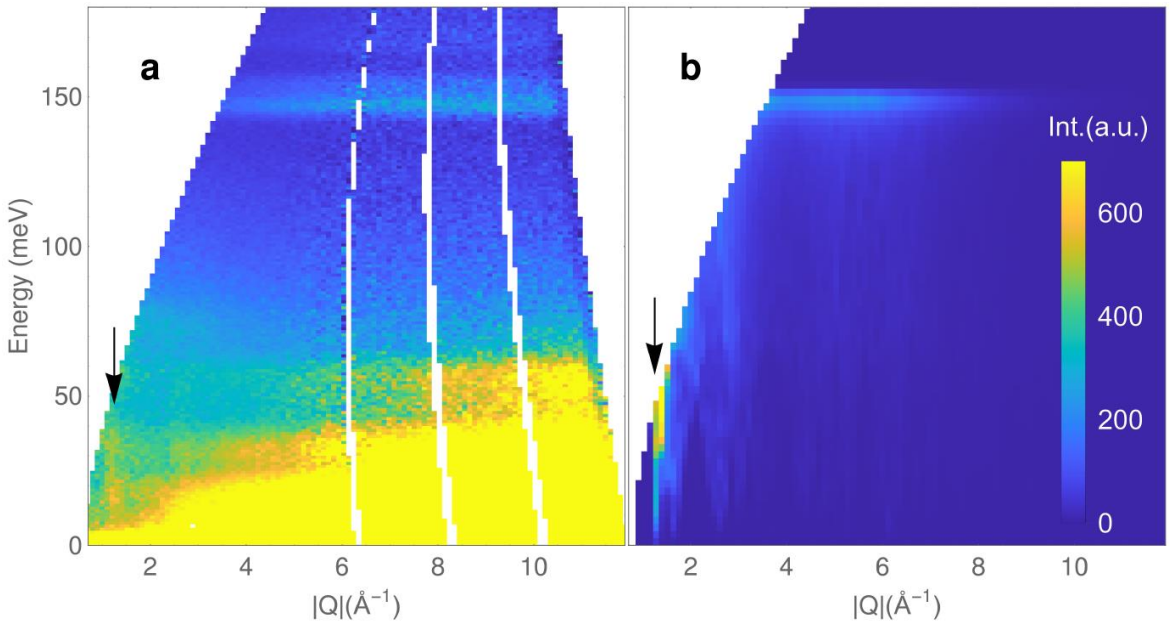

Fig. 124 – an inelastic neutron scattering patterns for AgF_2. Left side (a) depicts an experimental pattern with incident neutron energy equal 300 meV. An arrow points to a feature at a scattering vector length of $|\boldsymbol{Q}| = 1.2\ Å^{-1}$, corresponding to the propagation vector $\boldsymbol{Q} = (1,0,0)$ (in reciprocal lattice units) of the magnetic order. The signal at very low energy extending to a full range of measured scattering vector lengths corresponds to incoherent elastic scattering. The signal at high $|\boldsymbol{Q}|$ extending up to about 60 meV corresponds to scattering from phonons. The right side (b) depicts a calculation of powder-averaged neutron scattering cross-section, using intraplanar J = 70 meV and interplanar $J_\perp$ = 4 meV as suggested by DFT computations. Image from publication by Gawraczyński et al [153].

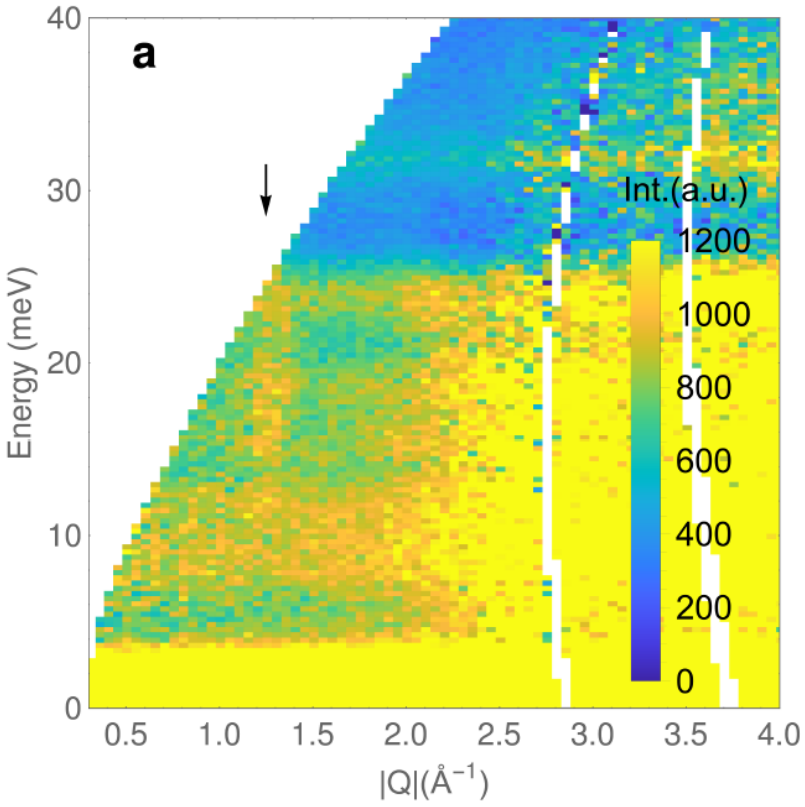

Fig. 125 - fragment of inelastic neutron diffraction data on AgF_2 with incident energy 60 meV

The measurements at ISIS were conducted using initial neutron energy of up to 300 meV. Fig. 124 depicts the obtained data in the 0-12 Å^{-1} |Q| range of momentum transfer value and 0–170 meV in transferred energy (at 300 meV incident energy), together with a simulated neutron powder diffraction pattern. Fig. 125 depicts a measurement at incident energy of 60 meV.

The data collected at ISIS proved to be consistent with the conclusions from the Raman measurements. At about 1.2 Å^{-1} there is an increase in value of scattering indicated by arrows on Fig. 124 and Fig. 125, that corresponds to (1,0,0) propagation vector (in reciprocal lattice units). This can be interpreted as a propagation vector of antiferromagnetic ordering in the AgF_2 structure. Additionally, a strong flat signal at about 148 meV (=2*(70+4)) is reproduced very by simulated powder-averaged neutron diffraction pattern introducing an intraplanar magnetic superexchange component J = 70 meV and interplanar $J_\perp$ = 4 meV [153]. Those observations indicate a presence of antiferromagnetic ordering with value of intrasheet superexchange constant equal to the one derived from Raman experiments.

B.2.6 $AgFBF_4$

$AgFBF_4$ is another magnetically ordered compound of divalent silver that I decided to study. One of the most pronounced differences, but also an interesting point of comparison between AgF_2 and $AgFBF_4$, is their dimensionality: 2D *vs.* 1D. To better understand the influence of structure on properties of those compounds, I decided to characterize $AgFBF_4$ using spectroscopic methods.

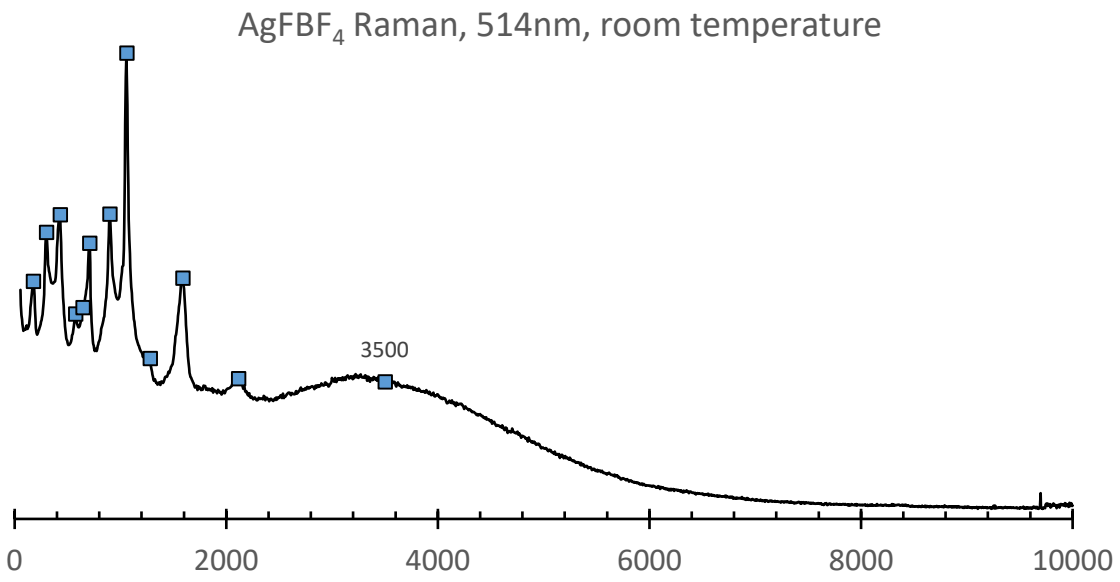

Fig. 126 - Raman spectrum of $AgFBF_4$ at room temperature, excitation line 514 nm

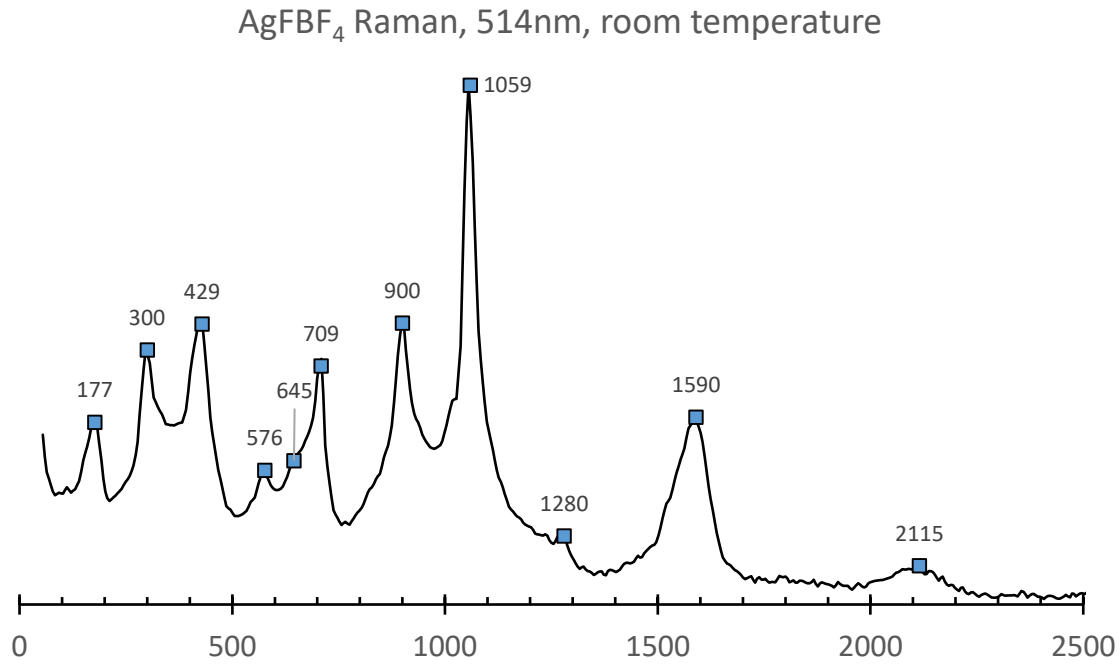

Fig. 127 – blown-out region 0-2500 cm^{-1} of the $AgFBF_4$ Raman spectrum.

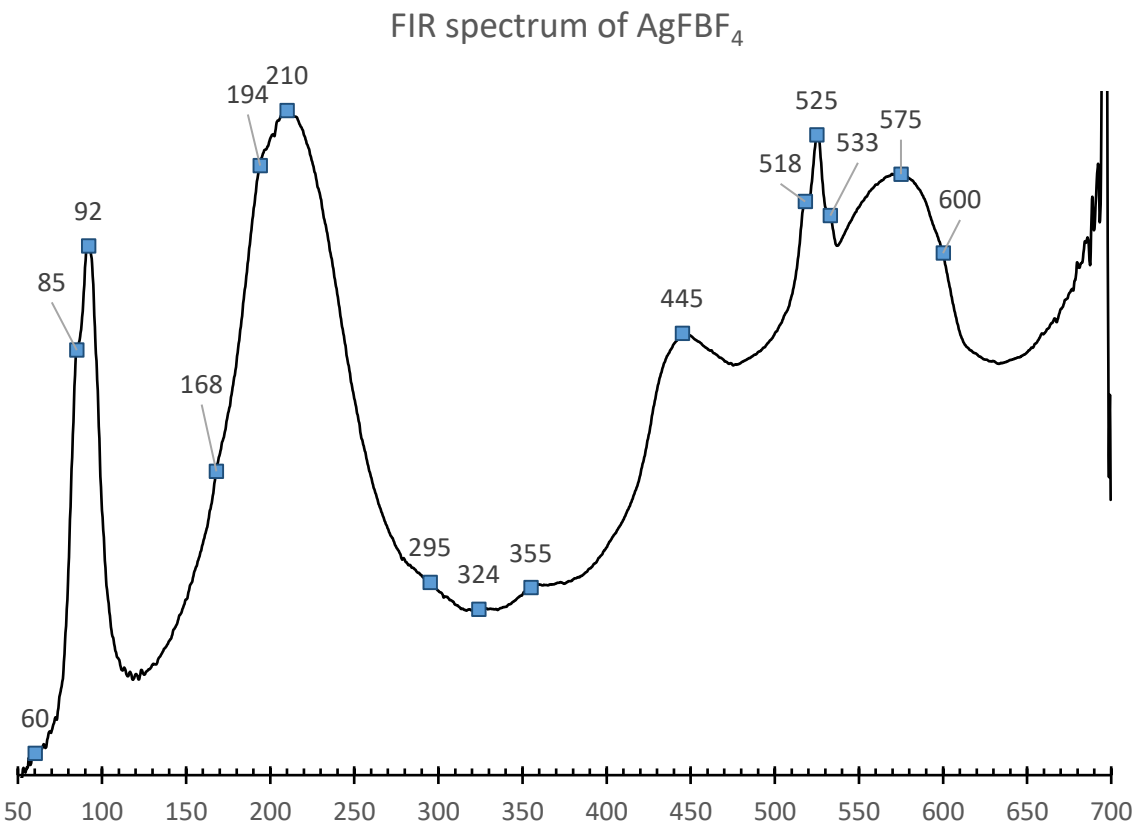

Fig. 128 - FIR spectrum of $AgFBF_4$

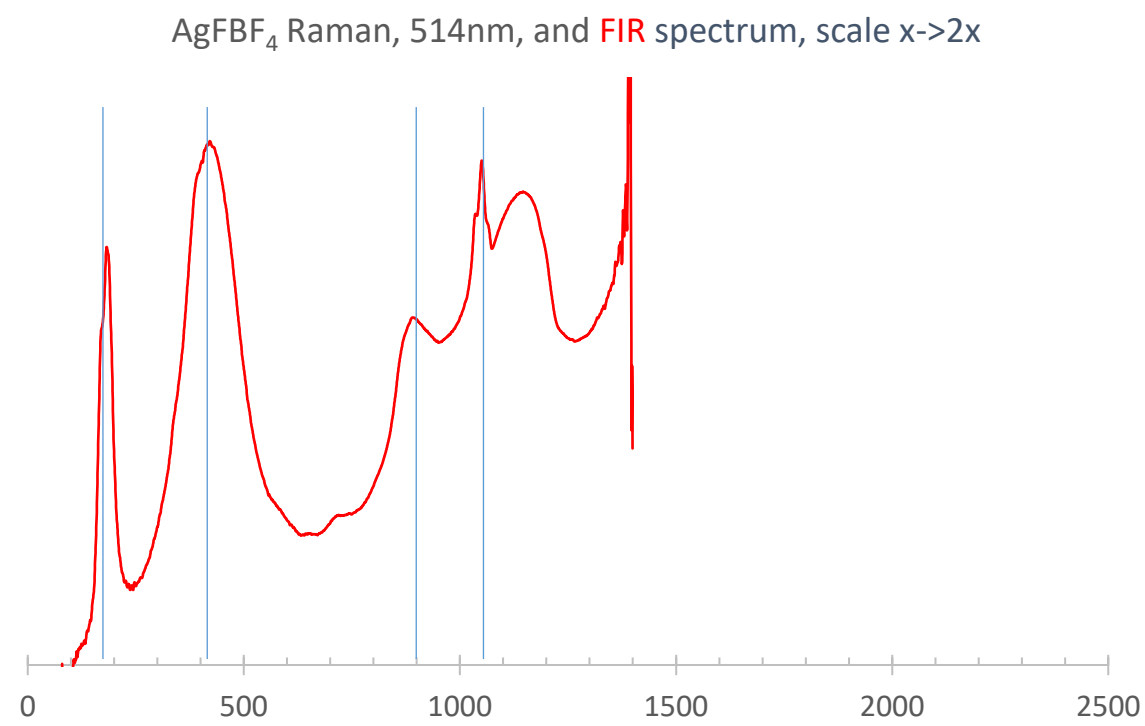

Fig. 129 - scaled (x->2x) FIR spectrum of $AgFBF_4$ superimposed on Raman spectrum of $AgFBF_4$. Blue lines indicate very good agreement between the positions of bands in the two spectra.

Superimposing a stretched FIR spectrum over reveals a relationship between positions of several bands in both spectra. Most notably, doubled position of strong FIR bands 210 cm^{-1}, 445 cm^{-1}, 525 cm^{-1} coincide very well with Raman bands at 429 cm^{-1}, 900 cm^{-1} and 1059 cm^{-1}. This suggests that the mentioned Raman bands might be IR overtones – either pure overtones, or some affected by Fermi resonance.

Some insight is shed on this situation by comparison with compounds containing BF_4^- - for example $NaBF_4$ and KBF_4 seen in a publication by Bonadeo and Silberman [158]. The authors described the spectra by analyzing energies and symmetries of bands that are derived from fundamental vibrations of the tetrahedral BF_4^- group. The band at 1059 cm^{-1} has an energy comparable to that of ν_3 (T_2 symmetry, asymmetric stretching) band in MBF_4 – about 1100 cm^{-1}. The IR spectrum of MBF_4 compounds contains a very strong set of absorption bands in the 1000-1200 cm^{-1}. Apart from the already mentioned ν_3 band, the first overtone of ν_4 mode (T_2 symmetry, atoms move similarly to an umbrella inverting during strong winds) also has an energy that falls inside this range.

Another interesting feature of the Raman spectrum of $AgFBF_4$ is a broad band at 3500 cm^{-1}. The absolute position of this feature is 627.5 nm, which corresponds to red-orange emission. Because measurements were conducted only on 514.5 nm excitation line, right now there is not enough data to tell for sure whether this is a fluorescence, a spinon or some other exotic band (not, however, that magnetic excitations are not allowed in Raman spectra for 1D systems). Additional experiments using INS were prepared to study this compound.

B.2.6.1 Inelastic neutron scattering of $AgFBF_4$ sample

A 12 g sample of $AgFBF_4$ has been prepared for inelastic neutron scattering measurement at ISIS neutron spallation source. Incident energies of 600 meV, 180 meV, 100 meV and 50 meV were used in experiments. Theoretical calculations indicated that magnetic excitations in $AgFBF_4$ should occur at energies on the order of 300 meV, therefore the magnetic signal could be detected (in theory) only in the highest incident energy scan.

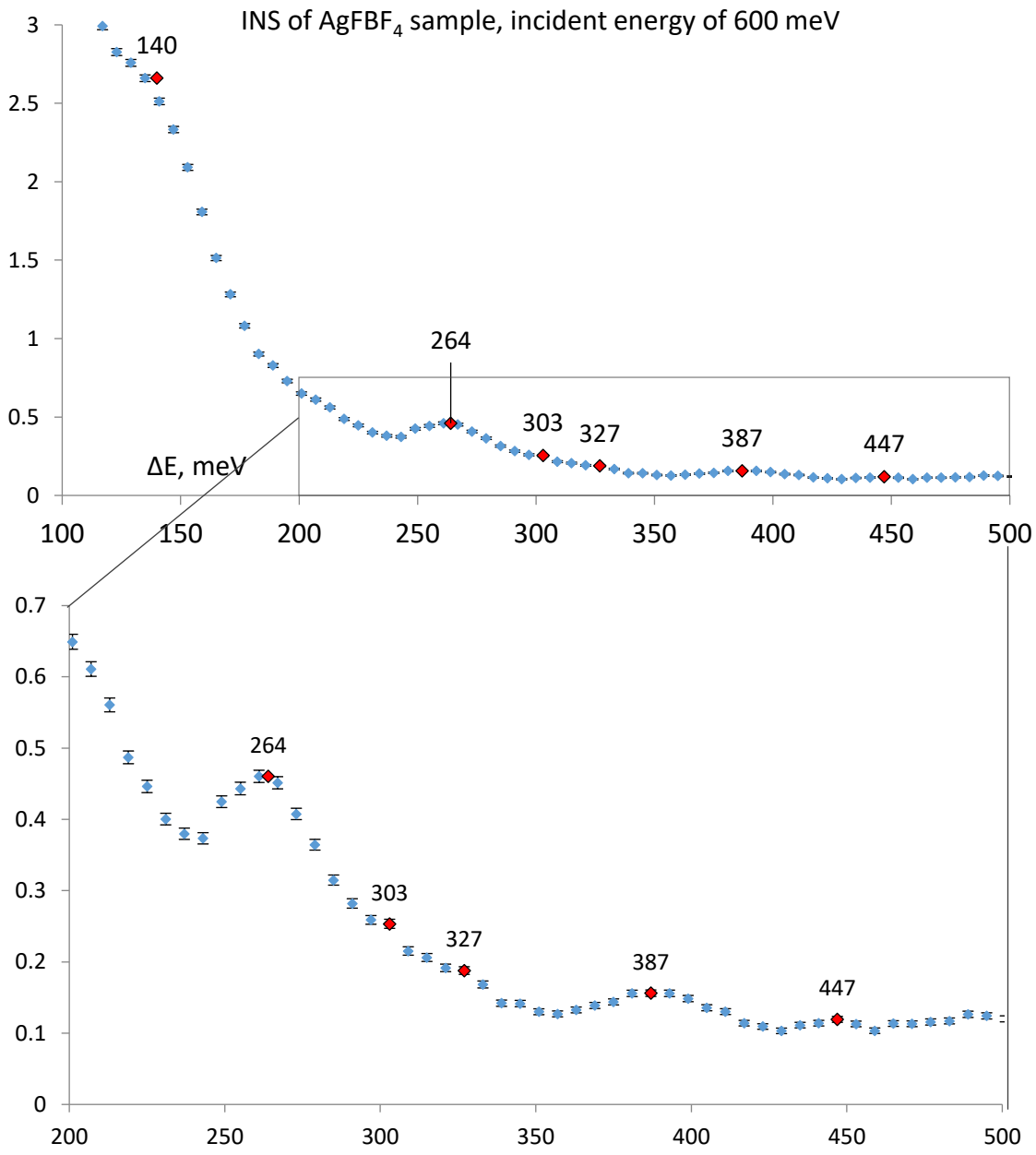

Fig. 130 - The integrated INS spectrum of $AgFBF_4$ sample, incident energy of 600 meV. An exploded view of the 200-500 meV range is presented.

Signals at 140 meV (1130 cm^{-1}), 264 meV (2130 cm^{-1}) and 387 meV (3121 cm^{-1}) likely correspond to first, second and third order ν(B-F) stretching. Signals at 303 meV and 327 meV might be caused by magnetic transitions. Because other measurements share similar shape, *i.e.*, they consist of rather weak signals superimposed on strong background, spectra recorded for other incident energies will be presented in an exploded view.

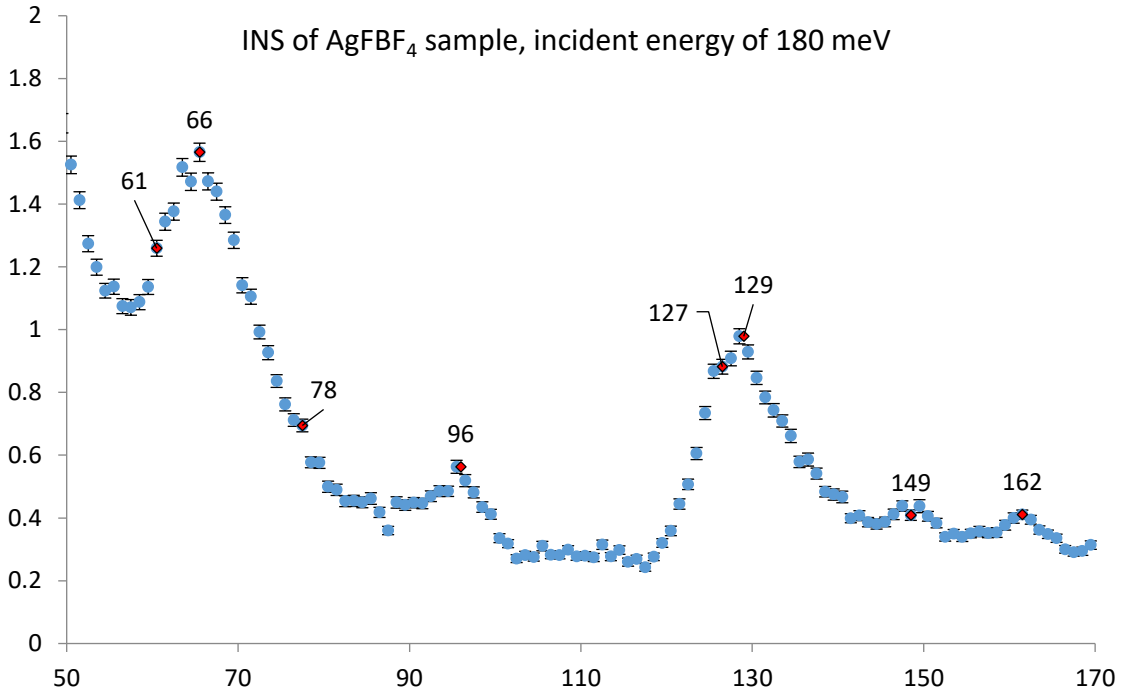

Fig. 131 - INS spectrum of $AgFBF_4$ at incident energy of 180 meV

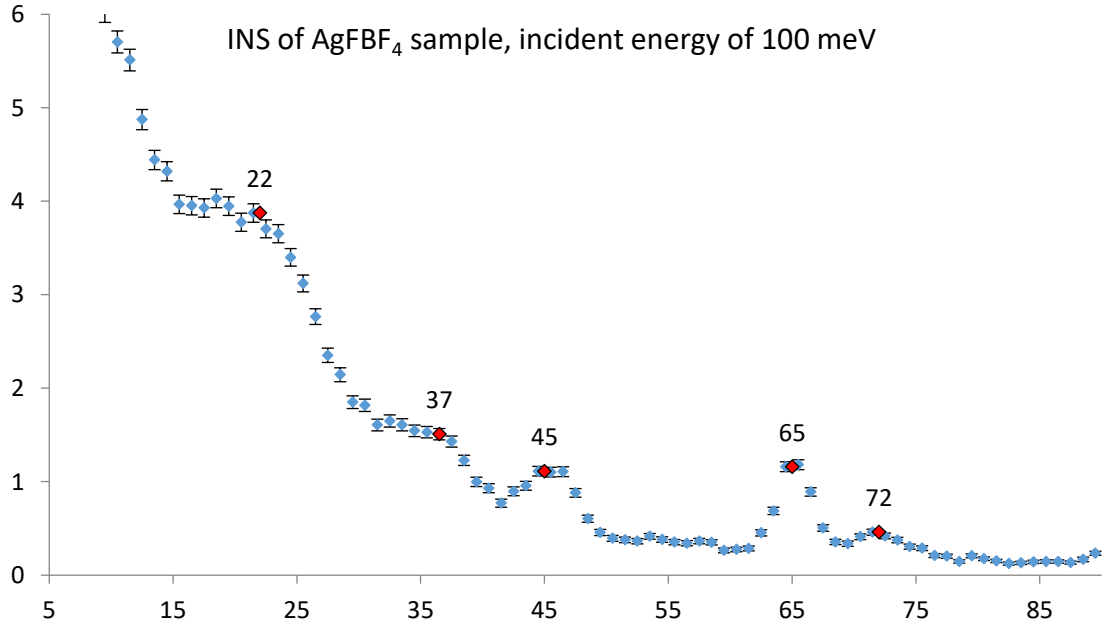

Fig. 132 - The integrated INS spectrum of $AgFBF_4$ at incident energy of 100 meV

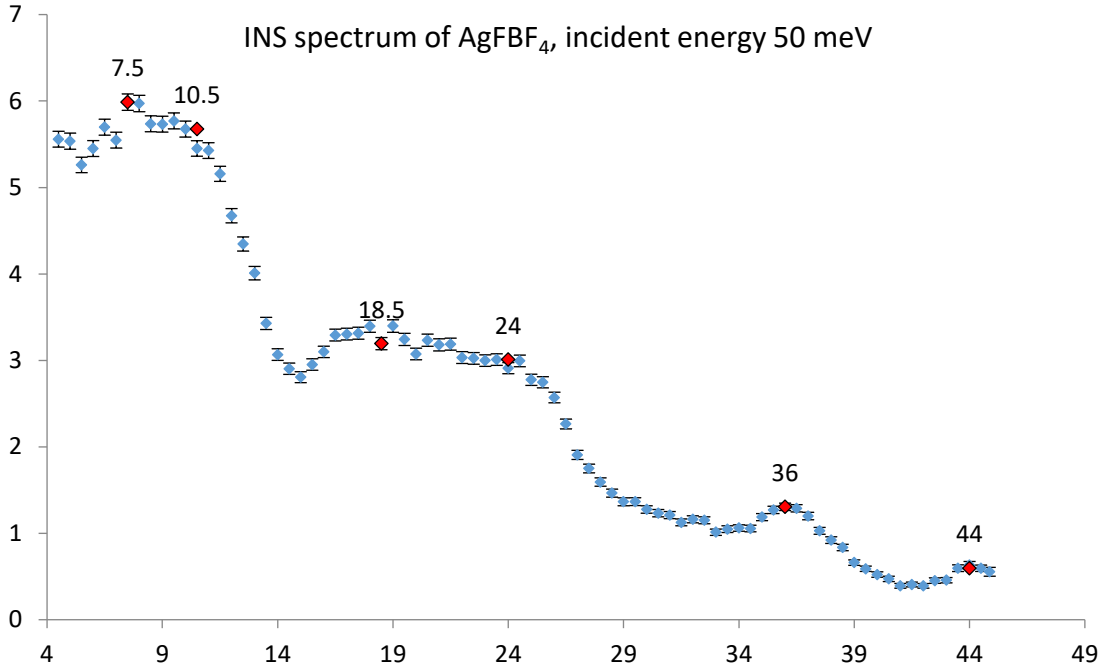

Fig. 133 – The integrated INS spectrum of $AgFBF_4$, incident energy of 50 meV

The data collected in the FIR, Raman and INS measurements of $AgFBF_4$ samples is presented in Tab. 17. The outcome of the measurements showed only vibrational features, which usually agreed with those measured using optical spectroscopies. However, no signal originating from magnetic scattering was observed. One major reason for that failure is that the amount of the sample was very small (*ca.* 12 g) as compared to analogous study conducted for AgF_2 (*ca* 150 g, as described in an earlier subchapter). Another reason is that powder sample and not the oriented single crystal was studied. The third supposed reason was that magnetic bands are much broader for large-J 1D system ($AgFBF_4$) than for smaller-J 2D system (AgF_2) while most of the signal originates from the very top of the band where dispersion is nearly flat (hence, density of states is large). Moreover, due to the shape of the spinon dispersion line $\varepsilon(k) \sim \cos(k)$, the strongest magnetic signal is acquired at low Q, and subsequent binning of data from the whole range of scattering vector might "dilute" the magnetic signal. The fourth sound reason is that $AgFBF_4$ is magnetically diluted (one spin-½ center per 7 atoms) as compared to AgF_2 (one spin-½ center per 3 atoms), while scattering intensity for spin-½ centers is generally low, as it depends on the square of the spin. Last but not least, although the sample of $AgFBF_4$ was synthesized using isotopically enriched boron ^{11}B precursor, yet some 1-2% of strongly neutron absorbing ^{10}B was still present in the sample, thus decreasing the overall signal.

The INS data of $AgFBF_4$ samples contain some artifacts identified by the on-site beam scientist. The signals at 380 meV and 447 eV are to some degree a consequence of traces of oil (most likely ejected in very small amount from a vacuum pump) present in the measurement chamber of the ISIS beamline. The oil vapor does not come into contact with the sample, therefore $AgFBF_4$ did not decompose during the measurements.

B.2.6.1.1 Positions [cm^{-1}] of vibrational bands in $AgFBF_4$: comparison of INS, FIR and Raman data

INS	FIR	Raman	Assignment
60	60		
85	85		
	92		
149	168		
177		177	Possible overtone of 85 cm^{-1} IR band
194	194		
	210		
290	295		
294		300	Possible overtone of the 168 cm^{-1} IR band
	324		
355	355		
363			
		429	Possible overtone of 210 cm^{-1} IR band
	445		
488			
	518		
524	525		
528	533		
581	575		
		576	
	600		
625			
		645	
		709	
774			
		900	Possible overtone of 445 cm^{-1} IR band
1020			Possible overtone of 518 or/and 525 cm^{-1} IR bands. Possible "descendant" of asymmetric stretching of BF_4^-
1036			Possible overtone of 518 or/and 525 cm^{-1} IR bands. Possible "descendant" of asymmetric stretching of BF_4^-
		1059	Possible overtone of 518 or/and 525 cm^{-1} IR bands. Possible "descendant" of asymmetric stretching of BF_4^-
1129			
1198			
1303		1280	
		1590	
2129		2115	Possible overtone of 1059 cm^{-1} Raman band.
2444			
2637			
3121			
3605		3500	Possible second overtone of 1059 cm^{-1} Raman band.

Tab. 17 - Positions and assignments of bands in $AgFBF_4$ spectrum collected from FIR, Raman and INS measurements.

The full assignment of the spectra necessitates good quality theoretical calculations to be performed.

B.2.6.2 NIR spectra of $AgFBF_4$ and AgF_2

The magnetic signals in INS spectra of $AgFBF_4$ could not be detected, due to some reasons described above. Therefore I decided to try supporting the INS data with MIR-NIR absorption experiment, similarly to the method first used by Suzuura for Sr_2CuO_3 [88]. The initial experiments using standard FTIR machine in the 600–4400 cm^{-1} range, with $AgFBF_4$ powder dispersed on the surface CaF_2 windows, have showed the presence of absorption rising systematically towards NIR edge (with a shallow maximum) and then flatting out at higher energies. However, in this setup much of the beam was lost due to scattering on microcrystals, and it was not possible to account for reflectivity and light losses.

Therefore, in the second attempt, since the genuine absorption signal was expected to be weak, the absorption spectra were collected here using a special setup on the machine equipped with the integrating sphere, to eliminate or minimize losses due to scattering on small powder particles.

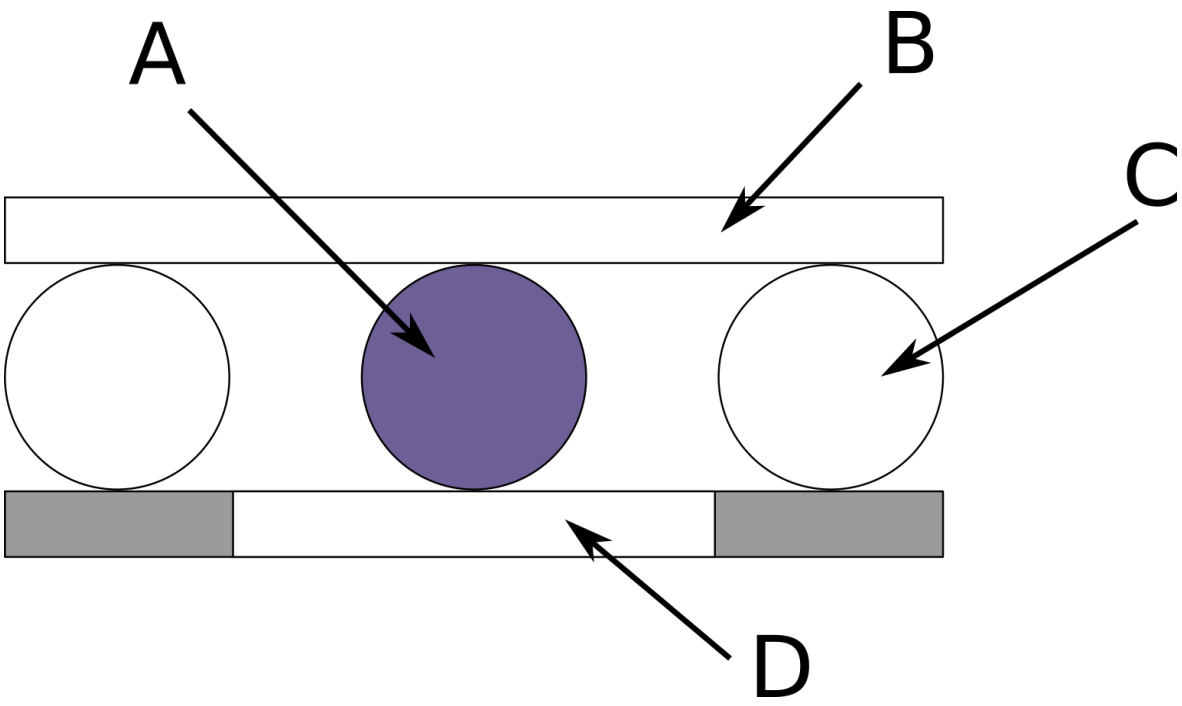

Fig. 134 - scheme of NIR reflectance setup

The NIR spectra were measured using a reflectance measurement component, part of which is schematically presented on Fig. 134. The light illuminates the sample (A) through the hole (D). The reflected light is collected and measured by the detector. Two capillaries (C) ensure that the NIR reflective mirror (B), a disk of a known and very high diffuse reflectivity in the measurement range is perpendicular to the light beam. The diameter of the incoming beam was modified via an aperture to be smaller than the size of the sample-filled capillary.

The NIR spectra of two silver(II) compounds: 1D ($AgFBF_4$), 2D (AgF_2), and a reference Sr_2CuO_3 sample were measured using a Thermo FTIR spectrometer with a InGaAs detector, KBr beamsplitter, halogen NIR source. The samples were enclosed and measured in a quartz capillaries. The spectrum of an empty capillary was used as a blank. Data was collected as reflectance *vs.* wavenumber but is presented in this work as absorbance *vs.* wavenumber. The measurements were conducted at the Institute of Biotechnology and Antibiotics in Warsaw with technical help from Mr Maciej Zosicz, to whom I would like to extend my gratitude.

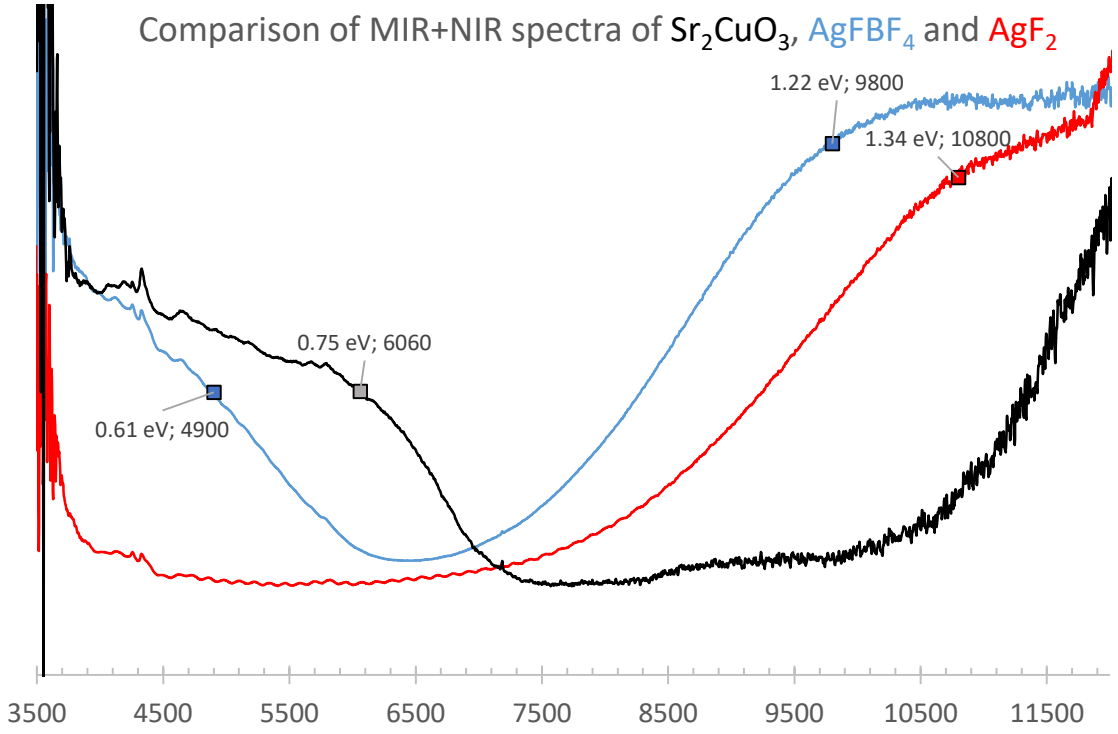

Fig. 135 - comparison of NIR spectra of Sr_2CuO_3, $AgFBF_4$ and AgF_2. Abscissa is wavenumber in cm^{-1} while the ordinate is absorbance in arbitrary units.

The spectra in Fig. 135 are presented as a function of absorbance *vs.* wavenumber in cm^{-1}. Because the measurement range equaled the maximum detector range, the edges of the spectra are very noisy. All spectra contain some artifacts in the vicinity of 4500 cm^{-1} which are caused by deterioration of the reflective NIR mirror (B in Fig. 134).The Sr_2CuO_3 spectrum contains a band roughly at 6060 cm^{-1} that might correspond to an edge of the phonon-assisted multimagnon band found in MIR spectrum of Sr_2CuO_3 (see Fig. 41). The $AgFBF_4$ spectrum contains a band at about 4900 cm^{-1} and 9800 cm^{-1}. While the second band is most likely an electronic d-d transition (as seen in the other compounds containing divalent silver at a similar energy range [159–161]; note that there is also slope of an absorption band

in this range for AgF_2 reference), the first one might correspond to a phonon-assisted multimagnon/spinon band, because $AgFBF_4$ contains 1D antiferromagnetic AgF^+ chains – similar to those present in the Sr_2CuO_3 structure. Importantly, AgF_2 lacks a band at 4900 cm^{-1}, as may be expected for a 2D compound with much smaller J of 70 meV. Therefore, it is justified to derive differential spectrum ($AgFBF_4$ – AgF_2) which should reflect magnetic contribution to the spectrum of $AgFBF_4$ in the low energy range (Fig. 136).

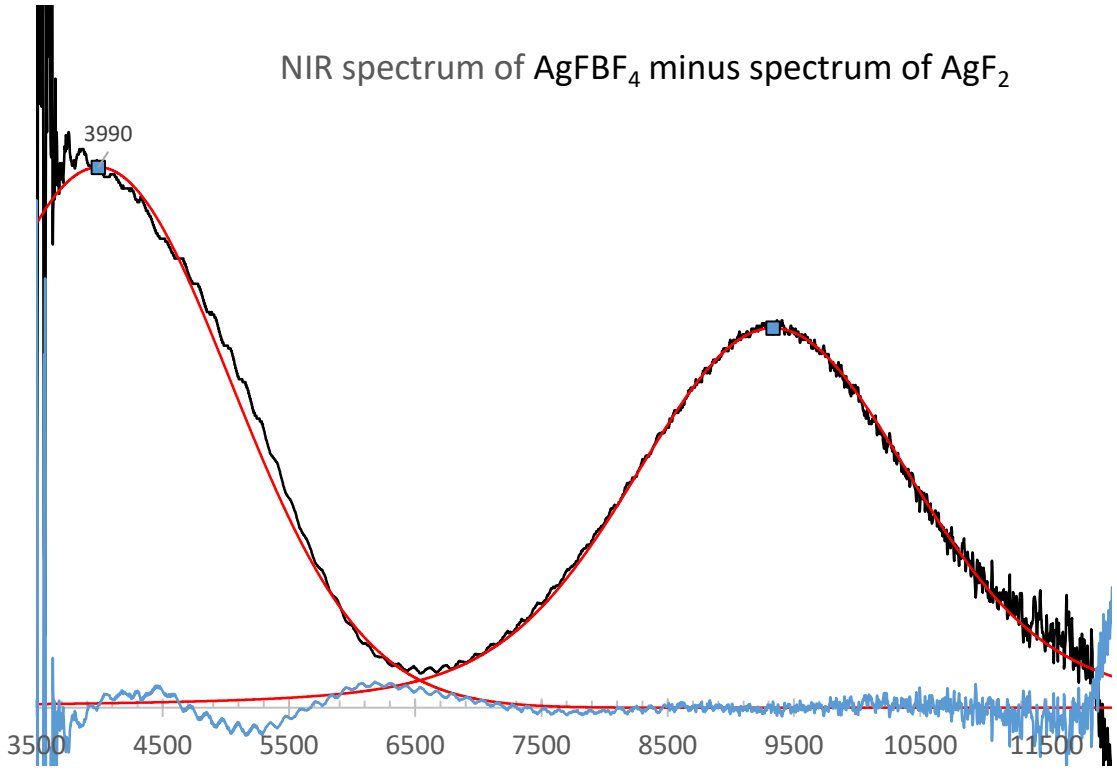

Fig. 136 - differential NIR spectrum of $AgFBF_4$ minus AgF_2. Voigt functions were used to model the spectrum. Maximum of the low-energy band is positioned at 3990 cm^{-1}.

The position of maximum of the low-wavenumber part of the difference spectrum lies at about 3990 cm^{-1} (495 meV)[17]. The energy of the maximum is close to the one obtained by Suzuura for Sr_2CuO_3 (cusp at 0.48 eV) [88]. The spectrum measured here lacks the presence of a characteristic cusp, however, this may be due to polycrystalline form of the sample studied. As mentioned in an earlier subchapter, an energy of the phonon assisted bimagnon transition in a ½-spin antiferromagnetic chain equals an energy of a phonon assisting the process plus $\frac{\pi}{2}J$. The assisting phonon in case of the Sr_2CuO_3 is described as stretching of the $[CuO_{4/2}]$ subunits. A similar Ag–F intrachain stretching phonon is expected to couple most strongly to magnetic fluctuations in $AgFBF_4$. Calculations of phonon dispersion

[17] The exact energy of the maximum is only an estimate, because it is positioned at the edge of the measurement range. This is a consequence of a used reflection-absorption experimental setup.

spectrum are needed to pinpoint the exact energy of the phonon driving the transition, although in this case an educated guess is sufficient. The highest wavenumber bands seen for AgF_2 and corresponding to Ag–F stretching modes did not exceed 500 cm^{-1}. Since the chemical bonding in 1D chain is somewhat stronger than in the 2D case, the associated phonon should have larger energy. Indeed, there is a narrow band at 525 cm^{-1} observed in the FIR spectrum of the $AgFBF_4$ which differs from much broader bands originating from deformations of BF_4 units. Assuming that this is the phonon in question, from:

$$3990 = 525 + \frac{\pi}{2}J$$

we obtain that intrachain J equals *ca.* 2207 cm^{-1} or 273.6 meV. This indicates that the magnetic superexchange constant in $AgFBF_4$ is higher than the one measured in Sr_2CuO_3, 240 meV [162], *i.e.* it sets a new record of the strength of superexchange interactions in solids. We also note that the experimental value is somewhat smaller than the calculated value of 300 meV which was published in a recent theoretical study by Kurzydłowski and Grochala [77].

While this result is certainly interesting, additional confirmation of immense J value should be searched for, for example using RIXS method, before the results are published.

B.2.7 AgO

A sample of commercially available AgO purchased from Alfa Aesar (99.9% purity, grain diameter roughly 50 μm, black color) was used in the Raman measurements under high-pressure. Diamond culet used in the experiment was 250 μm wide. A rhenium gasket 250 μm thick was preindented in two steps, and a 140 μm hole was laser-drilled in it. The sample was loaded under an inert atmosphere and then filled with high-pressure neon reaching 170 MPa. Raman measurements were conducted using 532 nm laser; Rayleigh line was removed using a pair of notch filters. Pressure determination was performed using high-edge frequency of the first-order diamond band measured at the center of culet. The study was done in parallel with hybrid DFT calculations (structure prediction, geometry optimization, vibrational properties). Structural models were fully optimized using HSE06 functional with a plane-wave cut-off of 520 eV and k-spacing of 0.3 $Å^{-1}$ using VASP package. The electronic and total energy calculations were conducted with k-spacing of 0.2 $Å^{-1}$. Lattice dynamics was calculated by dr. Mariana Derzsi D.Sc. using PHONOPY package.

The Raman spectra were collected in the 14.1–74.8 GPa range. The spectrum at the lowest pressure point did not differ qualitatively from the ambient pressure spectrum published by Waterhouse *et al.* [81] – both number and relative positions of bands are similar. The bands move to higher wavenumbers relative to ambient pressure positions, and the first band in the set is more intensive at higher pressure.

DFT calculations for ambient pressure $P2_1/c$ phase of AgO yielded phonon energies of six Raman active vibrations for that structure. The calculated positions were scaled by a factor of 0.96 (within reasonable bounds of DFT error) to better match the experimental data. Obtained values of phonon energies were 223, 307, 414, 480, 483 and 517 cm^{-1}.

The most intense band in the spectrum (414 cm^{-1} calculated, 429 cm^{-1} experimental value) has been assigned to deformation of $[Ag^{III}O_4]$ squares. Lower energy modes were described as in-phase (223 cm^{-1} calc., 217 cm^{-1} exp.) and out-of-phase (307 cm^{-1} calc. and 300 cm^{-1} exp.) stretching vibrations of $[Ag^{I}O_2]$ dumbbells. Higher energy modes were found to be different vibrations of $[Ag^{III}O_4]$ squares. The weak mode seen in AgO spectrum published by Waterhouse *et al.* at 375 cm^{-1} was left unassigned.

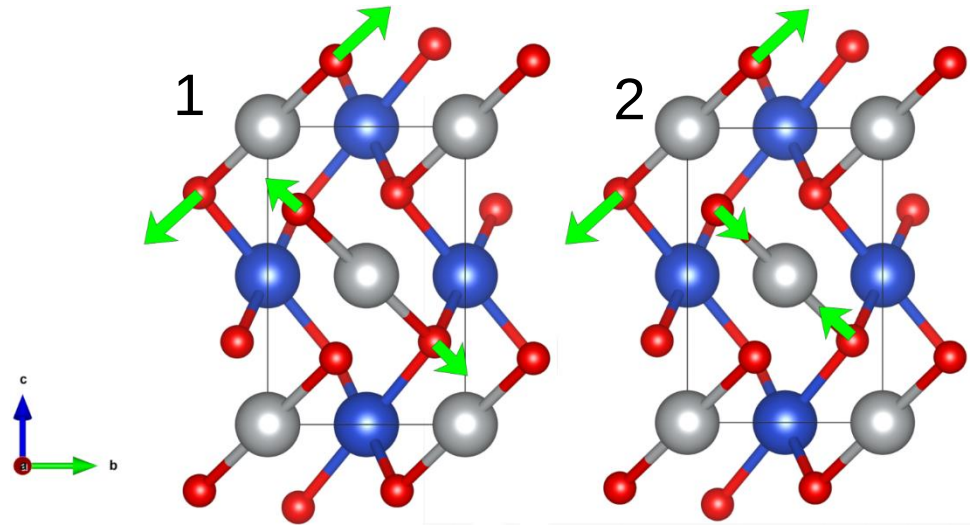

Fig. 137 - dumbbell Raman modes in AgO. Green arrows indicate direction of movement of selected atoms in the cell. Mode no. 1, the in-phase stretching of [$Ag^{I}O_2$] dumbbells has energy of 217 cm^{-1} under ambient pressure. Mode no. 2 is an out-of-phase stretching of [$Ag^{I}O_2$] dumbbells, 300 cm^{-1} at 0 GPa.

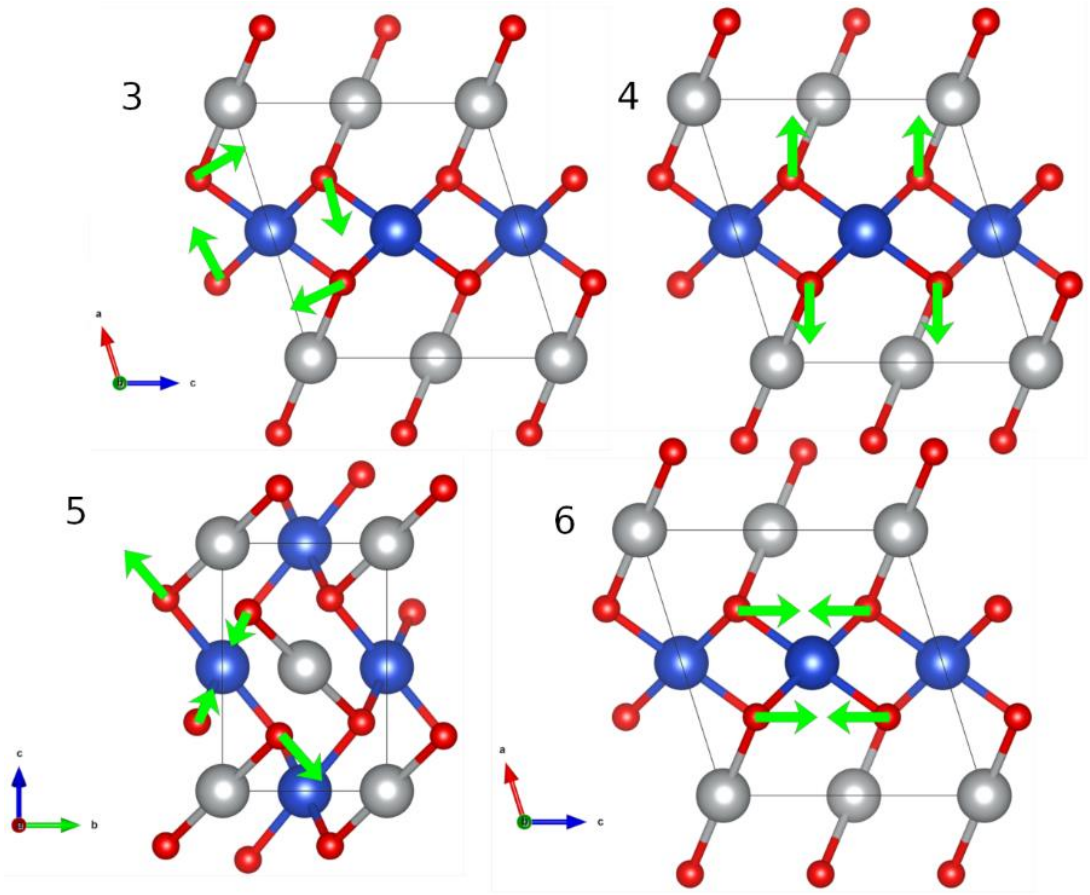

Fig. 138 – [$Ag^{III}O_4$] modes of ambient pressure AgO polymorph. Mode no. 3 (twisting mode) is most intense under 0 GPa.

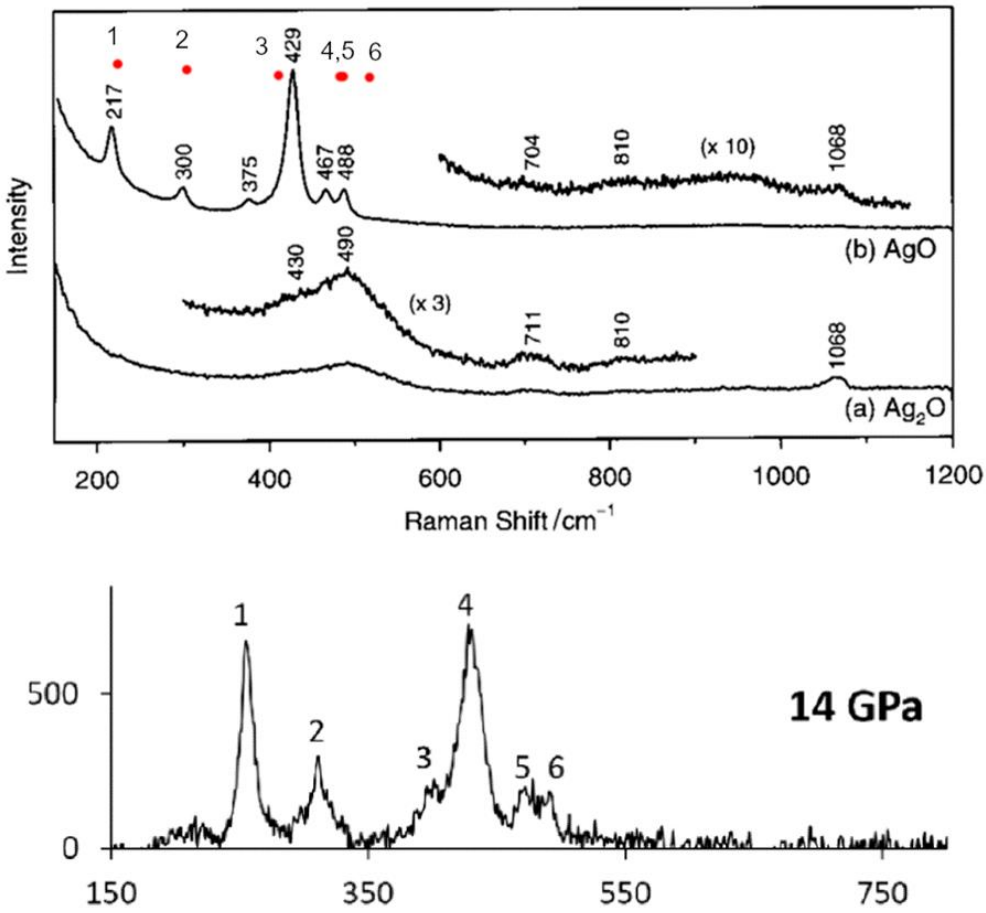

Fig. 139 - comparison of ambient pressure Raman spectrum published by Waterhouse et al. [81], *with one obtained at 14 GPa by Grzelak, Gawraczyński et al.* [163]. *Red dots on the upper spectrum indicate positions of bands obtained through DFT+U calculations, published by Grzelak, Gawraczyński et al.* [163].

Spectrum collected at 22 GPa pressure is similar to the one collected at 14 GPa, although differences are visible. At higher pressure band number 1 decreases in intensity relative to the other bands in the spectrum. Bands 3 and 4 cannot be resolved at the resolution of measurement which indicates a quasi-degeneration of those two phonons. Band number 5 loses intensity, while band number 6 stays more or less the same. All bands shift to the higher wavenumbers as expected.

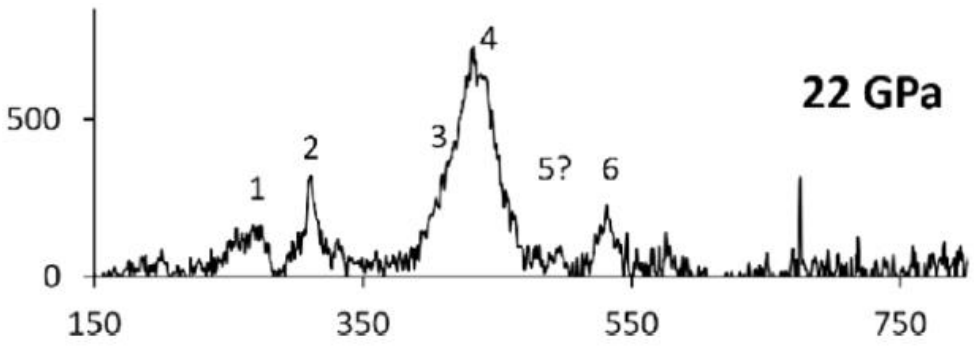

Fig. 140 - Raman spectrum of AgO collected at 22 GPa.

The XRD measurements coupled with DFT calculations indicated, that in the 16-20 GPa range AgO undergoes a phase transition. It occurs with a small but not negligible step decrease in volume. The best representation of the high-pressure polymorph is a monoclinic $P2_1/c$ space group, just like in the ambient pressure structure. The main difference between the two structures lies in the coordination of Ag(I) cations, which changes from linear, CN=2, to cubic, CN=8. This has a consequence in character of Ag(I)-O bonds – changing coordination from linear to a more spherically symmetric must increase the ionic character of the bonds. An expected outcome of this is decrease in intensity of Ag(I)-O vibration modes, which can be seen in Fig. 140. Mode 1 becomes much weaker in the high-pressure phase and possibly splits in two.

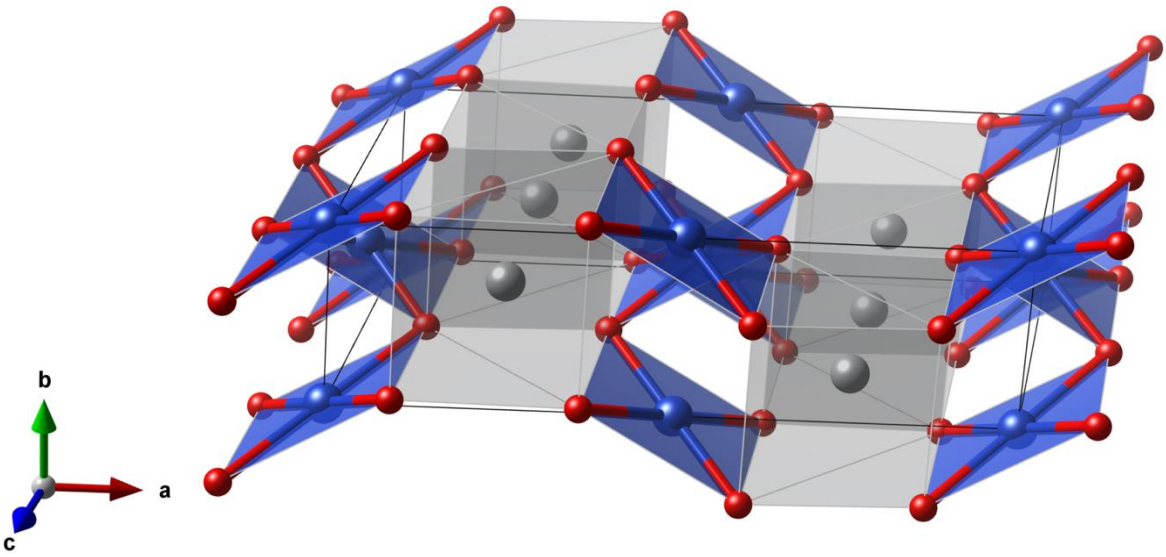

Fig. 141 - a ball-and-stick model of high-pressure phase of AgO (AgO-HP-I) at 20 GPa. For clarity, the Ag(I)-O bonds were omitted. Coordination of Ag(I) cations is slightly distorted cubes. Ag(III) cations are square-coordinated and form a substructure similar to one found in ambient pressure AgO.

Further compression of AgO leads to another phase transition, this time at pressure in 37-42 GPa range. The new phase belongs to an orthorhombic *Imma* group, Z = 8. According to group theory rules, this structure should contain 21 optic modes: 9 Raman-active ($2A_g$ + $2B_{1g}$ + $2B_{2g}$ + $3B_{3g}$) + 10 IR-active ($4B_{1u}$ + $3B_{2u}$ + $3B_{3u}$) + and two silent A_u modes.

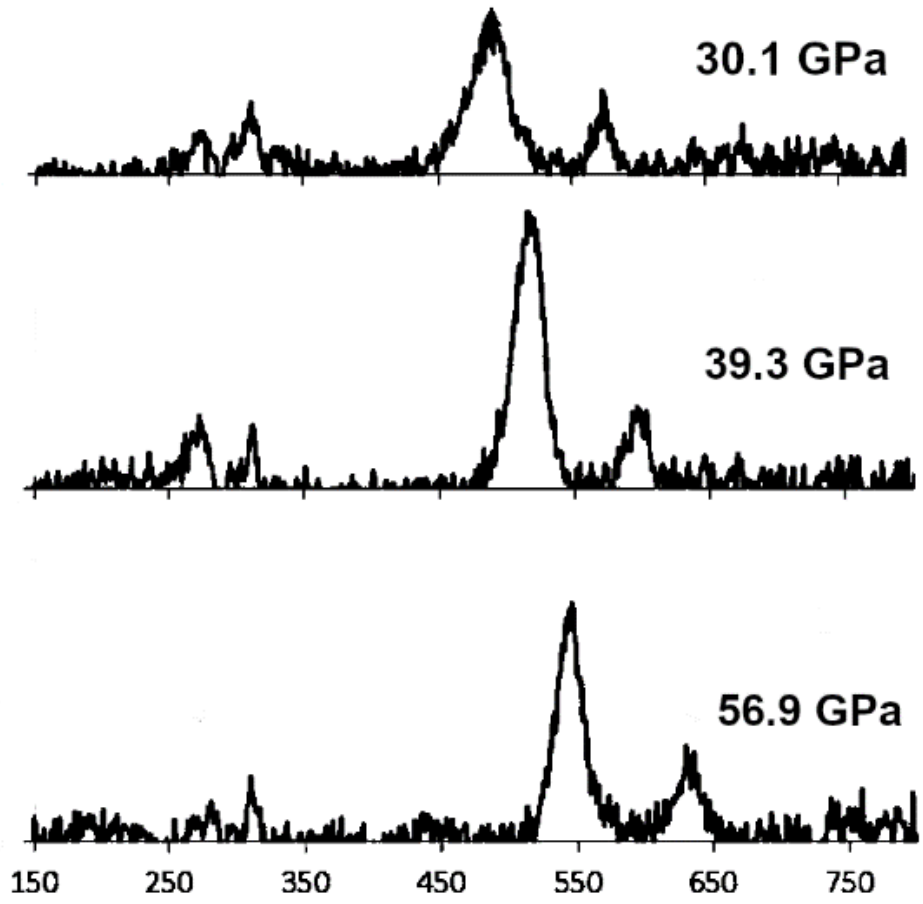

Fig. 142 - Raman spectra of AgO at three different pressures. First measurement was conducted for the pressure range in which AgO-HP-I structure exists. Second one was measured at a pressure in the range of phase transition between HP-I and HP-II forms, and the last one belongs to the HP-II polymorph.

Band no. 2, positioned at about 300 cm^{-1} is present in all measured Raman spectra. It also shifts with pressure much less than any other band in the spectra, almost staying at the position measured at ambient pressure This indicates that some portion of the LP structure has survived the compression in the low-pressure region of the diamond anvil cell.

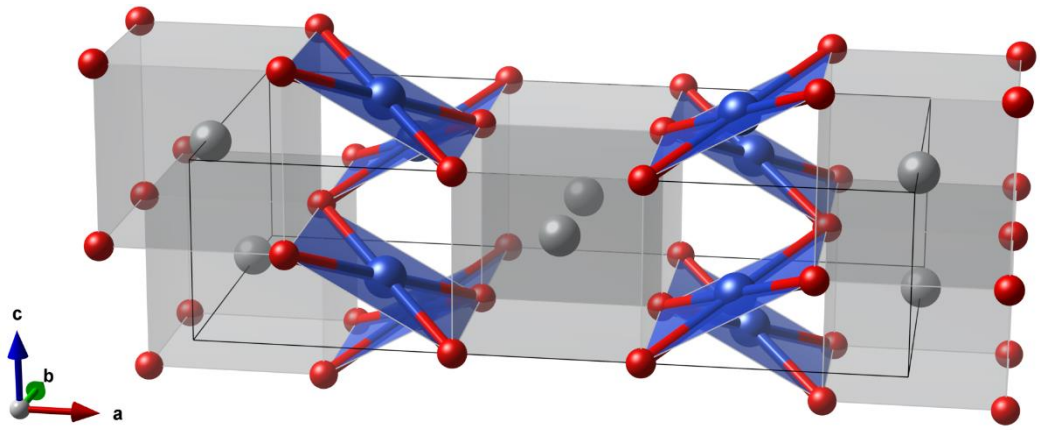

Fig. 143 - a ball and stick model of high-pressure phase of AgO (AgO-HP-II) at 58 GPa. The space group is Imma, each Ag(I) cation is cubically coordinated by 8 oxygen atoms.

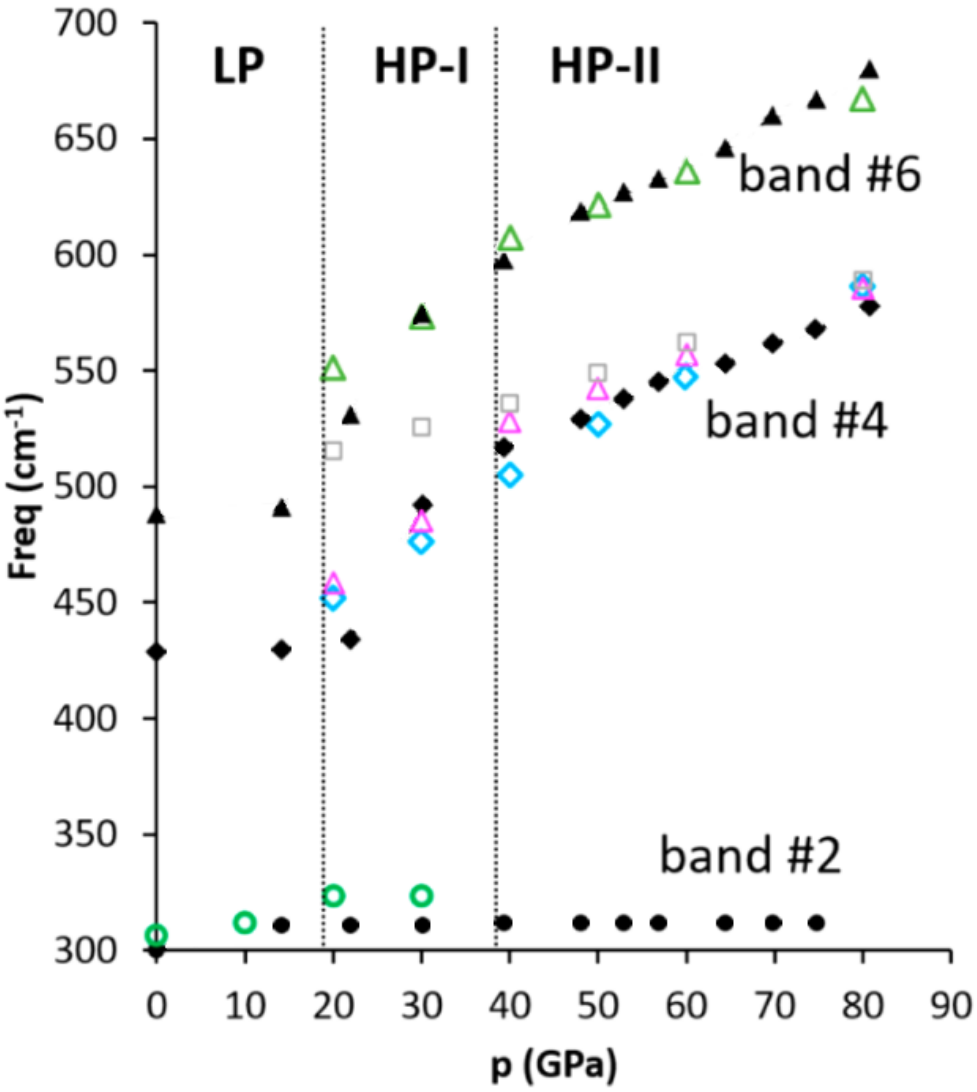

Fig. 144 - pressure dependence of Raman bands in AgO spectra. Filled symbols denote experimental positions of most prominent bands – circles indicate band 2, squares band 4 and triangles band 6. Empty symbols indicate positions of bands calculated from theory – green circles are band 2, blue squares are band 3, pink triangles are number 4, gray squares are number 5 and green triangles are number 6.

The positions of bands calculated by Dr. Derzsi D.Sc. diverge slightly from the experimental values obtained by me (in the 20-40 GPa pressure range). According to calculations, bands 3,4 and 5 converge in the high-pressure limit, which is consistent with behavior observed in the experiment. The experimental positions of band 6 at pressure larger than 30 GPa are very well reproduced via theoretical calculations. However, as the calculations were done along XRD measurements, this provides strong evidence regarding the actual phase transitions occurring in AgO under high pressure and confirms the XRD data collected by Dr. Grzelak.

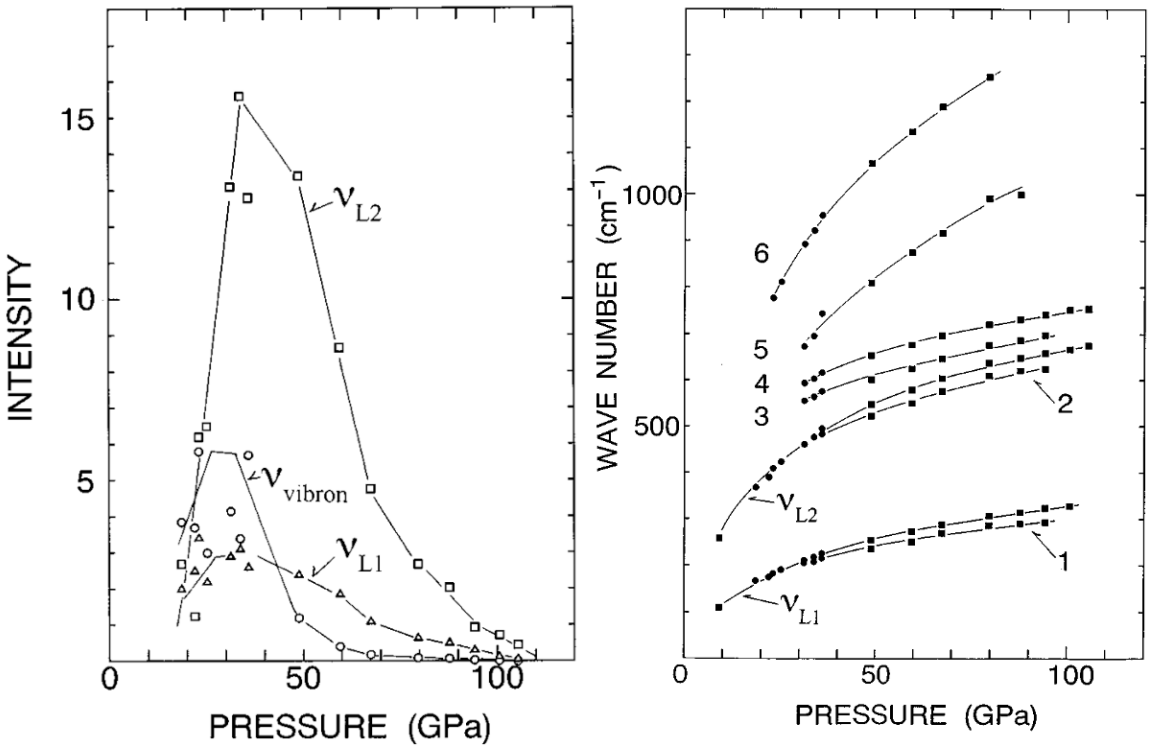

Fig. 145 - vibrational modes of solid oxygen. The left diagram depicts the intensities of three selected vibrational modes of solid oxygen. The right sight depicts a plot of wavenumber vs. pressure for all bands in the Raman spectrum of oxygen.

As seen in Fig. 145 and Fig. 144, the Raman bands of solid oxygen and high-pressure polymorphs of AgO exist in the same wavenumber range. It might in principle be possible that AgO decomposes to solid oxygen some compound of silver (for example Ag_2O, via the reaction: $4AgO \rightarrow 2Ag_2O + O_2$). The counterargument that rules out that possibility is that the number of bands in the experimental AgO spectra is less than the expected number of bands in the solid oxygen. Additionally, as seen in Fig. 142, one cannot find a pair of bands that would approximate the position and intensity ratio of the pair: ν_{L1} and ν_{L2} from the oxygen spectrum (Fig. 145, right side). Thus, chemical decomposition does not occur in the pressure range studied in the experiment.

Summarizing this section, it is worth to notice, that Raman scattering spectroscopy satisfactorily assisted confirmation of the scenario (originating from DFT calculations and x-ray diffraction experiments) of two consecutive pressure-induced phase transitions; since no dramatic changes are seen of the position of Raman bands upon the HP-I to HP-II transition, this transition is of the second order type.

B.2.8 HT-$KAgF_3$, $RbAgF_3$ and $CsAgF_3$

$MAgF_3$ phases are the simplest ternary fluoroargentates(II). They have been studied in the past to understand their crystal structures and magnetic properties [20,58,60,160]. Here, I have analyzed their IR absorption spectra to see, whether they might reveal differences and similarities of the crystal structure of homologous compounds with M=K, Rb, Cs.

The FIR spectra of $KAgF_3$, $CsAgF_3$ and $RbAgF_3$ were measured in solid sample cell for Vertex 80V spectrometer. As in the case of other studied compounds, I used HDPE windows to disperse the samples onto. The powder was loaded under an inert atmosphere in an Ar-filled glovebox. No first-order bands were expected at wavenumbers higher than the upper limit of 700 cm^{-1} shown here.

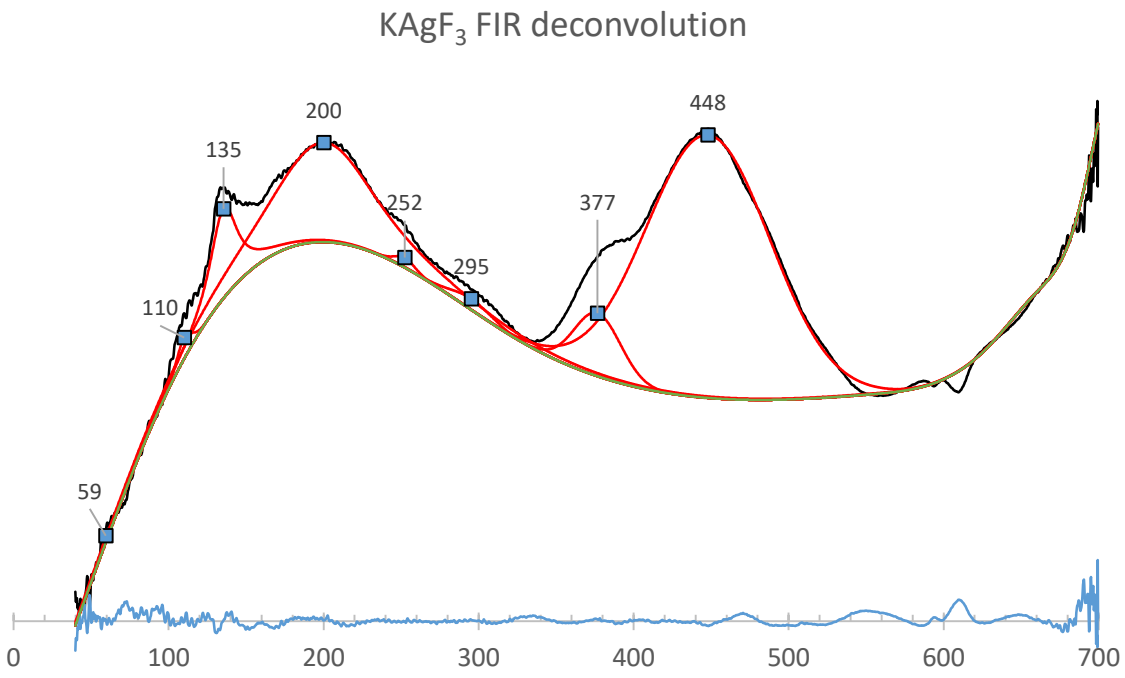

Fig. 146 - FIR spectrum of HT-$KAgF_3$

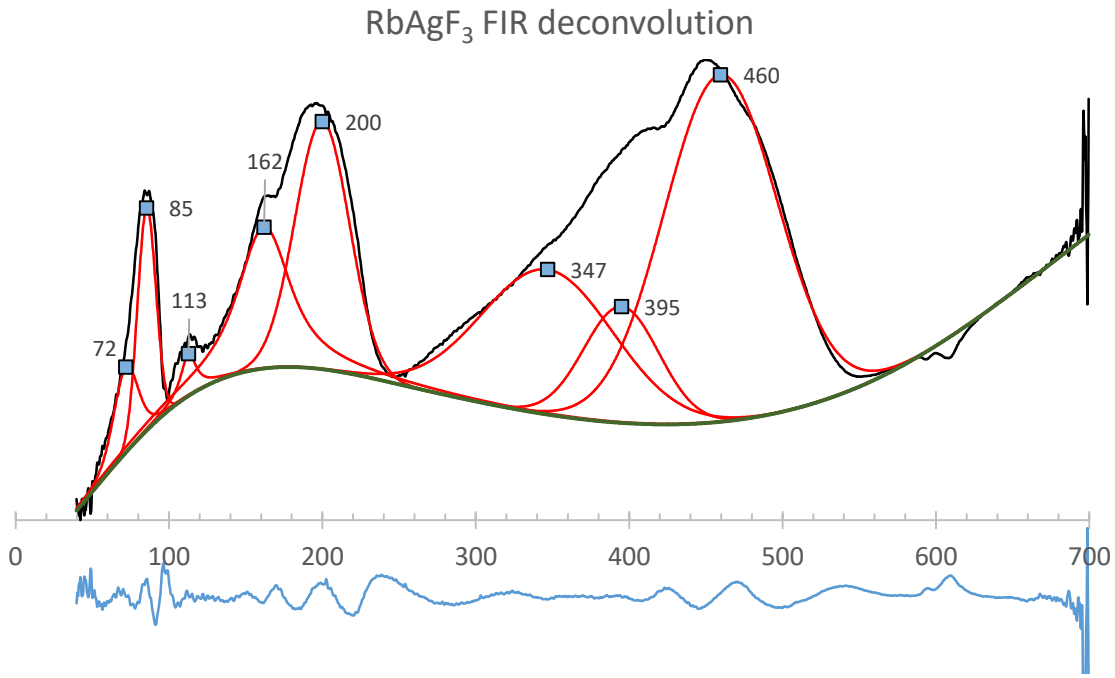

Fig. 147 - FIR spectrum of $RbAgF_3$

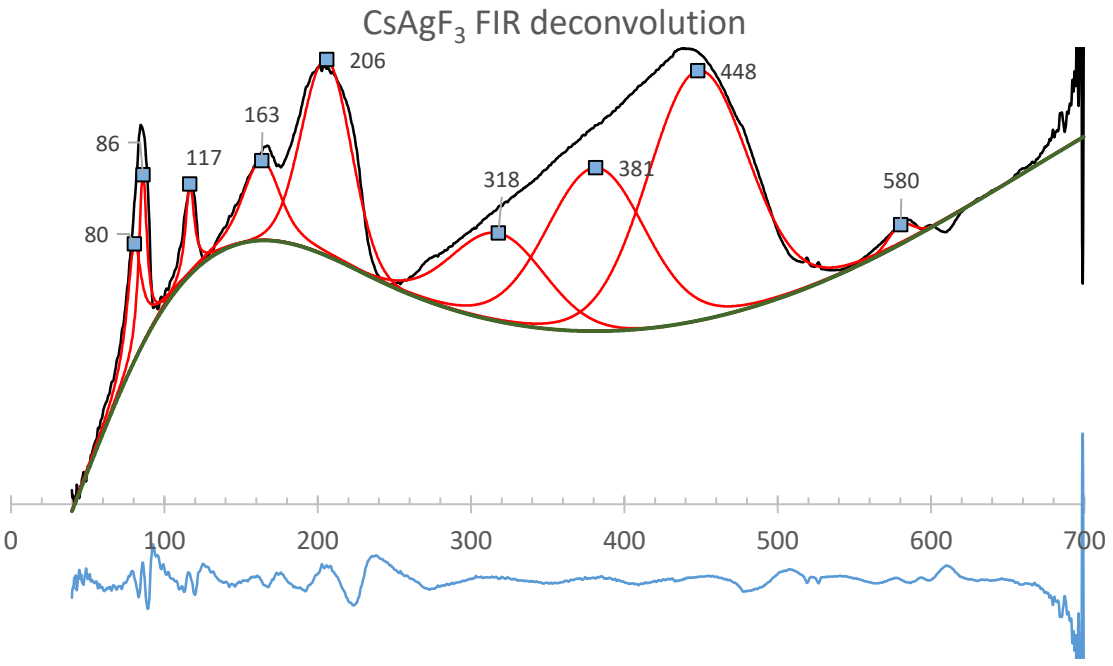

Fig. 148 - FIR spectrum of CsAgF3

Even a cursory look at the spectra the three studied fluoroargentates(II) indicates a great deal of similarity between them. Most of the differences can be seen in the 0–90 cm^{-1} range, where $KAgF_3$ lacks a pair of bands that can be found in Cs and Rb derivatives. This region reflects lattice modes and is naturally strongly alkali-metal dependent. Some difference in intensity ratios of bands between the spectra $CsAgF_3$ and $RbAgF_3$ can be observed, as

described in Tab. 18 below. The structures of three studied fluoroargentates(II) belong to different space groups: *Pcma* (HT-$KAgF_3$), *Pnma* ($RbAgF_3$) and *I4/mcm* ($CsAgF_3$); however, these differences are due rather small structural changes between them. Group theory calculations also predict a different number of IR active vibrational modes: 51 for the HT-$KAgF_3$ phase, 25 for Rb analogue and 9 for Cs one. This might indicate, that their IR spectra should differ significantly. However, a closer look at the structures of both compounds indicates a similar set of structural motifs: chains composed of $[AgF_{2+2/2}]$ squares. The squares belonging to structures have similar average Ag-F bond lengths (2.09 Å in $KAgF_3$, 2.13 Å in $RbAgF_3$, and 2.12 Å in $CsAgF_3$). The difference in motifs geometry is correlated with the size of alkaline metal cation: larger cations induce straightening of the chains (Fig. 150), not changing Ag-F distances dramatically. This might explain some of the similarities found in the FIR spectra of the three fluoroargentates.

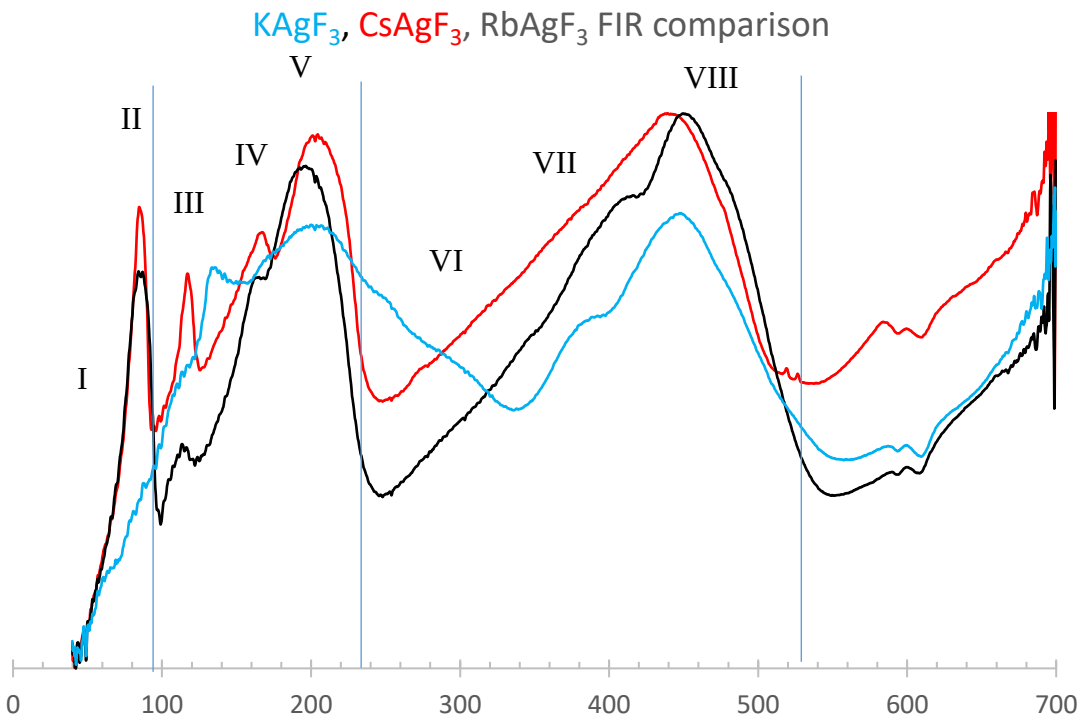

Fig. 149 - comparison of FIR spectra of $CsAgF_3$ and $RbAgF_3$.The blue lines divide spectra into four regions containing similar groups of bands. The roman numerals describe approximate positions of corresponding bands in both spectra.

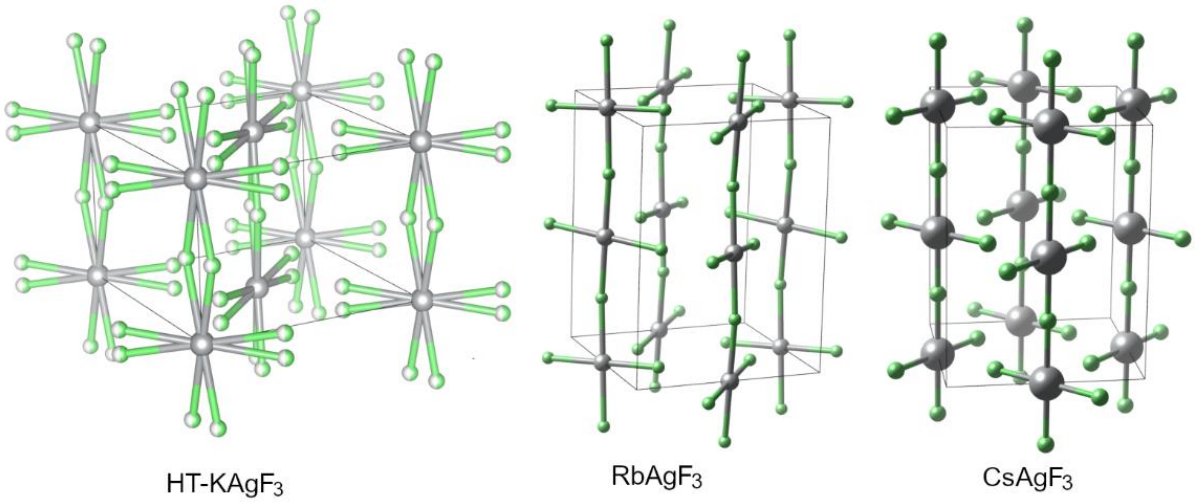

Fig. 150 - comparison of [$AgF_{2+2/2}$] chains in structures of three studied fluoroargentates(II)

The table below depicts ratios of intensities between analogous bands found in FIR spectra of $CsAgF_3$ and $RbAgF_3$, as their spectra are more similar to each other than to HT-$KAgF_3$. The pairs of roman numerals describe which bands were compared. I have computed area and height ratios for each pair of deconvoluted bands and highlighted ratios that differ significantly between two fluoroargentates. For example, in case of pair II/I the ratio of bands area is lower than one for $CsAgF_3$, but higher than one for $RbAgF_3$. Similar difference can also be found for several other pairs. Complete assignment of bands in the spectra will require performing precise DFT calculations of the phonon structure, and will be performed in the future for full assignment of the spectra.

Bands	$CsAgF_3$ Int.Ratio(Height)	$RbAgF_3$ Int.Ratio(Height)	$CsAgF_3$ Int.Ratio(Area)	$RbAgF_3$ Int.Ratio(Area)
II/I	1.446	2.609	0.784	1.738
V/IV	2.461	1.753	2.669	1.295
V/III	2.146	5.872	8.231	13.637
IV/III	0.872	3.349	3.084	10.530
VIII/VII	1.530	2.985	1.528	4.495
VIII/VI	2.833	2.394	3.150	2.050
VII/VI	1.851	0.802	2.061	0.456

Tab. 18 - intensity ratios of selected bands in $CsAgF_3$ and $RbAgF_3$ FIR spectra

B.3 Summary

B.3.1 (EN) Results

Based on my experimental research, supplemented by theoretical calculations carried out by Dr. Mariana Derzsi D.Sc., I have managed to spectroscopically characterize selected silver compounds at atmospheric pressure ($Ag^{II}SO_4$, $[Ag(OH_2)_2][Ag(SO_4)_2]$). X-ray diffraction measurements made by Dr. Adam Grzelak (with my assistance) along with theoretical calculations (again by Dr. Derzsi D.Sc.) and measurements of Raman scattering made by myself under high pressure conditions, have led to understanding of phase transitions and structures of two high pressure silver(I, III) oxide phases. In addition, analysis of silver(I) fluoride and the product of photochemical decomposition of silver(II) fluoride (decomp-AgF_2) over a wide range of pressures showed the presence of a new phase, which likely corresponds to $Ag(I)_2Ag(II)F_4$ and constitutes the product of photochemical decomposition of AgF_2 in the laser beam used for experiments. The series of various measurements on samples of AgF_2 and $AgFBF_4$ resulted in observation of magnetic transitions using spectroscopic methods. I have been able to determine magnetic superexchange constants for low-pressure structures of these important model 2D and 1D systems, respectively. Measurements of the IR absorption of highly reactive ternary compounds ($KAgF_3$, $CsAgF_3$, $RbAgF_3$) showed similarity in their IR spectra despite differences in their crystal structure.

Measurements of Raman spectra for silver(II) sulfate(VI) showed its photosensitivity resulting in decomposition after exposure to sufficiently intense light. I have shown that the decomposition reaction is dependent on the wavelength of the excitation beam – illumination with the infrared beam (1064 nm) led to formation of $Ag_2S_2O_7$, whereas the red beam (632.8 nm) illumination led to formation of an unknown product. Vibrational spectroscopy measurements carried out on the product of Ag_2SO_4 electrosynthesis in concentrated sulfuric(VI) acid played their part in identifying the product as genuine $Ag^{II}SO_4$, more pure and forming larger crystals than the previously known product of chemical synthesis. The so-obtained silver(II) sulfate reacted with water vapor yielding silver(II) sulfate(VI) monohydrate – in contrast to the chemically synthesized $AgSO_4$, which decomposes in contact with atmospheric water. The newly synthesized monohydrate was also studied with vibrational spectroscopy, showing the presence of a broad band centered at about 3300 cm^{-1}, which proved the presence of water molecules in the crystal lattice. The result of the x-ray diffraction experiments and structure solution carried out by Mr. Tomasz Gilewski, as well

as theoretical calculations made by dr. Mariana Derzsi D.Sc. firmly confirmed the presence of water molecules in the structure of the monohydrate. This is a quite interesting result, because this makes silver(II) sulfate(VI) monohydrate the first compound containing in its structure water molecules and highly oxidizing silver(II) cations at the same time.

A sample of silver(I) fluoride studied with Raman spectroscopy in the pressure range from 0 to 27 GPa yielded spectra with an excess of bands in relation to the number expected from group theory. A careful study of spectra as a function of pressure allowed to identify four bands, present in all spectra up from the atmospheric pressure. This suggests that these bands are indicative of the presence of AgF – but their assignment is not straightforward.

Measurements of Raman spectra suggested the decomposition of silver(II) fluoride induced by 514 nm laser light. The decomposition product has not yet been identified, although I have been able to observe a number of spectral features that represent a specific fingerprint of this compound in the range of 0 to 74 GPa. The presence of a 420 cm^{-1} band at atmospheric pressure suggests that it may be a disilver(I) fluoroargentate(II), Ag_2AgF_4. In addition, these measurements allowed to estimate the maximum intensity of the beam that does not yet cause AgF_2 decomposition. This enabled the observation and identification of bimagnon transitions in Raman scattering spectrum of pristine silver(II) fluoride. This result, in combination with the DFT+U calculations and inelastic neutron scattering measurements led to the determination of the magnetic superexchange constant for AgF_2 (equal to 70 meV). This is a valuable result in the perspective of further research on derivatives of this compound, the only known proper analog of copper oxides. Adequate doping may lead to the formation of a superconductor. The modification that would lead to flattening of the corrugated $[AgF_{4/2}]$ layers in AgF_2 should increase almost twice the strength of magnetic interaction, reaching a J value higher than in the model La_2CuO_4 compound (higher than 120–130 meV), as indicated by DFT calculations.

Extensive studies have been carried out for $AgFBF_4$. Measurements of far-infrared absorption spectroscopy, Raman scattering and inelastic neutron scattering allowed to determine the position of bands in the range from 60 to about 3600 cm^{-1}. The measurement of reflection-absorption spectroscopy in the range from 3500 to 12000 cm^{-1} revealed the electronic d-d transition with an energy of approximately 9800 cm^{-1} (1020 nm, 1.2 eV) and a band with a maximum at approximately 3990 cm^{-1} (495 meV). The second signal likely comes from a combined phonon-spinon transition previously observed in other compounds

containing antiferromagnetic chains (notably for Sr_2CuO_3). The intra-chain superexchange constant, J, derived for $AgFBF_4$ from this measurement, exceeds 267 meV. The analogous value for record-holding Sr_2CuO_3 is smaller (240 meV), which suggests that the $AgFBF_4$ is the most strongly coupled system currently known.

Measurements of Raman scattering *vs.* pressure conducted for the AgO sample allowed to reaffirm the high-pressure phase structures (HP-I: with $P2_1/c$ symmetry, adopted in 16-20 GPa range and HP-II, with $Imma$ symmetry, adopted in 37-42 GPa range) obtained from powder X-ray diffraction analysis and theoretical calculations. Presence of bands corresponding to both $[Ag^{I}O_2]$ dumbbells and $[Ag^{III}O_4]$ squares in all spectra suggests that at the compound stays disproportionated in the studied pressure range. The HP-I phase contains silver(I) cations in a slightly distorted cube composed of oxygen anions. In the HP-II phase the oxygens form a perfect cube which correlates well with the weakening of the $[Ag^{I}O_2]$ dumbbell modes. Good agreement of the positions of the bands obtained from the calculations with the positions obtained as a result of the measurements in both high-pressure phases verifies the predicted pressure-induced structural changes in silver(I, III) oxide. In addition, analysis of Raman spectra excluded the decomposition of AgO to oxygen and other silver compounds up to a pressure of about 75 GPa.

Measurements of far-infrared absorption spectroscopy for fluoroargentates(II): $KAgF_3$, $CsAgF_3$ and $RbAgF_3$, showed very similar structure of the vibrational spectra of those compounds, despite adopting different space groups. Explanation of this phenomenon is most likely related to the similarity of structural motifs in both compounds. Full assignment of vibrational features necessitates performing of the precise DFT calculations of phonon dispersion.

Research conducted during the doctoral studies resulted in six associated original scientific articles, with four more coauthored papers that were not directly associated with the thesis.

B.3.2 (PL) Podsumowanie wyników

Na podstawie przeprowadzonych przeze mnie badań, uzupełnionych przez obliczenia teoretyczne przeprowadzane przez dr hab. Marianę Derzsi, udało się scharakteryzować wybrane związki srebra pod ciśnieniem atmosferycznym ($Ag^{II}SO_4$, $[Ag(OH_2)_2][Ag(SO_4)_2]$). Pomiary dyfrakcji rentgenowskiej wykonane przez dr. Adama Grzelaka (przy mojej asyście) wraz z obliczeniami teoretycznymi (dr hab. Derzsi) i pomiarami rozproszenia ramanowskiego wykonanymi przeze mnie pod wysokim ciśnieniem doprowadziły do zrozumienia natury przemian fazowych indukowanych ciśnieniem i rozwiązania struktur dwóch wysokociśnieniowych faz tlenku srebra(I,III). Ponadto przeanalizowałem dane dotyczące fluorku srebra(I) i produktu fotochemicznego rozkładu fluorku srebra(II) (decomp-AgF_2) w szerokim zakresie ciśnień. Zapewne odpowiada on wzorowi chemicznemu $Ag(I)_2Ag(II)F_4$.

Dzięki przeprowadzeniu serii różnorodnych pomiarów na próbkach AgF_2 i $AgFBF_4$, udało się w rzeczonych substancjach zaobserwować przy użyciu technik spektroskopowych przejścia magnetyczne. Na podstawie pomiarów wyznaczyłem również stałe nadwymiany magnetycznej dla niskociśnieniowych struktur tych ważnych związków modelowych (odpowiednio: dwuwymiarowego i jednowymiarowego). Wstępne pomiary spektroskopii absorpcyjnej w zakresie dalekiej podczerwieni związków trójskładnikowych o wysokiej reaktywności ($KAgF_3$, $CsAgF_3$, $RbAgF_3$) wykazały podobieństwo ich widm pomimo różnic w strukturze krystalicznej.

Pomiary spektroskopii Ramana przeprowadzone dla siarczanu(VI) srebra(II) wykazały jego fotoczułość skutkującą rozkładem po naświetleniu światłem o odpowiedniej intensywności, ponadto zaobserwowano tworzenie różnych produktów rozkładu w zależności od długości fali wiązki wzbudzającej – wiązka podczerwona (1064 nm) prowadziła do powstania $Ag_2S_2O_7$, zaś wiązka czerwona (632.8 nm) do powstania nieznanego jeszcze produktu. Produkt elektrosyntezy Ag_2SO_4 w stężonym kwasie siarkowym(VI), m.in. dzięki przeprowadzonym przeze mnie pomiarom spektroskopii oscylacyjnej, został zidentyfikowany jako $Ag^{II}SO_4$, czystszy chemicznie; charakteryzuje się on większymi kryształami niż wcześniej znany produkt syntezy chemicznej. Czystość chemiczna nowego produktu miała swoje konsekwencje w reakcji z parą wodną: zsyntezowany chemicznie siarczan(VI) srebra(II) ulega w kontakcie z nią rozkładowi, podczas gdy elektrochemiczny $AgSO_4$ tworzy z nią monohydrat siarczanu(VI) srebra(II). Ten nowy związek został również zbadany za pomocą spektroskopii oscylacyjnej. W widmie FTIR zarejestrowane zostało

szerokie pasmo scentrowane na ok. 3300 cm^{-1}. Wyniki analiz pomiarów dyfrakcji rentgenowskiej wykonanych przez mgr. Tomasza Gilewskiego oraz obliczeń teoretycznych wykonanych przez dr hab. Marianę Derzsi jednoznacznie potwierdził obecność w strukturze monohydratu cząsteczek wody. Jest to ciekawy wynik, gdyż monohydrat siarczanu(VI) srebra(II) stanowi pierwszy i jedyny znany do tej pory przykład związku zawierającego w swej strukturze jednocześnie cząsteczki wody i silnie utleniające srebro(II).

Próbka fluorku srebra(I) zbadana z zastosowaniem spektroskopii Ramana w zakresie ciśnień od 0 do 27 GPa odznaczała się nadmiarem pasm w stosunku do liczby oczekiwanej z rozważań na gruncie teorii grup. Zestawienie widm w funkcji ciśnienia pozwoliło na zidentyfikowanie czterech pasm, obecnych we wszystkich widmach już od pomiaru przeprowadzonego poza kowadłem diamentowym, pod ciśnieniem atmosferycznym. To sugeruje, że te pasma są faktycznie związane z obecnością AgF choć ich przypisanie jest nieoczywiste.

Pomiary spektroskopii ramanowskiej wykazały istnienie procesu rozkładu fluorku srebra(II) wywołanego oświetlaniem laserem o długości fali 514 nm. Produkt rozkładu nie został jeszcze zidentyfikowany, aczkolwiek udało mi się zaobserwować szereg cech spektralnych stanowiących swoisty odcisk palca tego związku w zakresie od 0 do 74 GPa. Obecność pasma 420 cm^{-1} przy ciśnieniu atmosferycznym sugeruje, iż może to być fluorosrebrzan(II) srebra(I), Ag_2AgF_4. Ponadto pomiary te pozwoliły na oszacowanie intensywności wiązki pozwalającej zminimalizować rozkład AgF_2, co poskutkowało przeprowadzeniem pomiarów rozpraszania Ramana w których zarejestrowałem przejścia bimagnonowe. Wynik ten w połączeniu z obliczeniami DFT+U oraz pomiarami nieelastycznego rozpraszania neutronów doprowadził do wyznaczenia stałej nadwymiany magnetycznej dla AgF_2 (równej 70 meV). Stanowi to cenny wynik w perspektywie dalszych badań nad pochodnymi tego związku, będącego pełnoprawnym analogiem kupratów. Odpowiednie domieszkowanie go może bowiem doprowadzić do wytworzenia nadprzewodnika. Modyfikacja polegająca na wyprostowaniu pofałdowanych warstw $[AgF_{4/2}]$ powinna bowiem zwiększyć niemal dwukrotnie stałą nadwymiany magnetycznej, osiągając wartość wyższą niż w modelowym związku La_2CuO_4 (więc powyżej 120–130 meV) jak pokazują obliczenia teoretyczne.

Szeroko zakrojone badania zrealizowano dla $AgFBF_4$. Pomiary spektroskopii absorpcyjnej w dalekiej podczerwieni, rozpraszania ramanowskiego i nieelastycznego rozproszenia neutronów pozwoliły na wyznaczenie pozycji pasm w zakresie od 60 do około 3600 cm^{-1}.

Pomiar spektroskopii odbiciowo-absorpcyjnej w zakresie od 3500 do 12000 cm^{-1} ujawnił przejście elektronowe d-d o energii około 9800 cm^{-1} (1020 nm, 1.2 eV) oraz pasmo o maksimum równym około 3990 cm^{-1} (495 meV). Drugi sygnał najprawdopodobniej pochodzi od jednoczesnego przejścia fononowo-spinonowego, obserwowanego wcześniej w innych związkach zawierających antyferromagnetyczne łańcuchy (przykładowo Sr_2CuO_3). Stała nadwymiany wewnątrzłańcuchowej wyznaczona dla $AgFBF_4$ przekracza 267 meV. Analogiczna stała dla Sr_2CuO_3 wynosi 240 meV, co sugeruje, że $AgFBF_4$ jest najsilniej sprzężonym magnetycznie układem znanym obecnie.

Pomiary rozproszenia ramanowskiego w funkcji ciśnienia przeprowadzone dla próbki AgO pozwoliły na potwierdzenie wysokociśnieniowych struktur (HP-I, grupa przestrzenna $P2_1/c$, przejście fazowe w zakresie 16–20 GPa, HP-II, grupa przestrzenna $Imma$, przejście fazowe w zakresie 37–42 GPa) uzyskanych z analizy proszkowej dyfrakcji rentgenowskiej i obliczeń teoretycznych. Obecność pasm odpowiadających zarówno skoordynowanym liniowo fragmentom $[Ag^{I}O_2]$ jak i kwadratom $[Ag^{III}O_4]$ we wszystkich widmach sugeruje, że związek ten nie ulega synproporcjonacji w badanym zakresie ciśnień. Faza HP-I zawiera kationy srebra(I) skoordynowane przez aniony tlenu tworzące zniekształcony sześcian. Koordynacja owych kationów w fazie HP-II przybiera postać sześcianu, co dobrze koreluje z osłabianiem się modów związanych z drganiem liniowych grup $[Ag^{I}O_2]$. Dobra zgodność (w obu fazach wysokociśnieniowych) pozycji pasm uzyskanych z obliczeń z pozycjami uzyskanymi w wyniku pomiarów uwiarygadnia wnioski dotyczące przemian strukturalnych tlenku srebra(I,III) indukowanych ciśnieniem. Ponadto, analiza widm ramanowskich wykluczyła rozkład AgO do tlenu i innych tlenków srebra aż do ciśnienia około 75 GPa.

Pomiary spektroskopii absorpcyjnej w zakresie dalekiej podczerwieni fluorosrebrzanów(II): $KAgF_3$, $CsAgF_3$ i $RbAgF_3$, pokazały bardzo duże podobieństwo struktur oscylacyjnych tych związków, pomimo krystalizacji w różnych grupach przestrzennych. Wyjaśnienie tego zjawiska najprawdopodobniej związane jest z podobieństwem motywów strukturalnych w związkach. Pełne przypisanie widm wymaga przeprowadzenia obliczeń teoretycznych.

Wyniki badań eksperymentalnych przeprowadzonych w trakcie doktoratu zostały opublikowane w sześciu publikacjach wydanych przez czasopisma z listy Filadelfijskiej. Dodatkowo, w trakcie doktoratu byłem współautorem czterech innych prac niezwiązanych bezpośrednio z moimi badaniami (dwie z nich znajdują się również na liście Filadelfijskiej).

B.3.3 (EN) Prospects for future research

Some of the problems undertaken during the research so far proved to be more complex than expected at the beginning. For example, measurements of Raman spectroscopy of an AgF_2 sample carried out under high pressure were found to be problematic due to the laser-induced decomposition. Future research should set out to overcome some of these problems - for example, by collecting spectra on different laser lines, or at a reduced temperature, or by spinning the sample studied. In the case of high-pressure studies of silver(II) fluoride, an additional advantage is the existence of experimentally confirmed high-pressure structural models – possible experiments may thus be supplemented with theoretical calculations.

Experimental redetermination of the magnetic superexchange constant (e.g. with RIXS method) as well as its dependence on external pressure for AgF_2 and $AgFBF_4$ is also a viable direction for future research (theoretical data exists [77,164]). For AgF_2 it can also be an indispensable preliminary step for research into electron/hole doping – and in the long run on the synthesis of new superconductors.

Another interesting research direction would be a study of excitons in the AgF_2. The examination of MIR, NIR and higher energy regions spectra of silver(II) fluoride could probe the exotic processes that might occur in this compound.

The ability to study highly reactive compounds by spectroscopic methods acquired during the Ph.D. will certainly help in the future characterization of magnetic properties (also in high pressure regime) of other silver compounds (II) – for example, perovskites ($MAgF_3$) or double perovskites (M_2AgF_4). The experiments conducted *in silico* would also be immeasurably useful, for example for achieving full assignment of bands appearing in the spectra of $KAgF_3$, $CsAgF_3$ and $RbAgF_3$.

B.3.4 (PL) Perspektywa przyszłych badań

Część z problemów podjętych w trakcie przeprowadzonych do tej pory badań okazała się być bardziej złożona niż zakładano na początku. Przykładowo, pomiary spektroskopii ramanowskiej próbki AgF_2 przeprowadzane pod wysokim ciśnieniem okazały się być problematyczne z uwagi na wywołany światłem lasera rozkład próbki. Przyszłe badania powinny postawić jako jeden z celów przezwyciężenie tych problemów – na przykład poprzez pomiary na innych liniach wzbudzających, w obniżonej temperaturze, lub z wirowaniem próbki badanej. W przypadku wysokociśnieniowych badań nad fluorkiem srebra(II) dodatkową zaletą jest istnienie potwierdzonych eksperymentalnie modeli faz wysokociśnieniowych – ewentualne doświadczenia będą mogły być wobec tego uzupełnione o obliczenia teoretyczne.

Interesującą kontynuacją przeprowadzonych badań będzie też próba eksperymentalnego potwierdzenia wartości stałej nadwymiany magnetycznej (np. z użyciem metody RIXS) oraz wyznaczenia jej zależności od ciśnienia dla AgF_2 i $AgFBF_4$ (problem ten był już badany z użyciem obliczeń teoretycznych [77,164]). Dla AgF_2 może stanowić to również niezbędny wstępny etap do badań nad domieszkowaniem – i w dalszej perspektywie nad syntezą nowych nadprzewodników.

Innym interesującym kierunkiem badań byłyby wzbudzenia ekscytonowe w AgF_2. Zarejestrowanie widm MIR, NIR i w wyższych energiach umożliwiłoby przestudiowanie nietypowych właściwości tego związku i procesów w nim zachodzących.

Nabyta w trakcie doktoratu umiejętność badania metodami spektroskopowymi związków wysoce reaktywnych na pewno przysłuży się w przyszłości do lepszego scharakteryzowania właściwości magnetycznych (również w zakresie wysokich ciśnień) innych związków srebra(II) – przykładowo perowskitów ($MAgF_3$) czy podwójnych perowskitów (M_2AgF_4). Warte uwagi wydaje się też przeprowadzenie wspomnianych badań *in silico*: pomogłoby to na przykład w kompletnym przypisaniu pasm obserwowanych w widmach $KAgF_3$, $CsAgF_3$ i $RbAgF_3$.

C. Literature

[1] N. W. Ashcroft, D. N. Mermin, *Solid State Physics*, Harcourt College Publishers, **1976**.

[2] P. Połczyński et al., *Chem. Commun.* **2013**, *49*, 7480–7482.

[3] *CRC Handbook of Chemistry and Physics, 96th Edition (Internet Version 2016)*, CRC Press/Taylor And Francis, Boca Raton, FL, **2016**.

[4] Z. Mazej et al., Unique Silver(II) Fluorides: The Emerging Electronic and Magnetic Materials in*: Photonic and Electronic Properties of Fluoride Materials: Progress in Fluorine Science Series*, Elsevier, **2016**.

[5] Z. Mazej et al., *Dalt. Trans.* **2015**, *44*, 10957–10968.

[6] C. Friebel, D. Reinen, *Z. Anorg. Allg. Chem.* **1975**, *413*, 51–60.

[7] W. Grochala, R. Hoffmann, *Angew. Chemie Int. Ed.* **2001**, *40*, 2742–2781.

[8] J. G. Bednorz, K. A. Müller, *Z. Phys. B - Condens. Matter* **1986**, *64*, 189–193.

[9] W. Grochala et al., *ChemPhysChem* **2003**, *4*, 997–1001.

[10] K. Yvon et al., *J. Solid State Chem.* **1986**, *65*, 225–230.

[11] J. A. McMillan, *J. Inorg. Nucl. Chem.* **1960**, *13*, 28–31.

[12] H. Firouzabadi et al., *Bull. Chem. Soc. Jpn.* **1992**, *65*, 2878–2880.

[13] J. L. Manson et al., *J. Am. Chem. Soc.* **2009**, *131*, 4590–4591.

[14] P. C. Leung et al., *Can. J. Chem.* **1979**, *57*, 326–329.

[15] P. J. Malinowski et al., *CrystEngComm* **2011**, *13*, 6871.

[16] G. W. A. Fowles et al., *J. Chem. Soc. A* **1968**, 1108–1113.

[17] C.-Q. Jin et al., *Proc. Natl. Acad. Sci.* **2008**, *105*, 7115–7119.

[18] S. Margadonna, G. Karotsis, *J. Am. Chem. Soc.* **2006**, *128*, 16436–16437.

[19] T. Tomio et al., *J. Appl. Phys.* **1994**, *76*, 5886–5890.

[20] R. H. Odenthal et al., *Z. Anorg. Allg. Chem.* **1974**, *407*, 144–150.

[21] J. M. Longo, P. M. Raccah, *J. Solid State Chem.* **1973**, *6*, 526–531.

[22] D. Balz, K. Plieth, *Ber. Bunsenges. Phys. Chem.* **1955**, *59*, 545–551.

[23] M. Hidaka, P. J. Walker, *Solid State Commun.* **1979**, *31*, 383–385.

[24] M. Ishizuka et al., *J. Magn. Magn. Mater.* **1998**, 725–726.

[25] L. Pauling, *J. Am. Chem. Soc.* **1929**, *51*, 1010–1026.

[26] P. Bhardwaj, *Acta Phys. Pol. A* **2013**, *124*, 677–684.

[27] P. M. Halleck et al., *J. Phys. Chem. Solids* **1972**, *33*, 769–773.

[28] B. Okai, *Phys. B+C* **1986**, *139–140*, 221–223.

[29] K. M. Glassford et al., *Solid State Commun.* **1990**, *76*, 635–638.

[30] J. Riga et al., *Phys. Scr.* **1977**, *16*, 351–354.

[31] R. D. Shannon, *Solid State Commun.* **1968**, *6*, 139–143.

[32] W. H. Baur, *Acta Cryst. B* **1976**, *32*, 2200–2204.

[33] D. Gerlich et al., *Phys. Rev. B* **1984**, *29*, 2142–2147.

[34] P. A. Popov et al., *Phys. Solid State* **2010**, *52*, 504–508.

[35] C. Chatzichristodoulou et al., *J. Electroceramics* **2015**, *34*, 100–107.

[36] V. G. Keramidas, W. B. White, *J. Chem. Phys.* **1973**, *59*, 1561–1562.

[37] J. Haines et al., **1997**, *14*, 1910–1914.

[38] L. S. Dubrovinsky et al., *Nature* **2001**, *410*, 653–654.

[39] J. S. Wang et al., **2012**, *186*, 231–234.

[40] J. A. Barreda-Argüeso et al., *Phys. Rev. B* **2013**, *88*, 214108.

[41] J. Haines et al., *Phys. Rev. B* **2001**, *64*, 134110.

[42] D. Kurzydłowski, *Crystals* **2018**, *8*, 140–152.

[43] J. B. Kirwin et al., *J. Phys. Chem.* **1963**, *67*, 1617–1621.

[44] H. Ott, *Z. Krist.* **1925**, *63*, 222–230.

[45] A. P. Marchetti, G. L. Bottger, *Phys. Rev. B* **1971**, *3*, 2604–2607.

[46] D. J. Wilson et al., *Phys. Rev. B* **2008**, *77*, 064115.

[47] S. Hull, P. Berastegui, *J. Phys. Condens. Matter* **1998**, *10*, 7945–7955.

[48] M. S. Ebert et al., *J. Am. Chem. Soc.* **1933**, *55*, 3056–3057.

[49] C. Shen et al., *Inorg. Chem.* **1999**, *38*, 4570–4577.

[50] P. Fischer et al., *J. Phys. Chem. Solids* **1971**, *32*, 1641–1647.

[51] A. Jesih et al., *Z. Anorg. Allg. Chem.* **1990**, *588*, 77–83.

[52] P. Fischer et al., *J. Phys. Chem. Solids* **1971**, *32*, 543–550.

[53] I. Dzyaloshinsky, *J. Phys. Chem. Solids* **1958**, *4*, 241–255.

[54] T. Moriya, *Phys. Rev. Lett.* **1960**, *4*, 228–230.

[55] W. J. Casteel et al., *J. Solid State Chem.* **1992**, *96*, 84–96.

[56] J. William Jack Casteel, The synthesis and structural characterization of novel transition metal fluorides, PhD Thesis, University of California, **1992**.

[57] W. Grochala, *J. Supercond. Nov. Magn.* **2017**, 1–16.

[58] R. H. Odenthal, R. Hoppe, *Monats. Chem.* **1971**, *102*, 1340–1350.

[59] D. Kurzydłowski, Fluorosrebrzany (II) metali alkalicznych – struktura krystaliczna, przejścia fazowe oraz właściwości magnetyczne, PhD Thesis, University of Warsaw, **2012**.

[60] D. Kurzydłowski et al., *Chem. Commun.* **2013**, *49*, 6262–6264.

[61] D. Kurzydlowski, W. Grochala, *Phys. Rev. B* **2017**, *96*, 155140.

[62] J. Kanamori, *J. Phys. Chem. Solids* **1959**, *10*, 87–98.

[63] J. B. Goodenough, *Magnetism and the Chemical Bond*, John Wiley & Sons, Inc., New York, **1963**.

[64] P. W. Anderson, *Solid State Phys. - Adv. Res. Appl.* **1963**, *14*, 99–214.

[65] Z. Mazej et al., *CrystEngComm* **2009**, *11*, 1702–1710.

[66] R. H. Odenthal, R. Hoppe, *Z. Anorg. Allg. Chem.* **1971**, *385*, 92–101.

[67] D. Kurzydłowski et al., *Inorg. Chem.* **2016**, *55*, 11479–11489.

[68] D. Kurzydłowski et al., *Eur. J. Inorg. Chem.* **2010**, 2919–2925.

[69] P. J. Malinowski et al., *Angew. Chemie Int. Ed.* **2010**, *49*, 1683–1686.

[70] M. Derzsi et al., *CrystEngComm* **2013**, *15*, 192–198.

[71] M. B. Robin, P. Day, *Adv. Inorg. Chem. Radiochem.* **1968**, *10*, 247–422.

[72] P. Tissot, *Polyhedron* **1987**, *6*, 1309–1311.

[73] von C. L. Teske, H. Muller-Buschbaum, *Z. Anorg. Allg. Chem.* **1969**, *371*, 325–332.

[74] A. C. Walters et al., *Nat. Phys.* **2009**, *5*, 867–872.

[75] S. Chakravarty et al., *Phys. Rev. B* **1989**, *39*, 2344–2371.

[76] R. Coldea et al., *Phys. Rev. Lett.* **2001**, *86*, 5377–5380.

[77] D. Kurzydłowski, W. Grochala, *Angew. Chemie Int. Ed.* **2017**, *56*, 10114.

[78] G. L. Bottger, A. L. Geddes, *J. Chem. Phys.* **1972**, *56*, 3735–3739.

[79] E. Burstein et al., *Phys. Rev.* **1965**, *139*, 1239–1245.

[80] M. Derzsi et al., *Vib. Spectrosc.* **2011**, *57*, 334–337.

[81] G. I. N. Waterhouse et al., *Phys. Chem. Chem. Phys.* **2001**, *3*, 3838–3845.

[82] I. Włodarska, Modeling of the electronic and magnetic structure as well as crystal lattice dynamics of silver oxide AgO under high pressure using Density Functional Theory, PhD Thesis, Warsaw Technical University, **2014**.

[83] Y. S. Lee et al., *Phys. Rev. B* **2000**, *62*, 5285.

[84] O. V. Misochko et al., *Phys. Rev. B* **1996**, *53*, R14733–R14736.

[85] A. S. Moskvin et al., *Phys. Rev. Lett.* **2003**, *91*, 037001.

[86] K. H. Kim et al., *Phys. Rev. Lett.* **1996**, *77*, 1877–1880.

[87] S. Sugai, *Phys. Rev. B* **1989**, *39*, 4306–4315.

[88] H. Suzuura et al., *Phys. Rev. Lett.* **1996**, *76*, 2579–2582.

[89] J. Lorenzana et al., *Proc. SPIE - Int. Soc. Opt. Eng.* **1996**, *2696*, 160.

[90] J. Lorenzana, R. Eder, *Phys. Rev. B* **1997**, *55*, R3358–R3361.

[91] K. B. Lyons et al., *Phys. Rev. B* **1988**, *37*, 2353–2356.

[92] S. Sugai et al., *Phys. Rev. B* **1988**, *3*, 6436–6439.

[93] A. M. Zaitsev, *Optical Properties of Diamond*, Springer, Berlin, **2001**.

[94] J. Walker, *Reports Prog. Phys.* **1979**, *42*, 1605–1659.

[95] K. Iakoubovskii, A. T. Collins, *J. Phys. Condens. Matter* **2004**, *16*, 6897–6906.

[96] C. D. Clark et al., *Phys. Rev. B* **1995**, *51*, 16681–16688.

[97] W. G. Stirling, M. J. Cooper, **1999**, *200*, 755–773.

[98] J. W. Kim et al., *J. Phys. Condens. Matter* **2005**, *17*, L493–L497.

[99] M. Usuda et al., **2004**, *345*, 30–33.

[100] M. G. Cottam, D. J. Lockwood, *J. Magn. Magn. Mater.* **1986**, *54–57*, 1143–1144.

[101] E. Meloche et al., *J. Magn. Magn. Mater.* **2004**, *272–276*, 275–277.

[102] E. Meloche et al., *Phys. Rev. B* **2010**, *81*, 024426.

[103] R. Newman, R. M. Chrenko, *Phys. Rev.* **1959**, *114*, 1507–1513.

[104] M. C. Aronson et al., *Phys. Rev. B* **1991**, *44*, 4657–4660.

[105] V. V. Struzhkin et al., *Mater. Sci. Eng. A* **1993**, *168*, 103–106.

[106] P. A. Fleury, R. Loudon, *Phys. Rev.* **1968**, *166*, 514–530.

[107] J. Lorenzana, A. Sawatzky, *Phys. Rev. B* **1995**, *52*, 9576–9589.

[108] M. J. Massey et al., *Phys. Rev. B* **1990**, *42*, 8776–8779.

[109] R. W. Johnston, D. C. Cronemeyer, *Phys. Rev.* **1954**, *93*, 634–635.

[110] V. V. Struzhkin et al., *Phys. Rev. B* **2000**, *62*, 3895–3899.

[111] V. V. Struzhkin, X. J. Chen, *Low Temp. Phys.* **2016**, *42*, 884–890.

[112] M. Ishizuka et al., *J. Phys. Condens. Matter* **2006**, *18*, 2935–2941.

[113] V. V. Struzhkin, X. Chen, *Low Temp. Phys.* **2016**, *42*, 884–890.

[114] L. J. De Jongh, R. Block, *Phys. B+C* **1975**, *79*, 568–593.

[115] D. Bloch, *J. Phys. Chem. Solids* **1966**, *27*, 881–885.

[116] A. Van Der Pol et al., *Phys. B+C* **1976**, *19*, 177–179.

[117] S. R. Chinn et al., *J. Appl. Phys.* **1970**, *41*, 894–895.

[118] J. Pebler et al., *Z. Anorg. Allg. Chem.* **2004**, *630*, 829–840.

[119] R. Korber et al., *Supercond. Sci. Technol.* **2016**, *29*, 113001.

[120] Y. Liu et al., *Phys. C Supercond. its Appl.* **2014**, *497*, 34–37.

[121] C. Anzolini et al., *Am. Mineral.* **2018**, *103*, 69–74.

[122] E. S. Izraeli et al., *Earth Planet. Sci. Lett.* **1999**, *173*, 351–360.

[123] H. Kagi et al., *Mineral. Mag.* **2000**, *64*, 1089–1097.

[124] Y. Feng et al., *Nat. Commun.* **2014**, *5*, 1–6.

[125] R. J. Angel et al., *J. Appl. Crystallogr.* **1997**, *30*, 461–466.

[126] W. B. Holzapfel, *J. Appl. Phys.* **2003**, *93*, 1813–1818.

[127] Y. Akahama, H. Kawamura, *J. Phys. Conf. Ser.* **2010**, *215*, 012195.

[128] D. L. Heinz, R. Jeanloz, *J. Appl. Phys.* **1984**, *55*, 885–893.

[129] A. Dewaele et al., *Phys. Rev. B* **2008**, *77*, 094106.

[130] R. J. Hemley et al., *Phys. Rev. B* **1989**, *39*, 11820–11827.

[131] M. Matsui et al., *J. Appl. Phys.* **2009**, *105*, 013505.

[132] D. M. Trots et al., *J. Geophys. Res. Solid Earth* **2013**, *118*, 5805–5813.

[133] S. V. Rashchenko et al., *J. Appl. Phys.* **2015**, *117*, 145902.

[134] S. Klotz et al., *J. Phys. D. Appl. Phys.* **2009**, *42*, 075413.

[135] K. Takemura et al., *J. Phys. Conf. Ser.* **2010**, *215*, 012017.

[136] G. J. Piermarini et al., *J. Appl. Phys.* **1975**, *46*, 2774–2780.

[137] H. K. Mao et al., *J. Geophys. Res* **1986**, *91*, 4673–4676.

[138] A. Dewaele et al., *Phys. Rev. B* **2008**, *78*, 104102.

[139] S. N. Vaidya, G. C. Kennedy, *J. Phys. Chem. Solids* **1971**, *32*, 951–964.

[140] J. C. Jamieson et al., *J. Phys. Chem. Solids* **1975**, *36*, 939–944.

[141] I. Włodarska et al., *Phys. status solidi - Rapid Res. Lett.* **2015**, *9*, 401–404.

[142] C. J. Hou et al., *Phys. Chem. Chem. Phys.* **2016**, *18*, 15322–15326.

[143] M. Derzsi, W. Grochala, *Phys. Chem. Chem. Phys.* **2016**, *18*, 31973–31974.

[144] P. Połczyński et al., *Eur. J. Inorg. Chem.* **2016**, *2016*, 5401–5404.

[145] T. E. Gilewski et al., *Dalt. Trans.* **2016**, *45*, 18202–18207.

[146] T. E. Gilewski et al., *Chem. - A Eur. J.* **2017**, *23*, 1805–1813.

[147] P. J. Leszczyński et al., *J. Fluor. Chem.* **2019**, *218*, 105–110.

[148] A. Grzelak et al., *Inorg. Chem.* **2017**, *56*, 14651–14661.

[149] G. Lucazeau, *J. Raman Spectrosc.* **2003**, *34*, 478.

[150] J. Zhao et al., *Phys. Rev. B* **2006**, *73*, 184434.

[151] D. S. Ellis et al., *Phys. Rev. B - Condens. Matter Mater. Phys.* **2010**, *81*, 1–12.

[152] P. J. Freitas, R. R. P. Singh, *Phys. Rev. B - Condens. Matter Mater. Phys.* **2000**, *62*, 5525–5530.

[153] J. Gawraczyński et al., *Proc. Natl. Acad. Sci.* **2019**, *116*, 1495–1500.

[154] J. Romiszewski et al., *J. Phys. Condens. Matter* **2007**, *19*, 116206.

[155] A. Grzelak, Crystal structure and selected physical properties of AgO, AgF_2 and $AgCl_x$ phases under high pressure, PhD Thesis, University of Warsaw, **2018**.

[156] M. Wojdyr, *J. Appl. Crystallogr.* **2010**, *43*, 1126–1128.

[157] P. Knoll et al., *Phys. Rev. B* **1990**, *42*, 4842–4845.

[158] H. A. Bonadeo, E. Silberman, *Spectrochim. Acta Part A Mol. Spectrosc.* **1970**, *26*, 2337–2343.

[159] J. Tong et al., *Z. Anorg. Allg. Chem.* **2012**, *638*, 1792–1795.

[160] X. Yang, H. Su, *Sci. Rep.* **2015**, *5*, 15849–15854.

[161] R. Valiente et al., *J. Phys. Condens. Matter* **1994**, *6*, 4515–4525.

[162] C. de Graaf, F. Illas, *Phys. Rev. B* **2000**, *63*, 014404.

[163] A. Grzelak et al., *Inorg. Chem.* **2017**, *56*, 5804–5812.

[164] J. Lorenzana et al., *Chem. Commun.* **2018**, *54*, 10252–10255.

D. List of coauthored publications

D.1 Publications associated with the PhD thesis

1. J. Gawraczyński, D. Kurzydłowski, R. A. Ewings, S. Bandaru, W. Gadomski, Z. Mazej, G. Ruani, I. Bergenti, T. Jaroń, A. Ozarowski, S. Hill, P. J. Leszczyński, K. Tokár, M. Derzsi, P. Barone, K. Wohlfeld, J. Lorenzana, W. Grochala,"Silver route to cuprate analogs", *Proc. Natl. Acad. Sci.* **2019**, *116*, 1495

2. A. Grzelak, J. Gawraczyński, T. Jaroń, D. Kurzydłowski, A. Budzianowski, Z. Mazej, P. J. Leszczyński, V. B. Prakapenka, M. Derzsi, V. Struzhkin, W. Grochala, „High-Pressure Behavior of Silver Fluorides up to 40 GPa", *Inorganic Chemistry*, **2017**, *56*, 14651 (equal contribution of the first two authors)

3. A. Grzelak, J. Gawraczyński, T. Jaroń, D. Kurzydłowski, Z. Mazej, P. J. Leszczyński, V. B. Prakapenka, M. Derzsi, V. Struzhkin, W. Grochala, „Metal fluoride nanotubes featuring square-planar building blocks in a high-pressure polymorph of AgF_2", *Dalton Transactions*, **2017**, *46*, 14742 (equal contribution of the first two authors)

4. A. Grzelak, J. Gawraczyński, T. Jaroń, M. Somayazulu, M. Derzsi, V. Struzhkin, W. Grochala, „Persistence of Mixed and Non-intermediate Valence in the High-Pressure Structure of Silver(I,III) Oxide, AgO: A Combined Raman, X-ray Diffraction (XRD), and Density Functional Theory (DFT) Study", *Inorganic Chemistry*, **2017,** *56*, 5804 (equal contribution of the first two authors)

5. T. E. Gilewski, J. Gawraczyński, M. Derzsi, Z. Jagličić, Z. Mazej, P. Połczyński, R. Jurczakowski, P. J. Leszczyński, W. Grochala, „$[Ag(OH_2)_2][Ag(SO_4)_2]$: A Hydrate of a Silver(II) Salt", *Chem. Eur. J.*, **2017**, *23*, 1805 (equal contribution of the first two authors)

6. P. Połczyński, T. E. Gilewski, J. Gawraczyński, M. Derzsi,P. J. Leszczyński, W. Gadomski, Z. Mazej, R. Jurczakowski, W. Grochala, (2016), „Efficient Electrosynthesis of $Ag^{II}SO_4$: A Powerful Oxidizer and Narrow Band Gap Semiconductor", *Eur. J. Inorg. Chem.*, **2016**, 5401

D.2 Other papers published during the PhD studies

7. A. Budniak, M. Masny, K. Prezelj, M. Grzeszkiewicz, J. Gawraczynski, Ł. Dobrzycki, M. Cyrański, W. Koźmiński, Z. Mazej, K. Fijałkowski, W. Grochala, P. J. Leszczyński, „Reconnaissance of reactivity of an Ag(II)SO_4 one-electron oxidizer towards naphthalene derivatives", *New J. Chem.*, **2017**, *41*, 10742

8. P.J. Leszczyński, A. K. Budniak, M. Grzeszkiewicz, J. Gawraczyński., Ł. Dobrzycki, P.J. Malinowski, T. Jaroń, M. K. Cyrański, P. Szarek, Z. Mazej, W. Grochala, „Insights into reactivity patterns of Ag(II)SO_4 with respect to fluoro- and trifluoromethyl-substituted aromatics", *J. Fluor. Chem.*, **2019**, *218*, 105

9. O. Łabędź, A. Huczko, J. Gawraczyński, H. Lange, C. Czosnek, J. F. Janik, „Carbon arc plasma: characterization and synthesis of nanosized SiC", *J. Phys.: Conf. Ser.*, **2014**, *511*

10. K. Nowak, D. Markiewicz, J. Gawraczyński, P. Mazurkiewicz, „Cross-Country Comparisons of Environmental Concern", *Problemy Zarządzania*, **2016**, *14*, 83

D.3 Copies of papers and supplementary materials associated with the PhD thesis